Synthesis and characterisation of some osmium and ruthenium complexes and the application of $Os(bpy)_2$-(pyridine-4-COOH)-Cl in an electrochemical DNA biosensor

Denis McCrudden

Letterkenny Institute of Technology

Department of Science

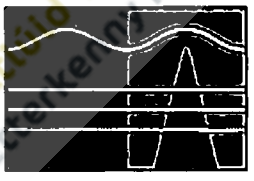

Internal Supervisor : Dr. John Slater, Letterkenny Institute of Technology

External Supervisor : Dr. Donal Leech, National University of Ireland Galway

Submitted to the Higher Education and Training Awards Council (HETAC) in fulfilment of the requirements for the degree of Doctor of Philosophy

August 2008

Abstract

This thesis details the synthesis and characterisation of seven osmium and ruthenium bipyridyl complexes, reports on their electrochemical characteristics and outlines an application for one of the synthesised complexes in an electrochemical DNA biosensor.

Complexes synthesised included cis-bis(2,2-bipyridine-N,N)dichlororuthenium, cis-bis(2,2-bipyridine-N,N)dichloroosmium, $[Os(bpy)_2$-(4-tetrazine)-Cl$](PF_6)$, $[Ru(bpy)_2$(4-tetrazine)-Cl$](PF_6)$, $[Os(bpy)_2$-(pyridine-4-COOH)-Cl$](PF_6)$, $[Ru(bpy)_2$-(pyridine-4-COOH)-Cl$](PF_6)$, $Ru(bpy)_2(4\text{-tetrazine})_2(PF_6)_2$. Diffusion coefficients determined using a glassy carbon electrode ranged from 1.51×10^{-6} to 3.28×10^{-6} cm^2 s^{-1} for the osmium complexes and from 2.39×10^{-5} to 4.76×10^{-5} cm^2 s^{-1} for the ruthenium complexes. Using the Laviron approach, solution phase electron transfer rates ranged from 0.29 cm s^{-1} for $[Os(bpy)_2$-(4-tet)-Cl$](PF_6)$ to 1.61 cm s^{-1} for $Ru(bpy)_2(4\text{-tet})_2(PF_6)_2$. Self assembled monolayers of $[Os(bpy)_2$-(4-tet)-Cl$](PF_6)$, $[Ru(bpy)_2$-(4-tet)-Cl$](PF_6)$ and $Ru(bpy)_2(4\text{-tet})_2(PF_6)_2$ formed spontaneously on platinum electrodes and electron transfer rate constants were determined as 9.0×10^3, 5.7×10^3 and 1.4×10^4 s^{-1} respectively. Monolayers of $[Os(bpy)_2$-(pyridine-4-COOH)-Cl$](PF_6)$ and $[Ru(bpy)_2$-(pyridine-4-COOH)-Cl$](PF_6)$ were formed on gold electrodes in a two-step assembly and the former complex shown to spontaneously adsorb on indium tin oxide. Complexes adsorbed by the two-step assembly exhibited much reduced electron transfer rate constants for example 33.86 s^{-1} for $[Os(bpy)_2$-(pyridine-4-COOH)-Cl$](PF_6)$. Rates of adsorption on platinum were determined *in-situ* and closely followed Langmurian adsorption and first order adsorption kinetics. Adsorption rate constants determined for complexes where adsorption occurred on a single site ranged from 14.30 ± 4.35 M^{-1} s^{-1} for $[Os(bpy)_2$-(4-tet)-Cl$](PF_6)$ to 30.93 ± 9.15 M^{-1} s^{-1} for $Ru(bpy)_2(4\text{-tet})_2(PF_6)_2$. Rates of desorption followed first order kinetics for the complexes investigated and desorption rate constants ranged from 2.33×10^{-5} s^{-1} to 5.66×10^{-5} s^{-1}.

In a further two-step assembly procedure, a 5' thiolated hairpin ssDNA probe specific to the bacterial genus *Salmonella* spp.: 5' SH-$(CH_2)_6$- GCA GTA ACA AGA ATA AAA CGC ACT GC- $(CH_2)_6$- NH_2 3' was immobilised on a gold electrode surface and then $[Os(bpy)_2$-(pyridine-4-COOH)-Cl$](PF_6)$ coupled to the amine group at the 3' end using carbodiimide coupling. This DNA biosensor was capable of hybridisation detection in the presence of a

complementary sequence due to the conformational change in hairpin structure. This is the first report of the use of a covalently attached osmium bipyridyl complex as a redox label for the purpose of hybridisation detection.

Acknowledgements

I would like to express my sincere thanks to my supervisor, Dr John Slater for all his enthusiasm, encouragement and help which allowed me to complete this thesis. I would also like to thank my external supervisor, Dr Donal Leech from NUIG for all his helpful advice and guidance during the project.

In addition I would like to acknowledge the contribution during the early part of this research programme of Dr. Jim Clear.

Thanks also to all the technical staff at LYIT for their help during this work in particular to John Gillespie for his help in the provision of materials and access to instruments as required during the project.

I acknowledge the help and support from my fellow postgraduate students and the postdoctoral researchers at Letterkenny Institute of Technology; Yvonne, Anne-Louise, Wolfram, Maria, Aaron, Kim, Susan, Grainne and Sonya.

I wish to acknowledge the financial support provided by the Irish Research Council for Science Engineering and Technology and Enterprise Ireland without which this research would not have been possible.

Finally to my mother and father for their continued support for so many years and last but not least to my wife Mary and my family for remaining so patient as I brought this research work to completion.

Table of Contents

Literature Review

Future improvements in the diagnosis, prevention and treatment of human disease will require the development of more efficient and inexpensive tools for determining DNA and RNA sequences. Such tools will likely find use in many other applications in food science, veterinary medicine, forensic science and environmental testing. Advances in fields such as nanotechnology and microelectronics towards the development of such tools has resulted in an expanded interest in electrochemistry since electrochemical detection systems offer significant advantages compared to other techniques because of their low-cost, rapid response time, simple design and suitability for incorporation in point-of-care diagnostics with small dimensions and low power requirements. Progress in the incorporation of electrochemical detection systems in the future will demand a thorough knowledge and understanding of the complex discipline of electrochemistry and its many challenging concepts.

This review outlines the relevant theories behind some of these challenging concepts, explains the background behind the principal techniques used in this study and summarises the findings of earlier workers in the field. The first section details how theories have evolved to account for charging currents at electrode/electrolyte interfaces which in most cases are interfering currents. These theories explain how altering the charge by changing the potential of an electrode, affects the arrangement of counter ions close to the electrode surface and present in the bulk electrolyte solution. This is of critical importance since all electron transfer occurs at this interface. A brief overview of cyclic voltammetry, the electrochemical technique used to determine electron transfer kinetics for a range of ruthenium and osmium complexes synthesised in this study is provided. Adsorption of these electroactive molecules onto electrode surfaces is considered in terms of how variation in the concentration of the electroactive species present in solution influences surface coverage and how the kinetics of monolayer formation is dependant on the types of interactions, whether attractive or repulsive, which exist between these adsorbing molecules. Alternative designs of microelectrodes and the advantages of using these electrodes over conventional electrodes is reviewed in terms of reduced non-faradaic currents, faster response times and how their use allows for much faster scan rates with reduced distortion due to uncompensated resistance. Modification of microelectrode surfaces with monomolecular layers, which has

resulted in significant advances compared to electrochemistry at bare electrode surfaces, has been reviewed with particular attention to systems containing ruthenium or osmium metal centres with attached polypyridyl ligands. These transition metal complexes have in recent times shown great promise for solid state electrochemistry [1]. Such co-ordination complexes comprise inorganic molecules with a metal centre which can be bound to a ligand(s) containing different free functional groups such as sulphur, nitrogen or carboxylic acids rendering them suitable for attachment to different substrates [2-5]. The most common metal centres used are transition metals such as ruthenium, osmium, rhenium, copper or iron. The electrode potential of such complexes can be controlled by the addition of electron-donating or electron-withdrawing groups to the attached ligands allowing the synthesis of complexes where the potential can be tuned for use in specific applications.

The ability of transition metal complexes to exist and be stable in more than one oxidation state makes them suitable catalysts for biological processes that require the transfer of electrons. Over the last 20 years investigators have studied ruthenium (II) and osmium (II) catalysts as model systems for the study of electron transfer reactions. This review encompasses a synopsis of recent results with these complexes including the influence of the choice of electrolyte, electrolyte concentration, solvent, temperature, pH and electron transfer distance on the electrochemical response [6].

The final section of this review considers biosensors based on deoxyribonucleic acid (DNA). Different electrochemical labels and configurations used to detect the hybridisation event are considered with particular emphasis given to the methods used to immobilise oligonucleotides onto the electrode surface. Molecular organisation and structure of the immobilised DNA film is of major significance since a well-defined probe orientation which is readily accessible to the target must be assembled to allow hybridisation and its detection by changes in the electrochemical signal.

1.1. Electric double layer

Electrochemistry is an interfacial science. Every electrochemical process takes place at an interface between two different phases whether that is liquid / liquid or metal / liquid. Understanding the electric double layer formation, ion adsorption and ion transport is of great importance to many electrochemical problems [7-9]. Electrochemistry between two immiscible liquids dates back to the beginning of the 20th century when Nernst and Riesenfeld observed the transfer of ions across the water / phenol interface using coloured inorganic electrolytes [10]. Thermodynamic-based studies undertaken by Frumkin and co-workers in the early 1900's progressed our understanding of the composition of the metal-solution interface [11].

Charged species that are repelled or attracted to a metal / solution interface cause a separation in charge resulting in a thin layer of solution that has a different composition to the bulk solution. The area affected is known as the electric double layer.

In electrochemical processes at a metal / liquid interface the surface structure of the electrode plays a very important role, since it influences the electronic density of the metal and the electrochemical structure of the electric double layer which is the region where charge transfer takes place. In terms of the interface between a metal and a liquid, where a charged surface exists there will always be a balancing counter charge. Different theories relate to how these counter charges are arranged with respect to the metal surface i.e. whether they are distributed evenly throughout the liquid, or if they are more concentrated near the charged surface. The word "double layer" refers to displacement of electrical charges associated with most surfaces exposed to aqueous solution. The layer is "double" because it involves two parts, the net charge on the surface, and the excess counter-ions in the adjacent solution. There have been many studies undertaken to explain how ions are distributed within the counter-ion field.

The model proposed by Helmholtz in the 1850's first described the electrical double layer [12]. In this model, no electron transfer reactions occur at the electrode and the solution contains only electrolyte (Figure 1.1). This is the simplest model and the ions on the solution side of the interface line up in one plane (Helmholtz plane) very close to the electrode surface

i.e. the excess charge on the metal side is neutralised by a monolayer of ions of opposite charge to that on the metal side [13].

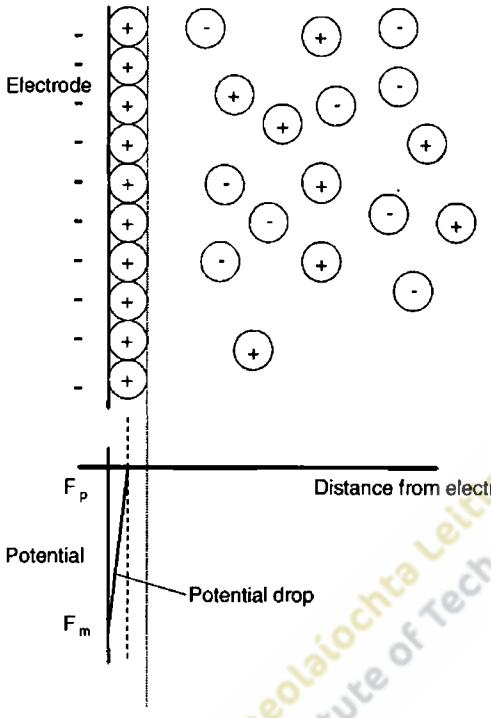

Figure 1.1. The Helmholtz model (adapted from Ref. No. 13).

The attracted ions approach the electrode surface and form a layer to balance the electrical charge. The distance of closest approach is limited by the radius of the counter ion and a single sphere of solution around the counter ion. This results in two layers of charge (the double layer) and a potential drop, which is confined to this region, termed the outer Helmholtz plane (OHP) in solution. In effect, this arrangement resembles an electrical capacitor with two plates of charge separated by a distance (d) as shown in Figure 1.2.

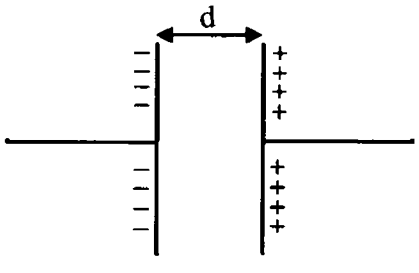

Figure 1.2. Schematic diagram of an electrical capacitor.

The relationship between the stored charge density, σ, and the voltage drop, V, between the plates can be expressed as:

$$\sigma = (\varepsilon \varepsilon_o/d)V \quad (1)$$

where ε is the dielectric constant of the medium, ε_o is the permittivity of free space and d is the interplate spacing which gives a differential capacity of:

$$\delta\sigma/\delta V = C_d = \varepsilon \varepsilon_o/d \quad (2)$$

This theory predicts that C_d is a constant, which is not the case in real systems. Experimental results have demonstrated that C_d varies with both the potential and the concentration meaning that either ε or d depends on these variables. Hence a more precise model is required to explain how ions are distributed within the counter-ion field [8].

Gouy and Chapman [14-16] made significant improvements by using a diffuse model of the double layer that resulted in the potential at the charged surface decreasing exponentially due to adsorbed counter-ions from the solution. In the Gouy-Chapman model, ions are non-uniformly distributed in the vicinity of the electrode where the concentration of excess charge is greatest near the surface of the electrode and decreases non-linearly until it reaches the bulk concentration. An average distance replaces d in this system and as the electrode becomes highly charged the diffuse layer becomes more compact and C_d should rise. As the electrolyte concentration becomes greater there should be a similar compression of the diffuse layer that causes capacitance to increase. The thickness of this layer is variable but is typically of the order of magnitude of about a millionth of a centimetre. This model predicts an unrealistically large concentration of ions since it assumes that the ions are infinitely small and can therefore get infinitely close to the electrode surface.

The Helmholtz model does not take into account factors such as diffusion, the possibility of adsorption to the electrode surface or the interaction of solvent dipoles and the electrode. A model described by Stern [17], based on a modification of the Gouy-Chapman model, addressed some of these limitations. This model, which became known as the Gouy-Chapman Stern model is illustrated in Figure 1.3.

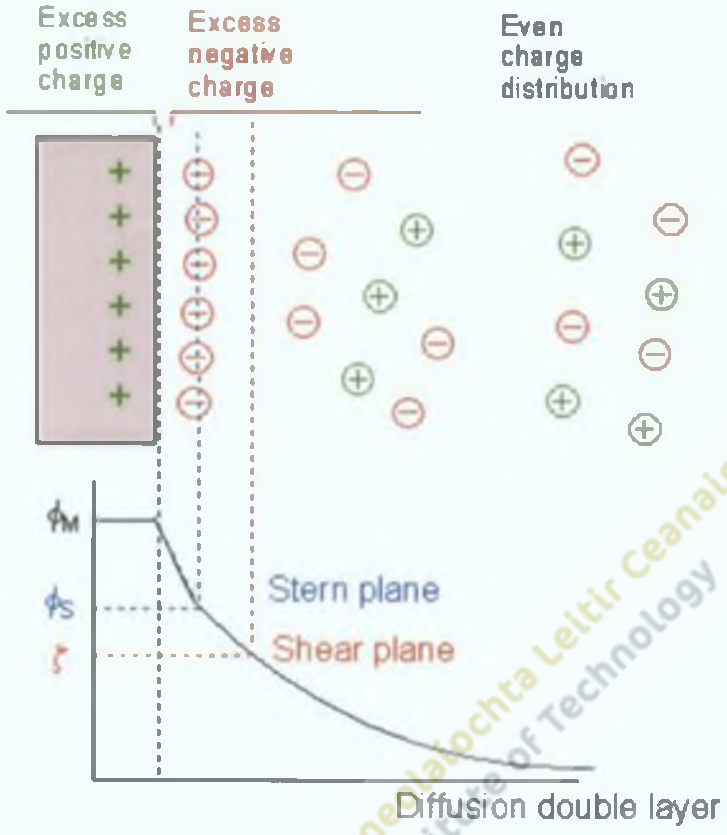

Figure 1.3. The Gouy-Chapman Stern model (adapted from Ref. No. 17)

In this model the ions are assumed to be able to move in solution and so the electrostatic interactions are in competition with Brownian motion. This model still results in an excess of one type of ion close to the electrode surface, but now the potential drop occurs over a region known as the diffuse layer.

The effect of monolayer formation on the charging or capacitative current can be easily observed using cyclic voltammetry. The cyclic voltammogram of a bare gold electrode and the same electrode after formation of a self-assembled monolayer (SAM) of thioctic acid is illustrated in Figure 1.4. After monolayer formation a marked decrease in charging current or capacitative current was observed since the charging or capacitative current is proportional to the area of the electrode exposed to the electrolyte solution [18].

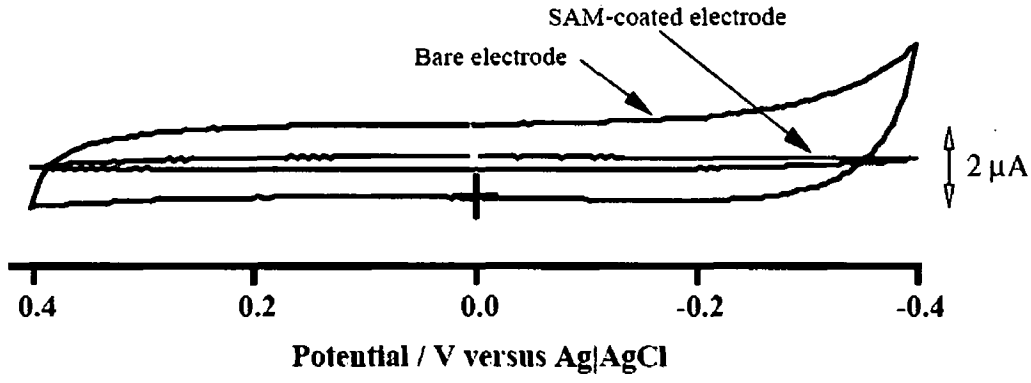

Figure 1.4. The capacitance of a cyclic voltammogram at a bare gold electrode and a gold electrode coated with a self-assembled monolayer (SAM) of thioctic acid in 0.1M KNO_3 [18].

The technique of cyclic voltammetry can also provide information in the study of thermodynamic and kinetic processes. The principle behind the technique and its use in the study of redox reactions containing an electroactive species in solution or to probe the electrochemistry of redox molecules adsorbed as monolayers on electrode surfaces demands an understanding of the current / voltage curve or cyclic voltammogram. The fundamentals of cyclic voltammetry and the information which can be extracted from the voltammogram are provided below.

1.2. Cyclic voltammetry

Electrochemistry is a branch of chemistry that is used in industry as well as being of interest in the academic world. Physical electrochemistry relates to a broad area of electrochemistry which includes theoretical as well as experimental aspects of the double layer structure, kinetic studies, heterogeneous electron transfer at electrode / electrolyte interfaces and the entropy and enthalpy change for a reaction. In all cases electrochemistry involves the transfer of electrons through interfaces and in general terms this interface is usually between an electrolyte and an electrode. By using a supporting electrolyte, a reference electrode and a counter electrode the potential of the working electrode can be controlled.

Linear sweep voltammetry is a method whereby the potential applied to a working electrode is varied with time. The rate of change in potential has units of volts per unit of time and is called the scan rate. A faradaic current is generated as a result of the reduction or oxidation of species present at the interface between the electrolyte and the electrode. At faster scan rates this faradaic current is increased due to an increased flux of electroactive material to the electrode.

A variation of this technique is cyclic voltammetry in which the direction is switched at the end of the first scan as shown in Figure 1.5. Significant contributions to the development of this technique have been made by Kolthoff in 1935 [19], Randles in 1952 [20] and later Nicholson in 1964 [21].

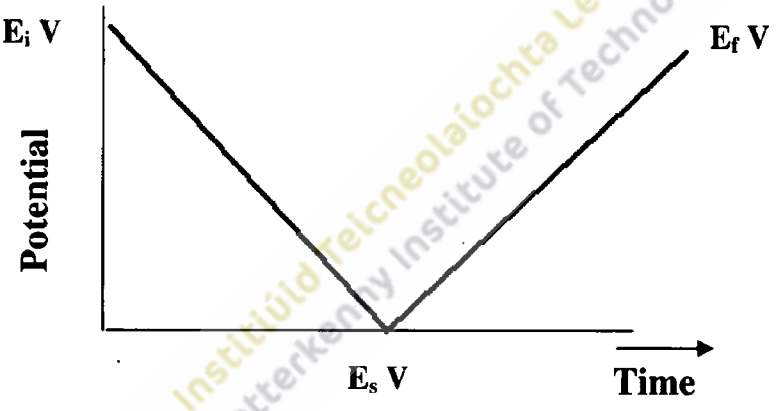

Figure 1.5. Schematic diagram of the change in potential with time. E_i = initial potential, E_s = switching potential and E_f = final potential

The advantage of cyclic voltammetry is that the product of electron transfer in the first scan can be studied again in the reverse scan. Electron transfer generates currents, the magnitude of which provides information about the analyte or species under investigation. Cyclic voltammetry is also useful for determination of the reversibility of reactions, formal potentials, diffusion co-efficients and the kinetics of electron transfer.

A typical cyclic voltammogram is illustrated in 1.6. From an initial voltage (A) the potential is scanned in a positive direction. As the formal potential (B) of the analyte under

investigation is approached, a current begins to flow indicating that the molecule is being oxidised. As the voltage increases the rate of the reaction increases until a point (C) where the reaction is limited by the mass transport of electroactive species from the bulk solution to the electrode surface and as the current decays a peak is produced. At point (D) the direction of the sweep is switched and at point (E) the oxidised material in the vicinity of the electrode is reduced resulting in a peak (F) of similar magnitude to the initial scan. The regions (B)-(C) and (E)-(F) of the voltammogram are both kinetically controlled whereas the regions (C)-(D) and (F)-(A) are diffusion-controlled.

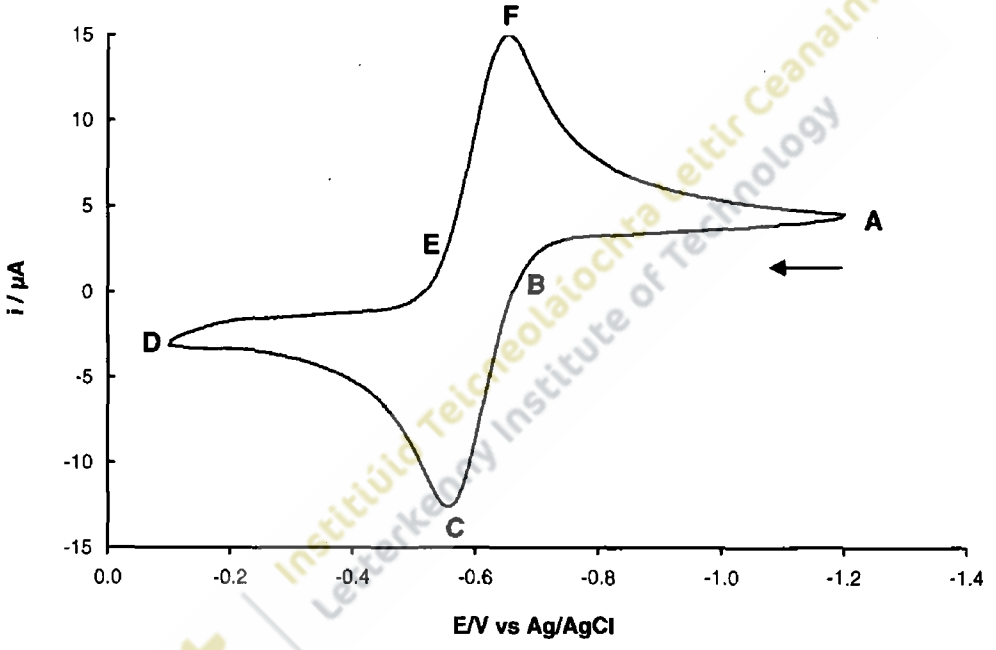

Figure 1.6. Cyclic voltammogram of 3,6-bis(4-pyridyl)-1,2,4,5-tetrazine in acetonitrile with 0.1 M $TBABF_4$ as the supporting electrolyte. The electrode used was a 0.5mm radius glassy carbon and the scan rate was 0.5 V s^{-1}. The scan direction is shown by the black arrow.

1.3. Solution phase electrochemistry

The peak shape shown in Figure 1.6 is typical for semi-infinite diffusion using a macroelectrode. The main parameters which can be extracted from the cyclic voltammogram are labelled in Figure 1.7.

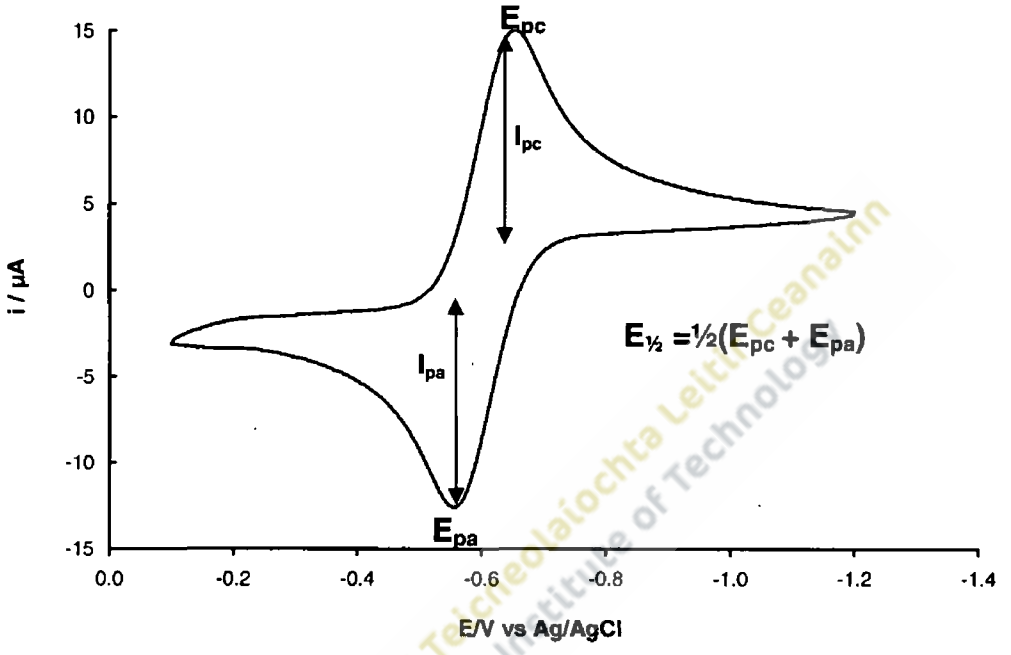

Figure 1.7. The main parameters which can be extracted from a cyclic voltammogram are shown using Figure 1.6 as a typical example. I_{pa} is the anodic peak current and I_{pc} is the cathodic peak current. E_{pa} and E_{pc} are the anodic and cathodic peak potentials respectively.

The peak current at 25°C for a reversible system can be determined from the Randles-Sevcik equation [22, 23]:

$$I_p = (2.687 \times 10^5)\, n^{3/2}\, \nu^{1/2}\, D^{1/2}\, A\, C \qquad (3)$$

where the constant 2.687×10^5 has units of C mol^{-1}, n is the number of electrons, ν the scan rate in volts sec^{-1}, D the diffusion co-efficient $cm^2\ s^{-1}$, A the electrochemical area of the electrode in cm^2 and C is the concentration in moles cm^{-3}.

From this equation the diffusion co-efficient for a known concentration of an electroactive species dissolved in solution can be estimated, if the electrochemical area of the electrode is

known. Alternatively if the diffusion co-efficient of the redox molecule is accurately known, then the equation can be used to determine the electrochemical area of the electrode.

The peak current I_p is linearly proportional to the concentration C and to the square root of the scan rate $v^{1/2}$. Therefore a plot of I_p versus $v^{1/2}$ should be linear if mass transport to the electrode surface is controlled by diffusion alone, i.e. the mass transport of the electroactive species to the electrode surface is across a concentration gradient. A quiet unstirred solution is required to minimise convection, whilst the presence of an electrolyte minimises movement of the charged electroactive species due to migration in the electric field gradient. The thickness of the diffusion layer δ can be estimated from $\delta = (\pi Dt)^{1/2}$ where π is pi, D the diffusion co-efficient in $cm^2\ s^{-1}$ and t is the time [24].

1.4. Surface-confined electrochemistry

For adsorbed species the electrochemical response is different to that of the same species dissolved in solution. Where Langmuir adsorption is obeyed the current response is illustrated in Figure 1.8.

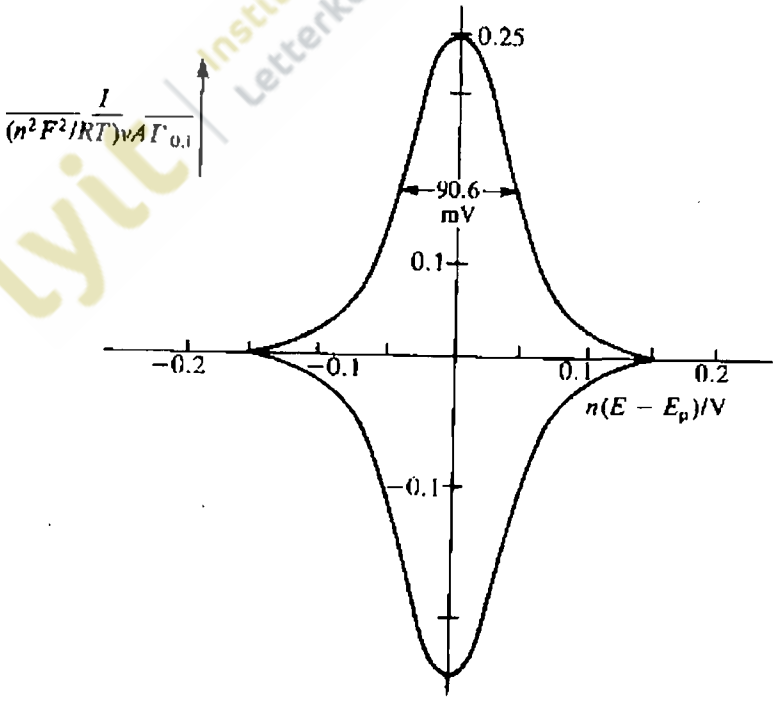

Figure 1.8. Langmuir current response for a thin layer or monolayer [8].

The current response for thin layers or monomolecular layers under Langmurian conditions assumes no attractive or repulsive interactions between adsorbates and the peak current I_p can be determined from the equation:

$$I_p = \frac{n^2F^2\nu A\Gamma}{4RT} \qquad (4)$$

where n is the number of electrons transferred, F the Faraday constant, ν the scan rate, A the electrochemical area, Γ the surface coverage, R the real time constant and T is the temperature.

A modification of the Langmuir, the Frumkin isotherm equation that describes the situation when intermolecular interactions are present within the monolayer is given by the equation below:

$$I_p = \frac{n^2F^2A\nu\Gamma_0}{RT}\left[\frac{\theta_R(1-\theta_R)}{1-2\nu g\theta_T\theta_R(1-\theta_R)}\right] \qquad (5)$$

where θ_R is the number of reduced species, g the interaction parameter and θ_T is the total number of species.

This equation (5) relates the measured current with the interaction parameter g of the Frumkin model for an adsorbed electroactive species and the number of reduced species θ_R relative to the total θ_T. The parameter g has a strong effect on the shape of the cyclic voltammograms, which can be described in terms of the peak width at half height, ΔE_{FWHM}. The g parameter describes interactions between adsorbed oxidised species a_o for (O-O), reduced species a_r for(R-R) and oxidised, reduced species a_{or} (O-R) so:

$$g = a_o + a_r - 2a_{or} \qquad (6)$$

When $g = 0$, $\Delta E_{FWHM} = 90.6mV$. If $g < 0$, $\Delta E_{FWHM} > 90.6mV$ and when g is greater than 0, $\Delta E_{FWHM} < 90.6mV$ [25].

Therefore the voltammetric response of an electroactive molecule in a self-assembled monolayer can be used to probe the chemical environment within the film. For an ideal Nernstian reaction with no interactions $E_{pa} = E_{pc}$ and the total width at half height of either the cathodic or anodic wave is given by:

$$\Delta E_{FWHM} = \frac{3.53RT}{nF}$$

At 25°C

$$\Delta E_{FWHM} = \frac{90.6}{n} mV \qquad (7)$$

Experimentally, cyclic voltammograms of adsorbed species are generally broader than ideal. These deviations from the ideal are usually caused by the chemical environment within the monolayer. Generally the width of the peaks depends on the type of interaction within the monolayer; peaks become broader where repulsive forces exist and narrower and sharper where attractive interactions are present [26].

The surface coverage of adsorbed species within a monolayer can be calculated from the area under the oxidation or reduction peak in a cyclic voltammogram. Under repeated oxidation/reduction of the modifying layer, the faradaic charge, Q, under the current/potential curve can be used to determine the total surface coverage Γ_T (mol cm^{-2}) according to the equation [27]:

$$\Gamma_T = \frac{Q}{nFA} \qquad (8)$$

Charge measurements that use a simple current base line assume that alterations in surface ionic charge caused by oxidation and reduction, responsible for dispersion in the double layer capacitance current, are insignificant.

From the real surface area, the number of molecules per unit area can be calculated:

$$\text{Therefore 1 molecule} = \frac{1cm^2}{\Gamma_T (6.022 \times 10^{23})} \qquad (9)$$

where 1 cm^2 contains Γ_T (6.022 x 10^{23}) molecules cm^2

For a surface coverage Γ_T of 1 x 10^{-10} mol cm^{-2} this gives an area occupied per molecule of 160 Angstroms^2

Where the radius of the head group of an adsorbed molecule in a self-assembled monolayer is known or can be determined, valuable information can be extracted regarding the packing density and orientation of molecules in the monolayer. Additional contributions to the molecular volume such as solvent shell and counterions must also be considered [4].

1.5. Electron transfer kinetics

Butler and Volmer expressed the one electron transfer reaction as:

$$A + e \underset{k_b}{\overset{k_f}{\rightleftharpoons}} B \qquad (10)$$

where k_f and k_b are the rate constants for the reductive and oxidative steps respectively.

The kinetics of electron transfer can be determined by recording cyclic voltammograms over a range of increasing scan rates (v) until the time scale of the experiment becomes comparable to the rate of electron transfer. At this point the separation between the cathodic and anodic peak increases as shown in Figure 1.9.

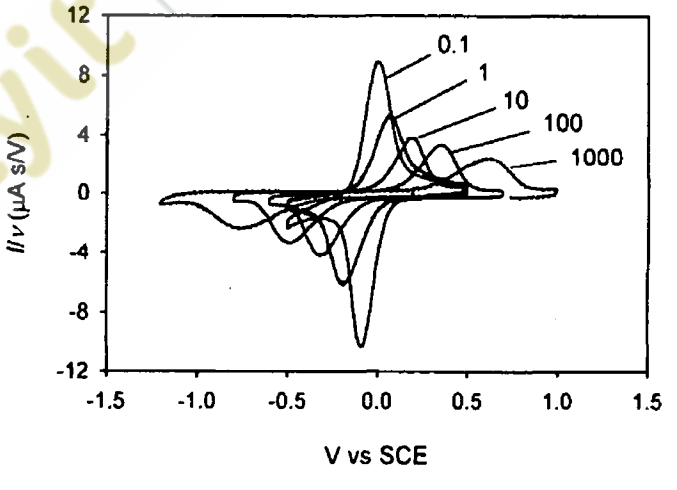

Figure 1.9. Scan-rate-normalized cyclic voltammograms of a gold bead coated with a $HS(CH_2)_{15}COOH$ SAM with attached $pyRu(NH_3)_5$ redox centres. Scan rates in V s^{-1} for each cyclic voltammogram are shown [28].

For solution phase reactants the heterogeneous electron transfer rate constant (k^0) can be determined from equation 11 [29]:

$$k^0 = 2.18\left(\frac{DnF}{RT}\right)^{1/2}(\alpha v)^{1/2}\exp\left(\frac{-\alpha^2 nF\Delta E}{RT}\right) \qquad (11)$$

where α is the transfer coefficient, ΔE the difference in potential between the cathodic and anodic peak and all other symbols are as stated previously.

This equation can be expressed to give ΔE in terms of ln v:

$$\Delta E = m \ln[v] + C \qquad (12)$$

Where the slope $m = \frac{RT}{2nF}\frac{1}{\alpha^2}$

When $\Delta E = 0$, $v = v_0$

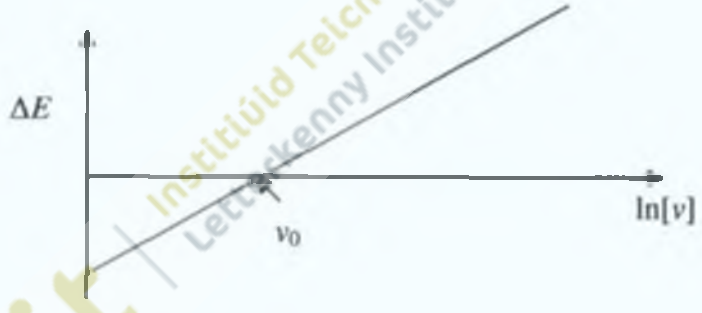

Figure 1.10. Plot of the difference in potential between the anodic and cathodic peaks (ΔE) and the natural log of the scan rate (ln[v]).

This allows determination of the electron transfer rate constant (k^0) in terms of the slope and the intercept on the y-axis.

Cyclic voltammetry can also be used to determine the electron transfer rate constant (k^0) for diffusion-less electrochemical systems where the oxidised and reduced forms of an electroactive species are strongly adsorbed on an electrode surface. The electron transfer rate constant of the electrochemical reaction is determined by experimental study of the variation of the peak potential (ΔE_p) as a function of the scan rate (v) as shown in Figure 1.11 [30].

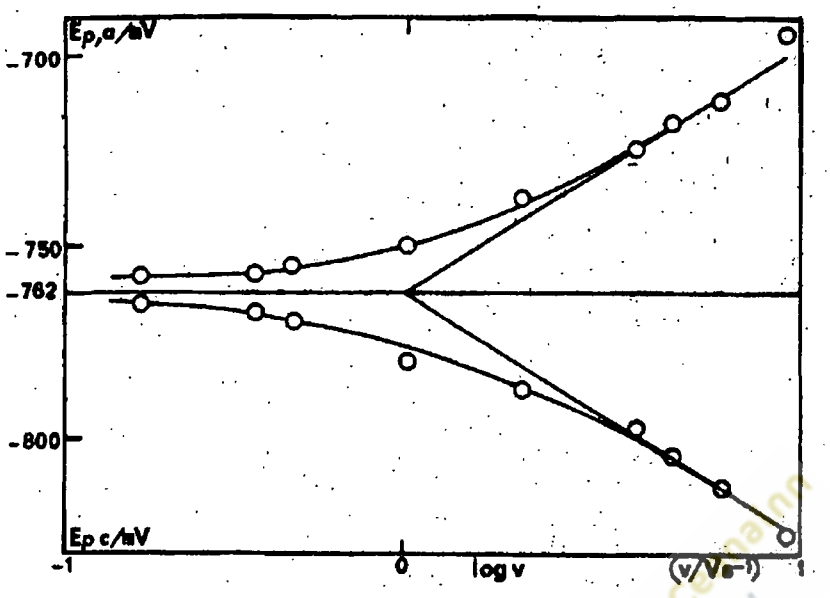

Figure 1.11. Variation of E_{pa} and E_{pc} as a function of log v [29].

Ideally a plot of E_{pc} and E_{pa} against ln v should yield two straight lines. The slope from the cathodic data (k_c) and the slope from the anodic data (k_a) are given by the equations:

$$\text{Slope from the cathodic data } (k_c) = \frac{-RT}{\alpha nF} \qquad (13)$$

$$\text{Slope from the anodic data } (k_a) = \frac{RT}{(1-\alpha)nF} \qquad (14).$$

Therefore the transfer coefficient (α) can be determined from the equation:

$$\alpha = \frac{k_a}{(k_a - k_c)} \qquad (15)$$

The electron transfer rate constant (k^0) is determined from:

$$k^0 = \frac{\alpha nFvc}{RT} = \frac{(1-\alpha nFva)}{RT} \qquad (16)$$

If E^0 is the formal potential ($E_{pc} + E_{pa} / 2$) and v_a and v_c are the cathodic and anodic scan rates respectively then both $E_{pa} - E^0$ and $E_{pc} - E^0$ are equal to zero [31].

1.6. Microelectrodes

Cyclic voltammetry is a versatile electroanalytical technique that has proven particularly useful for electrochemical analysis associated with the miniaturisation of electronic devices and development of nanotechnological applications. Direct measurement of the oxidation and reduction kinetics of electronically-excited states is not possible by conventional voltammetry because it is limited to millisecond or longer time scales. Electronically-excited states are transient species, typically existing for less than a microsecond. With the use of ultrafast electrochemical techniques and the utilisation of microelectrodes it is now possible to directly probe the properties of these species [29].

Although there are no clear cut boundaries between what constitutes a microelectrode and what constitutes a macroelectrode, it is generally accepted that the term microelectrode refers to any electrode whose characteristic dimensions under the given experimental conditions, is comparable or smaller than the diffusion layer thickness. Forster defined microelectrodes as "miniature electrodes" where the critical dimension is less than 10 μm yet remains much greater than the electrical double layer, which is typically 10-100 Angstroms [32].

The use of microelectrodes for biological and medical research dates back to the 1800's, however it was not until the 1970's that the advantageous properties of small electrodes were investigated by electrochemists. Widespread use of microelectrodes in electrochemical investigations has developed only in the last 10-15 years driven by the fact that very small currents were difficult to measure and early fabrication techniques were not reproducible. Microelectronics has made it possible to measure very small currents and to construct very small electrodes reproducibly [24]. In the mid 1980's, Bard and Faulkner described an electrochemical instrument that could perform voltammetric experiments by software control. Bioanalytical Systems, CH Instruments and Cypress Instruments as well as others used this approach to create instruments based on computer control and recording with analogue-integrated circuit interfaces for potentiostatic control [33]. Systems such as these have allowed measurement of currents in the microamp, picoamp and even femtoamp range using micrometre-sized electrodes. Many different types of electrode materials have been used in the construction of microelectrodes including gold, platinum, silver, copper, glassy carbon and graphite [34-39].

Electrochemical properties of redox active molecules are often characterised using cyclic voltammetry. For complexes that possess very fast electron transfer rate constants such as ruthenium and osmium polypyridyl complexes, very fast scan rates are required. The use of microelectrodes in such circumstances is advantageous because they allow high scan rates to be used with only small interference from ohmic drop.

Generally accepted requirements for microelectrodes are that they should:

- Be simple to fabricate
- Be capable of being fabricated reproducibly
- Have mechanical stability
- Be chemically resistant
- Possess well-defined electrochemical properties

Microelectrodes have been constructed in a range of different geometries including disc, ring, cylinder, sphere and arrays of each type (Figure 1.12).

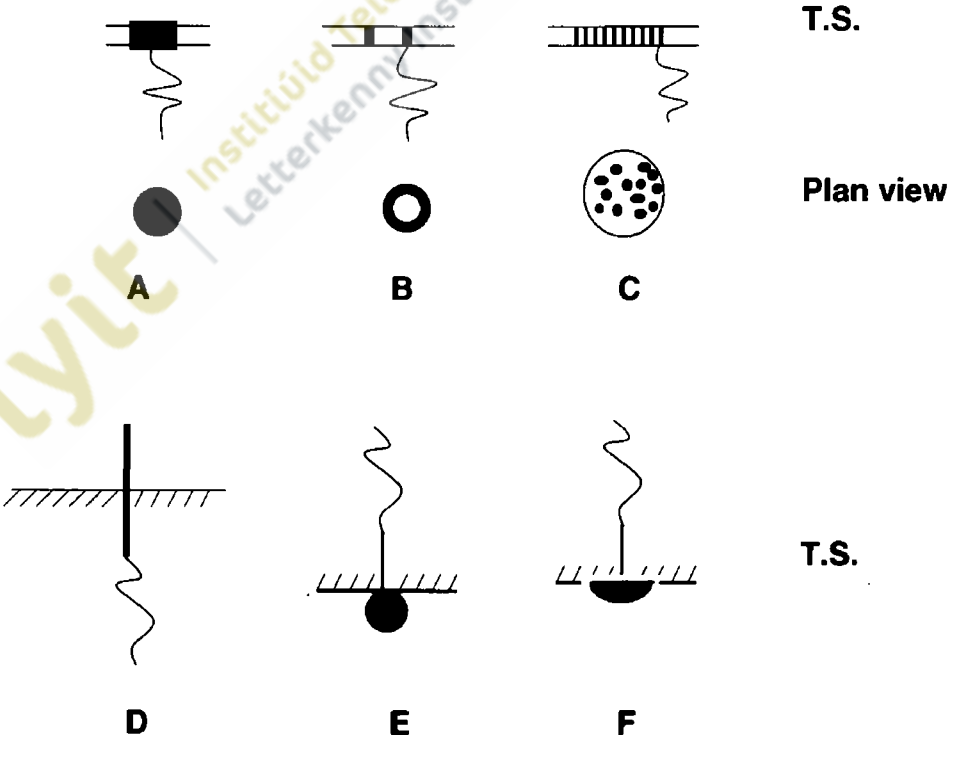

Figure 1.12. Microelectrode geometries A = micro-disc, B = micro-ring, C = micro-disc array, D = single fibre, E = sphere, F = hemisphere.

The most common microelectrode geometry used in electrochemical investigations is the disc (Figure 12A) because of the ease with which this arrangement can be fabricated, the fact that it can be manually polished, is easily maintained and conforms closely to mass transport theory [40].

Three types of mass transport are possible in an electrochemical measurement i.e. diffusion, convection and migration, defined as:

- Diffusion is the movement of molecules along a concentration gradient from an area of high concentration to an area of low concentration.

- Migration is the movement of species under the influence of an electric field. The addition of a large excess of a non-electroactive salt eliminates the mass transport effects due to migration, as these ions become the charge carriers.

- Convection is the transport of species due to agitation such as stirring or movements of the electrode such as occurs in rotating disc electrodes.

Very high diffusion rates both to and from the electrode surface can be achieved with microelectrodes compared to conventional electrodes and as a consequence high quality data obtained within short experimental timescales.

The electrochemical reaction at an electrode can be represented as:

$$O + (e^{-1})_n \leftrightarrow R \qquad (17)$$

where O is the oxidised species and R is the reduced species.

When electrolysis occurs, the oxidised species is consumed at the electrode surface causing a concentration gradient between the bulk concentration and the electrode. Therefore oxidised molecules move towards the electrode to compensate for those being consumed in the electrochemical reaction. The region affected during electrolysis is known as the diffusion layer.

The natural movement of a species by diffusion is described by Ficks first law:

$$J = -D\frac{\delta c}{\delta x} \tag{18}$$

where J is the flux of a species and $\delta c/\delta x$ the concentration gradient in direction x.

The negative sign accounts for the fact that material moves down a concentration gradient from a region of high concentration to a region of low concentration.

The variation in concentration with time is given by Ficks second law:

$$\frac{\delta c}{\delta t} = D\frac{\delta^2 c}{\delta x^2} \tag{19}$$

The concentration gradient is caused by the consumption of electroactive species at the electrode surface and the steeper the change in concentration the greater the rate of diffusion.

For a conventional planar electrode, the variation of current with time from Ficks second law is given by the Cottrell equation:

$$I_t = nFAJ = \frac{nFAD^{1/2}c}{\pi^{1/2}t^{1/2}} \tag{20}$$

where I is the current measured at time (t) at an electrode of area (A) being directly proportional to the bulk concentration of electroactive species (c).

For a microdisc of radius (r), the variation of current with time contains a time-independent and a time dependant term given by the equation [41]:

$$I_t = \frac{4nFDc}{\pi r} + \frac{nFD^{1/2}c}{\pi^{1/2}t^{1/2}} \tag{21}$$

For short experimental times, i.e. fast scan rates, diffusion is described by the second term in the equation. In this instance the thickness of the depleted layer of reactants is smaller than that of the radius of the electrode and planar diffusion similar to that at conventional electrodes dominates as shown in Figure 1.13.

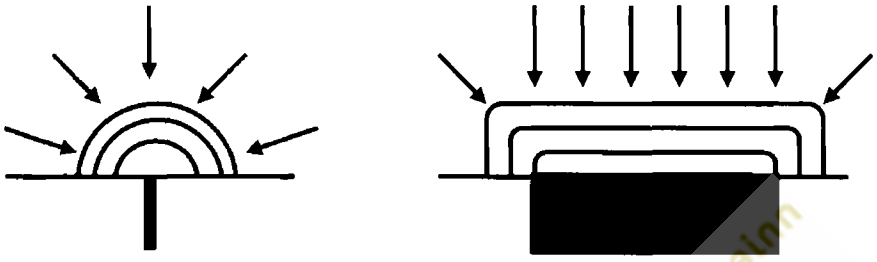

Figure 1.13. Schematic representation of hemispherical and planar diffusion.

A microelectrode at fast scan rates (>1V s^{-1}) will exhibit planar diffusion resulting in peak shapes in cyclic voltammograms similar to that of a macroelectrode.

For longer experimental times, i.e. slow scan rates, the second term in the equation to determine the transient current (Equation 21) is reduced to a level where its overall contribution is negligible. This is the steady state current for a microdisc when diffusion is dominated by the first term and is given by the equation [8] below:

$$I_{ss} = 4nFDcr \qquad (22)$$

where I_{ss} is the steady state current, n the number of electrons in the electron transfer process, F the Faraday constant, D the diffusion co-efficient, *c* the concentration in the bulk solution and r is the radius of the electrode.

Therefore when using slow scan rates the diffusion layer becomes greater than the diameter of the microelectrode and hemispherical diffusion takes place to the electrode (Figure1.13). This arises because the edge of the electrode is the nearest approach for the diffusing species. The cyclic voltammetry response of a microelectrode when spherical diffusion dominates is

characterised by a sigmoidal shape when slow scan rates (<1V s^{-1}) are used [42] as shown in Figure 1.14.

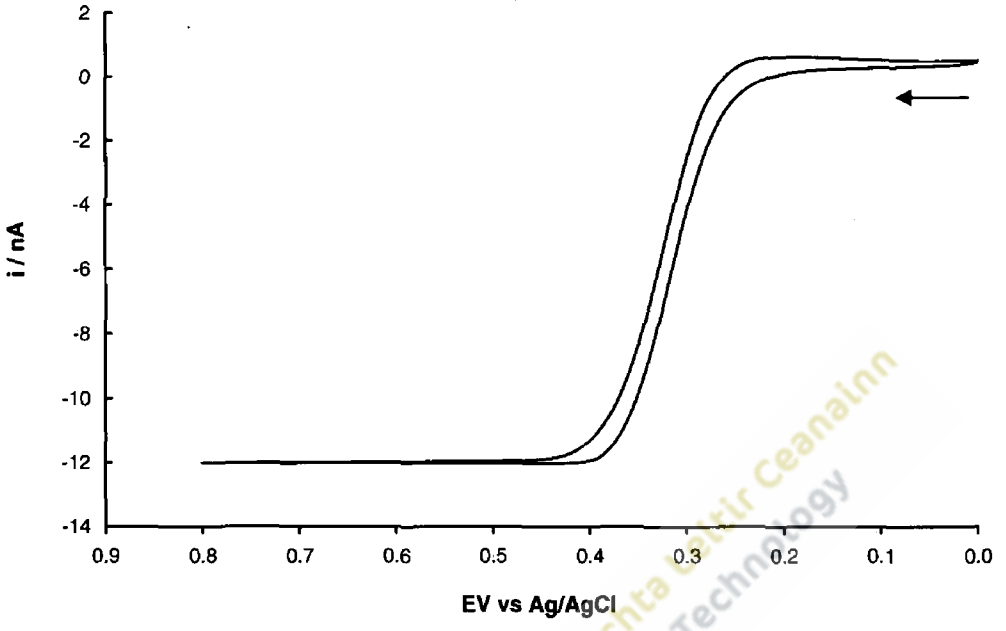

Figure 1.14. Cyclic voltammogram for 1mM [$Os(bpy)_2$-(pyridine-4-carboxylic acid)-Cl] in acetonitrile at a scan rate of 20 mV s^{-1}. Electrolyte is 0.1 M $TBABF_4$. Cyclic voltammogram recorded using a 12.5 μm radius Pt electrode and Ag/AgCl reference electrode.

Since microelectrodes can operate in different mass transport regimes it is important that one or other of these transport modes dominates. Therefore experimental timescales where combinations of both transport modes are present should be avoided as interpretation of results using such timescales is difficult.

In summary, the growth of the diffusion layer into the solution at microelectrodes is similar to that at larger electrodes over short times, but at longer experimental timescales it slows considerably. Hence the thickness of the diffusion layer is smaller for microelectrodes and the concentration gradient greater. Since the rate of mass transport to microelectrodes is more efficient because of the reduced thickness and hemispherical diffusion, steady state currents are much more rapidly established. For example using a typical diffusion co-efficient of 10^{-5} cm^2 s^{-1}, 99% of the steady state current can be achieved within 3 seconds for a 1μm diameter electrode [43]. This property of microelectrodes makes them suitable for the study of rapid electron transfer and coupled chemical reactions.

1.7. Ohmic drop

A typical electrochemical experiment is performed using 3 electrodes: a working electrode, a counter or auxiliary electrode and a reference electrode. The current flows between the working electrode and the counter electrode and the potential at the working electrode is measured with respect to a non-polarisable reference electrode. When faradaic and charging currents are flowing in an electrochemical cell, there is a voltage drop between the reference electrode and the working electrode. This drop in potential is caused by the electrolyte conductivity, the distance between the two electrodes and the magnitude of the current. Using Ohms law the voltage drop, or as it is sometimes called the ohmic drop or *I*R drop (ΔE), can be calculated as the product of the current (I) and the resistance (R):

$$\Delta E = IR \qquad (23)$$

Microelectrodes have several important practical advantages compared to macroelectrodes including fast establishment of a steady-state signal, an increased current due to enhanced mass transport at the electrode boundary and a decreased ohmic drop. Nevertheless the effects of ohmic drop must always be accounted for in any electrochemical measurement. These effects can be minimised by using relatively high concentrations of supporting electrolyte (typically > 0.2M) and reduction of the distance between the working and reference electrode by using a luggin capillary.

In cyclic voltammetry the ohmic drop can lead to inaccurate measurements of electron transfer rate constants due to an increase in peak separation, not attributed to slow electron transfer, and a decrease in the magnitude of the current [43]. Effects of *I*R drop become more evident at faster scan rates as a result of increased currents. However increases in peak separation may also be caused by a quasi-reversible process, i.e. the rate of electron transfer is slow compared to the rate of the experiment [44, 45].

1.8. RC time constant

When the potential of an electrode placed in an electrolyte solution is changed, a double layer is formed causing the charge on the metal side to be compensated by ions of opposite charge present in the solution. It is desirable that this interfering, non-faradaic charging current is minimised. It is possible and advantageous to separate faradaic and non-faradaic currents by careful control of the timescale of the experiment, i.e. the time taken for a capacitative current to flow through a solution of resistance R and capacitance C. The time over which this occurs is referred to as the RC time constant. Varying the potential of the electrode by an amount (ΔE) causes a capacitative current to flow. This current decays with time according to the equation:

$$Ic = \frac{\Delta E}{R}\exp\left[\frac{-t}{RC}\right] \qquad (24)$$

where Ic is the capacitative current, t the time in seconds.

If the faradaic process is slow compared to the RC time constant, then the capacitative current will interfere to a much lesser extent with the faradaic process. Reduction in the RC time constant can be achieved by maintaining a high electrolyte concentration which results in a reduced resistance. Reduction in the size of the electrode will increase the resistance (R) as shown in the equation:

$$R = \frac{1}{4\pi\kappa r} \qquad (25)$$

where k is the specific conductance of the medium and r is the radius of the electrode.

Since the capacitance is proportional to the area of the electrode and the resistance is proportional to reciprocal of the electrode radius then:

$$RC\alpha\frac{1}{r}r^2 = r \qquad (26)$$

Hence reductions in the time constant (RC) can be achieved by decreasing the radius of the electrode, for example by reduction of the electrode radius from 1mm to 1μm, the time constant can be decreased by a factor of 1000. By using microelectrodes the timescale of the experiment can be reduced since it is only possible to extract meaningful electrochemical measurements when using times that exceed the RC by a factor between 5-10 [46] as this allows sufficient separation of the capacitative and faradaic currents. This is significant in cyclic voltammetry when using self-assembled monolayers of complexes that have fast electron transfer properties since higher scan rates can be used to extract meaningful electrochemical data. Overall by reducing the size of the electrode, the capacitative current can be reduced in proportion to the faradaic current with less interference due to the different time regimes of the two processes as the cell response time is reduced.

1.9. Real area of electrodes

Since the response of an electrode is always proportional to the surface area exposed to the analyte, the surface area is an important characteristic for the extraction of meaningful data in any electrochemical measurement. The presence of kinks or terraces on an electrode surface, irrespective of the degree of apparent smoothness or the amount of polishing, will result in a geometric area much less than the real area of the electrode

The real surface area, or electrochemical area as it is sometimes referred, can be determined by electrochemical methods such as cyclic voltammetry. Comparison of the real surface area with the geometric area allows determination of the surface roughness factor of an electrode. Typically this roughness factor is between 1.2 and 3 for a well-polished disc electrode. Measurement of the real surface area of a gold electrode using cyclic voltammetry is based on the induced deposition of an oxygen monolayer on the electrode surface and measurement of the charge associated with this monolayer (Figure 1.15). This calculation is possible because every oxygen molecule is attached to one metal atom on the electrode surface, forming a gas monolayer.

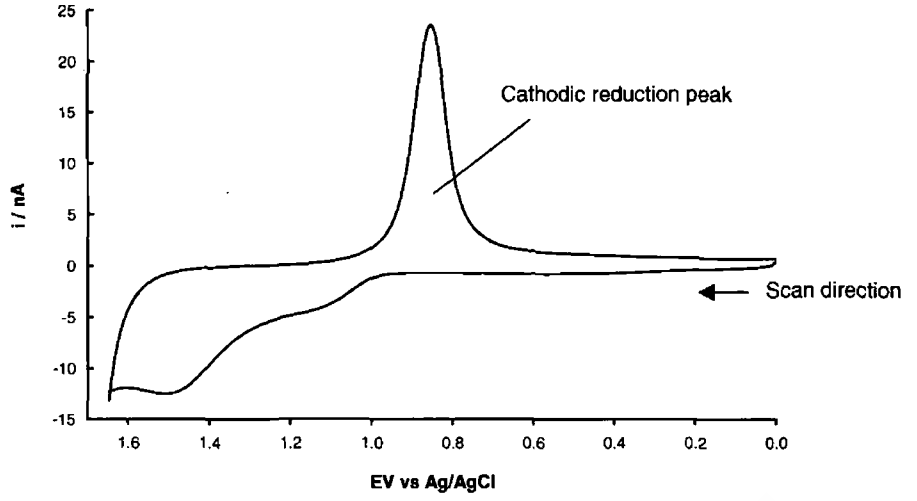

Figure 1.15. Typical cyclic voltammogram for a 25 μm gold electrode in 0.5M H_2SO_4.

The voltammogram shows anodic peaks between 1.40V and 1.65V vs. the Ag/AgCl reference electrode which correspond to the formation of an oxide layer on the electrode surface. Electrochemical desorption of the oxide layer results in a single cathodic peak at approximately 0.8V vs. Ag/AgCl reference electrode. The electrochemical area of the electrode can be estimated, but not precisely confirmed, by dividing the area under the cathodic peak by a correction factor of 390 μC cm^{-2} for gold [47].

With platinum electrodes the real area can be estimated from either the oxide reduction peak, at approximately 0.45V vs. Ag/AgCl reference electrode (Figure 1.16), or the area under the hydrogen adsorption/reduction peak. In this instance the electrochemical area is estimated by dividing the area under the oxide reduction peak by a factor of 420 μC cm^{-2} for platinum [48].

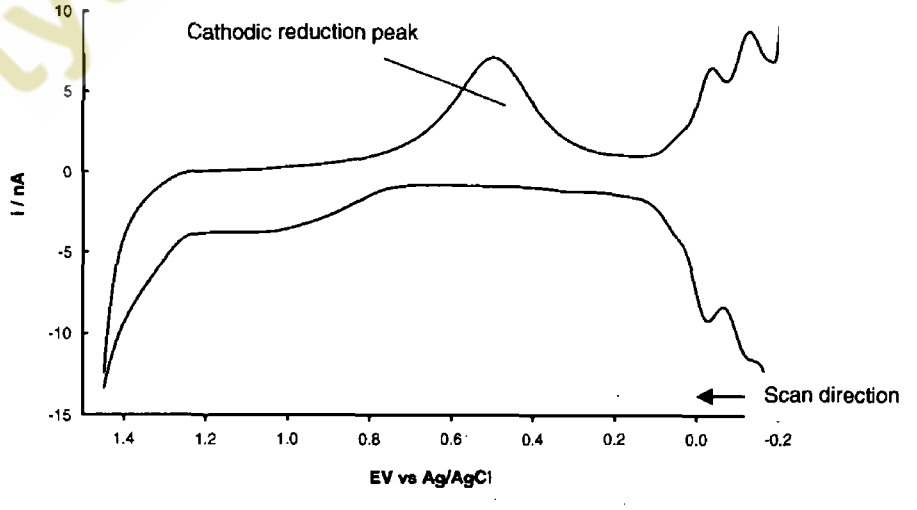

Figure 1.16. Typical cyclic voltammogram for a 25 μm platinum electrode in 0.5M H_2SO_4.

1.10. Modified electrodes

Conventional amperometric electrodes are used to donate or accept electrons in an electron transfer process. Such electrodes can be modified by the deposition of various chemical layers, overcoming the lack of selectivity, sensitivity and specificity at "naked" or "bare" electrodes which has been a major factor in the shortcomings of electrochemistry as an analytical method. In this context the term modification refers to the immobilisation on the electrode surface of reagents that change the electrochemical characteristics of the bare electrode. This ability to control the electrode surface at a molecular level represents a tremendous challenge for the future [49]. Chemically modified electrodes are of interest because of their potential use in electrocatalysis and many other applications where control of the electrode/solution interface is desirable. Advantages over solution-based electrocatalysis include:

- A higher active concentration of catalyst than can be achieved in solution
- Facilitated transfer of multiple redox equivalents to individual sites
- Ease of extraction of the catalyst from the electrolyte solution
- Enhanced co-operative effects between catalyst components due to small physical separation [50]

The self-assembly approach to electrode surface modification, pioneered by Sagiv and co-workers [51] is an attractive method because it produces well-ordered and very stable systems. Particular interest has been expressed in these systems in recent years because of the ease with which the physical and chemical properties of electrode surfaces can be altered [52-56]. Two types of adsorption to a clean electrode surfaces are possible namely; physisorption and chemisorption. In physisorption, molecules are maintained on the electrode surface by relatively weak van der Waals' forces of a physical nature. In chemisorption, much stronger and more stable covalent bonds are formed between the adsorbate and the electrode surface. Early literature focused on chemisorbed self-assembled thin films, where the chemical character of the molecule used included a head group such as a thiol or a carboxylic acid and generally a linear hydrophobic and aliphatic overlayer. More recent literature reports molecules with a number of functional groups in addition to the group responsible for chemisorption to the electrode surface. These groups can be buried near the film/substrate

interface, distributed within the film interior and/or located as a tail group on the molecule. Variation in the chemical contact between the molecule and the substrate affects the stability of the assembly and also how easily electrons are transmitted from the molecule to the metal under an applied potential [57]. Much research has taken place over the last decade to modify noble metal surfaces by forming ordered films of nanometre thickness [58-61].

Alkanethiols form stable self assembled monolayers (SAMs) on gold electrodes due to the chemical reaction between the sulphur and the gold surface. This interaction is the result of chemisorption that forces a thiol group to adsorb to the gold lattice. Tail to tail interaction of the molecules created by inter-chain, non-bonded, alkane interactions such as van der Waals, steric, repulsive and electrostatic forces are strong enough to align the molecules parallel on the gold surface and create a crystalline film [62].

Upon exposure of the gold surface to alkanethiols, bonds between the gold and sulphur molecules form rapidly, typically between seconds and minutes, however complete ordering of the monolayer can take several hours or days [63]. At low surface coverages the alkanethiolate molecules lie flat with their hydrocarbon backbones parallel to the gold surface. At higher concentrations the molecules begin to stand up with their tails tilting at approximately 30° from the surface, normally in the all trans-configuration so as to maximise van der Waals interactions [64].

The simplest method of forming these layers is to immerse the substrate in a solution containing millimolar concentrations of the organic molecules, usually redox active complexes. The films that form on the electrode surface are known as self assembled monolayers and are illustrated diagrammatically in Figure 1.17.

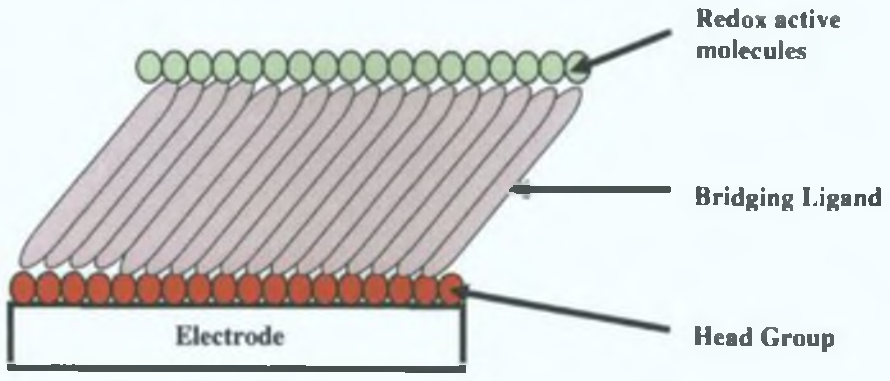

Figure 1.17. Diagrammatic representation of a self-assembled monolayer (SAM)

Self-assembled monolayers comprise a single layer of molecules on a substrate where the molecules exhibit a high degree of orientation, molecular order and packing [65]. SAM formation is an easy method for the functionalisation of selected metals such as gold, platinum, silver, copper, mercury and indium tin oxide with organic molecules, aliphatic or aromatic, containing suitable functional groups such as thiols, carboxylic acid or pyridine N heterocycles [66-68]. The fact that these monolayers are stable for long times even at elevated temperatures in aqueous solutions has allowed the electron transfer properties of the attached redox-active molecules to be probed in great detail under different conditions [69].

Another method of film preparation is the Langmuir-Blodgett (LB) method whereby a thin film of pre-orientated, amphiphilic molecules is deposited from the surface of a liquid onto a solid by immersing the solid substrate into the liquid [70].

The nature and surface roughness of the metal surfaces can affect the formation and packing density of the monolayers. Other factors that affect their formation are the type of adsorbate used, the temperature during adsorption and the concentration of the adsorbate. Cleanliness and crystallinity are also important for forming a compact monolayer free from pin-hole defects; however the purity of the gold is more important than its smoothness [54]. Electrochemical techniques such as cyclic voltammetry have been used to characterise monolayers where defects such as the presence of pin-holes can be identified and the redox properties and kinetics of the attached groups determined [4, 71-73].

1.11. Mediated electron transfer

An essential characteristic of all electrochemical sensors, whether based on the modification of electrode surfaces with monolayers or on reactions occurring in solution, is the ability to transfer electrons to the electrode surface in order to generate detectable currents. In some biosensors it has proven necessary to use chemical mediators for the electron transfer process to ensure that electrons are transferred to electrodes and measurable currents generated. Examples of such mediators, which function both in the solution phase or when immobilised as a monolayer, include ferrocene, ruthenium and osmium polypyridyl complexes.

For example, the study of electron transfer to redox proteins is hampered by the fact that these proteins are easily denatured at the electrode surface and the co-ordinated metal ion is insulated because it is buried deep within the interior of the protein matrix. Therefore direct electron transfer between redox active sites of proteins and the electrode is not normally possible [74]. Mediated electron transfer can be enhanced by the use of diffusional electron transfer mediators, which can transfer electrons indirectly from the enzyme reaction centre to the electrode (Figure 1.18).

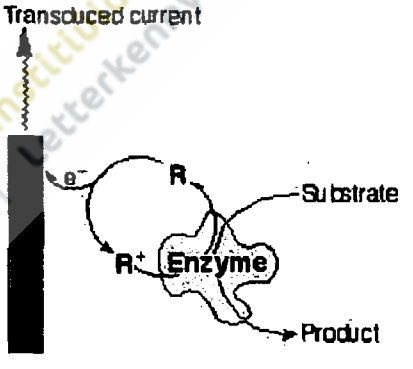

Figure 1.18. Electron transfer from the enzyme to the electrode through a mediator [75].

The effectiveness of compounds to act as mediators is influenced by their size, their shape and their hydrophobic/hydrophilic properties. Ferrocene derivatives, ferricyanide and ruthenium and osmium complexes have all been used as mediators for diffusional mediated electron transfer of soluble redox active enzymes lacking direct electrical contact with a solid electrode [76]. Cyclic voltammetry has been used to evaluate their effectiveness by determining the second order rate constants for the enzyme/mediator combination [77].

Several examples are shown diagrammatically below for the attachment of electron transfer mediators to the enzyme glucose oxidase. To facilitate electron transfer this enzyme can be covalently immobilised by:

(i) Carbodiimide coupling of ferrocene carboxylic acid to a lysine amino group via an amide bond [78].

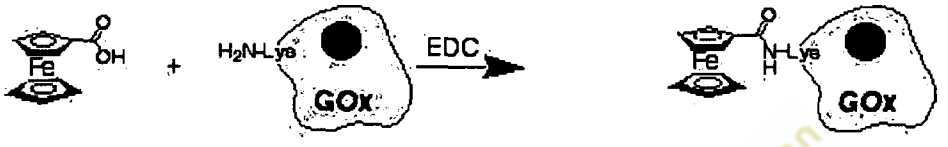

Figure 1.19. Glucose oxidase attached to a ferrocene carboxylic acid

(ii) Carbodiimide coupling of an osmium complex to a lysine amino group via an amide bond [79].

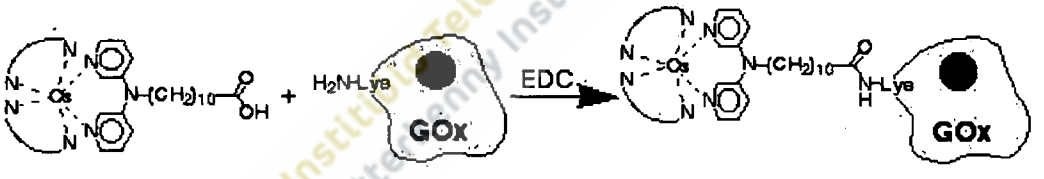

Figure 1.20. Glucose oxidase attached to an osmium polypyridyl complex

(iii) Coupling of a ruthenium complex to a histidine residue [80].

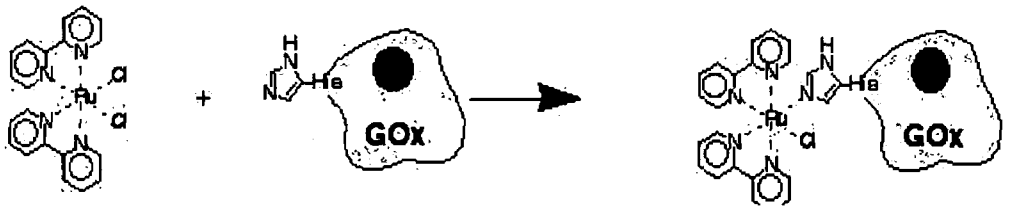

Figure 1.21. Glucose oxidase attached to a ruthenium polypyridyl complex

1.12. Enzyme monolayers

Enzymes can also be immobilised on electrode surfaces. Direct immobilisation of the enzyme onto the electrode surface, for example where the enzyme is held in a random manner behind a polymer matrix covering the electrode, results in sensors that are neither reproducible nor stable. Indirect immobilisation of the enzyme whereby the enzyme is attached to a functional group present in a pre-formed self-assembled monolayer on the electrode surface provides a more reproducible method with much improved control over the molecular structure. An alternative method for enzyme immobilisation which has been used by some researchers is modification of the enzyme with a functional group to provide a mechanism for attachment. For example by modifying the primary amine group on the enzyme with a thiol group, McRipley and Linsenmeier [81] immobilised glucose oxidase on a clean gold electrode. This method allowed a monolayer of the enzyme to be formed on the electrode, although a very long incubation time of approximately 250 hours was required.

Self-assembled monolayers are popular for enzyme immobilisation because of the ease with which they can be formed and their greater stability [82]. Proteins are less likely to suffer denaturing structural changes when they are attached to a hydrophilic SAM compared to their direct immobilisation on a bare metal surface [69]. A popular and versatile method of covalently attaching proteins is using carbodiimide coupling, which couples amine groups on the enzyme to free carboxylic acid groups in the SAM. In this reaction N-ethyl-N[diethylaminopropyl] carbodiimide (EDC) converts a carboxylic acid to a reactive intermediate which is susceptible to attack from amines. In some cases EDC is used in conjunction with N-hydroxysuccinimide (NHS) as it produces a more stable reactive intermediate that has been shown to give a greater reaction yield [83]. Gooding *et al.* [84] used this method to covalently attach glucose oxidase to a mercaptopropionic acid (MPA) self-assembled monolayer where the bond occurred through the free lysine chains on the enzyme. This enzyme electrode had a large dynamic range and responded to glucose concentrations greater than 50 mM. This method of enzyme immobilisation is applicable to many other different enzymes.

1.13. Adsorption of organic substances

The first experimental work on the study of adsorption of organic substances was Gouys electrocapillary work at the beginning of the century [85]. The first qualitative work on the effect of the electric field on adsorbed species was formulated by Frumkin in his two papers in 1925 and 1926 and the theory proposed in these works remains in use [86, 87]. Further contributions to the understanding of adsorption, based on molecular microscopic structure, were developed in 1929 by Butler [88]. Although attractive from a physical point of view, Butler's work encountered many theoretical difficulties and was practically less useful.

The adsorption reaction of a species on a solid surface from the gas phase is relatively simple and can be represented as:

$$A \longrightarrow A_{ads}$$

where A is the species in the unadsorbed gaseous state and A_{ads} is the same species adsorbed on a solid surface.

The free energy of adsorption (ΔG_A) for this reaction at low coverage is essentially determined by the interaction of the molecules of the adsorbing species and the electrode surface. At higher coverages, attractive or repulsive interactions between adsorbing molecules themselves, may have an influence. Adsorption from solution of the same species is more complicated. In this case for a species to adsorb to a metal surface, it must first displace one or more solvent molecules and can be represented as:

$$A_{sol} + {}_nS_{ads} \longrightarrow A_{ads} + {}_nS_{bulk}$$

where A_{sol} is the species dissolved in solution, ${}_nS_{ads}$ are the solvent molecules adsorbed on the electrode surface, A_{ads} is the same species adsorbed on a solid surface and ${}_nS_{bulk}$ are the solvent molecules present in the bulk solution.

In summary, adsorption from solution depends on species/metal, species/species, solvent/metal and solvent/solvent interactions and must be considered as a competition

between all the species present for the available sites on an electrode surface [89]. Adsorption from solution has been shown in a schematic model of the electric double layer in Figure 1.22.

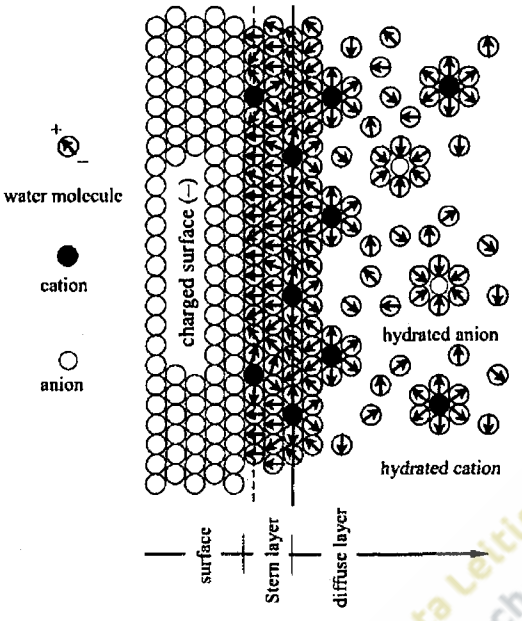

Figure 1.22. Schematic model of the electric double layer showing the specifically adsorbed cations and the fully hydrated anions and cations on a negatively charged surface [90].

The potential of the electrode can also have an influence on adsorption as this causes changes in the distribution of ions in the diffusion layer adjacent to the electrode. For a positively charged electrode this will lead to the adsorption of anions to neutralise the charge, while for more negatively charged electrodes it will have the opposite effect, i.e. adsorption of cations. Other factors which may influence adsorption include the composition of the deposition solution, the concentration of the adsorbing complex, use of a two component complex or limiting the deposition time [91-94]. The molecules that comprise a monolayer align in a particular order with respect to the electrode surface. This orientation is such that they attain the most negative free energy of adsorption. Changes in the orientation can occur due to differences in pH, concentration, temperature and the electrolyte used.

1.14. Adsorption Isotherms

For adsorbate molecules to self-assemble on the surface of a substrate, ions or solvent molecules already adsorbed must first be displaced. Competition for the available binding sites on the electrode influences the rate of adsorption. Adsorption from liquids is usually

described through adsorption isotherms which describe the relationship between the bulk solution concentration and the concentration on the surface, expressed as a surface coverage.

The Langmuir adsorption isotherm for single layer adsorption describes the fraction of the surface area of the adsorbent covered with adsorbate molecules (Γ), as a function of their concentration in the liquid phase (C^*) at a constant temperature and pressure. The Langmuir isotherm is a curve, convex to the solute concentration axis which flattens out when the total surface is covered with adsorbate molecules. The Langmuir equation applies where the only factor considered is molecular size and no adsorbate-adsorbate interactions occur. The Langmuir isotherm is described by:

$$\beta C^* = \frac{\theta}{1-\theta} \qquad (27)$$

where β is the adsorption co-efficient and θ is the fractional coverage Γ / Γ_s where Γ_s is the saturation coverage. Deviations from the Langmuir isotherm are often observed and have been attributed to surface heterogeneities, adsorbate-adsorbate interactions or the formation of more than one monolayer, often referred to as multilayers [95]. When repulsive or attractive interactions occur between adsorbates, an exponential term is added to the Langmuir isotherm, the simplest of which was proposed by Frumkin:

$$\beta C^* = \frac{\theta}{1-\theta} \exp(-2a\theta) \qquad (28)$$

where a is the interaction parameter. When a = 0, the Langmuir and Frumkin isotherms are identical. Repulsive forces are described by $a > 0$ and attractive forces by $a < 0$.

An adsorption isotherm, which does not require a saturation or maximum coverage and can be used where multilayers are formed, is the Freundlich isotherm:

$$\Gamma = K(C^*)^{1/n} \qquad (29)$$

where K is related to the adsorption capacity and n characterises the energies of the adsorption sites. For this isotherm, a plot of $\log \Gamma$ vs. $\log C^*$ should be linear with a slope of $1/n$ [96].

1.15. Adsorption cyclic voltammetry

Acevedo and co-workers [97] used cyclic voltammetry to study the effects of pH and ionic strength on the thermodynamics of adsorption during the self-assembly process of a range of redox-active transition metal complexes $[Os(bpy)_2(L)Cl]^+$ where L = 4,4'bipyridine, 1,2-bis-(4-pyridyl)ethylene and 1,3-bis(4-pyridyl)propane on platinum electrodes. Reduced adsorption isotherms were reported with decreasing pH and attributed to the fact that these complexes are known to adsorb onto the electrode surface through the pendant pyridine. At pH values below the pKa of the complex the pyridine group becomes protonated. As the pH is lowered, a larger fraction of the complex becomes unavailable for chemisorption. The ionic strength of the supporting electrolyte had no effect on the adsorption isotherm.

Bretz and Abruña [98] studied the adsorption of transition metal complexes $[Os(bpy)_2Cl(py-(CH_2)_n-SH](PF_6)$ where n = 4, 6 and 9, on gold and platinum electrodes. The quantity of material adsorbed was strongly dependant on the potential applied during deposition. The progress of the reactions was monitored in-situ. This was possible because the solution concentrations were in the micromolar range and would therefore contribute an insignificant amount to the total current. At potentials negative of 150 mV the complex exists in the (Os)(II) state with a 1^+ charge while at potentials positive of 150 mV it exists in the (Os)(III) state with a 2^+ charge. At more negative potentials, attractive forces between the osmium complex and the electrode resulted in increased adsorption demonstrating that the electrode potential can be used to control adsorption. There was no relationship between the length of the carbon chain and in subsequent adsorption and desorption studies with the same complexes the formation of multilayers rather than monolayers was reported [99]. The experimental data could not be described by the Langmuir isotherm because of the shape of the curves produced and the fact that multilayers were formed, however it did fit the Freundlich adsorption isotherm model. The multilayers formed were porous (pin-holes) and other redox active materials in solution could still be detected. Desorption of these complexes followed a simple exponential relationship and was slower with longer chain length ligands suggesting that such complexes formed more stable multilayers.

Adsorption studies on platinum electrodes by Abruña and co-workers [100] of transition complexes of the general formula $[Os(bpy)_2(L)Cl]^+$ where L = 4,4'bipyridine, 1,2-bis-(4-

pyridyl)ethylene and 1,3-bis(4-pyridyl)propane were undertaken with a bipotentiostat which controls the voltage and measures the current at two working electrodes immersed in an electrolyte. This allowed identical conditions to be used for both electrodes with the exception of the applied potential. The potential of the first electrode was maintained at 200 mV where the overall charge on the complex is 1^+ and the potential of the second electrode was maintained at 400 mV where the overall charge is 2^+. At all complex concentrations, the surface coverage was reduced on the electrode maintained at 400 mV. It was concluded that the reduced coverage occurred because of repulsive interactions between the positively charged electrode and the oxidised metal centre in the complex.

Forster and O'Kelly [92] examined the adsorption and desorption of $[Os(bpy)_2(p3p)_2]^{2+}$, where p3p is 4,4'- trimethylenedipyridine, onto platinum and gold microelectrodes. Cyclic voltammetry was used to determine the increase in surface coverage *ex situ* in aqueous perchlorate solution. The role of mass transport to the electrode was considered and it was estimated that a dense monolayer would assemble within 3 seconds. Since monolayer formation in practice required between 400 and 7000 seconds it was concluded that the rate-determining step was not mass transfer but the kinetics of surface binding. On both gold and platinum electrodes, assembly of the monolayer blocks the formation of an oxide coating and decreases double layer capacitance, however this decrease is reduced on platinum suggesting a more open film structure. In contrast to gold, multilayers are formed on platinum at longer exposure times and at higher concentrations. The rate constant for monolayer formation on gold was twice that for platinum. Adsorption on gold or platinum was best described by a second order model and was not consistent with Langmurian adsorption. Overall conclusions were that deposition times, bulk concentration and the type of electrode all affect monolayer assembly. Desorption from both gold and platinum followed single exponential desorption kinetics suggesting that lateral interactions between adsorbates are not significant.

Campbell and Anson [101] studied the extent and dynamics of the adsorption of Os (II) complexes with the general formula $Os(bpy)_2(L)Cl_2$, where L = 1-2bis(4-pyridyl)ethane, 4-phenylpyridine, 4-(1-n-butylpentyl)pyridine, on platinum, gold and graphite electrodes. The pendant pyridine group of the Os (II) complexes was important for adsorption on platinum but not necessary with gold or graphite, though enhanced adsorption on gold was reported.

Although adsorption on gold was faster than on graphite, a larger surface coverage was eventually achieved with the latter.

Forster and co-workers [102] investigated the electrochemical properties of ruthenium and osmium complexes $[M(bpy)_2bpe\ Cl]^+$ where M represents the metal and bpe is *trans*-1,2-bis(4-pyridyl)ethylene). Irradiation of the ruthenium complex with visible light causes the replacement of the chloride with a water molecule to give $[Ru(bpy)_2(bpe)H_2O]^{2+}$. The charge effects on adsorption were examined by depositing a two component monolayer from a solution which contained 2.5μM of both complexes $[Ru(bpy)_2(bpe)H_2O]^{2+}$ and $[Os(bpy)_2(bpe)Cl]^+$. Surface coverage of the osmium centre was found to be 5 times higher than that of the ruthenium centre demonstrating that factors other than the type of bridging ligand can have an influence on adsorption. It was suggested that the hydrophobicity of the ruthenium centre due to its 2^+ charge resulting from the replacement of the chloride ion with the H_2O molecule was the cause of the lower coverage of the ruthenium centre.

Abruña used cyclic voltammetry to monitor, in-situ, the formation of mixed self-assembled monolayers of osmium and ruthenium complexes [102]. These complexes had a 1,3-bis(4-pyridyl)propane (dipy) ligand attached with a pendant nitrogen that binds to a platinum surface. The formal potentials of the two complexes are separated by more than 400 mV allowing quantification of the amount of each complex present in the monolayer. Results showed that an Osdipy monolayer would be fully replaced by a Rudipy monolayer when placed in a 2 μM solution of Rudipy containing no dissolved Osdipy or vice versa. When different ratios of each complex were placed in solution it was found that the resulting monolayer showed a slight adsorptive preference for the osmium complex. The shape of the peaks was also used to determine if near-neighbour interactions existed between the adsorbed complexes. In an ideal situation the full width at half maximum of the voltammetric peak should be 90.6/n mV [25]. In the presence of mixed monolayers of ruthenium and osmium complexes, the formal potential of the Osdipy shifted positively by approx. 40mV and there was a broadening of the wave associated with the ruthenium complex. This suggested a change in the chemical environment around the Rudipy monolayer as near-neighbours Osdipy is in the 2^+ state resulting in larger electrostatic repulsion and also that the Osdipy and the Rudipy molecules are randomly distributed in the monolayer rather than being present in separate domains.

Rowe and Creager [103] immobilised ferrocenylhexanethiol, Fc-$(CH_2)_6$-SH, and longer chain alkanethiols on gold electrodes. Thiols with longer chains were always preferentially adsorbed due to the free energy difference resulting from the additional methylene units. The time required to achieve a limiting surface coverage ranged from several hours to several days.

Collard and Fox [104] used cyclic voltammetry to study the formation of alkanethiol monolayers on gold. When a mixed monolayer consisting of an electroactive ferrocene substituted thiol and a non-electroactive thiol was exposed to a solution of a non-electroactive thiol approximately one third of the electroactive thiol was replaced within 48 hours. This was attributed to defect sites present on the gold surface caused by the bulky ferrocene molecule which resulted in lower than expected surface coverage. These defect sites were rapidly exchanged with non-electroactive alkanethiol from solution resulting in a reduction in the ferrocene content of the monolayer.

Whiteside and co-workers [105] studied the composition of a two component self-assembled monolayer of the long chain CH_3-$(CH_2)_{21}$-SH and short chain CH_3-$(CH_2)_{11}$-SH alkanethiols on gold. Mixed monolayers comprised a single phase and not regions of separate phases. Exchange reactions, where a single component SAM of CH_3-$(CH_2)_{11}$-SH or CH_3-$(CH_2)_{21}$-SH were immersed in ethanol solutions containing different mixtures of thiols demonstrated that the longer chain thiol was removed more slowly. Unlike Langmuir monolayers (at the air/water interface) two component SAMs did not phase into separate domains when immersed in different thiol compositions.

Finklea [106] formed mixed monolayers on gold of non-electroactive thiols HS-$(CH_2)_n$-CH_3 where n = 10, 11 and 15 and electroactive thiols $CONH(CH_2)_n$-Py-$Ru(NH_3)_5^{2+/3+}$ where n = 10, 11 and 15. Immersion in ethanol, containing only electroactive thiols, resulted in multilayer formation whereas with mixed electroactive and non-electroactive thiols this did not arise. Multiple peaks were observed in cyclic voltammograms after initial depositions but were eliminated after repeated immersions. Multiple peaks were attributed to the presence of different environments around the redox centres. It was suggested that cyclic voltammetry caused a flux of ions around the molecules resulting in a more ordered and better orientated closely packed monolayer with a single peak. It was recommended that for

the formation of well behaved electroactive monolayers of this type a combination of deposition followed by cyclic voltammetry be used.

Wrighton and co-workers [107] exposed gold and indium tin oxide (ITO) electrodes to equimolar solutions of a ferrocene-tagged thiol and a ferrocene-tagged carboxylic acid. Selective attachment of the thiol to the gold electrode and the carboxylic acid to the ITO were demonstrated. Coverage ratios of the thiol to the carboxyl determined by cyclic voltammetry were 100-1 on gold and 1-45 on ITO. This selective surface attachment, known as "orthogonal self assembly" (OSA), provided a method where molecules containing different functional groups could be selectively adsorbed, orientated and connected between closely spaced electrodes and the possibility of connecting individual macromolecules between externally addressable contacts. The motivation for further work in this area is to exploit the properties of molecular materials to achieve switching or amplification of electrical or chemical signals. It may also be useful in studying the conductivities of molecular materials over small distances. A schematic representation of orthogonal self assembly is provided in Figure 1.23.

Figure 1.23. A schematic representation of orthogonal self assembly. The thiol group is represented by (•) and the carboxylic acid group by (o).

Ulman [108] formed self-assembled monolayers of 4-mercaptobiphenyls on gold surfaces. Alkanethiols have been extensively studied and these differ from the biphenyls by the fact that the biphenyls contain a rigid π character. This π conjugation between the adsorbing thiolate and the substituent at the 4 position of the phenyl group creates a dipole moment that affects adsorption.

The rate of adsorption has been investigated using Quartz Crystal Microbalance (QCM). Electrochemical Quartz Crystal Microbalance (EQCM) measures the resonant frequency of a

quartz crystal when one of the electrodes is exposed to an electrolyte solution and maintained at a controlled potential. In many cases the working electrode is a cut quartz crystal covered with gold, sputtered on a titanium layer.

Self assembled monolayers of alkylthiols with an $[Os(bpy)_3]^{2+}$ terminal group were prepared on gold electrodes and EQCM used to investigate the current response accompanying the adsorption of $[Os(bpy)_2(bpy\text{-}C_nSH]^{2+}$ on gold and the corresponding mass transport of counter anions towards and away from the SAM. The adsorption of the complex was observed by monitoring the decrease in frequency equivalent to the increase in mass. Full monolayer coverage was achieved in approximately ten minutes from a 0.1M concentration of the complex in methanol. Desorption of the monolayer decreased to approx. 75% of the full coverage after 90 mins of repetitive cycling in 0.1M $NaClO_4$ [109].

The molecular assembly of long chain alkanethiols has become popular in recent years because of their strong adhesion to substrates, their high degree of chemical and thermal stability and their mechanical strength. Although work has focused on the structural properties of these thin films, few studies have examined the formation mechanism involved. Although QCM is not a very selective technique it responds very quickly and quantitatively to any mass increase and provides information that is difficult to acquire by other means.

The self-assembly process of ferrocenylundecanethiol was measured in situ using EQCM by Shimazu [110]. Adsorption comprised an initial fast step followed by a much slower process. The number of adsorbed thiol molecules estimated from the frequency change suggested the formation of a monomolecular layer. EQCM was also used to monitor the mass change during oxidation/reduction of the ferrocenylundecanethiol monolayer and confirmed that anions were incorporated into the self-assembled layer during oxidation of the ferrocene group. This confirmed previous electrochemical studies that the ferricenium cation forms an ion pair with anions in solution [111].

Dong Ho Kun and co-workers [112] studied the self-assembled formation of octadecanethiol $(CH_3(CH_2)_{17}SH$ on a gold substrate. QCM measurements were performed at various concentrations and confirmed that the adsorption process comprised of two steps; the first being fast but disordered adsorption and the second a thermodynamically-controlled

rearrangement for uniform packing. The rate of adsorption was faster in ethanol than in hexane and this was attributed to the lower solubility of the thiol in ethanol which could assist monolayer formation. In this experiment a 1Hz change in the frequency of the QCM was equal to a one nanogram mass loading on the gold plate.

1.16. Electron transfer

Progress towards development in areas such as corrosion, electroanalysis, medical device operation and molecular electronics will require a better understanding of the processes involved in electron transfer. Such processes are influenced by both the molecular species involved and the nature of the electrode surface. Adsorbed monolayers offer many advantages over solution phase experiments for studies of the effects of changing the molecular species and electrode material on electron transfer dynamics, in particular the elimination of diffusive mass transport. By careful selection of the bridging ligand, double layer effects can be minimised and the system can be made non-adiabatic because the electron travel distance can be controlled. Many studies have been carried out using ordered electroactive monolayers to determine the factors that affect electron transfer but fewer studies have taken place on the effect of changing the electrode material.

Gosavi and Marcus [113] studied how the rate of electron transfer was influenced by the density of the electronic states (ρF) of the metal at the Fermi level with particular emphasis on how it affected the exchange current (i_{ex}). Rate constants (k_{et}) for alkanethiol monolayers formed on platinum and gold were determined. Whilst the density of states (ρF) of platinum is approx. five times that of gold, a difference attributed to the d band of platinum, k_{et} only increased by a factor of 1.8. For the exchange current i_{ex} to be proportional to ρF, each electronic orbital in the metal s, p and d must contribute equally. The d orbitals responsible for ρF in platinum and palladium lie near the Fermi level and are much less coupled to the acceptor than the s electrons which dominate ρF in gold and silver, with the result that the exchange rate would not be proportional to the total ρF for non-adiabatic processes. Forster and co-workers [68] formed monolayers of $[Os(Ome\text{-}bpy)_2(p3p)Cl]^+$ where $(Ome\text{-}bpy)_2$ is 4,4'dimethoxy-2,2'bipyridyl and p3p is trimethylenedipyridine on platinum, mercury, gold, silver, carbon and copper microelectrodes to study the effect of the electrode density of states on the heterogeneous electron transfer dynamics.

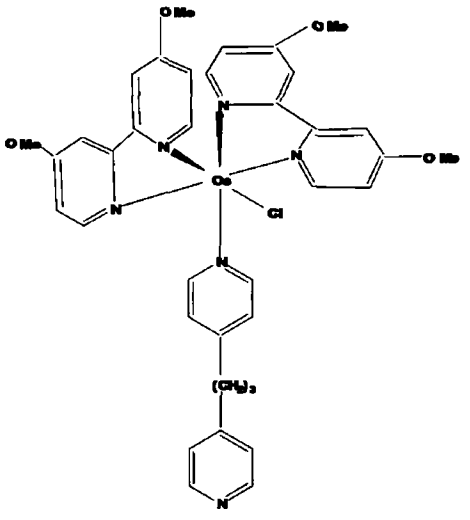

Figure 1.24. Chemical structure of $[Os(Ome\text{-}bpy)_2(p3p)\text{-}Cl]^{+}$ [68].

This complex was selected for the investigation because the redox potential of 50 mV allows electrochemical measurements using electropositive metals. Formal potentials (E°) became sequentially more positive from platinum to gold, carbon and mercury. Contributions from electron coupling effects (A_{et}) and the free energy of activation (ΔG) were decoupled by measuring the rate constant at a single temperature over a range of driving forces. Results showed that ΔG was independent, while the electron transfer rate constant (k°) was dependant on the electrode material. The ratio of $k^\circ_{pt}/ k^\circ_{au}$ determined in this study was 2.2, in general agreement with the value derived from the Marcus theory of 1.8.

Forster and O'Kelly [114] examined how varying the pH of a spontaneously adsorbed monolayer of $[Os(bpy)_2 (p3p)_2]^{2+}$ affected the electron transfer across the metal/monolayer interface. With this complex one of the pyridine units binds to the electrode surface whilst the other is free for protonation. Heterogeneous electron transfer was affected because of the protonation of the free pyridine. A sigmoidal relationship was found between the electron transfer rate constant (k°) and the pH with k° decreasing from 3.4×10^5 to 6.6×10^4 s^{-1} when the solution pH decreased from 5.05 to 1.77. The results suggested that protonation affected the heterogeneous electron transfer rate constant either because it caused a different tilt angle between the adsorbate and the electrode or the methylene spacers became more extended.

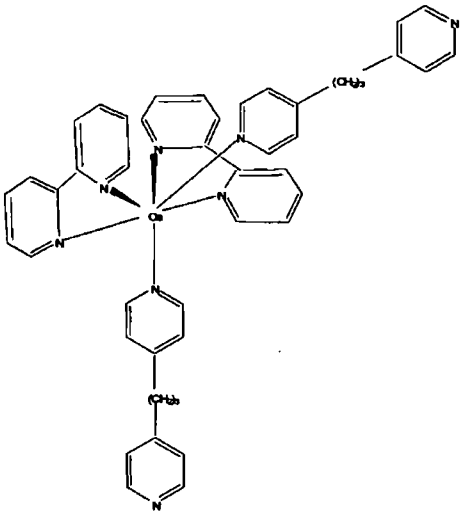

Figure 1.25. Chemical structure of $[Os(bpy)_2\ (p3p)_2]^{2+}$ [115].

Forster and Faulkner [115] formed spontaneously adsorbed monolayers of $[Os(bpy)_2\ pNp]$ where pNp is either 4,4'-bipyridyl, 1,2-bis(4-pyridyl)ethane or 4,4'-trimethylenepyridine. In this study, ion pairing between the osmium redox centre and perchlorate anions was dependant on the electrochemical solvent. Oxidation of the metal centre in the solvent tetrahydrofuran caused one extra anion to bind while two extra anions were bound in aqueous media upon oxidation.

Forster and Keyes [116] formed monolayers on platinum microelectrodes of the dimeric complex [p0p $Os(bpy)_2$ 4-tet $Os(bpy)_2$ Cl] where pOp is 4,4'bipyridyl and 4-tet is 3,6-bis(4-pyridyl)-1,2,4,5-tetrazine shown on Figure 1.26

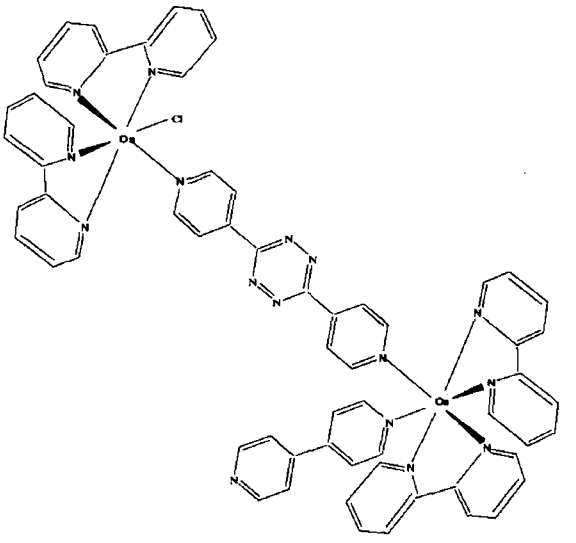

Figure 1.26. Chemical structure of [p0p $Os(bpy)_2$ 4-tet $Os(bpy)_2$-Cl] [116].

These dimeric complexes were studied to assist in understanding the effect of switching the oxidation state of the bridge on the dynamics of electron transfer. This cannot be tested with monolayers that contain a single redox centre. The electronic coupling between the two metal centres was compared with results for a monolayer with a single redox centre, which contained the same tetrazine bridge anchored to the electrode surface. The effect of switching the oxidation state of the "inner" centre on the dynamics of electron transfer to the "outer" centre was investigated. Electronic coupling across the tetrazine bridge was much higher between the two osmium centres than between the electrode and osmium. Larger k° values were reported for the inner redox couple due to coupling effects, suggesting that converting the metal centre from the oxidised to the reduced form changes the strength of electronic coupling between the outer metal centre and the electrode. This has significance in the development of molecular switches where electronic coupling across a bridge must be controllable.

Forster and co- workers [117] formed monolayers of $[Os(bpy)_2(4\text{-tet})\text{-Cl}]^+$ where 4-tet is 3,6-bis(4-pyridyl)1,2,4,5-tetrazine.

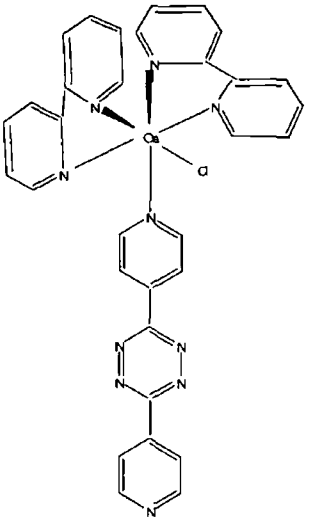

Figure 1.27. Chemical structure of $[Os(bpy)_2(4\text{-tet})\text{-}Cl]^{+}$ [117].

The 4-tet ligand is electroactive and can undergo protonation/deprotonation reactions at the bridge by changing the pH of the electrolyte solution and is thus of interest for the development of microelectronic switches. The effect of protonation on the electron transfer rate constant (k°) and the free energy of activation (ΔG) was determined. Analysis revealed that ΔG was insensitive to pH, but the electron transfer rate constant decreased when the tetrazine bridge was protonated. This result was consistent with mediated electronic states within the bridge (superexchange) playing an important role in the redox switching process. This superexchange is most likely when the highest occupied molecular orbital (HOMO) of the bridge is similar in energy to the acceptor states of the $Os^{2+/3+}$ metal centre. Protonation of the bridge increased the energy difference and as a result caused the standard rate constant to decrease.

Finklea and Hanshew [118] investigated mixed monolayers on gold electrodes comprising electroactive $(pyRu(CH_3)_5^{2+/3+}$ and diluent thiols $(HS(CH_2)_nCH_3)$ or $(HS(CH_2)_nCOOH)$ where n = 10, 11 or 15 (Figure 1.28).

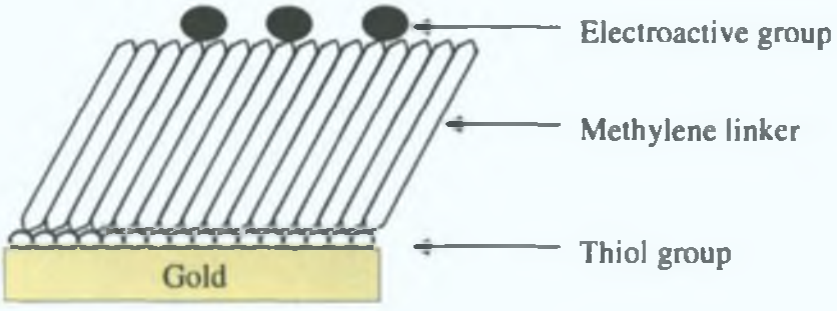

Figure 1.28. Diagrammatic representation of a mixed monolayer of electroactive and diluent alkanethiols.

A mixed monolayer of electroactive and non-electroactive molecules allowed a close-packed structure when the radius of the head group was much greater than the radius of the tether. For optimal tightly-packed structures, the length of the electroactive molecule should be the same as the tether. The electron transfer rate constant (k^o) of the mixed monolayer decayed exponentially with increasing chain length. Cyclic voltammograms exhibited increased peak splitting when the scan rates were sufficiently fast and allowed the standard rate constant (k^o) to be calculated. The nature of the terminal group (CH_3 or COOH) in the diluent thiol had no significant effect on k^o.

1.17. DNA-based biosensors

Biosensors are devices that feature a biological entity as the main part of the sensing process and convert the physical parameters of the biological interaction into a measurable analytical signal [124]. DNA-based biosensors contain deoxyribonucleic acid (DNA), one of the most intensely studied biomolecules of the past decade, as the biological entity of the sensor.

DNA is a very long, thread-like macromolecule comprising millions of monomer units called nucleotides. Each nucleotide consists of three distinct parts; one of four nitrogen containing bases, a deoxyribose (a five-carbon sugar) molecule attached to the base and a phosphate group attached to the sugar (Figure 1.29).

Figure 1.29. Basic structure of the nucleotide.

The four nitrogen-containing bases are adenine, guanine, thymine and cytosine. Nucleotides are named according to which of the four bases are present, often referred to by the first letter of the base, hence A, G, T and C. Adenine and guanine are classified as purine bases and are the larger of the two types of base found in DNA, thymine and cytosine are classified as pyrimidine bases and are the smaller of the two types of base (Figure 1.30).

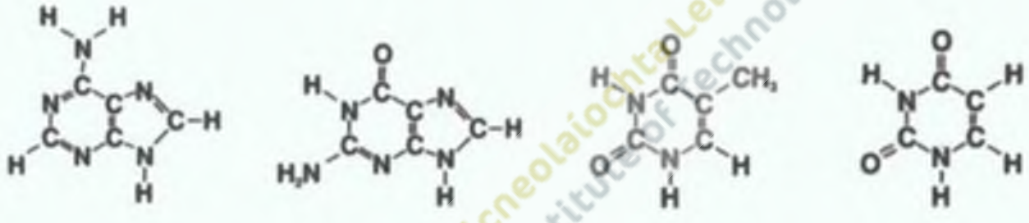

Figure 1.30. Structure of the four bases.

The nine atoms that make up the fused rings in the purine bases (5 carbon, 4 nitrogen) and the six atoms that make up the ring in the pyrimidine bases (4 carbon, 2 nitrogen) are numbered 1-9 and 1-6, respectively, and in each base all ring atoms lie in the same plane. The deoxyribose sugar of the DNA backbone has 5 carbons atoms numbered sequentially from right to left as 1', 2', 3', 4', and 5', to distinguish them from the numbering of the atoms of the purine and pyrimidine rings (Figure 1.31).

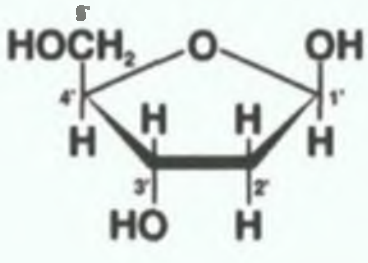

Figure 1.31. Structure of the deoxyribose sugar.

One of the four nitrogenous bases is attached to the 1' carbon. The hydroxyl groups on the 5'- and 3'- carbons link to phosphate groups allowing the formation of a single strand of DNA (Figure 1.32).

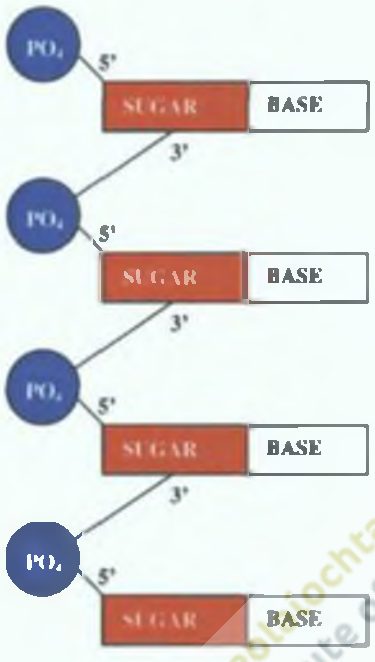

Figure 1.32. Structure of a single strand of DNA

For any nucleotide, the phosphate attached to the hydroxyl group at the 5' position of the sugar is in turn bonded to the hydroxyl group on the 3' carbon of the sugar on the next nucleotide. This method of linkage confers polarity on the single strand of DNA (ssDNA) as one end of the chain has an unlinked 5' hydroxyl group and the other a free 3' hydroxyl group. The four different types of nucleotide in DNA differ only in their nitrogenous base; adenine (A), guanine (G) thymine (T) and cytosine (C). The sequence of the bases is open to variation, and it is this sequence that carries the genetic information, while the sugar and phosphate provide a structural role [119, 120]. In nature, DNA comprises two strands (dsDNA) wound round each other to form a double helix with the bases on the inside and the sugar-phosphate groups on the outside. The strands of the double helix are organised in an anti-parallel arrangement, i.e. the two strands run in opposite directions, one strand being oriented in a 5'-3' direction and the other in a 3'-5' direction as shown in Figure 1.33.

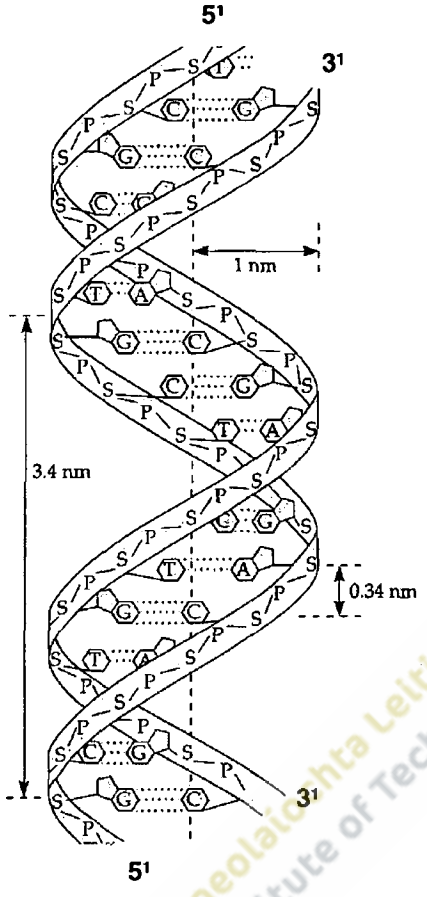

Figure 1.33. DNA double helix and anti parallel arrangement (adapted from Ref. No. 121).

The bases of the double helix hold the structure together, a purine base always binding with a pyrimidine base to form a base pair. Adenine always binds with thymine to form the A-T base pair, and guanine always binds with cytosine to form the C-G base pair. Weak hydrogen bonds exist between these base pairs, two in the A-T base pair and three in the G-C base pair, and it is these weak hydrogen bonds that are responsible for the double helix shape of DNA. Because of base pairing between the DNA strands, the sequence of nucleotides in one strand determines the sequence of nucleotides in the other strand, A always pairing with T and G always pairing with C, the two strands being described as complementary to one another. The series of bases in a DNA chain is by convention always written in the direction of 5'-3', an important consideration when describing the sequence, given the anti-parallel arrangement of the two strands.

Because of these very specific and robust base-pairing interactions, DNA is very well suited for applications in biosensor development [122]. If the sequence of bases of one strand of DNA is known, then the complementary base sequence can be synthesised. In DNA hybridisation the target gene sequence (ssDNA) is identified by a complementary DNA probe that can form double stranded DNA (dsDNA) with its complementary bases. This hybridisation process can occur with high efficiency and high specificity even in the presence of a mixture of nucleic acids. Detection of hybridisation has involved a variety of techniques, most of which have been based on optical methods commonly involving fluorescence.

Widespread DNA testing requires the development of small, fast and easy-to-use devices which can provide sensitive and selective detection of DNA hybridisation. The main problem to be overcome with DNA biosensors is reproducible detection in the presence of extremely small amounts of target analytes [123]. At the atomolar level this can only be overcome by amplification of the sample by the polymerase chain reaction (PCR) where in theory even a single copy of the target can be amplified to obtain a detectable signal. Interest in recent years has focussed on the development of electrochemical DNA biosensors or E-DNA sensors. Such sensors commonly depend on the immobilisation of a single-stranded (ss) oligonucleotide probe onto an electrode surface. Hybridisation between this immobilised probe and its complementary target sequence is translated into a useful electrical signal that can be used to signify the hybridisation process [124]. The advantages of an electrochemical-based detection system compared to an optical-based detection system are that it is simple-to-use, highly sensitive, inexpensive, easily made portable and compatible with micro-fabrication technologies.

DNA biosensors based on nucleic acid hybridisation and electrochemical detection are currently under development for applications in diagnostic medicine, gene sequencing and environmental testing [125-131]. In such applications electrochemical detection of hybridisation is commonly based on an increased current signal of a redox indicator that recognizes the DNA duplex, or from alteration of the electron transfer process after hybridisation. The development of electrochemical DNA biosensors which function without additional reagents has been accelerated by advances in DNA synthesis. Many commercial companies now offer site specific labeling of synthetic oligonucleotides with functional groups capable of

attachment to a particular substrate and suitable for a particular application. Much of the pioneering research on electrochemical DNA sensors has been undertaken using commercially available electrodes produced by sealing gold wires into plastic or glass supports. Modified electrodes following electrochemical investigations can be regenerated to a bare gold surface to allow re-immobilisation by mechanical polishing and chemical and electrochemical cleaning procedures. Both reproducibility and the time consuming nature of these regeneration processes are problematic. The availability of disposable screen printed or photo-lithographed gold electrodes have overcome the need for any regeneration step [124, 132, 133]. This has facilitated the development of disposable, low-cost DNA biosensors suitable for use with simple, portable instrumentation and represents a most attractive option for future commercial developments in this field [125, 134-136]. Miniaturisation of such devices and their compatibility with advanced microelectronic technology make them an excellent choice for DNA diagnostics, however much work remains to be undertaken before the sample preparation process and detection system can be applied to a 'Lab-on-a-Chip' format [136, 137].

A variety of approaches other than electrochemical measurement exist for the detection of DNA hybridisation including X-ray photoelectron spectroscopy (XPS) [138, 139], radiolabeling, surface plasmon resonance (SPR) [140] and quartz crystal microbalance (QCM) [141]. Electrochemical measurements, in contrast to XPS, are nondestructive; hence surfaces characterised electrochemically remain available for use as electrochemical DNA sensors post-characterisation. Radiolabeling suffers from a number of disadvantages including short shelf life, risks associated with exposure of personnel to radiation, cost, storage and disposal problems, while electrochemical measurements are nontoxic and avoid disposal problems. Mass-sensitive QCM [142,143] measurements are often prone to interferences while in contrast electrochemical measurements are usually sensitive and qualitative [144]. Enzymatic or luminescence labels are less sensitive and flexible in terms of design and application [145].

One key feature that has been highlighted by the research effort is the need for a fundamental understanding of the molecular organisation and structure of the immobilised DNA film to ensure modified electrode surfaces that exhibit high biological activity and selectivity. Immobilisation must result in a well-defined probe orientation which is readily accessible to the target to allow duplex formation that can be detected by changes in the electrochemical signal [146].

For the development of E-DNA sensors a number of different approaches have been used to immobilise DNA onto the solid surface of a range of different electrodes. Several carbon-based electrodes have been investigated for use as biosensors of DNA hybridisation including carbon paste [147], pencil lead electrodes [148], screen printed electrodes [149], and disposable carbon strips [124]. Both platinum and polypyrrole electrochemical transducers have also been used as solid surfaces for DNA immobilisation [150]. Paleček *et al.* [151] proposed the use of magnetic beads on which the DNA hybridisation occurred in conjunction with electrochemical detection electrodes. Self-assembled monolayers on gold have shown themselves to be model systems in these studies [124, 142, 146, 152-160]

Many different methods have been used for immobilising DNA onto the surface of gold electrodes. Early efforts involved adsorption of DNA on gold by simply allowing tiny amounts of DNA solution to dry onto the electrode [161]. Although this simple method of immobilisation required neither reagents nor any modification of the nucleic acid probe some of the immobilised DNA probe was prone to desorption from the surface during the hybridisation step. Because of the risk of desorption of the non-covalently bound hybridised DNA, stringent washings, necessary to ensure a high selectivity against mismatched sequences, could not be performed. In addition since DNA molecules adsorb onto the surface of the electrode through multiple sites and the rate of hybridisation is directly linked to the accessibility of the DNA probe, poor hybridisation efficiency occurred since much of the immobilised DNA probe was not accessible for hybridisation (Figure 1.34) [124, 150].

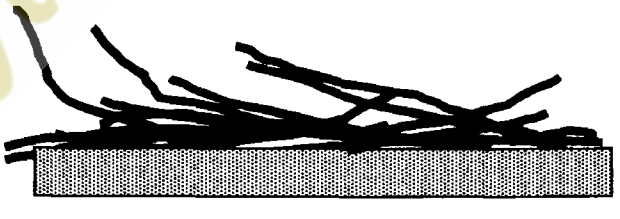

Figure 1.34. Immobilisation of DNA probe to gold electrode through adsorption.

Despite these disadvantages adsorption has been used for the immobilisation of DNA onto gold electrodes to study interactions with other molecules. Small amounts of ssDNA or dsDNA spotted on electrodes and air-dried overnight have been used to investigate the potential of a range of substances as electroactive indicators including benzyl viologen,

$Co(phen)_3^{3+}$, $Co(bpy)_3^{3+}$ and $Co(tppz)_2^{3+}$ (where tppz = tetra-2-pyridyl-1, 4-pyrazine) for differentiating ssDNA from dsDNA [162, 163].

Surface density of the probe is a key factor that determines the kinetics of target capture and the extent to which immobilised probes are able to capture solution-phase targets. At low probe densities, fast hybridisation of essentially 100% of the probes can occur, whereas at a high probe density, hybridisation efficiencies decrease and the kinetics are much slower. To ensure biological activity of the immobilised DNA, covalent coupling to the electrode surface through one of the ends of the DNA chain has proven to be the most suitable method of DNA attachment. Using this approach, the immobilised probe possesses greater accessibility to target analytes and changes in conformation of the probe occur at hybridisation [164]. Random covalent binding of DNA to electrode surfaces, involving chemical modification of the bases along the strand, rather than modification at one of the ends, has been reported to decrease the specificity and is not recommended [129]. With regard to achieving attachment at one end of the DNA probe, thiols as well as other sulphur-containing compounds, have attracted much attention since they are capable of forming self-assembled monolayers (SAMs) on gold [65,165,166], silver [167], platinum [168], iron [169], mercury [170] and other solid supports. Self-assembly involving the direct chemisorption of thiolated DNA probes on gold electrodes is one of the simplest approaches to obtaining a well-defined and organised surface and provides an excellent platform for biosensor applications [128, 171-173]. Monolayers are reported to be electrochemically stable over a wide potential range (−700 mV to +700 mV versus SCE) [134].

Methods for the immobilisation are relatively straightforward; however attention must be given to several critical aspects [152, 174]. Del Pozo [159] established the following procedure to achieve reproducible results: 10µl of a 300µM solution of mercaptohexyloligonucleotide was placed on a previously conditioned gold electrode positioned upside-down and then the end of the electrode was covered with a plastic cap to protect the solution from evaporation. After 1 hr at room temperature the electrode was soaked in sterile water for 30 min and then rinsed carefully with deionised water to remove any non-adsorbed oligomer. Electrodes prepared in this manner could be stored in sterile water in a refrigerator for at least 3 days.

Accessibility of immobilised probes to complementary target sequences can be enhanced by treating the surface with spacer molecules such as 6-mercapto-1-hexanol (MCH). The thiol group of MCH rapidly displaces the weaker, non-specifically adsorbed DNA nucleotides from the substrate, leaving the probes tethered primarily through the thiol end groups. After MCH treatment, the initially compact ssDNA extends further into solution improving the accessibility of the probes to the target; almost complete hybridisation efficiencies have been reported [154, 175]. Another reported advantage of MCH treatment is that it results in almost defect free monolayers with the result that only redox active molecules interacting with the immobilised DNA determine the electrochemical response rather than these redox molecules reaching the electrode surface directly (Figure 1.35). Formation of the MCH monolayer also leads to a reduction in the double layer charging, which improves the accuracy with which the probe coverage can be measured.

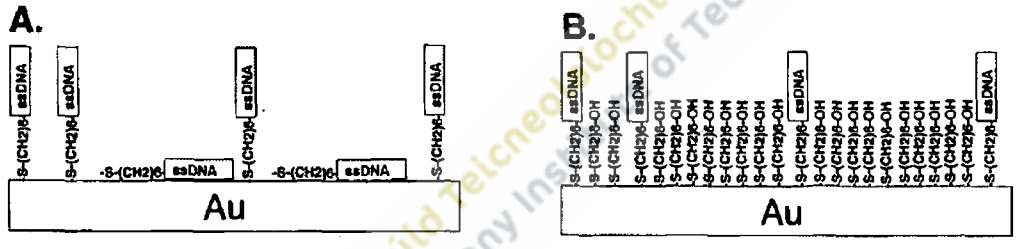

Figure 1.35. Thiolated ssDNA adsorbed on gold electrode before MCH treatment (A.) and after MCH treatment (B.) [150].

DNA immobilisation at gold surfaces investigated using cyclic voltammetry and chronocoulometry suggested that DNA monolayers immobilised at gold surfaces were not homogeneous and that nonspecific gold-DNA interactions existed to some degree even after MCH treatment. Non-specific gold-DNA interactions have been linked with decreased biosensor performance. Optimum performance can only be possible when all non-specific gold-DNA interactions have been eliminated [176].

In a study of the adsorption kinetics of thiolated DNA probes, between 8-48 nucleotides in length, on gold electrodes, adsorption curves were used to determine the maximum surface probe densities possible over durations ranging from 5 min to 20 hours. Probe coverage was determined from the number of cationic redox molecules electrostatically associated with the

anionic DNA backbone after MCH treatment. The concentration of the thiolated DNA probe in the deposition solution had limited effect on the surface coverage. For all probe lengths investigated, surface coverage increased rapidly in the first hour, attained 80% coverage after 2 hours and only minimal increases occurred after 20 hours. In theory the surface coverage attained by short or long thiolated DNA probes should be equal, however longer probes behave as coil-like polymers that adsorb non-specifically at random sites to the gold substrate, similar to the adsorption of non-thiolated DNA (Figure 1.36).

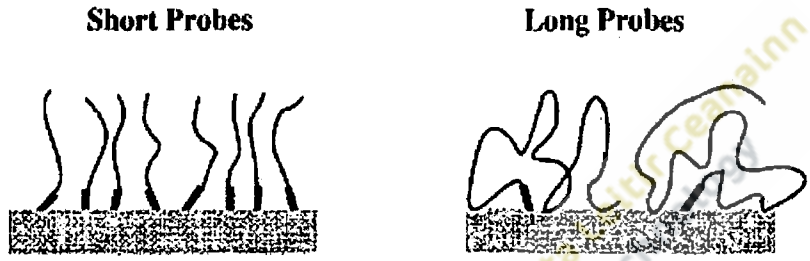

Figure 1.36. Representation of short and long thiolated ssDNA probes. Short probes pack in extended configurations; longer probes exist in more flexible configurations [154].

After treatment with MCH the amount of covalently attached DNA is much less for longer probes than short probes as non-specific DNA bound to the electrode surface is replaced by the stronger gold/sulphur bond of the MCH. Probes less than 16 bases in length attained the maximum surface coverage with very little non-specific gold/DNA interaction whereas between 16 - 48 bases the surface coverage decreased by more than an order of magnitude after MCH treatment. Treatment with MCH whilst essential to reduce non-specific DNA binding to the gold will also desorb some covalently attached DNA due to thiol-thiol exchange, aided by electrostatic repulsion of the adsorbed DNA molecules, however this process occurs at a much slower rate [154].

Almost complete passivation of the surface of a gold electrode by single-stranded thiolated DNA has been reported within 2–3 min of incubation whilst more rigid thiolated double-stranded DNA adsorbed at a slower rate. The reduced rate of adsorption was attributed to greater steric hindrance encountered by double-stranded structures and difficulties in packing

rigid duplexes rather than the more flexible single strands. Monolayers comprising tightly-packed single-stranded oligonucleotides were prevented from hybridisation to some degree. In contrast, monolayers with surface coverages that are too low may yield insufficient signal responses to allow detection. This has important implications for the development of biosensors and DNA-sensing arrays and emphasizes the importance of identifying a suitable packing density. Varying the deposition time, and prior heating of the probe surface, can be used to generate films of single-stranded oligonucleotides with moderate coverages [177, 178]. Other workers in this field have adopted an alternative approach to achieve a suitable surface coverage whereby dsDNA is immobilised and then denatured. The rational behind this approach is that the density of the remaining ssDNA probe should be near optimal for target capture [179].

Another factor which can influence probe immobilisation on a gold electrode is the application of a positive potential to attract the negatively charged DNA to the electrode surface. Probe immobilisation was reported to occur at a faster rate when a positive potential was applied, however, the final surface coverage exhibited little difference compared to electrodes without an applied potential (Figure 1.37) [177].

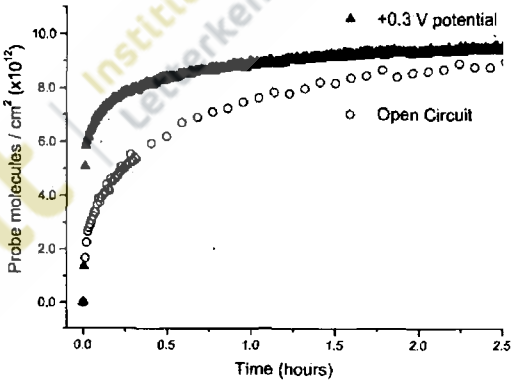

Figure 1.37. Immobilisation kinetics for ssDNA-C_6-SH solutions in 1 M NaCl in the presence and absence of an applied potential [177].

Difficulties encountered in the synthesis of mercapto-modified DNA resulting in poor yields of product for self-assembly on electrodes led to investigations of alternative methods for DNA immobilisation. Zhao and co-workers investigated the covalent immobilisation of dsDNA onto gold surfaces through a layer-by-layer assembly [180]. Self-assembled

monolayers of thiols were first formed on gold electrodes followed by a condensation reaction between the 3' hydroxy or the 5' phosphate end of the DNA to effect immobilisation onto the electrode surface. To optimise immobilisation onto the gold surface, the performance of three ethylene-containing thiols with hydroxyl, amino and carboxyl terminal groups were compared (Figure 1.38).

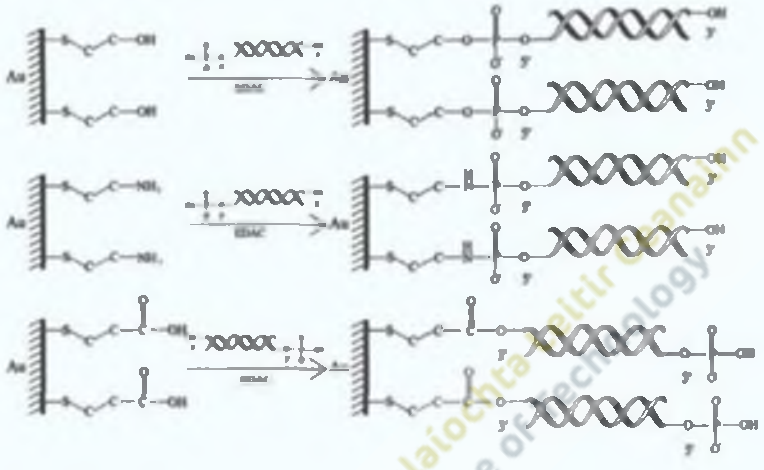

Figure 1.38. Representation of the covalent immobilisation of dsDNA on self-assembled monolayers with different terminal groups. Hydroxyl and amino groups react with the 5' phosphate end of DNA while the carboxyl group reacts with the 3' hydroxyl end [188].

DNA can interact with the modified electrode surface, either by adsorption and/or by covalent immobilisation. To be useful as biosensors as much as possible of the DNA should be covalently immobilised and as little as possible of the DNA adsorbed on the surface. Using $Co(bpy)_3$ as an electrochemical indicator, X-ray photoelectron spectrometry (XPS) and cyclic voltammetry (CV) were used to investigate the influence of the three different terminal groups on the covalent immobilisation of DNA. The hydroxyl terminated SAM was determined to be the best substrate for the covalent immobilisation of ds(DNA) on gold surfaces. Although with the carboxyl-terminated SAM a higher proportion of DNA was attached through covalent immobilisation, the total amount immobilised was very low compared to the hydroxyl-terminated SAM. This was attributed to possible disassociation of the carboxyl group and electrostatic repulsion of the negatively charged DNA molecules [188].

A combined approach using an applied potential and immobilisation of DNA to a self-assembled monolayer has more recently been used for the attachment of DNA to gold electrodes [181]. Using self-assembled monolayers (SAMs) of 2-aminoethanethiol (AET) on gold electrodes, the effect of an applied potential on DNA immobilisation was investigated using cyclic voltammetry and other methods (Figure 1.39).

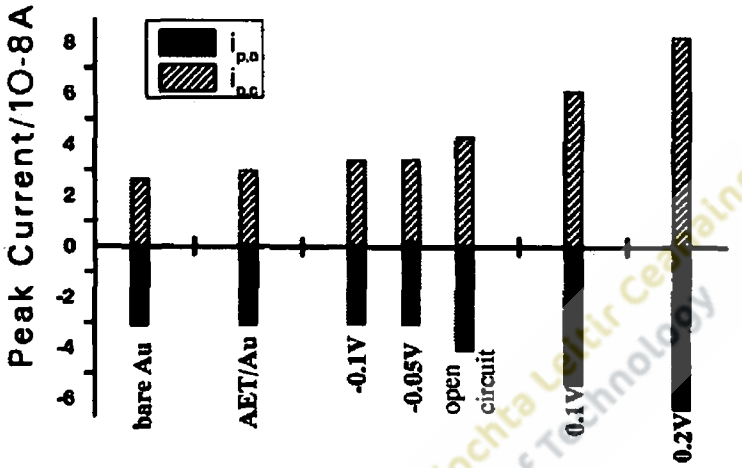

Figure 1.39. Comparison of peak currents for bare Au, AET/Au and DNA/AET/Au electrodes prepared at different control potentials [181].

Maximum peak currents observed after 1-hour deposition increased at more positive potentials compared to insignificant DNA immobilisation at -0.1V vs. SCE, thus demonstrating that control of the applied potential could be used to achieve more efficient immobilisation of DNA. Poor DNA immobilisation at negative potentials was attributed to the repulsion of the negatively charged DNA from the electrode surface [181].

Recently, modification of gold electrodes with gold nanoparticles has been reported to increase the surface area of the electrode and enhance the amount of DNA immobilised and its hybridisation efficiency [182-185]. Using electrodes modified in this way the detection limit for a 55bp target sequence, using a ssDNA probe electrode, was reduced to 10^{-11} mol L^{-1} compared to 10^{-6} mol L^{-1} for a planar gold electrode [184]. Recent work has demonstrated that in addition to improved detection limits the use of gold nanoparticles can enhance the stability of the Au-S bond, properties of significance in the construction of electrochemical sensors and biosensors [185]. Further improvements in stability without affecting the

hybridisation properties have been reported using novel trithiol-capped oligos and gold nanoparticle conjugates compared to monothiol and cyclic disulfide-capped oligos (Figure 1.40).

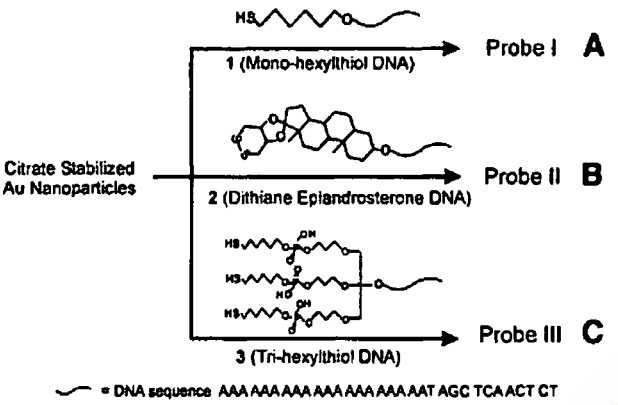

Figure 1.40. Structures of monothiol, cyclic disulphide and trithiol molecules used for oligonucleotide immobilisation [186].

Most research studies on the immobilisation of DNA have been undertaken with linear, thiolated, single-stranded oligonucleotide probes (HS-ssDNA) on gold surfaces. In recent times so-called molecular beacons or hairpin DNA has attracted much attention because of their potential application in DNA biosensors. For solution phase detection this hairpin-like, stem-loop structure contains a fluorescent label at one end and a quencher at the other. When the molecular beacon is in its folded stem-loop configuration, the fluorescent molecule and quencher moiety are held in close proximity and fluorescence is quenched. In the presence of complementary target DNA, the stem-loop structure is converted into a rigid linear DNA duplex, removing the fluorophore from the proximity of the quencher and inducing strong emission enhancement (Figure 1.41).

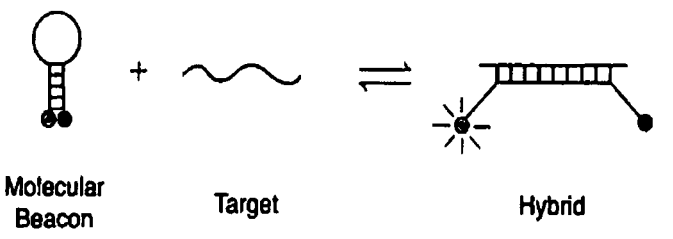

Figure 1.41. Operational principle of a molecular beacon [187].

Early attempts to immobilise molecular beacons in a solid-state version that could be potentially useful for chip-based optical detection were performed by Broude [188] and later Du *et al.* [158]. In their version a thiol molecule is attached to one end of the oligonucleotide sequence to allow attachment and a fluorophore to the other end. In the hairpin configuration, fluorescence is quenched by the close proximity of the fluorophore to the gold surface. After hybridisation the fluorophore is distanced from the electrode and a strong fluorescence is emitted (Figure 1.42).

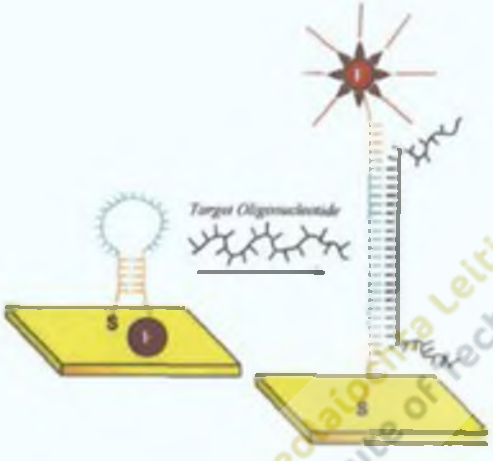

Figure 1.42. Principle of the immobilised DNA sensor using optical detection [194].

Development of electrochemical sensors based on the hairpin principle has progressed slowly compared with devices using optical detection but in recent years research results have been most encouraging [158, 188-190]. Fan *et al.* [190] used a 27-mer single-stranded probe immobilised on a gold electrode by a thiol group at the 3' end and labeled with ferrocene at its 5' end. The probe adopts a hairpin structure due to the presence of five complementary bases (stem) at each end of the 27-mer sequence. The ferrocene is located close to the electrode surface in this closed configuration and cyclic voltammetric redox peaks are observed in the absence of the complementary target DNA. Hybridisation between DNA and the immobilised complementary strand leads to a conformational change resulting in the formation of a rigid, rod-like duplex DNA structure causing the ferrocene label to move away from the electrode surface (Figure 1.43).

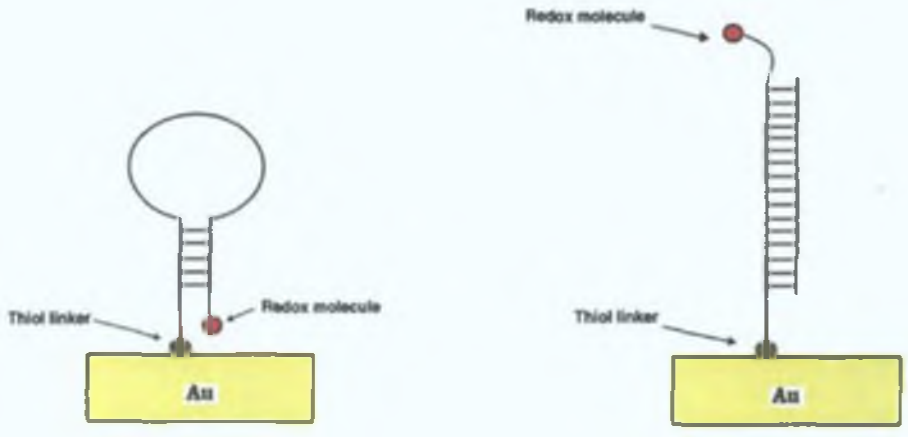

Figure 1.43. Principle of the immobilised DNA sensor using electrochemical detection.

Increasing the distance of the ferrocene label from the electrode surface results in a decrease or elimination of the ferrocene electrochemical signal, because the efficiency of electron tunneling decreases exponentially with increasing distance from the electrode. DNA biosensors of this type, where hybridisation results in a decrease or complete elimination of the signal, are often referred to as signal-off sensors. The sensor was reagentless, shown to be reusable, sensitive and simple to use and offered significant advantages over previously published electrochemical sensors. No significant changes in the sensor signal occur in the presence of 10 mM non-complementary probe, suggesting a high selectivity of the sensor. Detection limits for the sensor (10 pM) were comparable with other E-DNA sensors and substantially more sensitive than the 10 nM sensitivity for an optical sensor [157, 189]. Like other electrochemical DNA hybridisation systems, the approach used in this e-DNA sensor can be conveniently adapted for chip-based electrode arrays, giving a promising alternative to traditional fluorescence-based gene arrays.

Benight and co-workers [191] used the coupling efficiency of avidin-biotinylated probes to compare the coverage of linear and hairpin probes of different lengths. Hairpin oligonucleotides in this study were viewed as having similar properties to duplex DNA with regard to properties such as charge density and flexibility. Consistent with previous studies where greater ssDNA probe density was achieved compared to duplex DNA under the same solution conditions, linear probes attached at almost 50% higher density than hairpin probes [154, 178]. Shorter linear probes (16-mer) exhibited higher surface densities than longer linear

probes (32-mer) however, the probe length had little influence on the surface density with hairpins.

In addition to the ss/ds nature of the probe, other factors such as the solvents used, the duration of the deposition step and the ionic strength of the deposition solution can all influence the probe surface density. Surface plasmon resonance spectroscopy was used to demonstrate the significance of ionic strength of the deposition solution on the kinetics of immobilisation for ds and ssDNA, higher coverages being achieved in higher ionic strength solutions [177]. Similar results were reported by other researchers and attributed to the screening of the effects of electrostatic repulsion between the immobilised molecules in high ionic strength solutions [146].

Much research effort has been invested in the development of multiplex DNA sensors, so-called DNA chips. At the core of DNA chip technology are arrays of single-stranded DNA (ssDNA) chains or probes tethered to a substrate for the capture of complementary analyte DNA of targets [130]. For DNA chip technology to continue to emerge as an alternative to conventional diagnostic methods, questions about the conformation and activity of DNA at surfaces must be addressed [135, 192]. Many investigators have investigated the conformation of DNA oligonucleotides on gold by scanning tunneling microscopy. Single stranded DNA (ssDNA) appeared as "blobs," whereas double-stranded DNA (dsDNA) was rod-like [193]. Recent neutron reflectivity studies indicated that on bare gold, ssDNA oligonucleotides formed a compact layer - a picture consistent with the presence of multiple contacts between each strand and the substrate [153]. DNA nucleotides can adsorb to gold via multiple amine moieties thus interfering with hybridisation of the inaccessible immobilised strands.

As an alternative to the use of DNA sequences, synthetic peptide nucleic acid (PNA), an analogue of DNA has also been investigated for applications in biosensors. The structure of PNA differs from that of DNA since the entire sugar phosphate backbone is replaced by a neutral peptide backbone consisting of repeating N-(2-aminoethyl) glycine units linked together by amide bonds. The four nucleotide bases are attached via methylene carbonyl linkages to this peptide backbone at intervals such that the spacing between the bases is equal to that in DNA. Recently the use of PNA rather than DNA in biosensors has attracted attention because of a number of significant advantages. Firstly in contrast to DNA, PNA is not susceptible to degradation by nucleases or proteases and therefore has improved

biological stability. Secondly PNA/DNA duplexes formed at hybridisation are independent of the salt concentration in the hybridisation solution. Thirdly there is much less electrostatic repulsion between the neutral PNA and DNA than between two negatively charged DNA molecules, a fact that has great significance since it leads to a much improved hybridisation efficiency, critical for the development of sensitive commercial DNA biosensors. Finally the presence of mismatches in DNA/PNA duplexes are less stable than in the DNA/DNA duplex. For example a single base mismatch in a DNA/PNA duplex results in a lowering of the melting temperature by 15°C compared to an 11°C lowering of the melting temperature for the DNA/DNA duplex. This reduced stability in the presence of a mismatch makes PNA probes an extremely attractive option for the development of biosensors capable of detecting single nucleotide polymorphisms [194].

Like DNA sequences, PNA sequences can also be thiolated and immobilised to gold surfaces to create even more selective and specific DNA biosensors [195-199]. Studies have shown that using PNA probes rather than DNA probes resulted in a 4 x increase in hybridisation efficiency [200]. Despite the reported advantages of PNA probes over DNA probes, the major drawback limiting their application – their current high cost, particularly for PNA probes modified for immobilisation and electrochemical detection studies makes their widespread use somewhat prohibitive.

1.18. References

1. Penkumar, P., Beng-Koo, S. *Electrochemistry Comm.*, 2004, 6, 984-989.
2. Finklea, H.O., Liu, L., Ravenscroft, M.S., Punturi, S. *J. Phys.Chem.*, 1996, 100, 18852-18858.
3. Ulman, A. *Chem. Rev.*, 1996, 96, 1533-1554.
4. Forster, R.J. *Inorg. Chem.*, 1996, 35, 3394-3403.
5. Anderson, J.L., Coury, L.A., Leddy, J. *Anal. Chem.*, 1998, 70, 519-590.
6. Forster, R.J., Faulkner, L.R. *J. Am. Chem. Soc.*, 1994, 116, 5444-5452.
7. Gileadi, E. *Electrode Kinetics for Chemists, Chemical Engineers and Materials Scientists.* VCH: New York, 1993.
8. Bard, A.J., Faulkner, L.R. *Electrochemical Methods: Fundamentals and Applications.* Wiley: New York, 1980.
9. Forster, R.J. In: *Electrochemistry: Principles and Practice.* Smith, M.R. & Cunnane, V. (Eds.). Wiley: New York, 1997.
10. Nernst W., Riesenfeld. E.H. *Ann. Phys.*, 1902, 8, 600.
11. Frumkin, A.N. *Philos. Mag.*, 1920, 40, 363.
12. Von Helmholtz, H.L.F. *Ann. Physik.*, 1853, 89, 211.
13. Greef, R., Peat. R., Peter, L.M., Pletcher, D., Robinson, J. *Instrumental Methods in Electrochemistry.* New York: John Wiley & Sons, 1995.
14. Guoy, G. *J. Phys. Radium*, 1910, 9, 457.
15. Guoy, G. *Compt. Rend.*, 1910, 149, 654.
16. Chapman, D.L. *Phil. Mag.*, 1913, 25, 475.
17. Stern, O.Z. *Elektrochem.*, 1924, 30, 508.
18. Akram, M., Stuart, M.C., Wong, D.K.Y. *Anal. Chim. Acta*, 2004, 2, 243-251.
19. Kolthoff, I.M., Tomsicek, W.J. *J. Phys. Chem.*, 1935, 39, 945-954.
20. Randles, J.E.B. *Trans. Faraday Soc.* 1952, 48, 828-832
21. Nicholson, R.S., Shain, I. *Anal. Chem.*, 1964, 36, 706-723.
22. Randles, J.E.B. *Trans. Faraday Soc.*, 1948, 44, 327.
23. Sevcik, A. *Collect. Czech. Chem. Commun.*, 1948, 13, 349.
24. Stulik, K., Amatore, C., Holub, K., Marecek, V., Kutner, W. *Pure and Applied Chem.*, 2000, 72, 1483-1492.
25. Jenkins. A.T.A., Le-Meur, J.F. *Electrochemistry Comm.*, 2004, 6, 373-377.

26. Tirado, J.D., Abruña, H.D. *J. Phys. Chem.*, 1996, 100, 4556-4563.
27. Brown, A.P., Anson, F.C. *Anal. Chem.*, 1977, 49, 1589.
28. Finklea, H.O., Yoon, K., Chamberlain, E., Allen, J., Haddox, R. *J. Phys. Chem. B*, 2001, 105, 3088-3092.
29. Forster, R.J., O'Kelly, J.P. *J. Electroanal. Chem.*, 2001, 498, 127-135.
30. Laviron, E. *J. Electroanal. Chem.*, 1979, 101, 19-28.
31. Chen, S., Abruña, H.D. *J. Phys. Chem.* B, 1997, 167-174.
32. Forster, R.J. Ultrafast electrochemical techniques. *Chem. Soc. Review*, 1998.
33. Bard, A.J., Zoski, G.C. *Anal. Chem.* 2000, 346-352.
34. Gore, M.R., Szalai, V.A., Ropp, P.A., Yang, I.V., Silverman, J.S., Thorp, H.H. *Anal. Chem.*, 2003, 75, 6586-6592.
35. Elliott, J.M., Birkin, P.R., Bartlett, P.N., Attard, G.S. *Langmuir*, 1999, 15, 7411-7415.
36. Zheng, J., Li, X., Gu, R., Lu, T. *J. Phys. Chem. B.*, 2002, 106, 1019-1023.
37. Zen, J.M., Chung, H.H., Kumar, A.S. *Anal. Chem.*, 2002, 74, 1202-1206.
38. Luo, H., Shi, Z., Li, N., Gu, Z., Zhuang, Q. *Anal. Chem.*, 2001, 73, 915-920.
39. Bessel, C.A., Laubernds, K., Rodriguez, N.M., Baker, R.T.K. *J. Phys. Chem. B.*, 2001, 105, 1115-1118.
40. Bond, A.M. *Electrochemistry Newsletter*. 1991, 70.
41. Forster, R.J. *Chem. Soc. Rev.*, 1994, 23, 289.
42. Janata, J. *Principles of Chemical Sensors*. 1989, Plenum Press, New York.
43. Britz, D, J. *J. Electroanal. Chem.*, 1978, 88, 309-352.
44. Wipf, D.O., Wightman, R.M. *Anal. Chem.*, 1990, 62, 98-102.
45. Acevedo, D., Abruña, H.D. *J. Phys. Chem.*, 1991, 95, 9590-9594.
46. Forster, R.J., Faulkner, L.R. *J. Am. Chem. Soc.*, 1994, 116, 5444-5452.
47. Woods, R. Chemisorption at electrodes. In *Electroanalytical Chemistry*, (Ed) Bard, A.J. Marcel Decker, New York, 1976, 9, 1.
48. Katz, E., Schlereth, D.D., Schmidt, H.I. *J. Electroanal. Chem.*, 1994, 367, 59.
49. Krysinski, P., Brozostowska-Smolska, M., Mazur, M. *Material Science and Engineering*, 1999, 8, 551-557.
50. Cameron, G.C., Pickup, P.G. *J. Am. Chem. Soc.*, 1999, 121, 11773-11779.
51. Sagiv, J. *J. Am. Chem. Soc.*, 1980, 102, 92-98.
52. Deng, L.; Mrksich, M.; Whitesides, G. M. *J. Am. Chem. Soc.*, 1996; 118, 5136-5137

53. Di Giusto, D. A.; Wlassoff, W. A.; Giesebrecht, S.; Gooding, J. J.; King, G. C. *J. Am. Chem. Soc.*, 2004; 126; 4120-4121
54. Forster, R. J., Keyes, T. E. *J. Phys. Chem. B.*, 1998; 102, 10004-10012.
55. Terasaki, N., Akiyama, T., Yamada, S. *Langmuir*, 2002, 18, 8666-8671.
56. Bertoncello, P., Kefalas, E.T., Pikramenou, Z., Unwin, P.R., Forster, R.J. *J. Phys. Chem. B.*, 2006, 110, 10063-10069.
57. Brum, L.A., Arnold, J.J. *J. Phys. Chem.*, 1999, 103, 8122.
58. Acevedo, D., Abruña, H.D. *J. Phys. Chem.*, 1991, 95, 9590.
59. Campbell, J.L.E., Anson, F.C. *Langmuir*, 1996, 12, 4008.
60. Takehara, K., Takemura, H. *Bull. Chem. Soc. Jpn.*, 1995, 68, 1289.
61. Haddox, R.M., Finklea, H.O. *J. Phys. Chem. B.*, 2004, 108, 1694.
62. Schonenberger, J.C., Jorritsma, J., Sondag-Huethorst, J.A.M., Fokkink, L.C.J. *J. Phys. Chem.*, 1995, 99, 3259.
63. Bain, C.D., Troughton, E.B., Tao, Y.T., Evall, J., Whitesides, G.M., Nuzzo, R.G. *J. Am. Chem. Soc.*, 1989, 111, 321-335.
64. Poirier, G.E., Pylant, E.D. *Science*, 1996, 272, 1145.
65. Finklea, H.O. Self assembled monolayers on electrodes. In: *Electroanal. Chem.*, A.J. Bard, I Rubinstein (Eds.), Marcel Dekker, New York, Vol. 19, p.109.
66. Figgemieier, E., Merz, L., Hermann, B., Zimmermann, Y.C., Housecroft, C.E., Guntherodt, H.J., Constable, E.C. *J. Phys. Chem. B.*, 2003, 107, 1157.
67. Seong-Keuck, C. *Bull. Korean. Chem. Soc.*, 2004, 25, 786.
68. Forster, R.J., Loughman, P., Keyes, T.E. *J. Am. Chem. Soc.*, 2000, 122, 11948 - 11955.
69. Forster, R.J., Kelly, J.P. *J. Phys. Chem.*, 1996, 100, 3695-3704.
70. Ulman, A. *An introduction to ultrathin organic films from Langmuir-Blodgett to self-assembly*. Academic Press, San Diego, 1991.
71. Guo, L.H., Facci, J.S., McLendon, G., Mosher, R. *Langmuir*, 1996, 10, 4588.
72. Forster, R.J., Keyes, T.E., Majda, M. *J. Phys. Chem. B*, 2000, 104, 4425.
73. Amatore, C., Savaent, J.M., Tessier, D. *J. Electroanal. Chem.*, 1983, 147, 39.
74. Bolt, A.W. *Current Separations*, 1999, 18, 47-54.
75. Zayats, M., Katz, E., Willner, I. *J. Am. Chem. Soc*, 2002, 124, 2120-2121.
76. Bartlett, P.N., Tebbutt, P., Whitaker, R.C. *Prog. Reac. Kinetic*, 1991, 16, 55.
77. Davis, G. *Biosensors*, 1985, 1, 161-178.

78. Degani, Y., Hellar, A. *J. Phys. Chem.*, 1987, 91, 1285-1289.

79. Schuhmann, W., Hellar, A. *J. Am. Chem. Soc.*, 1991, 113, 1394-1397.

80. Ryabova, E.S., Goral, E., Csoregi, B., Mattiasson, A.D., Ryabov, A.D., *Angew. Chem. Int.* Ed. Engl., 1999, 38, 804-807.

81. McRipley, M.A., Linsenmeier, R.A. *J. Electroanal. Chem.*, 1996, 414, 235.

82. Mirksich, M., Whitesides, G.M. *Ann. Rev. Biophys. Biomol. Struct.*, 1996, 25, 55.

83. Staros, J.V., Wright, R.W., Swingle, D.M. *Anal. Biochem.*, 1986, 156, 220.

84. Gooding, J.J., Praig, V., Hall, E.A.H. *Anal. Chem.*, 1998, 70, 2396.

85. Gouy, G. *Anal. Chim. Phys.*, 1906, 8, 291.

86. Frumkin, A.N. *Z. Phys. Chem.*, 1925, 116, 466.

87. Frumkin, A.N. *Z. Phys. Chem.*, 1926, 35, 792.

88. Butler, J.A.V. *Proc. Roy. Soc. Sen. A*, 1929, 122, 399.

89. Trassati, S. *J. Electroanalytical Chem.*, 1974, 53, 335.

90. Yang, K.L., Yiacoumi, S., Tsouris, C. Electrical Double Layer Formation. In: *Encyclopedia of Nanoscience and Nanotechnology,* Marcel Dekker Inc., 2004.

91. Folkers, J.P., Laibinis, P.E., Whitesides, G.M. *J. Phys. Chem.*, 1994, 98, 563.

92. Forster, R.J., O'Kelly, J.P. *J. Electrochem. Soc.*, 2001, 148, 31-37.

93. Tirado, J. D., Abruña, H.D. *J. Phys. Chem.*, 1996, 100, 4556-4563.

94. Avecado, D., Bretz, R.L., Tirado, J.D., Abruña, H.D. *Langmuir*, 1994, 10, 1300-1305.

95. Bretz, R., Abruña, H.D. *J. Electroanal. Chem.*, 1996, 408, 199-211.

96. Freundlich, H. *Colloid and Capillary Chem.* E.P. Dutton & Co, NY., 1926.

97. Acevedo, D., Bretz, R.L., Tirado, J.D., Abruña, H.D. *Langmuir*, 1994, 10, 1300-1305.

98. Bretz, R., Abruña, H.D. *J. Electroanal. Chem.*, 1995, 388, 123-132.

99. Bretz, R., Abruña, H.D. *J. Electroanal. Chem.*, 1996, 408, 199-211.

100. Tirado, J.D., Acevedo, D., Bretz, R.L., Abruña, H.D. *Langmuir*, 1994, 10, 1971 - 1979.

101. Campbell, J.L.E., Anson, F.C. *Langmuir*, 1996, 12, 4008-4018.

102. Forster, R.J., Figgemeier, E., Lees, A.C., Hjelm, J. *Langmuir*, 200, 16, 7867.

103. Rowe, C.K., Creager, S.E. *Langmuir*, 1994, 10, 1186-1192.

104. Collard, D.M., Fox, M.A. *Langmuir*, 1991, 7, 1192-1197.

105. Folkers, J.P., Labinis, P.E., Whitesides, G.M. *J. Phys. Chem.*, 1994, 98, 563.

106. Finklea, H.O., Hanshew, D.D. *J. Electroanal. Chem.*, 1993, 347, 327-340.

107. Gardner, T.J., Frisbie, D.C., Wrighton, M.S. *J. Am. Chem. Soc.*, 1995, 117, 6927-6933.

108. Ulman, A. *Acc. Chem. Res.*, 2001, 34, 855-863.

109. Gyeong, S.B., Cheol, J. *Bull. Korean. Chem. Soc.*, 2001, 22, 281.

110. Shimazu, K., Yagi, I., Sato, Y., Uosaki, K. *Langmuir*, 1992, 8, 1385-1387.

111. Raive, G.K., Creager, S.E. *Langmuir*, 1991, 7, 2307

112. Kun, D.H., Jaegeun, N., Masahiko, H., Haiwon, L. *Bull. Korean. Chem. Soc.*, 2001, 22, 276-280.

113. Gosavi, S., Marcus, R.A. *J. Phys. Chem. B.*, 2000, 104, 2067-2072.

114. Forster, R.J., O'Kelly, J.P. *J. Phys. Chem.*, 1996, 100, 3695-3704.

115. Forster, R.J., Faulkner, L.R. *J. Am. Chem., Soc.*, 1994, 116, 5444-5451.

116. Forster, R.J., Keyes, T.E. *J. Phys. Chem. B*, 2001,105, 8829-8837.

117. Walsh, D.A., Keyes, T.E.; Hogan, C.F., Forster, R.J. *J. Phys. Chem. B*, 2001, 105, 2792-2799.

118. O'Finklea, H., Hanshew, D.D. *J. Am. Chem. Soc.*, 1992, 114, 3173-3181.

119. Diamond, D. *Principles of Chemical and Biological Sensors*. John Wiley and Sons, New York. 1998.

120. Hames, B.D., Higgins, S.J. 1985. *Nucleic Acid Hybridization- A Practical Approach*. Oxford University Press, Oxford. pp.78.

121. Campbell, N.A. *Biology*. The Benjamin/Cummings Publishing Company Inc., 1996.

122. Drummond, G.T, Hill, M.G., Barton, J.K. *Nature Biotechnology*, 2003, 21, 1192-1199.

123. Taylor, R.F., Schultz, J.S. *Handbook of Chemical and Biological Sensors*. Institute of Physics Publishing, Bristol, UK, 1996.

124. Lucarelli. F. *Biosensors and Bioelectronics*, 2004, 19, 515-530.

125. Mikkelsen, S.R. *Electroanalysis*, 1996, 8, 15-19.

126. Zhai, J., Hong, C., Yang, R. *Biotechnol. Adv.*, 1997, 15, 43-58.

127. Paleček, E., Fojta, M., Tomschick, M., Wang, J. *Biosensors and Bioelectronics*, 1998, 13, 621-628.

128. Paleček, E., Fojta, M. *Anal. Chem.*, 2001, 1, 7.

129. Paleček, E. *Talanta*, 2002, 56, 809.

130. Wang, J. *Anal. Chim. Acta*, 2002, 469, 63.

131. Christopoulos, T.K. *Anal. Chem.*, 1999, 71, 425-438.

132. Umek, R.M., Lin, SW., Vielmetter, J., Terbrueggen, R.H., Irvine, B., Yu, C.J., Kayyem, J.F., Yowanto, H., Blackburn, G.F., Farkas, D.H., Chen, Y.P. *J. Mol. Diagn.*, 2001, 3, 74-84.

133. Hashimoto, K., Ito, K., Ishimori, Y. *Sensors and Actuators B: Chemical*, 1998, 46, 220-225.

134. Ozkan, D. *Electrochemistry Comm.*, 2002, 4, 796-802.

135. Kelley, S.O., Barton, J.K. *Bioconjugate Chem.*, 1997, 8, 31-37.

136. Junhui, Z., Hong, C., Ruifu, Y. *Biotechnology Adv.*, 1997, 15, 43-58.

137. Wang, J. *Analyst*, 2005, 130, 421–426.

138. O'Donnell, M.J., Tang, K., Koster, H., Smith, C.L., Cantor, C.R. *Anal. Chem.*, 1997, 69, 2438-43.

139. Kimura-Suda, H., Petrovykh, D.Y., Tarlov, M.J., Whitman, L.J. *J. Am. Chem. Soc.*, 2003, 125, 9014.

140. Thiel, A.J., Frutos, A.G., Jordan, C.E., Corn, R.M., Smith, L.M. *Anal. Chem.*, 1997, 69, 4948-56.

141. Huang, E., Satjapipat, M., Han, S., Zhou, F. *Langmuir*, 2001, 17, 1215-1224.

142. Georagiadis, R., Peterlinz, K.P., Peterson, A.W. *J. Am. Chem. Soc.*, 2000, 122, 3166.

143. Olofsson, L., Rindzevicius, T., Pfeiffer, I., Kall, M., Hook, F. *Langmuir*, 2003, 19, 10414-9.

144. Boon, E.M., Ceres, D.M., Drummond, T.G., Hill, M.G., Barton, J.K. *Nature Biotechnology*, 2000, 18, 1096-100.

145. Wang, J., Xu, D., Polsky, R. *J. Am. Chem. Soc.*, 2002, 124, 4208-4209.

146. Herne, T.M., Tarlov, M.J. *J. Am. Chem. Soc.*, 1997, 119, 8916.

147. Wang, J., Cai, X., Jonsson, C., Balakrishnan, M. *Electroanalysis*, 1996. 8, 20-24.

148. Wang, J., Kawde, A.N., Erdem, A., Salazar, M. *Analyst*, 2001. 126, 2020-2024.

149. Marrazza, G., Chiti, G., Mascini, M., Anichcini, M. *Clin. Chem*, 2000, 46, 31-37.

150. Pividori, M.I., Merkoçi, A., Alegret, S. *Biosensors and Bioelectronics*, 2000, 15, 291-303.

151. Paleček, E., Fojta, M., Jelenm, F. *Bioelectrochemistry*, 2002. 56, 85-90.

152. Steel, A.B. Herne, T.M., Tarlov, M.J. *Anal. Chem.*, 1998, 70, 4670.

153. Levicky, R., Herne, T.M., Tarlov, M.J., Satija, S.K. *J. Am. Chem. Soc.*, 1998, 120, 9787.

154. Steel, A.B., Levicky, R.L., Herne, T.M., Tarlov, M.J. *Biophys. J.*, 2000, 79, 975.

155. Peterson, A.W., Heaton, R.J., Georgiadis, R. *J. Am. Chem. Soc.*, 2000, 122, 7837.

156. Maruyama, K., Yuji, M., Keiji, M., Junko, M. *J. Electroanal. Chem.*, 2001, 510: 96-102.

157. Peterson, A.W., Wolf, L.K., Georgiadis, R.M. *J. Am. Chem. Soc.*, 2002, 124, 14601.

158. Du, H., Disney, M.D., Miller, B.L., Krauss, T.D. *J. Am. Chem. Soc.*, 2003, 125, 4012-4013.

159. Del Pozo, M.V., Alonso, C., Pariente F., Lorenzo E. *Biosensors and Bioelectronics*, 2005, 20, 1549-1558.

160. Dharuman, V., Grunwald, T., Nebling, E., Albers, J., Blohm, L., Hintsche, R., *Biosensors and Bioelectronics*, 2005, 21, 645-654.

161. Pang, D.W., Zhang, M., Wang, Z L., Qi, Y.P., Cheng, J.K., Liu, Z.Y. *J. Electroanal. Chem.*, 1996, 403, 183.

162. Pang, D.W., Abruña, H.D. *Anal. Chem.*, 1998, 70, 3162-3169.

163. Pang, D.W., Abruña, H.D. *Anal. Chem.*, 2000, 72, 4700-4706.

164. Kieffer, J., Yang, E. *J. Theoretical Biology*, 1997, 188, 369-377.

165. Bain, C.D., Troughton, E.B., Tao, Y.T., Evall, Y., Whitesides, G.M., Nuzzo, R.G. *J. Am. Chem. Soc.*, 1989, 111, 321-335.

166. Nuzzo, RG., Dubios, L.H., Allara, D.L. *J. Am. Chem. Soc.*, 1990, 112, 558-569.

167. Bryant, M.A., Pemberton, J.E. *J. Am. Chem. Soc.*, 1991, 113, 3629-3637.

168. Mebrahatu, T., Berry, G.M., Bravo, B.G., Michelhaugh, S.L., Soriaga, M.P. *Langmuir*, 1988, 4, 1147-1151.

169. Cheng, L., Bocarsly, A.B., Bernasek, S.L., Ramanarayanan, T.A. *Langmuir*, 1994, 10, 4542-4550.

170. Rampi, M.A., Schueller, O.J., Whitesides, G.M. *Appl. Phys. Lett.*, 1998, 72 1781-1783.

171. Schonenberger, C., Jorritsma, J., Sondag-Huethorst, J.A.M., Fokkink, L.G.J. *J. Phys. Chem.*, 1995, 99, 3259-3271.

172. Kajikawa, K. *Molecular electronics and bioelectronics*, 1996, 7, 2.

173. Wang, J. *Nucleic Acid Res.*, 2000, 28, 3011.

174. Hashimoto, K., Ito, K., Ishimory, I. *Anal. Chim. Acta*, 1994, 286, 219-224.

175. Tarlov, M.J., Steel, A.B. DNA-based sensors. In: *Biomolecular Films. Design, Function and Application* (Rusling, J.F., ed.), pp. 545-608, M. Dekker, NY, 2003..

176. Lao, R., Song, S., Wu, H., Wang, L., Zhang, Z., He, L., Fan, C. *Anal. Chem.*, 2005, 77, 6475-6480.

177. Peterson, A.W., Heaton, R.J., Georgiadis, R.M. *Nucleic Acid Res.*, 2001, 29, 5163-5168.

178. Taft, B.J., O'Keefe, M., Fourkas, J.T., O. Kelley, S. *Anal. Chim. Acta*, 2003, 496, 81-91.

179. Kelley, S.O., Barton, J.K., Jackson, N.M., McPherson, L.D., Potter, A.B., Spain, E.M., Allen, M.J., Hill, M.G. *Langmuir*, 1998, 14, 6781.

180. Zhao, Y.D., Pang, D.W., Hu, S., Wang, Z.L., Cheng, J.K., Dai, H.P. *Talanta*, 1999, 49, 751-756.

181. Ge, C., Liao, J., Yu, W., Gu, N. *Biosensors and Bioelectronics*, 2003, 18, 53-58.

182. Lin, L., Zhao, H.Q., Li, J.R., Tang, J.A., Duan, M.X., Jiang, L. *Biochem. Biophys. Res. Commun.*, 2000, 274, 817.

183. Liu, S.T., Maoz, R., Schmid, G., Sagiv, J. *Nano. Lett.*, 2002, 2, 1055.

184. Liu, S.F., Li, Y.F., Li, J.R., Jiang, L. *Biosensors and Bioelectronics*, 2005, 21 789-795.

185. Liu, S.F., Li, X.H., Li, Y.C., Li, J.R., Li, Y.F., Jian, L. *Electrochim. Acta*, 2005, 51, 427-431.

186. Li, Z., Jin, R., Mirkin C.A., Letsinger R.L. *Nucleic Acids Res.*, 2002, 30, 1558-1562.

187. Tyagi, S., Bratu, D.P., Kramer, F.R. *Nature Biotechnology*, 1998, 16, 49-53.

188. Broude, N.E. *Trends in Biotechnology*, 2002, 20, 249-256.

189. Du, H., Strohsahl, C.M., Miller, B.L., Krauss, T.D. *J. Am. Chem. Soc.*, 2005, 127, 7932-7940.

190. Fan, C., Plaxco, K.W., Heeger, A.J. *Proc. Natl. Acad. Sci.*, 2003, 100, 9134-9137.

191. Riccelli, P.V., Merante, F., Leung, K.T., Bortolin, S., Zastawny, R.L., Janeczko, R. Benight, A.S. *Nucleic Acids Res.*, 2001, 29, 996-1004.

192. Chan, V., Graves, D.J., Fortina, P., McKenzie, S.E. *Langmuir*, 1997, 13, 320-329.

193. Rekesh, D., Lyubchenko, Y., Shlyakhtenko, L S., Lindsay, S.M. *Biophys. J.* 1996, 71, 1079-1086.

194. Wang, J. *Biosensors and Bioelectronics*, 1998, 13, 757-762.

195. Ozkan, D. *Electrochemistry Comm.*, 2002, 4, 796-802.

196. Wang, J., Nielsen, P.E., Jiang, M., Cai, X., Fernandes, J.R., Grant, D.H., Ozsoz, M., Beglieter, A., Mowat, M. *Anal. Chem.*, 1997, 69, 5200-5202.

197. Wang, J., Palecek, E., Nielsen, P.E., Rivas, G., Cai, X., Shiraishi, H., Dontha, N., Luo, D.B., Farias, P.A.M. *J. Am. Chem. Soc.*, 1997, 118, 7667.

198. Fojta, M.V., Vetterl, M., Tomschik, F. *Biophysical Journal*, 72, 1997, 2285-2293.

199. Lioubashevski, O., Patolsky, F., Willner, I. *Langmuir*, 2001, 17, 5134-5136.

200. Zhang, X., Ishihara, T., Corey, D.R. *Nucleic Acids Res.*, 2000, 28, 3332-3338.

2. Microelectrode fabrication and appraisal & the synthesis and characterisation of ruthenium and osmium complexes

This chapter comprises two main sections covering the principal materials used in this research programme. The first section provides an introduction to the topic of microelectrodes and the techniques used in their fabrication and appraisal. The second section provides an introduction to ruthenium and osmium complexes and details the synthesis and characterisation of a range of ruthenium and osmium complexes and a bridging ligand used in this research work.

2.1. Microelectrode fabrication and appraisal

In recent years increased interest has developed in microelectrodes [1-7]. Platinum electrodes of nanometre dimensions have been fabricated by electrophoretic coating of etched platinum wires with polyacrylic acid. Electrochemical areas for these electrodes have been determined by measuring the charge associated with the oxidation of adsorbed bis(2,2'-bipyridine)chloro(4,4'-trimethylenepyridine) osmium (II). Peaks due to the oxidation of as few as 7000 molecules have become detectable [8]. Use of these extremely small electrodes has been coupled with ultrafast cyclic voltammetry where scan rates in the megavolt per second range have been reported [9]. Significant benefit in using microelectrodes arises since measurements in solvents with low relative permittivity values or samples without added electrolyte are possible [10]. These factors have led to a renewed interest in electrochemical methods of analysis. During an electrochemical measurement the diffusion layer will grow further and further into the bulk solution as a function of time. Fast scan rates result in a decrease in the diffusion layer thickness as given in equation 1:

$$\delta = \left[\frac{\pi D t}{F v}\right]^{1/2} \qquad (1)$$

where δ is the diffusion layer thickness, D the diffusion coefficient, t the time, F the Faraday constant and v is the scan rate.

The time scale of an experiment (θ) is determined by the time required for a molecule to move from the electrode surface to the outer edge of the diffusion layer and is given by equation 2:

$$\theta = \frac{RT}{Fv} \tag{2}$$

where θ is the experiment time scale, R the real time constant and T the temperature.

Since the time required for a molecule to travel to the outer edge of the diffusion layer can be accurately controlled by extremely fast scan rates, voltammetry can be performed in the nanosecond time domain. As explained in Chapter 1, the limitations of this technique are imposed by the fact that the time scale of the experiment must be longer than the cell time constant and by the fact that extremely fast voltammetry causes large distortions due to ohmic drop. Both of these problems can be overcome by reducing the size of the electrode, hence the increased interest in the use of microelectrodes, and in some cases ultra-microelectrodes, in electrochemistry.

This section addresses the fabrication of both platinum and gold microelectrodes and macroelectrodes. These were constructed by sealing gold or platinum wires in soft soda glass tubing. The glass was collapsed around the wire by heating and this was followed by a stepwise polishing procedure, where the exposed disc was polished to a mirror finish. Even when great care is taken in the polishing procedure, recent studies have shown that microelectrodes sealed in glass cannot be considered as purely polycrystalline and as a consequence the surface structure of electrodes may vary. This can affect the results obtained, particularly when determining kinetic constants of electrochemical reactions which are significantly influenced by surface structure [11].

Microelectrodes with dimensions as small as 10 nm have been reported in the literature allowing the measurement of fast electron transfer rates, not possible with larger electrodes [12, 13]. The main problem in the fabrication of extremely small microelectrodes is that of reproducibility. Cardwell *et al.* established procedures for the reproducible polishing of microelectrodes and compared both manual and mechanical methods [14].

2.1.1. Microelectrode fabrication

One end of a piece of soft glass tubing (9 cm length x 4 mm ext. dia. and 2 mm int. dia.) was rotated over a butane flame until the glass tubing collapsed leaving a small aperture of approx 0.5 mm. The tubing was then cleaned in dilute nitric acid, rinsed in ultra pure water, soaked in acetone, rinsed in ultra pure water and then air-dried.

Aluminium wire (6 cm x 0.25 mm dia.) was soldered to a tin annealed copper wire (2 cm x 1 mm dia.). Platinum microwire (50 mm x 12.5 μm rad.) (Goodfellows Metals) was wrapped around the other end of the aluminium wire and soldered. The wires were then cleaned using the same procedure as that for the glass tubing.

After drying, the wire was threaded through the glass tubing until approx. 1 cm of platinum microwire had emerged at the aperture. The collapsed end of the glass tubing was again rotated over a butane flame until the glass completely collapsed around the microwire. The aluminium hook-up wire was zigzagged inside the glass tubing to give extra physical support to the assembly. A small hole was pierced in a plastic cap, pushed down over the copper wire and glued to the glass tubing using Araldite (Figure 2.1).

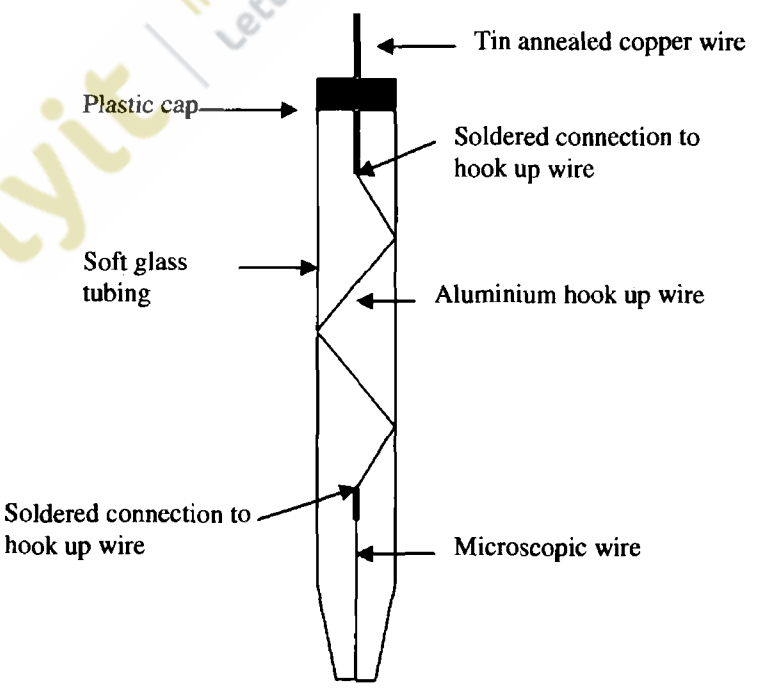

Figure 2.1. Diagrammatic structure of a fabricated microelectrode.

The tapered end of the microelectrode was sanded using emery paper until the microwire disc was exposed and the tip of the glass was flat. Cyclic voltammetry in blank electrolyte was performed to establish if there was electrical connection through the microwire.

A similar procedure was used for the fabrication of gold microelectrodes with several exceptions. Firstly, the glass tubing was placed in a clamp stand and after threading the connected and cleaned wires into the glass tubing, the non-collapsed end was connected to a vacuum pump. Secondly heating at the other end was performed with a microtorch rotated slowly around the tip of the glass to ensure an even distribution of the heat and avoid bending of the glass tube.

Figure 2.2. Photograph of an early version of a homemade microelectrode and Ag /AgCl reference electrode.

2.1.2. Characterisation of microelectrodes

Following fabrication both microelectrodes and macroelectrodes were manually polished using alumina polishes (Buehler, Chicago Illinois) on nap polishing pads (Struers). Procedures used for polishing of both gold and platinum electrodes were identical and were performed to ensure a smooth electrode surface of low resistance.

The microdisc at the tip of the electrode was exposed by removing excess glass using 600 grit emery paper and polished using a series of fine grades of alumina from 12.5, 5, 1, 0.3, 0.05 μm diameter. Polishing was performed by holding the microelectrode perpendicular to the polishing pad containing the alumina and rubbing lightly in a figure of eight hand movement. Plastic gloves were worn while polishing to prevent contamination of the electrode. Between each change in the particle size of alumina, polishing material from the previous grade adhering to the electrode was removed by sonication in ultra pure water for 5 mins.

After the final polishing step, cyclic voltammograms were recorded in 0.1M H_2SO_4 to confirm that the baseline was flat, indicative of low resistance. Where sloped backgrounds were recorded, polishing was repeated. If after repeating the polishing, sloped backgrounds were still recorded, further sanding with emery paper was performed and the polishing sequence repeated from the beginning. If the baseline was flat, the electrochemical area of the electrode was determined by cyclic voltammetry. Determination of the real surface area for gold electrodes is based on the electrochemically-induced deposition of an oxygen monolayer on the electrode surface. The charge associated with desorption of this monolayer, which results in a single cathodic peak at approximately 0.8V, is used to calculate the electrochemical area and surface roughness of the electrode [15]. For platinum electrodes the oxide reduction peak at approximately 0.4V was used for the determination of the real surface area. The electrochemical area of the electrode is determined by dividing the area under the reduction peak by a correction factor of 420 μC cm^{-2} for platinum [16, 17] and 390 μC cm^{-2} for gold [18].

2.1.3. Platinum electrodes

The electrochemical area of platinum electrodes can be determined by two different methods. In the hydrogen adsorption method, the charge under the voltammetric peak for hydrogen adsorption or hydrogen desorption is used to calculate the electrochemical area [19]. Alternatively the electrochemical area can, as in this study, be determined from the adsorbed oxygen / platinum oxide peak observed at approximately 0.4V.

Cyclic voltammograms produced during the final three steps of the polishing procedure are shown in Figure 2.3. The success of the stepwise polishing procedure was demonstrated by the progressive reductions in the area of the cathodic peak at approximately 0.45V and the decrease in capacitative currents as the particle size of the alumina polish decreased. The baseline produced as a result of the polishing procedure was flat indicative of low resistance.

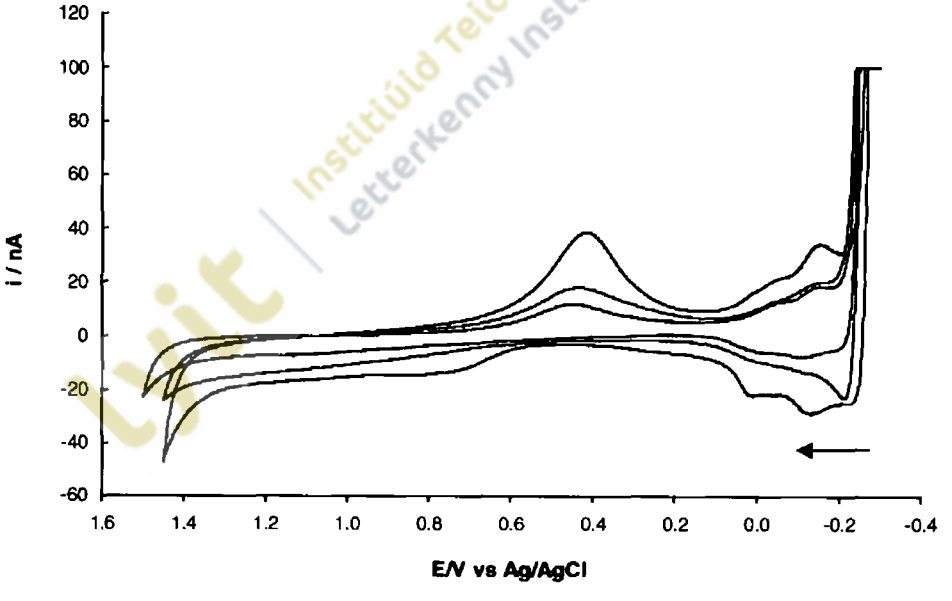

Figure 2.3. Cyclic voltammograms of a Pt microelectrode (12.5 μm rad.) immersed in 0.1M H_2SO_4. The oxide reduction peak occurs at approx 0.45V. Voltammograms from top to bottom were recorded after polishing with 1, 0.3 and 0.05 μm particle size alumina. The scan rate used was 0.5 V s^{-1} and the scan direction is shown by the black arrow. Potential limits -0.25V to 1.5V.

A cyclic voltammogram of a 12.5 μm rad. platinum microelectrode after completion of the polishing procedure has been provided in Figure 2.4.

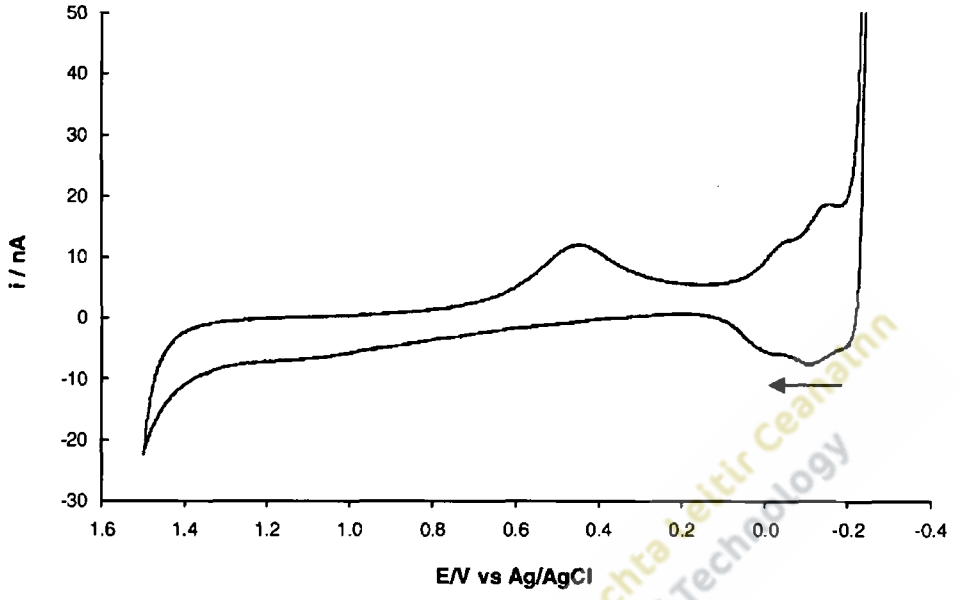

Figure 2.4. Cyclic voltammogram of a Pt microelectrode (12.5 μm rad.) immersed in 0.1M H_2SO_4 after the final polishing. Scan rate used 0.5 V s^{-1} and the scan direction is shown by the black arrow. Potential limits from -0.25V to 1.5V. The electrochemical area of the electrode was determined from this voltammogram.

The area under the reduction peak of 3.4 x 10^{-9} C in conjunction with the correction factor for platinum was used to determine the electrochemical area of 8.0 x 10^{-6} cm^2. The geometric area of this electrode was 4.9 x 10^{-6} cm^2. The surface roughness factor of 1.65 for this electrode was calculated by dividing the electrochemical area by the geometric area. For the platinum microelectrodes fabricated in this study, surface roughness factors ranged from 1.4 to 2.2.

2.1.4. Gold electrodes

Cyclic voltammograms of clean gold electrodes do not produce hydrogen adsorption peaks and the electrochemical area of these electrodes is calculated from the oxide layer chemisorbed to the electrode surface. In the anodic sweep, oxygen is chemisorbed in what is assumed to be a mono-atomic layer on the gold surface with a one to one relationship with each metal atom. Desorption of this oxide layer results in a single cathodic peak [15]. The area of this peak is used, in conjunction with the correction factor for gold, to calculate the electrochemical area.

Electrodes using gold wires of 12.5 μm, 0.125 mm and 1 mm radius were constructed. These wires were soldered to an aluminium hook up wire as described previously, although great difficulty was encountered in soldering the gold microwire (12.5 μm rad.) to the aluminium hook-up wire, with often many attempts being required before connection was successful. Another difficulty encountered in the construction of gold electrodes arose from the fact that the glass did not always make a perfect seal when collapsing around the gold wire during heating in the butane flame. In some instances leakage to the inside of the electrode occurred during overnight soaking in blank electrolyte. When viewed under the microscope tiny air bubbles were visible in the glass in some instances adjacent to the microscopic wire (Figure 2.5).

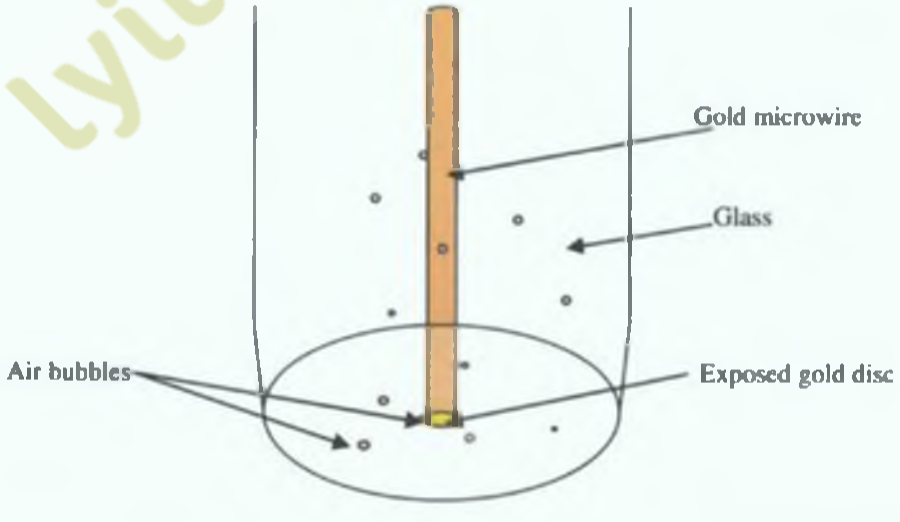

Figure 2.5. Diagrammatic representation of the electrode tip showing air bubbles.

A cyclic voltammogram for a gold microelectrode in acidic solution is shown in Figure 2.6. The sloping background currents and poorly defined peaks recorded probably arose as the result of microscopic gaps between the gold wire and the glass causing leakage of electrolyte into the electrode, or may have been due to air bubbles located adjacent to the gold wire. To some extent these difficulties were alleviated by application of a vacuum to the other end of the glass tubing during the heat-sealing step, which resulted in improved success in the fabrication of well-sealed, gold microelectrodes. Comparison of the success rate of fabrication, despite this improvement in the procedure for sealing, revealed that only about 25 % of gold microelectrodes were successfully constructed compared to 95 % for platinum microelectrodes.

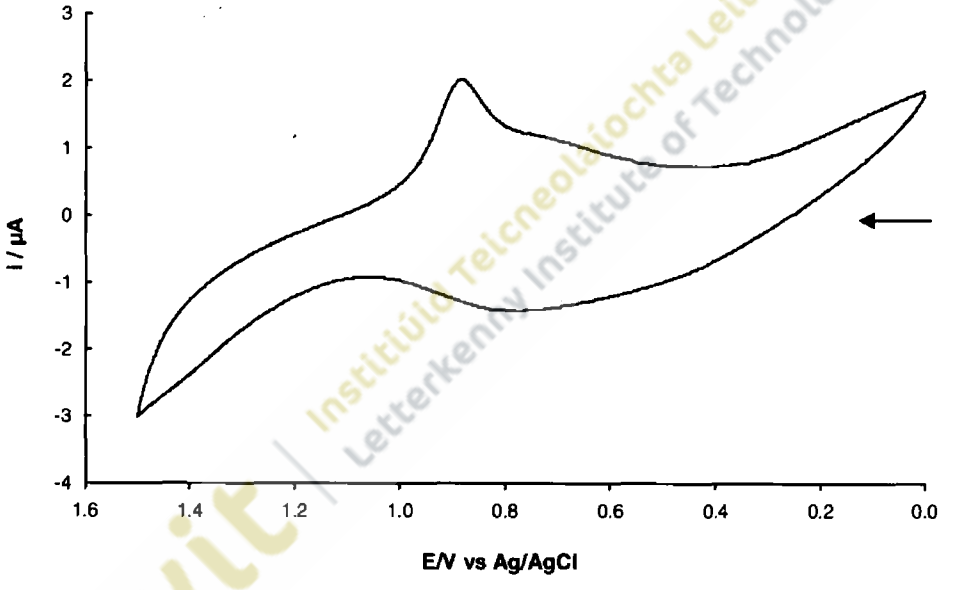

Figure 2.6. A cyclic voltammogram for a leaking gold electrode (0.125 mm rad.) immersed in 0.1M H_2SO_4. The scan rate used was 0.1 V s^{-1} and the scan direction is shown by the black arrow. Potential limits from 0.0V to 1.5V.

Cyclic voltammograms for 12.5 µm radius and 1 mm radius gold microelectrodes used for determination of the electrochemical area and surface roughness after completion of the polishing procedure have been provided in Figures 2.7 and 2.8 respectively.

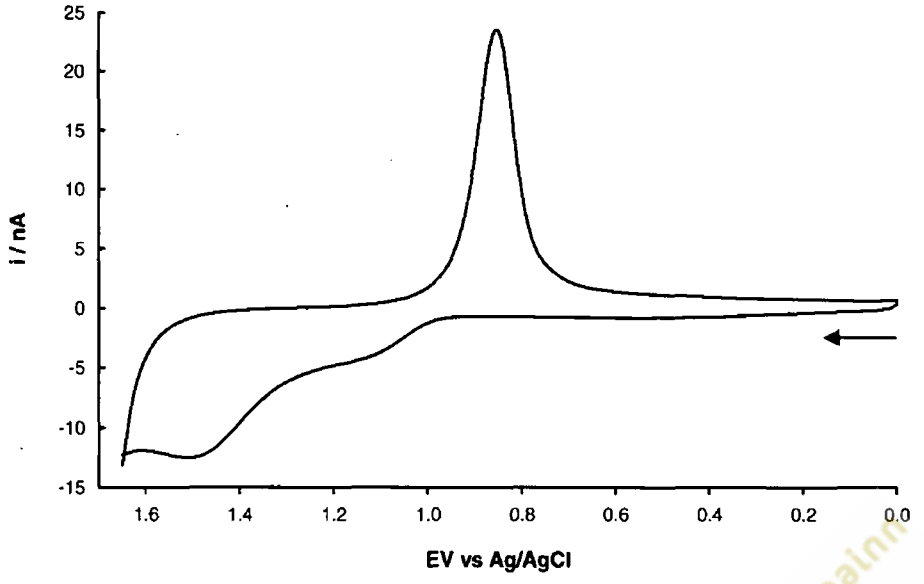

Figure 2.7. A cyclic voltammogram for a gold microelectrode (12.5 μm rad.) immersed in 0.1 M H_2SO_4. The scan rate used was 0.5 V s^{-1} and the scan direction is shown by the black arrow. Potential limits 0.0V to 1.65V. Using the cathodic peak the electrode area was calculated as 8.2 x 10^{-6} cm^2 and the surface roughness factor as 1.76.

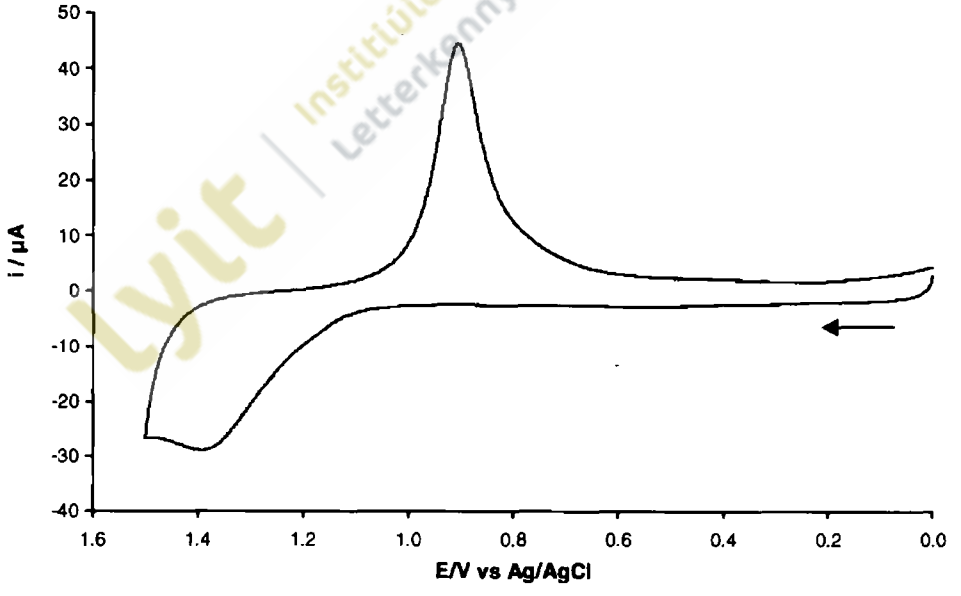

Figure 2.8. A cyclic voltammogram for a gold electrode (1 mm rad.) immersed in 0.5M H_2SO_4. The scan rate used was 0.1 V s^{-1} and the scan direction is shown by the black arrow. Potential limits 0.0V to 1.5V. Using the cathodic peak the electrode area was calculated as 3.5 x 10^{-5} cm^2 and the surface roughness factor as 2.45.

2.1.5. Discussion

The success rate for the fabrication of platinum microelectrodes was excellent with electrical contact being established in most fabricated electrodes. Electrochemical measurements in blank electrolyte using these electrodes produced flat voltammograms of low resistance typical of a perfect seal between the glass and the platinum wire. The high success rate of achieving a perfect seal was attributed to the fact that platinum has a coefficient of thermal expansion close to that of soda lime silica glass.

In contrast, difficulties were often encountered in fabricating gold microelectrodes. Two main problems were identified. Firstly, on many occasions no electrical contact was found to pass through the newly constructed electrode. This was attributed to a poor electrical connection between the microwire and the aluminium hook-up wire. The solder used to establish this connection comprised 85 % tin and 15 % lead. Solder of this composition separates on heating into a lead-rich phase and a tin-rich phase. As a result additional inter-metallic compounds can form as gold melts into the solder. These include $AuSn_4$ and $AuSn_2$ [20]. The electronics industry has long recognised a threshold level of 3 % by weight of gold that can be dissolved in the solder before joint failure is probable. The brittleness of these joints increases rapidly with increasing gold content and it is possible that joint failure experienced in this study may have resulted from excessive gold dissolved in the solder [21].

Secondly, the unsatisfactory fabrication of gold electrodes may have resulted from the nature of the glass tubing selected. The only type of glass used was soft soda glass and this all too often failed to yield a perfect seal around the wire. In some instances, air bubbles were exposed after polishing leading to larger than expected electrochemical areas of the gold being exposed to electrolyte and unacceptably high resistance values resulting in tilted voltammograms. Although better-sealed electrodes resulted when a vacuum was applied to the glass tube during the heating step, the success rate in constructing perfectly sealed gold electrodes remained low.

Solids typically expand on heating and contract on cooling due to changes in the length of intermolecular bonds; the coefficient of thermal expansion of a substance provides a measure of this fractional expansion or contraction per unit of temperature. Poor success in establishing a good seal during fabrication of gold electrodes may be attributed to the large difference between the coefficients of thermal expansion of gold and soda glass, 14.2 x 10^{-6} K^{-1} and 8.1 x 10^{-6} K^{-1} respectively. In other words, it is possible that during the heating step, gold expands at a greater rate than glass resulting in what one might imagine to be a good seal. However upon cooling, the reverse occurs, with gold contracting at a faster rate than glass and resulting in a microscopic gap between the two materials. Electrolyte penetrating into this microscopic gap would be responsible for larger than expected capacitative currents and tilted voltammograms due to increased cell resistance. By comparison, a better seal may arise during fabrication of platinum electrodes due to the similarity in coefficients of thermal expansion between platinum and glass, 8.8 x 10^{-6} K^{-1} and 8.1 x 10^{-6} K^{-1} respectively.

To overcome the difficulty of attaining a good seal, attempts have been made using epoxy resin comprising Araldite™ CY130 and hardener HY 1300 to seal gold wires of between 10 – 60 μm in glass tubing [22]. Higher capacitative currents were recorded for the microelectrode sealed in glass compared to epoxy resin. Results indicated that perfectly sealed electrodes could be constructed using the epoxy resin method and that electrochemical responses were not affected. Epoxy-sealed electrodes were stable in aqueous solution and caused no contamination of the sample. However, such electrodes are only suitable for applications performed in aqueous solvents since organic solvents can be absorbed by the resin causing interference with the electrode response [23].

Malem & Mandler [24] used a different approach to overcome these difficulties and inserted the gold wire through a small aperture in a partially collapsed glass Pasteur pipette (Figure 2.9). Special glass solder powder with a similar thermal expansion coefficient to gold was then poured into the pipette until the gold wire was almost covered. This assembly was heated slowly in an oven to 420°C, a temperature at

which the solder melted to create a perfect seal between the outer glass and inner gold wire. Electrical connection was made to the exposed wire using silver epoxy.

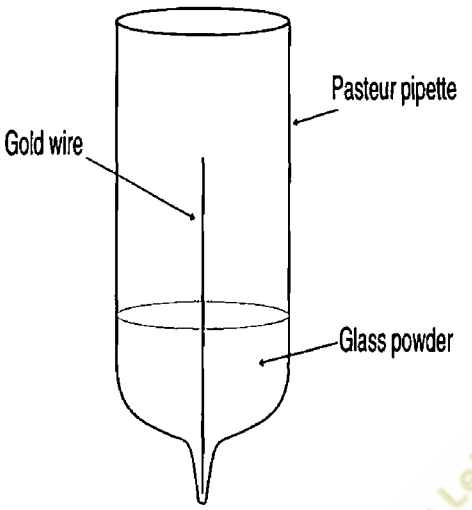

Figure 2.9. Schematic representation of the assembly of a gold electrode [24].

A precaution worthy of note is that it is of the utmost importance that particular attention be given to both the cleanliness of the electrode surface and that of the solution in which the electrode is immersed when undertaking electrochemical characterisation of electrodes.

2.2. Synthesis and characterisation of ruthenium and osmium complexes and bridging ligand

Early electrochemical studies using bare electrode surfaces demonstrated a lack of molecular activity that often resulted in poor sensitivity and specificity. This has been attributed as one of the major reasons why electrochemistry has not been more readily adopted as an analytical technique. Both theoretical and experimental studies have shown that the rate of electron transfer can be dramatically improved by modifying the electrode surface. Over the last number of years the development of methods to change the characteristics of the electrode surface and hence control the rate of electron transfer has become one of the major challenges faced by electrochemists. Several different approaches have been used to modify electrode surfaces including electroactive polymers, self-assembled monolayers and multilayers where the head group of the molecule has a strong affinity for the electrode surface [25-28].

Transition metal complexes, in particular self-assembled monolayers of ruthenium and osmium polypyridyl complexes, have great promise for electroanalytical applications [29]. These complexes are of interest because they are stable in more than one oxidation state, have fast electron transfer properties and have practically ideal, electrochemically-reversible redox properties, essential prerequisites for complexes that will be used as mediators. Electrochemical responses can be measured as a function of the electrolyte, solvent, temperature, pH and electron transfer distance [30]. The fact that monolayers of these complexes are stable for long periods, even at high temperature in aqueous perchlorate solutions, has allowed the rates and pathways of electron transfer to be probed in great detail under many different conditions [31].

Redox-active, transition metal complexes, often referred to as coordination compounds, are composed of a central metal atom often surrounded by counter-ions that neutralise the charge on the metal. Any ion or compound that surrounds these centres is known as a ligand. The ligands are most often bound to the metal ion by a co-ordinate covalent bond; the number involved being governed by the size, charge and electron configuration of the redox centre. Ligands containing one donor atom are known as monodentate, whereas those for example 2,2' bipyridyl or 1,10

phenanthroline, shown in Figure 2.10, are referred to as bidentate and contain two donor atoms capable of simultaneous co-ordination to the metal centre.

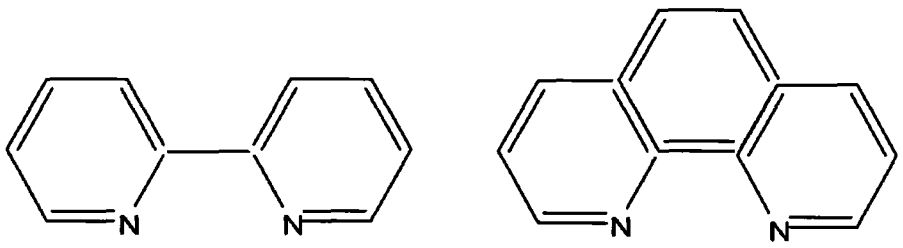

2,2' bipyridine 1,10 phenanthroline

Figure 2.10. Examples of bidentate ligands.

The two bidentate ligands above have been widely co-ordinated with ruthenium and osmium metal centres to form ruthenium and osmium polypyridyl complexes. These complexes form an octahedral structure as illustrated diagrammatically in Figure 2.11. Synthesis of these complexes can be complicated by the fact that both cis- and trans-isomers are often formed, leading to difficulties in isolating the desired molecule.

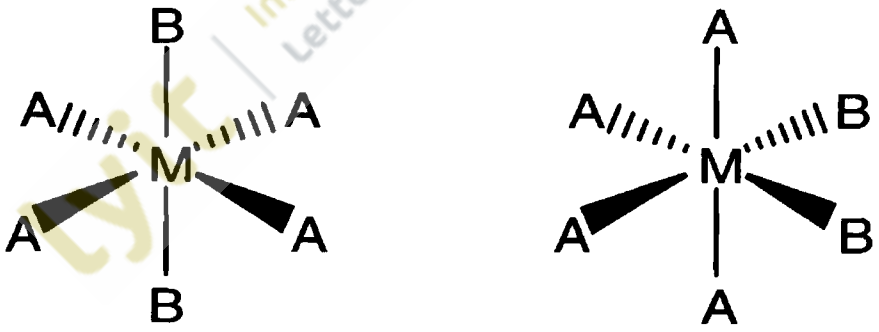

Trans Cis

Figure 2.11. Arrangement of two ligands denoted A and B in cis- and trans-formation.

Redox potentials of the complexes can be varied by substitution and/or derivatisation of the ligands. Electron-donating groups will lower the redox potential whereas electron-withdrawing groups will cause the potential to shift more positive [32].

Bridging ligands can also be coordinated to the metal centre. These ligands contain a free functional group capable of attachment to an electrode surface allowing formation of a self-assembled monolayer. Tailoring of the ligand allows the distance between the metal centre and the electrode to be accurately controlled. This provides a means of testing the effects of distance on electron transfer kinetics as well as allowing investigations of how changing functional groups within the ligand affects the electronic coupling across the bridge.

Much attention has been given to these metal complexes because of their potential for the development of molecular switches in nanoelectronics. They appear particularly useful in this area since they can be tailored to form low, stable and reversible redox couples. Switches can be developed by using two metal centres separated by a bridging ligand that when optimised will allow electrons to flow between the metal centres in one oxidation state (ON), but will restrict electron flow in the other position (OFF) [33-36].

Osmium and ruthenium polypyridyl complexes have also shown usefulness in recent years in the development of solid-state, light emitting devices. They are useful in this regard because of their stable reduction and oxidation as well as the fact that they luminesce with high efficiency [37-39].

The following section describes the methods used to synthesise a range of osmium and ruthenium bipyridyl complexes. Some of the methods used follow procedures from the literature whilst others are modifications of previously reported methods. Synthesis of some complexes was relatively straightforward involving only refluxing the required starting materials in a suitable solvent to produce the required complex. In other instances chromatographic separation and/or recrystallisation was necessary and purification proved to be quite an onerous task. Characterisation of the complexes using UV/Vis spectroscopy, HPLC and cyclic voltammetry was performed in-house. CHN elemental microanalysis and NMR were performed under contract with commercial laboratories.

2.2.1. Apparatus and reagents

High performance liquid chromatography (HPLC) was performed using a Shimadzu LC 10 VP pump equipped with a 20 µL injection loop and a Hichrom Excil 100-5SCX (sulphonic acid) cartridge. A Shimadzu SPD-M10A VP diode array detector used at a detection wavelength of 280 nm and interfaced to a personal computer was used for detection and readout. The mobile phase consisted of 80:20 (v/v) acetonitrile:water and 0.1M $LiClO_4$ was employed as an ion-pairing agent. A flow rate of 1.8 ml min^{-1} was used.

Electrochemical measurements were recorded from a CH Instruments model 600A potentiostat and a conventional three-electrode cell. The working electrode was either a 12.5 µm radius platinum or gold electrode or a 1.5 mm radius glassy carbon electrode. These electrodes were cleaned using alumina polishes and by electrochemical cleaning in 0.1M H_2SO_4. All potentials were referenced to a Ag/AgCl electrode. The counter electrode was a platinum wire. All electrochemical measurements were performed at room temperature. The solvent employed for solution phase cyclic voltammetry was HPLC grade acetonitrile. Tetrabutylammonium tetrafluoroborate dried *in vacuo* was used as supporting electrolyte at a concentration of 0.1M. All solutions were thoroughly degassed using nitrogen prior to measurement.

Ultraviolet-visible spectra were measured in spectroscopic grade acetonitrile or dimethylformamide and recorded using a Perkin-Elmer Lambda 5 UV/Vis spectrophotometer. The scan speed used was 120 nm min^{-1} and the slit width was 2 nm. A 1 cm quartz cell was used for all measurements.

Elemental microanalysis for carbon, hydrogen and nitrogen was undertaken by the Microanalysis Section, Chemistry Department, University College Dublin.

Proton nuclear magnetic resonance (NMR) spectra were obtained from the NMR Analysis Section, Chemistry Department, University College Dublin. Measurements were performed in deuterated acetonitrile or acetone.

2.2.2. Synthesis of cis-bis(2,2'-bipyridine-N,N')dichlororuthenium

2.2.2.1. Structure

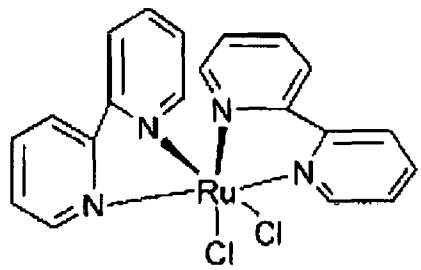

Figure 2.12. Structure of cis-bis(2,2'bipyridine-N,N')dichlororuthenium ($Ru(bpy)_2Cl_2$)

2.2.2.2. Method

This complex was synthesised by a modification of the literature method [40]. Briefly $RuCl_3$ (1.7 g, 8.22 mmol) and 2,2' bipyridine (2.57 g, 16.4 mmol) were placed in a 100 ml round-bottomed flask and magnetically stirred in 50 ml of dimethylformamide (DMF). Lithium chloride (2 g) was added. This mixture was refluxed under nitrogen for 5 hr. The solvent volume was reduced to 10 ml by rotary evaporation, diluted with 50 ml of acetone and placed in a fridge overnight. A dark solid (crude product) was collected by vacuum filtration, washed with ultra pure water (18 MΩ cm^{-1}) until the filtrates were colourless and then dried in air. The solid was placed in a 500 ml round bottomed flask and re-dissolved in 250 ml of 50 % aqueous ethanol by refluxing under nitrogen for 1 hr. After cooling 20 g of lithium chloride was added and the solution volume reduced to 75 ml by rotary evaporation. This was placed overnight in a fridge at 0°C yielding a dark solid that was collected by vacuum filtration, rinsed copiously with water and dried under vacuum.

2.2.3. Synthesis of cis-bis(2,2'-bipyridine-N,N') dichloroosmium

2.2.3.1. Structure

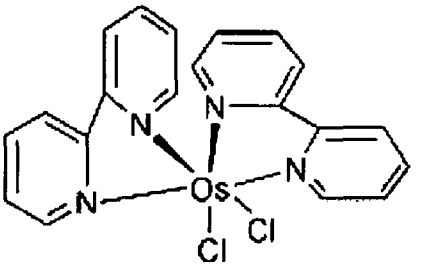

Figure 2.13. Structure of cis-bis(2,2'bipyridine-N,N')dichloroosmium ($Os(bpy)_2Cl_2$)

2.2.3.2. Method

This complex was synthesised by a modification of the literature method [41]. K_2OsCl_6 (0.95 g, 2 mmol) and 2,2' bipyridine (0.65 g, 4.2 mmol) were placed in a 50 ml round-bottomed flask. 20 ml of DMF was added and refluxed for one hour with constant stirring. The dark solution was cooled to room temperature and gravity filtered, diluted first with 10 ml of ethanol, and then with 250 ml of diethyl ether added by dropwise addition with vigorous stirring. The resulting brown/red solid was collected, rinsed with a small volume of diethyl ether and air-dried overnight.

The product of the preceding stage, cis-bis(2,2'-bipyridine-N,N')dichloroosmium, (1.14 g, 1.77 mmol) was dissolved in a mixture of 23 ml of DMF and 11.5 ml of methanol. A 1 % w/w solution of sodium dithionate in water (225 ml) was added by dropwise addition with stirring. Following overnight cooling in a fridge at 0°C, a dark solid was collected by filtration. This solid was rinsed with water (2 x 10 ml), methanol (2 x 10 ml) and diethyl ether (3 x 10 ml) and air-dried to give 0.9 g of product.

2.2.4. Synthesis of 3,6-bis(4-pyridyl)-1,2,4,5-tetrazine (4-tet)

2.2.4.1. Structure

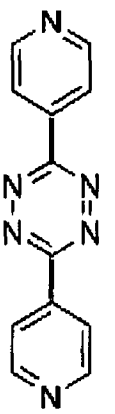

Figure 2.14. Structure of 3,6-bis(4-pyridyl)-1,2,4,5-tetrazine (4-tet)

2.2.4.2. Method

This synthesis was performed using a slight modification of the literature method [42]. 10.4 g of 4-cyanopyridine and 5 g of hydrazine monohydrate were placed in a 100 ml round-bottomed flask and stirred. Lithium chloride (2 g) was added and the flask was placed in a boiling water bath. The contents were refluxed for 5 hr with continuous stirring. A yellow brown solid (2.827 g) was collected after cooling and was recrystallised from hot ethanol/water 2:1 (500 ml). This solid was added slowly to stirred 95 % ethanol at room temperature and an equal weight of 2,3-dichloro-5,6-dicyano-1,4-benzoquinone (dehydrogenating reagent) added to the recrystallised product. The resulting bright pink solid was collected by vacuum filtration and recrystallised again as above.

2.2.5. Synthesis of $[Os(bpy)_2\text{-}(4\text{-tetrazine})\text{-}Cl](PF_6)$

2.2.5.1. Structure

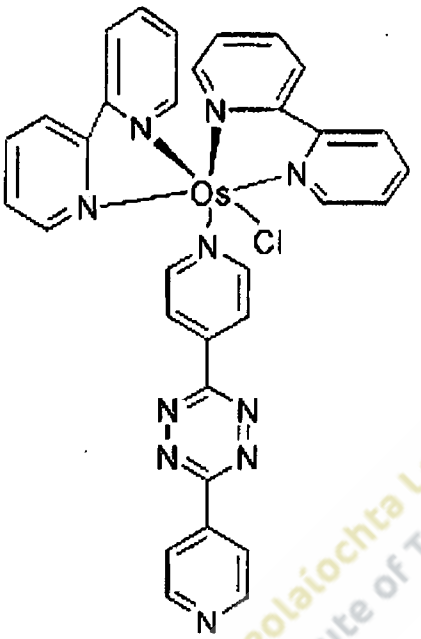

Figure 2.15. Structure of $[Os(bpy)_2\text{-}(4\text{-tetrazine})\text{-}Cl](PF_6)$

2.2.5.2. Method

4-tetrazine (0.12 g, 0.51 mmol) was dissolved in 20 ml of ethylene glycol and heated to reflux. Cis-$Os(bpy)_2Cl_2$ (0.257 g, 0.45 mmol) was dissolved in 50 ml of ethylene glycol and added to the refluxing solution dropwise over 30 min. The reaction mixture was allowed to reflux for a further 4 hr. The solvent volume was reduced to approximately 10 ml by rotary evaporation. After cooling a solution of concentrated aqueous ammonium hexafluorophosphate was added. The resulting solid was collected and recrystallised from acetone/water (1/1 v/v).

2.2.6. Synthesis of [Ru(bpy)$_2$(4-tetrazine)-Cl](PF$_6$)

2.2.6.1. Structure

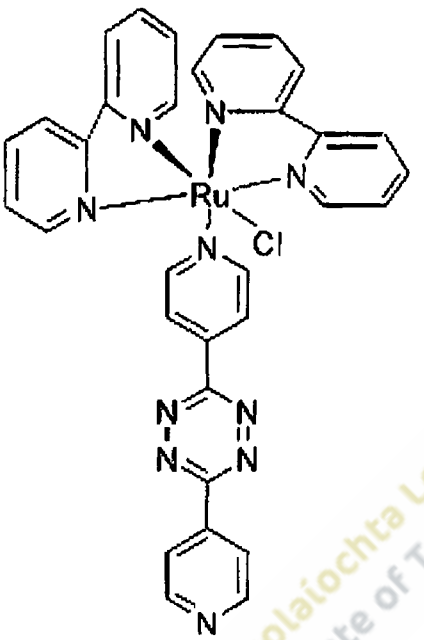

Figure 2.16. Structure of [Ru(bpy)$_2$(4-tetrazine)-Cl](PF$_6$)

2.2.6.2. Method

Ru(bpy)$_2$Cl$_2$ (0.2 g, 0.4 mmol) was dissolved, refluxed in ethanol (50 ml) for 10 min and then filtered whilst still warm. 4-tetrazine (0.096 g, 0.4 mmol) was dissolved in ethanol (20 ml) and added dropwise to the ruthenium bipyridyl dichloride solution over a 20 min period. This solution was refluxed for 6 hr and analysed for completion by HPLC and UV-Vis spectroscopy. To avoid photochemical decomposition the reflux flask was wrapped in aluminium foil and allowed to stand for 18 hr. This complex was precipitated using ammonium hexafluorophosphate and the resulting solid collected and recrystallised from acetone/water (1/1 v/v).

2.2.7. Synthesis of [Os(bpy)$_2$-(pyridine-4-carboxylic acid)-Cl](PF$_6$)

2.2.7.1. Structure

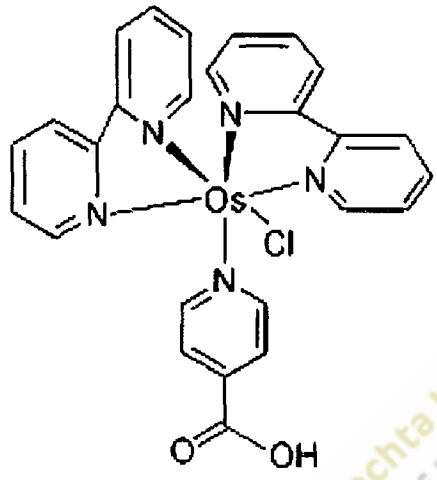

Figure 2.17. Chemical structure of [Os(bpy)$_2$-(pyridine-4-carboxylic acid)-Cl](PF$_6$)

2.2.7.2. Method

$Os(bpy)_2Cl_2$ (0.1 g, 0.18 mmol) was dissolved in 40 ml of ethylene glycol and refluxed for 10 min to ensure complete dissolution. Pyridine-4-carboxylic acid (0.0146 g, 0.20 mmol) was dissolved in 20 ml of ethylene glycol and added dropwise to the refluxing solution. The reaction mixture was allowed to reflux for a further 6 hr. After cooling, the solution was filtered whilst still warm to remove any unreacted ligand and the solvent was removed by rotary evaporation. The solid was then redissolved in ultra pure water and precipitated using a saturated solution of ammonium hexafluorophosphate. The crude product was purified by column chromatography using neutral alumina as the stationary phase and acetonitrile/ water as the mobile phase.

2.2.8 Synthesis of [Ru(bpy)$_2$-(pyridine-4-carboxylic acid)-Cl](PF$_6$)

2.2.8.1 Structure

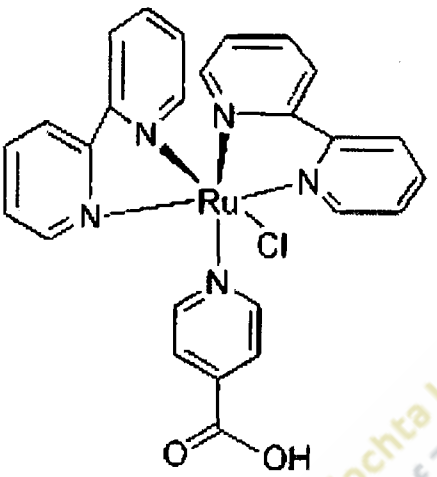

Figure 2.18. Chemical structure of [Ru(bpy)$_2$-(pyridine-4-carboxylic acid)-Cl](PF$_6$)

2.2.8.2. Method

Ru(bpy)$_2$Cl$_2$ (0.2 g, 0.4 mmol) was dissolved and refluxed in 80 ml of ethanol for 10 min. This was filtered whilst hot to remove any insoluble impurities. Pyridine-4-carboxylic acid (0.0492 g, 0.4 mmol) was dissolved in 20 ml of ethanol and added dropwise to the ruthenium bipyridyl dichloride solution over a 20 min period. This solution was refluxed for 8 hr. To avoid photochemical decomposition the reflux flask was wrapped in aluminium foil. The solution was filtered hot to remove any unreacted ligand and the solvent removed by rotary evaporation. The solid was redissolved in ultra pure water and precipitated using a saturated solution of ammonium hexafluorophosphate. The crude product was purified by column chromatography using neutral alumina as the stationary phase and acetonitrile/ water as the mobile phase.

2.2.9. Synthesis of $Ru(bpy)_2(4\text{-tetrazine})_2(PF_6)_2$

2.2.9.1. Structure

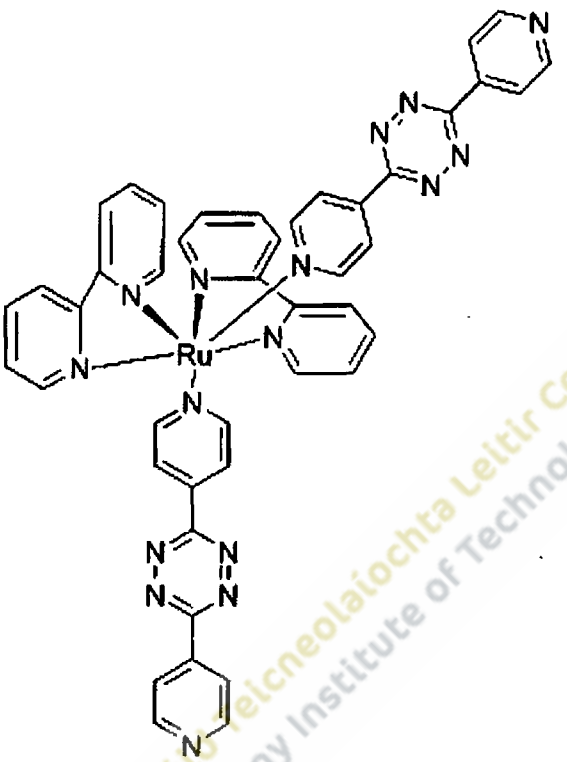

Figure 2.19. Chemical structure of $Ru(bpy)_2(4\text{-tetrazine})_2(PF_6)_2$

2.2.9.2. Method

$Ru(bpy)_2Cl_2$ (100 mg, 0.2mmol) was dissolved in 80 ml of methanol and refluxed for 10 min to ensure complete dissolution. A solution of 190 mg (0.8 mmol) of 3,6 bis(4-pyridyl)-1,2,4,5-tetrazine dissolved in 10 ml of ethanol together with 250 ml of ultra pure water was added and the resulting solution refluxed for 15 hr. The solution was maintained in the dark during refluxing to avoid photochemical decomposition. The volume of the solution was reduced to approximately 5 ml by rotary evaporation. A saturated solution of ammonium hexafluorophosphate was added and the product collected by filtration and washed with diethyl ether. The product was recrystallised from acetone/water (50/50) to yield brown crystals.

2.2.10. Characterisation of complexes

2.2.10.1. UV/Vis spectroscopy

Light absorption by transition metal polypyridyl complexes occurs over a wide range with electronic transitions of interest being generally between 190 nm to 600 nm. Valency electrons are found in three types of electron orbitals; single orbitals (σ bonding orbitals), double or triple orbitals (π bonding orbitals) and non-bonding orbitals (lone pair electrons). Sigma (σ) bonding orbitals tend to be lower in energy than pi (π) bonding orbitals, which in turn are lower in energy than non-bonding orbitals (Figure 2.20).

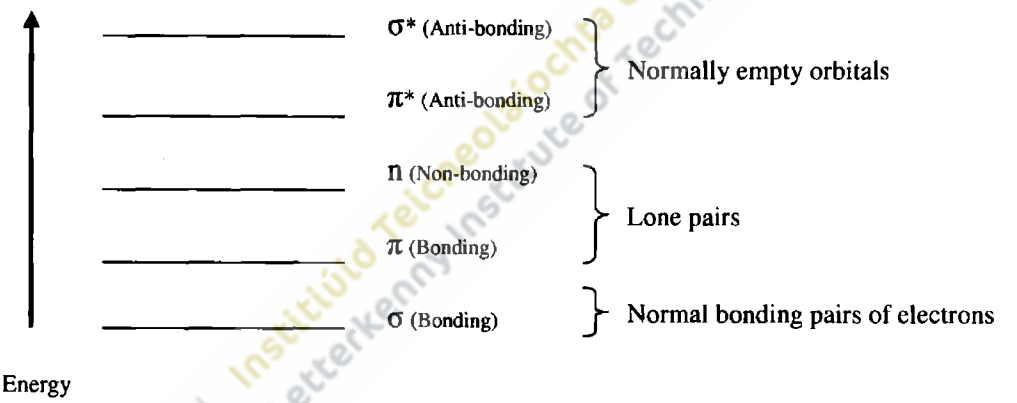

Figure 2.20. Simplified representative diagram showing the order of the energy levels of the different orbitals

When electromagnetic radiation of the correct frequency is absorbed a transition occurs from one of these orbitals to an empty orbital, usually an anti-bonding orbital (σ* or π*), i.e. π→π*, n→σ* and n→π* transitions.

The main electronic transitions typical of ruthenium and osmium polypyridyl complexes are illustrated in Figure 2.21. Orbitals relating to the metal or the ligand are represented as M and L respectively. In the ground state the ligand σ_L and π_L orbitals are completely filled while the metal π_M (t_{2g}) orbitals are filled or partially filled. Higher orbitals are usually empty. The energy gaps between these levels

determine the frequency (i.e. wavelength) of the light absorbed and will vary depending on the type of ligands attached to the metal centre.

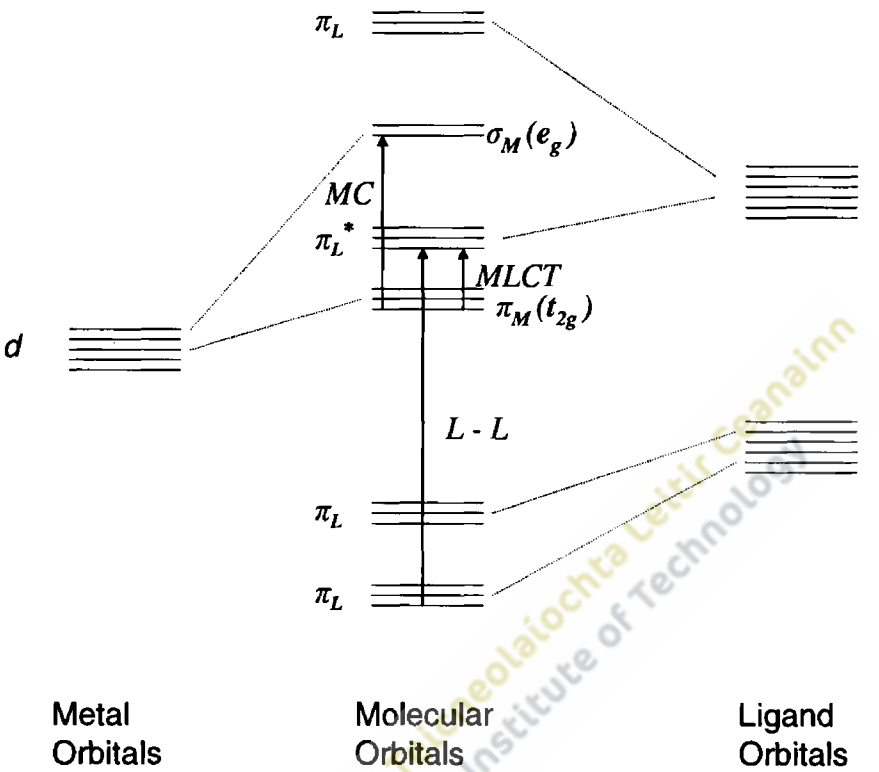

Figure 2.21. Electronic transitions which can occur in transition metal polypyridyl complexes, where MC is metal-centred, MLCT is metal-ligand charge transfer and L-L is ligand-centred transitions.

In complexes such as $Ru(bpy)_2XY$, where X and Y describe non-bipyridyl monodendate ligands co-ordinated along the $+x$ and $+y$ axes, the metal molecular orbitals of similar energy dxz, dyz and dxy of t_{2g} symmetry will be the highest occupied molecular orbitals ($HOMO_s$). The π^* bipyridyl orbitals are split into symmetric (χ) and anti-symmetric (ψ) orientations with respect to the C_2 axis of the bipyridine molecule and are the lowest unoccupied molecular orbitals ($LUMO_s$) [43] (Figure 2.22).

x ψ

Figure 2.22. Symmetric and anti-symmetric orientations of the unfilled π^* orbitals of bipyridine.

Hence transitions from the metal to the ligand can be described as π^* (ψ) ← dπ (t_{2g}) and π^* (x) ← dπ (t_{2g}) and have been shown to occur in the visible region [44]. Ligand to ligand electronic transitions also occur in the UV region of the spectrum.

Electronic transitions of ruthenium and osmium bipyridyl molecules typically show broad bands in the visible region between 350 and 600 nm, typical of metal to ligand charge transfer (MLCT) bands (d-π^*) or the effect of orbit spin coupling [41]. The position of these bands is due to the combination of the position of the anti-bonding orbital (π^*) with respect to the d-orbital of the metal. In the UV region the sharp peaks between 240 - 300 nm are typical of bipyridyl based (π-π^*) transitions [45-47]. Considerable differences have been reported between the UV/Vis spectra of cis- and trans- isomers of osmium bipyridyl complexes where the trans- isomer shows more structure due to narrower bands in the visible region while those of the cis- isomer are somewhat broader, thus providing a qualitative basis of distinguishing between isomers [48].

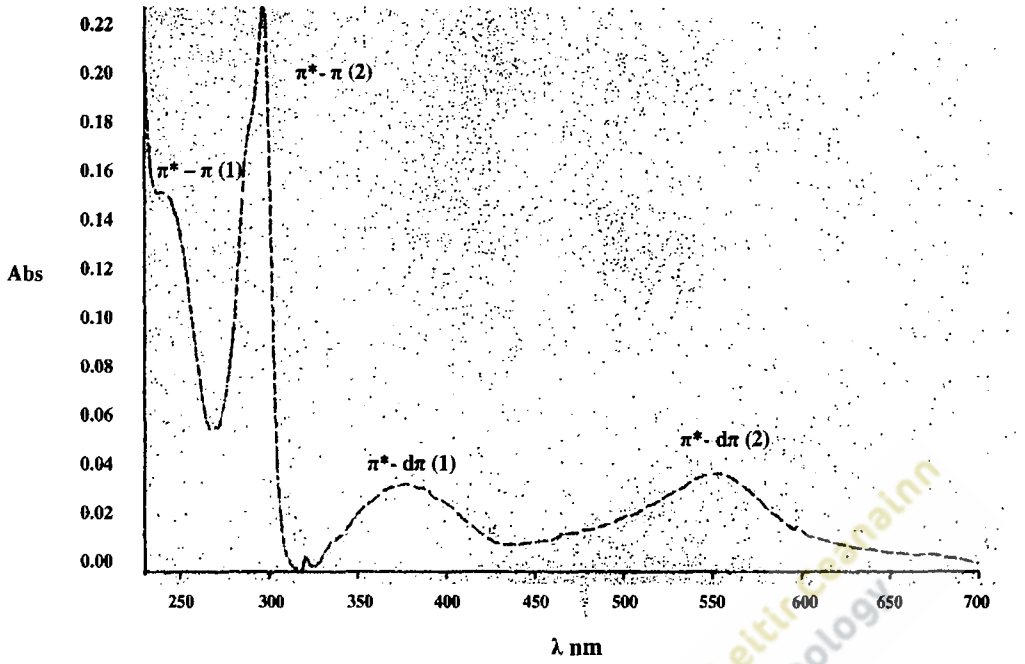

Figure 2.23. UV-visible absorbance spectrum for $Ru(bpy)_2Cl_2$ in acetonitrile.

The spectrum for $Ru(bpy)_2Cl_2$ is provided in Figure 2.23 with the intra-ligand transitions labelled as π - π(1) and π - π(2). In the literature the uncoordinated protonated bipyridine has been reported to exhibit intense bands at 232 and 279 nm but shifts to a lower energy on coordination to the metal ion [49]. Other researchers have attempted to correlate the magnitude of this shift with the nature of the metal and have demonstrated that the shift to lower energy for π-π^* transitions increases in the order $Os^{III} < Fe^{II} < Os^{II} < Ru^{II}$. It has been suggested that this order results from increasing covalent bond strength [50]. The spectrum for $Ru(bpy)_2Cl_2$ provided above shows this shift to lower energy with absorbance bands in the UV region at 242 and 293 nm. Absorption peaks in the visible region which are assigned to MLCT occurs at 376 and 550 nm in acetonitrile. The adsorption spectrum of $Os(bpy)_2Cl_2$ in the UV region is very similar to that found for the ruthenium complex but differs in the visible region where three absorption bands occur rather than two (Figure 2.25 & Table 2.1). The λ_{max} for these transitions occurred at 386, 468 and 564 nm and compare well with the literature values for this complex of 389, 467 and 561 nm for metal to ligand transfers in the visible region [48].

The UV/Vis spectrum of the tetrazine ligand in acetonitrile is provided in Figure 2.24. The spectra of similar tetrazine derivatives reported in the literature have displayed a very intense band in the UV region corresponding to a π-π^* transition with a much lower intensity band in the visible region corresponding to a n-π^* transition which is responsible for the colour of the compound [51].

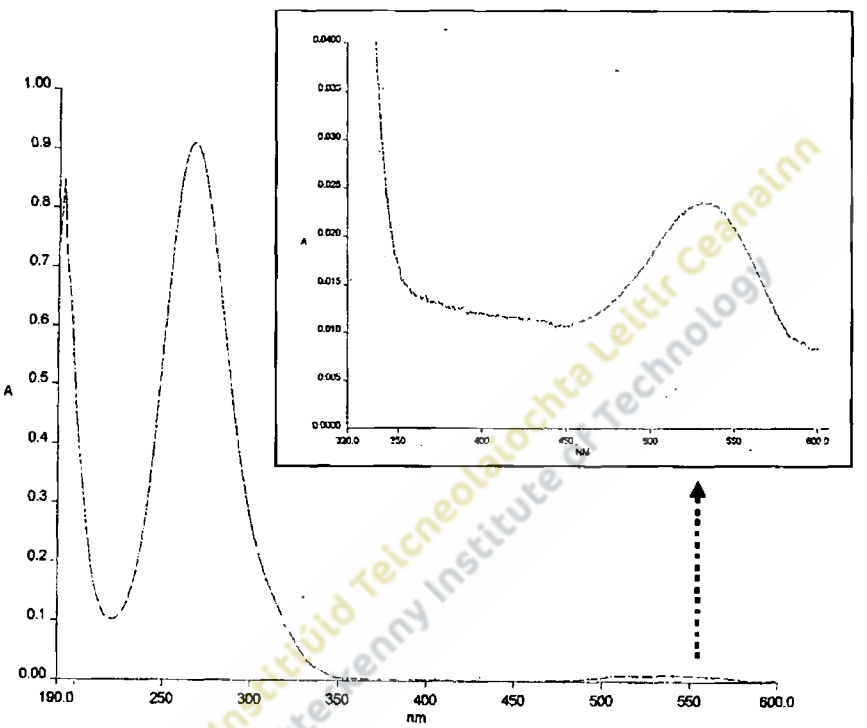

Figure 2.24. UV-visible spectrum of 3,6-bis(4-pyridyl)-1,2,4,5-tetrazine in acetonitrile.

The results for the tetrazine ligand synthesised in this study are in agreement with the literature reports where the intensity of the inter-ligand π-π^* transition is very strong while the n-π^* transition is weak (See inset of Figure 2.24).

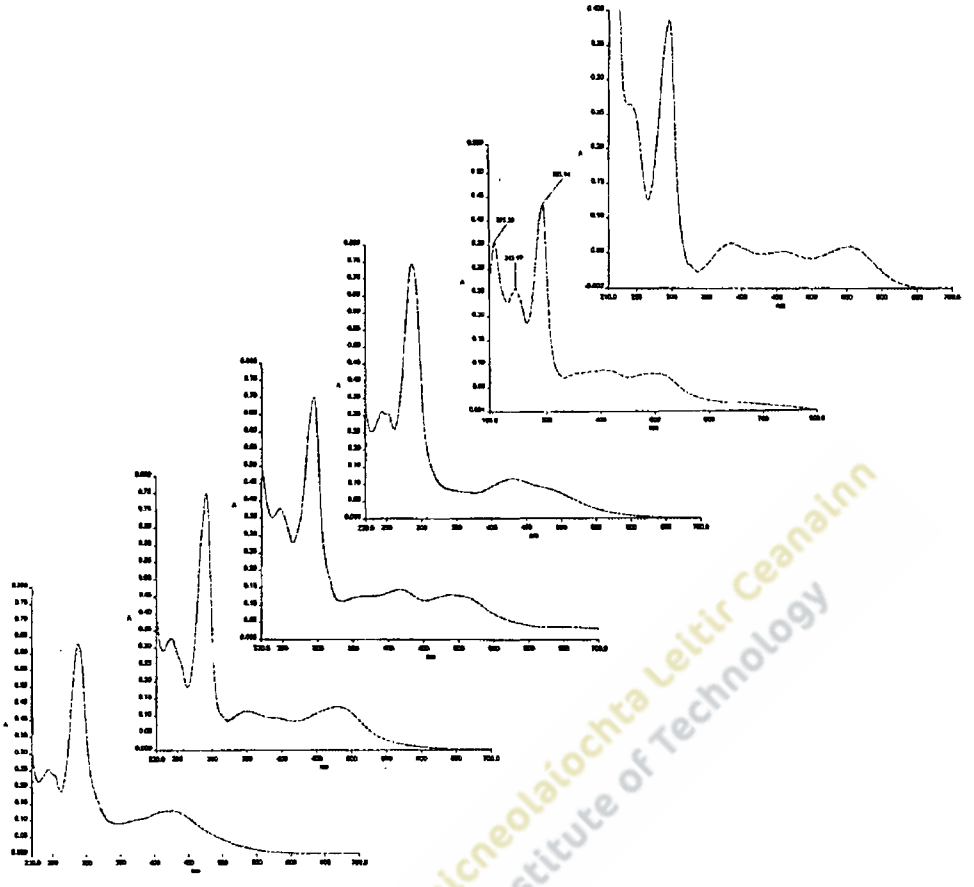

Figure 2.25. UV/Vis spectra of the complexes from top to bottom: $Os(bpy)_2Cl_2$, $[Os(bpy)_2\text{-}(4\text{-tet})\text{-}Cl](PF_6)$, $[Ru(bpy)_2\text{-}(4\text{-tet})\text{-}Cl](PF_6)$, $Os(bpy)_2\text{-}(pyridine\text{-}4\text{-}COOH)\text{-}Cl](PF_6)$, $[Ru(bpy)_2\text{-}(pyridine\text{-}4\text{-}COOH)\text{-}Cl](PF_6)$ and $Ru(bpy)_2(4\text{-tet})_2(PF_6)$.

The UV/Vis absorption spectra for the other synthesised complexes after substitution of the chloride with either the tetrazine or carboxylic acid ligands are shown in Figure 2.25. When substitution occurs, the MLCT is shifted to a higher energy for all complexes (Table 2.1). This may be explained by the fact that the chlorine ligand through σ bonding with the metal results in some back-bonding from metal to ligand. These σ interactions have the effect of raising the energy levels of the metal dπ orbitals which reduces the separation between the highest occupied metal orbital (HOMO) of the metal and the lowest unoccupied molecular orbital (LUMO) of the ligand as illustrated diagrammatically in Figure 2.26.

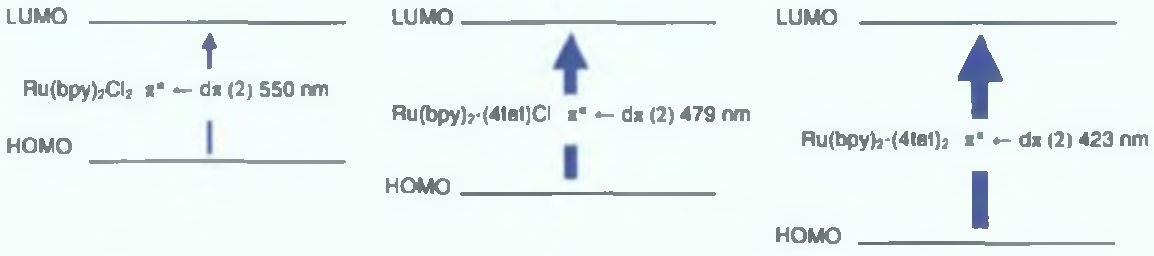

Figure 2.26. Simplified representation of the energy levels before and after substitution of the chlorine.

Substitution of the chlorine with the tetrazine or carboxyl ligand results in the MLCT $\pi^* \leftarrow d\pi$ (2) being shifted to a higher energy, i.e. a lower wavelength. This change has been attributed to more stable metal dπ orbitals with lower energy levels causing a greater separation between the metal dπ orbitals and the π^* orbitals of the bipyridyl ligand. In practice, this replacement of the chlorine with the tetrazine ligand causes a blue shift of 71nm. Further support for this explanation is provided by the further blue shift of 56nm upon substitution of the second chlorine by a further tetrazine ligand in the complex $Ru(bpy)_2(4\text{-tetrazine})_2(PF_6)_2$ (Table 2.1).

Compound	λ_{max} (nm) UV	λ_{max} (nm) visible
$Ru(bpy)_2Cl_2$	242, 293	376, 550
$Os(bpy)_2Cl_2$	242, 291	386, 468, 564
3,6-bis(4-pyridyl)-1,2,4,5-tetrazine	267	531
$[Os(bpy)_2\text{-}(4\text{-tetrazine})\text{-}Cl](PF_6)$	205, 244, 294	424, 494
$[Ru(bpy)_2\text{-}(4\text{-tetrazine})\text{-}Cl](PF_6)$	244, 286	428, 479
$[Os(bpy)_2\text{-}(py\text{-}4\text{-}COOH)\text{-}Cl](PF_6)$	245, 295	348, 418, 508
$[Ru(bpy)_2\text{-}(py\text{-}4\text{-}COOH)\text{-}Cl](PF_6)$	241, 292	349, 480
$Ru(bpy)_2(4\text{-tetrazine})_2(PF_6)_2$	243, 287	362, 423

Table 2.1. Spectroscopic data for the ruthenium and osmium complexes.

In summary, variation of inter-ligand transitions in the UV region for all complexes is small, by comparison with metal to ligand transitions which are larger and more

informative. Substitution of the non-bipyridyl ligands and the subsequent shift in MLCT bands to a higher energy results in more positive potentials for the $Os^{2+/3+}$ or $Ru^{2+/3+}$ complexes. This correlation between the energy of the first strong adsorption band and the electrode potential of the complex has been confirmed in previous studies [48].

2.2.10.2. High Performance Liquid Chromatography (HPLC)

High performance liquid chromatography (HPLC) as a means of separating/purifying compounds has many advantages compared to column chromatography in particular the speed of operation and greater efficiency. The fact that many different types of columns and detection systems are available makes this technique suitable for a large range of applications. The first reported use for the separation of organometallic complexes using liquid chromatography was made by Veening *et al.* in 1969 [52]. Because HPLC is a rapid technique performed at ambient temperature in a degassed solvent and shielded from visible light, it eliminates many of the problems which previously existed with column chromatography such as oxidative, thermal or photochemical instability possessed by some transition metal complexes.

In this research programme HPLC using strong cation exchange (SCX) columns were used to establish the purity of the synthesised complexes. In cation exchange chromatography, negatively-charged molecules present on the surface of the solid support attract positively-charged molecules present in the sample. Separation of mixtures of compounds is dependant on the magnitude of the charge present on each analyte. Limitations of this method arise with the separation of molecules with similar charges and have led to the use of ion pairing chromatography as a more efficient separation technique. In this modification, an ion pairing reagent is added to the mobile phase and improves the chromatographic separation possibly by adsorption of the ion-pairing agent onto the column packing material or alternatively through the formation of ion pairs with the analyte.

Ion pair chromatography using a Partisil®-SCX (cation exchange) column and perchlorate salts as the pairing ion was first applied to the separation of tris bipyridyl

ruthenium cationic metal chelates. Although an ion exchange column was used, separation of the metal chelate was not attributed to ion exchange but to the distribution of the chelate species paired with the perchlorate ion [53]. The retention times of the complexes on the column varied depending on the concentration of the pairing ion in the mobile phase. The same cationic exchange column was used to successfully separate bis bipyridyl ruthenium compounds using the mobile phase acetonitrile/water (80:20 v/v) containing 0.08 M $LiClO_4$ as the ion pairing agent [54]. Prior to the use of ion pair chromatography, ODS columns were used to separate compounds, however this could only be achieved satisfactorily when the compounds to be separated possessed differing charges. Thus separation of isomeric complexes containing the same charge was not possible. Using ion pair chromatography to separate compounds with the general formula $[Ru(bpy)_2XY]^{n+}$ it was demonstrated that compounds such as $[Ru(bpy)_2(L)Cl]^+$ with a single charge eluted from the column before compounds such as $Ru(bpy)_2(L_2)]^{2+}$ with a double charge (where L is the ligand). Chromatographic peaks of the single-charged species were sharper than the broader peaks of double-charged species which exhibited peak tailing [54].

Using a slightly higher concentration of $LiClO_4$ (0.1 M) as the ion pairing agent but otherwise similar HPLC procedures, the results in this study are supportive of those in the literature. HPLC chromatographs for the ruthenium complexes, $[Ru(bpy)_2(4\text{-}tet)Cl]^+$ and the $[Ru(bpy)_2(4\text{-}tet)_2]^{2+}$ are provided in Figure 2.27. The single-charged ruthenium complex eluted as a sharp peak at 1.44 min whilst the double-charged complex eluted at 3.98 min as a broader peak and exhibited substantial tailing. In circumstances where mixtures of compounds are present, tailing can be reduced by either increasing the flow rate after elution of the mono substituted product, and/or increasing the $LiClO_4$ concentration [54]. No attempt to resolve the issue of tailing by varying the flow rate was undertaken in this study since no other peaks were evident in the tail region and no change in the UV/Vis spectra was recorded between 3.98 to 6 min. The presence of impurities in the double-charged complex was recorded at 1.34 min. Retention times for the ligand and all the complexes synthesised in this study are provided in Table 2.2.

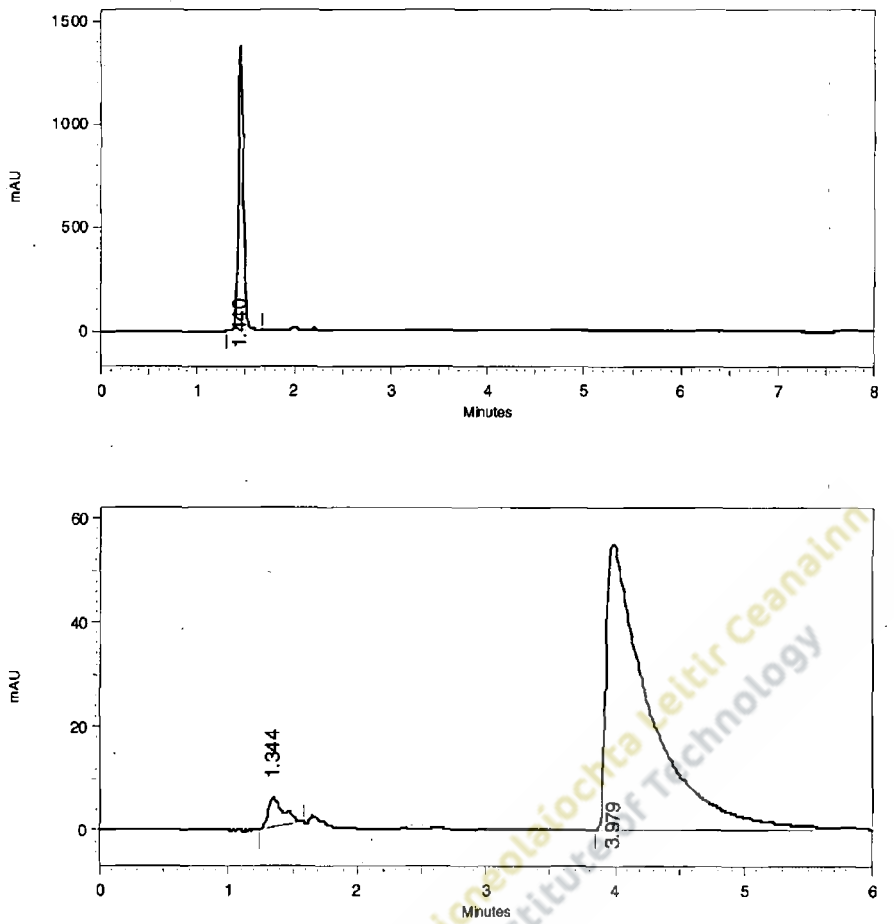

Figure 2.27. HPLC chromatographs for $[Ru(bpy)_2(4\text{-tet})Cl]^+$ and $[Ru(bpy)_2(4\text{-tet})_2]^{2+}$

Compound	Retention time (min)
$Ru(bpy)_2Cl_2$	1.34
$Os(bpy)_2Cl_2$	1.27
3,6-bis(4-pyridyl)-1,2,4,5-tetrazine	1.56
$[Os(bpy)_2\text{-}(4\text{-tetrazine})\text{-}Cl](PF_6)$	1.75
$[Ru(bpy)_2\text{-}(4\text{-tetrazine})\text{-}Cl](PF_6)$	1.44
$[Os(bpy)_2\text{-}(py\text{-}4\text{-}COOH)\text{-}Cl](PF_6)$	1.62
$[Ru(bpy)_2\text{-}(py\text{-}4\text{-}COOH)\text{-}Cl](PF_6)$	2.33
$Ru(bpy)_2\text{-}(4\text{-tetrazine})_2(PF_6)_2$	3.98

Table 2.2. Retention times for the ligand and the synthesised complexes.

In this study HPLC was used to establish the purity of the synthesised complexes. In situations where impurities were detected following HPLC; a sequence of column chromatography, fraction collection, re-checking of the purity of each fraction using HPLC and finally combination of similar pure fractions was employed to obtain the pure complex. This somewhat lengthy approach to purification was necessary since semi- preparative HPLC was not available for this research programme. Semi-preparative HPLC has been shown to be a very effective technique for the separation and purification of transition metal complexes with one study reporting that up to 100 mg of two deprotonated $Ru(bpy)_2$ compounds were separated and collected using a 1 cm^3 injector loop, a Whatman® 9 SCX column, a mobile phase of 80:20 acetonitrile/water (v/v) containing 0.08 M $LiClO_4$ and a flow rate of 5 ml min^{-1} [55].

More recently efficient separation of cis and trans isomers of $Ru(H_2O)_2(bpy)_2(PF_6)_2$ by RP-HPLC using a Shimadzu ODS column and a mobile phase of 25:75 methanol-water containing 0.1 % trifluroacetic acid has been reported providing an alternative to ion pair chromatography for determination of the purity of ruthenium bipyridyl complexes [56].

In summary HPLC is a useful technique for determination of the purity of complexes following synthesis and with modified procedures is suitable for the separation of isomers.

2.2.10.3. Elemental microanalysis

The theoretical percentage of carbon, hydrogen and nitrogen (CHN) of each synthesised complex and the bridging ligand determined from the molecular formula are compared with experimental measurements following elemental microanalysis in Table 2.3.

Element	Theoretical Composition	Measured Composition		Mean Composition
	(%)	Sample A (%)	Sample B (%)	(%)
$Ru(bpy)_2Cl_2.3H_2O$		Molecular formula $RuC_{20}H_{22}N_4Cl_2O_3$		
Carbon	44.60	44.45	44.45	44.45
Hydrogen	4.08	3.89	3.94	3.92
Nitrogen	10.40	10.20	10.08	10.14
$Os(bpy)_2Cl_2.2H_2O$		Molecular formula $OsC_{20}H_{20}N_4Cl_2O_2$		
Carbon	39.41	40.80	40.50	40.65
Hydrogen	3.28	3.18	3.03	3.10
Nitrogen	9.19	9.14	8.88	9.01
3,6-bis(4-pyridyl)-1,2,4,5-tetrazine(4-tet)		Molecular formula $C_{12}H_8N_6$		
Carbon	61.02	60.91	60.67	60.79
Hydrogen	3.39	3.56	3.43	3.49
Nitrogen	35.59	35.59	35.34	35.46
$[Os(bpy)_2(4\text{-tetrazine})Cl](PF_6)$		Molecular formula $OsC_{32}H_{24}N_{10}ClF_6P$		
Carbon	41.83	39.90	39.67	39.78
Hydrogen	2.61	3.35	3.43	3.39
Nitrogen	15.25	14.55	14.34	14.44
$[Ru(bpy)_2(4\text{-tetrazine})Cl](PF_6)$		Molecular formula $RuC_{32}H_{24}N_{10}ClF_6P$		
Carbon	46.32	47.85	47.15	47.50
Hydrogen	2.90	3.41	3.43	3.42
Nitrogen	16.88	16.11	16.25	16.18
$[Os(bpy)_2(\text{pyridine-4-carboxylic acid})Cl](PF_6)$		Molecular formula $OsC_{26}H_{21}N_5ClF_6PO_2$		
Carbon	38.75	38.74	38.65	38.69
Hydrogen	2.60	2.96	2.80	2.88
Nitrogen	8.68	8.15	8.24	8.20
$[Ru(bpy)_2(\text{pyridine-4-carboxylic acid})Cl](PF_6)$		Molecular formula $RuC_{26}H_{21}N_5ClF_6PO_2$		
Carbon	43.57	43.50	43.35	43.42
Hydrogen	2.93	2.95	2.80	2.87
Nitrogen	9.77	9.45	9.40	9.42
[illegible]		Molecular formula $RuC_{40}H_{32}N_{16}F_{12}P_2$		
Carbon	44.93	43.50	43.35	43.42
Hydrogen	2.70	4.44	4.15	4.29
Nitrogen	19.06	17.44	17.35	17.40

Table 2.3. Elemental microanalysis data for the synthesised complexes and ligand.

The percentages of carbon and nitrogen determined in the synthesised compounds were generally in good agreement with the theoretical compositions determined from the molecular formulas. The higher percentages of hydrogen determined in some of the synthesised compounds may be attributed to the presence of water molecules trapped within the complex which were not removed during the drying stage. The largest variation between the theoretical and experimental results was exhibited by the complex $Ru(bpy)_2(4\text{-tetrazine})_2(PF_6)_2$ and suggested the presence of small amounts of impurities. Similar conclusions regarding the presence of small amounts of impurities in this complex were demonstrated by the HPLC results provided in Figure 2.27.

2.2.10.4. Nuclear Magnetic Resonance (NMR) spectroscopy

Nuclear magnetic resonance (NMR) spectroscopy was used to elucidate the structure and confirm the purity of the synthetic preparations. The technique is especially useful for establishing the geometric nature of compounds particularly in circumstances where isomeric forms may arise. Trans- isomers of ruthenium or osmium bipyridine compounds produce a relatively simple ^1H NMR spectrum comprising two doublets and two triplets at a slightly higher field to the doublet. The relatively simple spectrum for trans-$Ru(bpy)_2(H_2O)_2$ results from the high level of symmetry of the bipyridines in the trans- isomer as shown in Figure 2.28. This is the same as the splitting pattern obtained for the highly symmetrical 2,2' bipyridine ligand in solution [57].

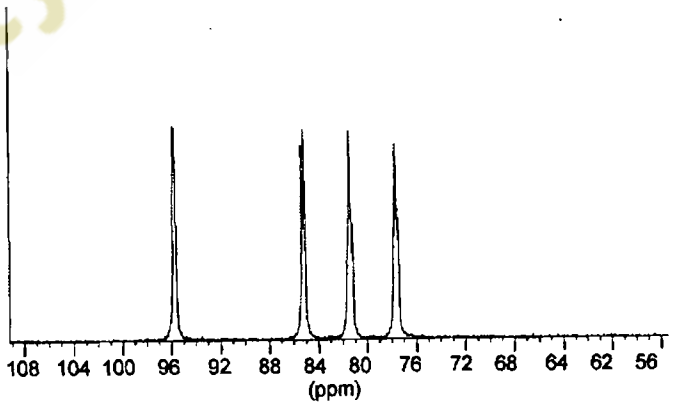

Figure 2.28. ^1H NMR spectrum of trans-$Ru(bpy)_2(H_2O)_2$ [33].

Cis- isomers of ruthenium or osmium bipyridine compounds show a more complex splitting pattern than the trans- isomers due to the unsymmetrical nature of the molecule since the individual rings of the bipyridine ligand are not magnetically equivalent. This results in spectra of two slightly dissimilar rings superimposed on one another [58]. The NMR spectrum for cis-$Ru(bpy)_2Cl_2$ synthesised in this study is shown in Figure 2.29.

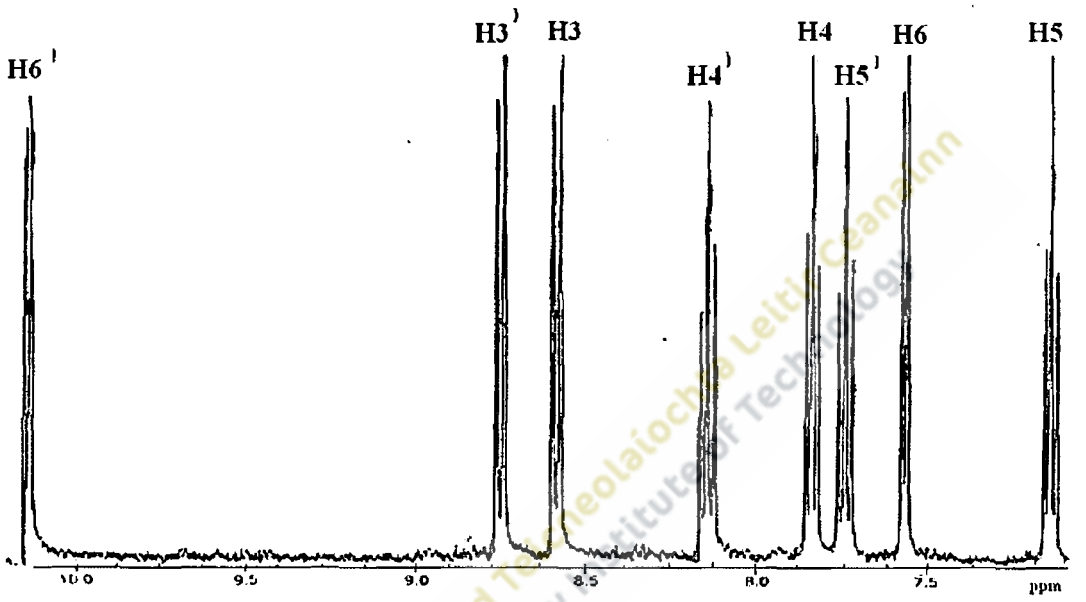

Figure 2.29. ^1H NMR of cis-$Ru(bpy)_2Cl_2$ in d-acetonitrile.

The spectrum shows the eight proton peaks expected for the cis- geometry. Each pyridyl ring revealed two doublets representing the protons nearest the nitrogen and two triplets representing the protons furthest from the nitrogen. All peaks were sharp and showed no broadening as would be typical for a pure complex. A large upfield shift of the H6' protons of the bipyridyl rings was recorded. This upfield shift has been reported previously for $Ru(bpy)_2$ type complexes and explained by what is known as diamagnetic anisotropic interactions of these protons with ring currents of other bipyridyl ligands [31]. Assignment of the proton resonance signals recorded were attributed to the different protons by comparison with literature data [57]. The ^1H NMR data (bipyridyl) [CD_3CN]: H^5 6.75-7.08 (t), H^6 7.51-7.53 (d), $H^{5'}$ 7.75-7.78 (t), H^4 7.78- 7.86(t), $H^{4'}$ 8.15-8.26 (t), H^3 8.56- 8.65 (d), $H^{3'}$ 8.74-8.83 (d), $H^{6'}$ 10.10-10.21 (d).

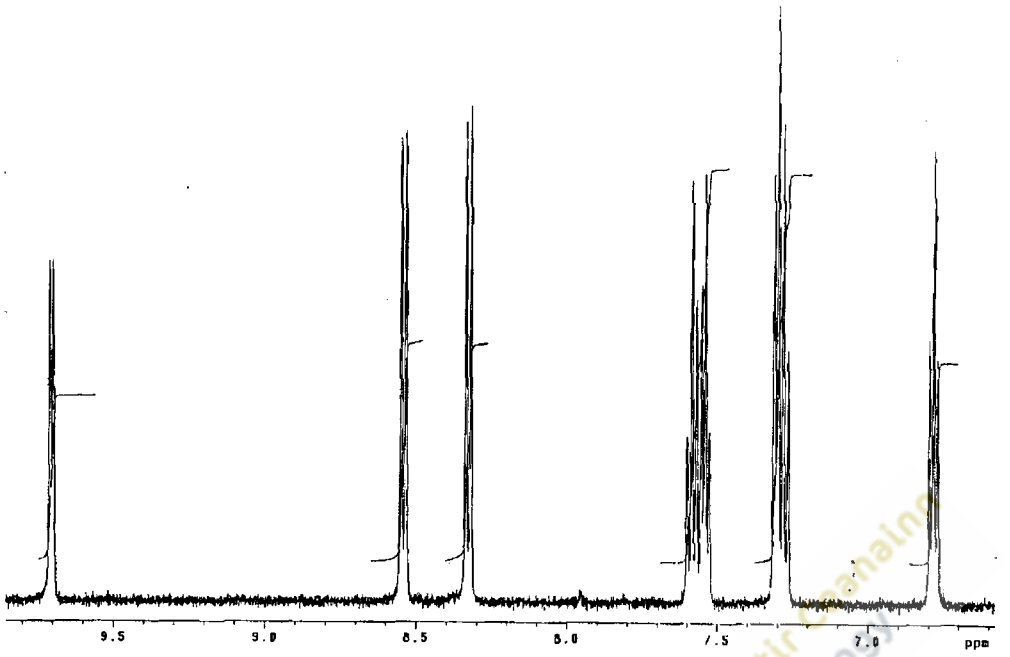

Figure 2.30. ^{1}H NMR of cis-Os(bpy)$_2$Cl$_2$ in d-acetonitrile.

The NMR spectra of cis-Os(bpy)$_2$Cl$_2$ as expected is very similar to that of Ru(bpy)$_2$Cl$_2$ where an expanded spectrum again shows the presence of 4 doublets and 4 triplets as expected for the cis- geometry of this complex (Figure 2.30). The ^{1}H NMR data (bipyridyl) [CD_3CN]: H^5 6.77-6.87 (t), H^6 7.27-7.28 (d), $H^{5'}$ 7.28-7.33 (t), H^4 7.51- 7.56 (t), $H^{4'}$ 7.56-7.61 (t), H^3 8.32- 8.35 (d), $H^{3'}$ 8.52-8.56 (d), $H^{6'}$ 9.68-9.73 (d).

A relatively simple ^{1}H NMR spectrum shown in Figure 2.31 was obtained for the tetrazine ligand due to the symmetrical nature of the molecule. The protons nearest the nitrogen are shifted higher upfield than the protons adjacent to the carbon. The chemical shifts obtained are in excellent agreement with literature values [59]. The ^{1}H NMR data [CD_3CN]: (4H) H^2, H^6, $H^{2'}$, $H^{6'}$ 8.93 (d), (4H) H^3, H^5, $H^{3'}$, $H^{5'}$ 8.48 (d).

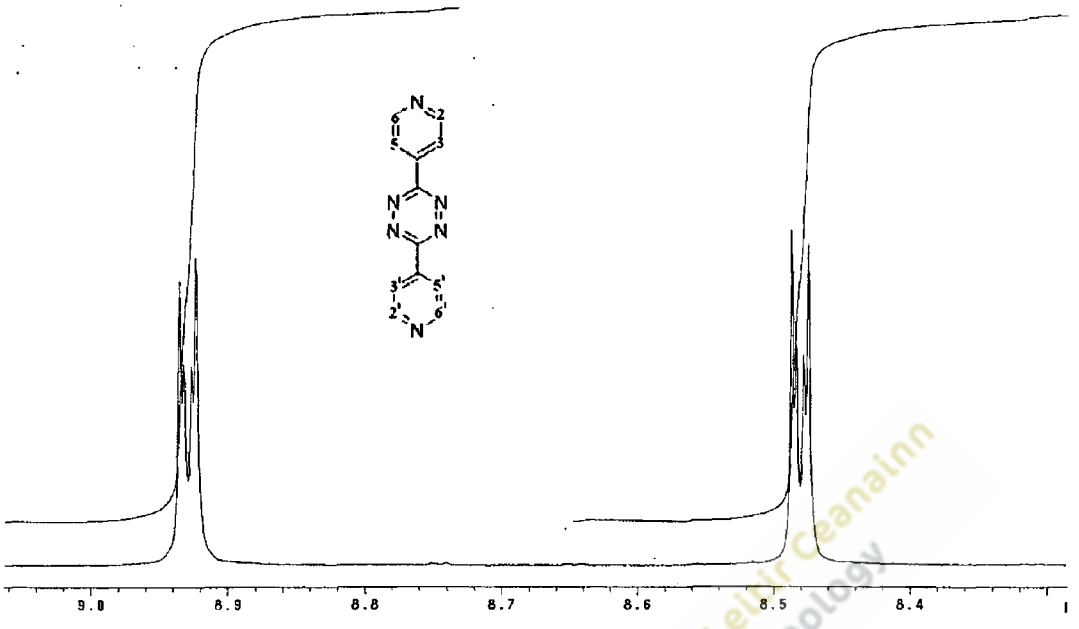

Figure 2.31. ^{1}H NMR of 3,6-bis(4-pyridyl)-1,2,4,5-tetrazine (4-tet)in d-acetonitrile.

In summary the NMR spectra recorded for the ruthenium and osmium bipyridyl complexes confirmed that the compounds existed in the cis- configuration rather than in the trans- configuration which would have resulted in much simpler spectra. The sharp peaks recorded in the NMR spectra when combined with information provided by the single HPLC peak confirmed the purity of the synthesised complexes.

2.2.10.5. Cyclic Voltammetry

The electrochemistry of the synthesised complexes was characterised using cyclic voltammetry. With all of the synthesised complexes only a single redox couple was recorded indicating that only one redox active complex was present. Redox potentials for all of the complexes were compared to literature values where possible.

Considering the ruthenium and osmium complexes possessing two chloride ligands, the redox potential of the osmium complex was approximately 400 mV more negative than that of the equivalent ruthenium complex. In similar studies osmium has been reported easier to oxidise than ruthenium leading to more negative potentials of

between 300 and 500 mV [60]. The redox potentials of osmium and ruthenium bipyridyl complexes can be adjusted by simple modification or substitution of the attached ligands. In general when chloride ligands are replaced by pyridyl groups, a significant positive shift in redox potential is observed [48].

A solution phase cyclic voltammogram for $Ru(bpy)_2Cl_2$ is provided in Figure 2.32. A single redox couple ($Ru^{2+/3+}$) was observed at approximately 0.38 V. This is the typical response for a one electron transfer of a ruthenium metal centre with two neutral ligands and two electronegative atoms.

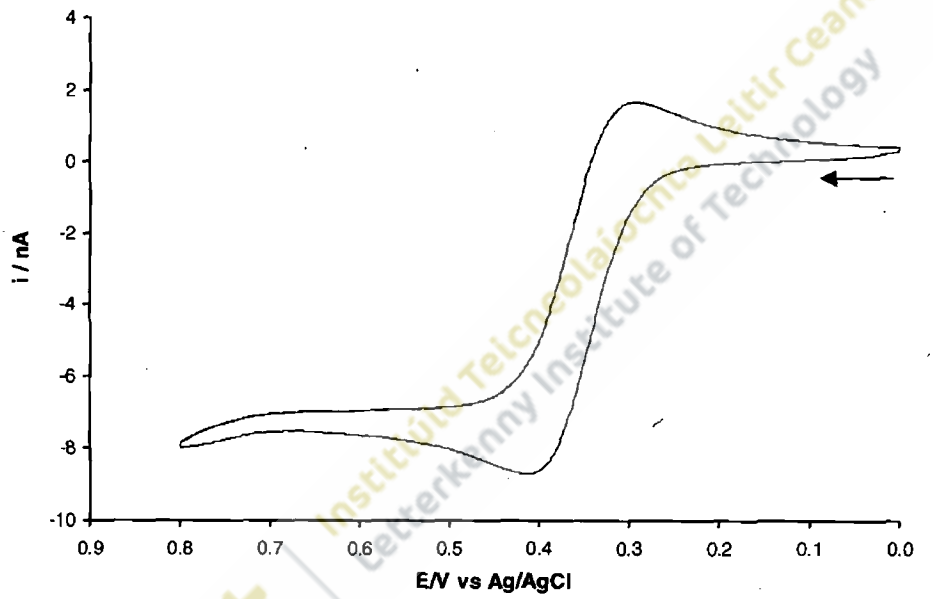

Figure 2.32. Cyclic voltammogram of $Ru(bpy)_2Cl_2$ in acetonitrile using a 12.5 μm radius Pt electrode. Supporting electrolyte was 0.1 M $TBABF_4$ and the scan rate used was 0.5 V s^{-1}. Scan direction shown by black arrow. Potential limits 0.00 to 0.80 V.

A solution phase cyclic voltammogram for $[Ru(bpy)_2$-(4-tetrazine)-Cl$](PF_6)$ in acetonitrile is provided in Figure 2.33. A single redox couple was observed at approximately 0.82 V.

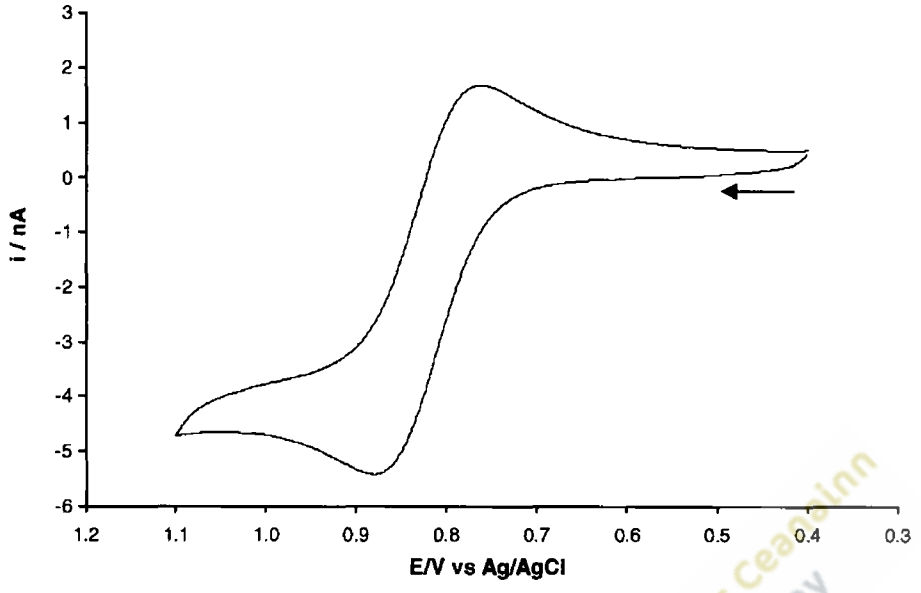

Figure 2.33. Cyclic voltammogram of $[Ru(bpy)_2\text{-}(4\text{-tetrazine})\text{-}Cl](PF_6)$ in acetonitrile with 0.1 M $TBAFB_4$ as electrolyte. The scan rate used was 0.5 V s^{-1} and the scan direction is shown by the black arrow. The potential limits were 0.4 to 1.1 V.

The positive shift in redox potential resulting from substitution of the chloride by the tetrazine ligand is clearly demonstrated by comparison of the cyclic voltammograms in Figures 2.32 and 2.33. Potential shifts due to ligand substitution have been attributed to effects of the electron density on the metal [61]. Ligands such as chlorine which are strong σ donors result in lower oxidation potentials. The tetrazine ligand which has much weaker σ donating capabilities will donate reduced electron density into the metal resulting in more stabilised d orbitals and consequently higher oxidation potentials.

The 3,6-bis(4-pyridyl)-1,2,4,5-tetrazine ligand is an electroactive heterocyclic compound. In combination with electron-rich, metal complexes this electron-poor, heterocyclic compound provides an alternating electron-rich / electron-poor assembly. Interest in such compounds is rapidly expanding for uses in both optical and electrochemical applications. Well defined cyclic voltammograms were observed for this ligand at much more negative potentials than that observed for the other complexes as shown in Figure 2.34.

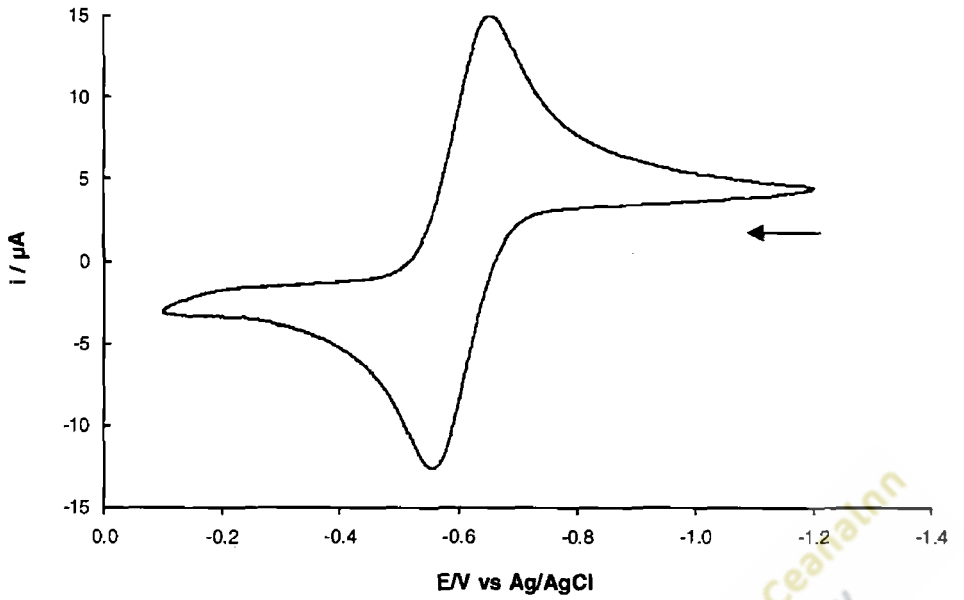

Figure 2.34. Cyclic voltammogram of 3,6-bis(4-pyridyl)-1,2,4,5-tetrazine in acetonitrile using a glassy carbon electrode of 0.5 mm radius with 0.1 M tetrabutyl ammonium tetrafluoroborate as supporting electrolyte. Scan rate 0.5 V s^{-1}. Scan direction shown by black arrow. Potential limits were –1.4 to -0.1 V.

The redox potentials in acetonitrile of all the ruthenium and osmium complexes and the tetrazine ligand synthesised in this research programme are provided in Table 2.4.

Compound	E^0 V vs. Ag/AgCl in acetonitrile	E^0 literature values	E^0 Lever calculated values
$Ru(bpy)_2Cl_2$	0.38	0.38[62]	0.35
$Os(bpy)_2Cl_2$	-0.02	-0.04[63]	-0.14
3,6-bis(4-pyridyl)-1,2,4,5-tetrazine	-0.60	Not available	-0.57
$[Os(bpy)_2$-(4-tetrazine)-Cl$](PF_6)$	0.28	0.26[64]	0.36
$[Ru(bpy)_2$-(4-tetrazine)-Cl$](PF_6)$	0.82	0.80[31]	0.87
$[Os(bpy)_2$-(py-4-COOH)-Cl$](PF_6)$	0.32	Not available	0.39
$[Ru(bpy)_2$-(py-4-COOH)-Cl$](PF_6)$	0.80	0.81[65]	0.85
$Ru(bpy)_2$-(4-tetrazine)$_2(PF_6)_2$	1.36	Not available	1.36

Table 2.4. Electrode potentials of the synthesised complexes and the ligand.

Redox potentials for the different ruthenium and osmium complexes and the tetrazine ligand compared well with values reported in the literature. Values for the redox potential of $Ru(bpy)_2(4\text{-tetrazine})_2(PF_6)_2$ were not available in the literature although values for di-substituted ruthenium complexes with a very similar 4,4'- dipyridyl ligand were in good agreement [62]. Comparison of the redox potentials of the different complexes in Table 2.4 highlights the shift in potential that occurs following mono-substitution and the further shift upon di-substitution. Replacement of the chloride ligand during mono-substitution in both ruthenium and osmium complexes with either the isonicotinic ligand or the tetrazine ligand resulted in a similar shift in the redox potential suggesting similar electron donating properties of these two ligands.

A theory for the calculation of redox potentials of metal complexes with attached bridging ligands was developed by Lever [66]. His investigation commenced with a study of $Ru(bpy)_3$ complexes. Since these complexes contain six Ru-N bonds in identical chemical environments, the contribution from each bipyridine ligand was evaluated. The $Ru^{2+/3+}$ potential occurred at 1.53V vs. NHE. Therefore the contribution from each pyridine was determined as 1.53/6 = 0.255V. On this basis, values for the potential according to the Lever theory (E_L) for over 100 ligands were defined. From E_L values of attached ligands other than bipyridine using a best fit least square average, the final E_L value for bipyridine was re-evaluated at 0.259V and this became the primary electrochemical standard value by which all other ligands were evaluated. A limitation to this theory is that all ligands would behave in a similar way to many redox metal couples. However it has previously been established that the corresponding potentials for analogous ruthenium and osmium complexes are linearly related and therefore the relative contribution of attached ligands on either metal centre can be accurately determined [67]. With regard to the assignment of redox potentials based on the Lever theory to the complexes synthesised in this study, an example for $[Ru(bpy)_2\text{-(py-4-COOH)-Cl}](PF_6)$ is provided below. In this complex the bipyridine is replaced with a chloride and a Py-4-COOH ligand. E_L values which are assigned to these ligands are -0.24V and 0.29V respectively [66].

Considering first the effect on electrode potential of the chloride replacement; since the pyridine ligand has been assigned a value of 0.259V, replacement with a chloride ligand with an E_L value of -0.24V results in a negative shift in potential by 0.499V. On the same basis, replacement of a second pyridine by the py-4-COOH ligand should theoretically result in a positive shift of 0.031V. By combining these two shifts in potential, an overall net negative shift of 0.468V results which when combined with the 1.53V for the complex should result in an electrode potential of 1.06V vs. NHE or 0.85V vs. Ag/AgCl reference electrode. This latter value is slightly higher than the observed experimental value of 0.80V vs. Ag/AgCl reported in Table 2.4.

For the analogous osmium complex, the observed value for $Os(bpy)_3$ is 1.06V vs NHE [67], the net negative charge due to the substitution is again 0.468V and hence the theoretical value (E_L) for the complex $[Os(bpy)_2\text{-}(py\text{-}4\text{-}COOH)\text{-}Cl](PF_6)$ can be determined as 0.387V vs Ag/AgCl.

Although no value has previously been assigned to the tetrazine ligand synthesised in this research programme, values can be estimated. From a plot of observed electrode potentials (E_{obs}) versus calculated electrode potentials (E_L) for over 100 mixed ligand ruthenium complexes, Lever derived the equation below:

$$E_{obs}\ (V) = 0.97[\Sigma E_L] + 0.04 \qquad (3)$$

The E_{obs} values observed for the three ruthenium complexes reported in Table 2.4 were used in conjunction with ΣE_L and a plot of E_{obs} (V) vs ΣE_L prepared as shown in Figure 2.35.

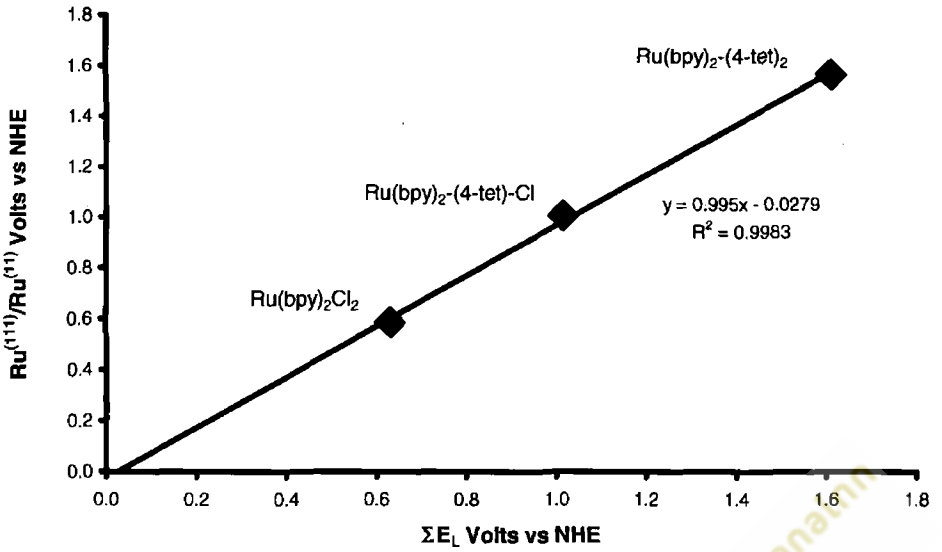

Figure 2.35. Plot of observed $Ru^{(III)}/Ru^{(II)}$ potentials for $Ru(bpy)_2Cl_2$, $Ru(bpy)_2$-(4-tet)-Cl and $Ru(bpy)_2$-$(4\text{-tet})_2$ against the ΣE_L. All data is versus the NHE.

The best fit line through the data points for the ruthenium complex with no tetrazine attached, one tetrazine ligand attached and two tetrazine ligands attached produced a best fit line with a slope similar to that given in equation (3).

Since ΣE_L values are known and values for all the attached ligands apart from tetrazine are known, assignment of a value of 0.264V for the tetrazine ligand was determined. The theoretical value for the redox potential (P_L) of the tetrazine ligand (Table 2.4) can then be determined from the E_L value using a previously established correlation (equation 2) between these two parameters [68].

$$P_L\,(V) = 1.17E_L - 0.86 \qquad (4)$$

The theoretical redox potentials calculated using this method for all the synthesised complexes and the tetrazine ligand are provided in Table 2.4.

Analysis of each complex by HPLC, with the exception of the di-substituted $Ru(bpy)_2(4\text{-tetrazine})_2(PF_6)_2$, showed a single chromatographic peak suggesting the

presence of a single product. The di-substituted complex yielded a major peak at 3.98 min and two other much smaller peaks close to the retention times for the monosubstituted product (Figure 2.27). Cyclic voltammetry of this complex revealed only one redox peak at a potential typical of a di-substituted ruthenium bipyridyl complex (E^0 = 1.36 V) with no voltammetric peak in the region expected for the monosubstituted ruthenium bipyridyl complex (Figure 2.36).

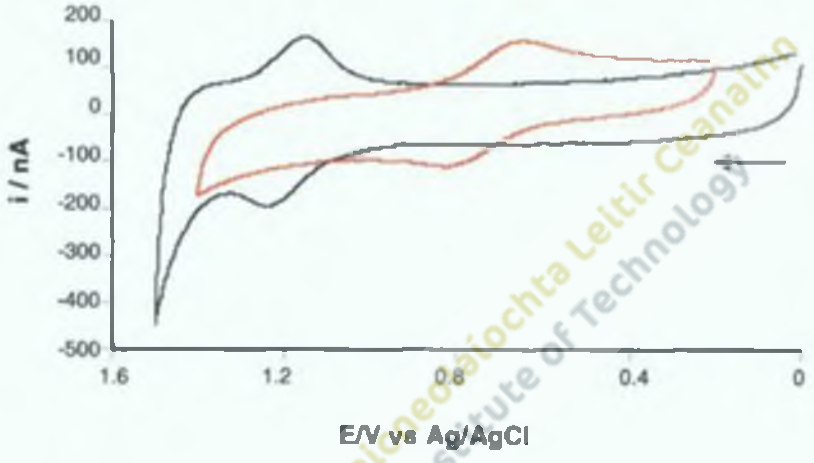

Figure 2.36. Cyclic voltammograms of $Ru(bpy)_2(4\text{-tetrazine})_2(PF_6)_2$ (—) and $[Ru(bpy)_2(4\text{-tetrazine})\text{-}Cl](PF_6)$ (—) overlaid.

There are several explanations as to why impurities were detected by HPLC and yet were not recorded by cyclic voltammetry. The concentration of the impurities may be below the detection limit of cyclic voltammetry and yet still be present in sufficient quantities to produce chromatographic peaks by HPLC. Another possibility to explain the absence in the voltammogram might be that the compounds recorded as impurities by HPLC were not electroactive and hence were not recorded as present in the voltammogram. Additional support for the hypothesis that impurities were present in this complex was provided by the difference between the theoretical and the measured CHN microanalysis data reported in Table 2.3.

2.3. References

1. Wightman, R.M., Amatore, C., Engstrom, R.C., Hale, P.D., Kristensen, E.W., Kuhr, W.G., May, L.G. *Neuroscience*, 1988, 25, 513.
2. Forster, R.J. *Chem. Soc. Review*, 1994, 289.
3. Stulik, K. *Pure and Applied Chemistry*, 2000, 72, 1483-1492.
4. Watkins, J.J., Chen, J., White, H.S., Abruña, H.D., Maisonhaute, E., Amatore, C. *Anal. Chem.*, 2003, 75, 3962-3971.
5. Diao, G., Zhang, Z. *J. Electroanal. Chem.*, 1996, 410, 155-162.
6. Benlotti, M., Pletcher, D., Braz, J. *Chem. Soc.*, 1997, 8, 391-395.
7. White, J.G., Jorgenson, J.W. *Anal. Chem.*, 1986, 58, 293.
8. Amatore, C., Bouret, Y., Maisonhaute, E., Abruña, H.D., Goldsmith, J.L. *C. R. Chimie*, 2003, 6, 99-115.
9. Baranski, A.S. *J. Electroanal. Chem.*, 1991, 300, 309.
10. Winkler, K., Baranski, A.S. *J. Electroanal. Chem.*, 1993, 346, 197.
11. Caruana, D.J., Bannister, J.V. *J. Electroanal. Chem.*, 1997, 424, 197-205.
12. Morris, R.B., Franta, D.J., White, H.S. *J. Phys. Chem.*, 1987, 91, 3559-3564.
13. Pendly, B.D., Abruña, H.D. *Anal. Chem.*, 1990, 62, 782-784.
14. Cardwell, J., Mocak, T.J., Santos, J.H., Bond, A.M. *Analyst*, 1996, 121, 357.
15. Woods, R. Chemisorption at electrodes. In: *Electroanalytical Chemistry*, A.J. Bard (Ed.), Marcel Dekker, New York, 1976, 9, 1.
16. Michri, A.A., Pshchenichnikov, A., Burshtein, R. *Kh. Elektrokhimiya.*, 1972, 8, 364.
17. Trassatti, S., Petrii, O.A. *Pure and Applied Chem.*, 1991, 63, 1-734.
18. Richardson, J.N., Rowe, G.K., Carter, M.T., Tender, L.M., Curtin, L.S., Peck, S.R., Murray, R.W. *Electrochimica acta*. 1995, 40, 1331-1338.
19. Frumkin, A.N. *Advances in electrochemistry and electrochemical engineering*. Volume 3. Wiley Interscience, New York 1963.
20. Gordon, E. Papers on soldering, *ASTM special publications*, 1962, 13.
21. Hwang, J.S. *Modern Solder Technology for Competitive Electronics Manufacturing*. McGraw-Hill, New York, 1996, page 412.
22. Menolasina, M. *Revista Technica*, 2004, 27, 26-32.
23. Farrington, A.M., Jagota, N. *Analyst*, 1994, 119, 233.

24. Malem, M., Mandler, D. *J. Electrochem. Soc.*, 1992, 139, L65.
25. Krysinski, P., Brzostowska-Smolska, M., Mazur, M. *Material Science and Engineering*, 1999, c8-9, 551-557.
26. Bettega, H.C.Y., Hissler, M., Moutet, J.C., Ziessel, R. *Chem. Mater.*, 1997, 9, 3-5.
27. Forster, R.J., Loughman, P., Keyes, T.E. *J. Am. Chem. Soc.*, 2000, 122, 11948-55.
28. Hogan, C.F., Forster, R.J. *Anal. Chim. Acta*, 1999, 396, 13-21.
29. Prenkumar, P., Beng Khoo, S. *Electrochem. Comm.*, 2004, 6, 984-989.
30. Forster, R.J., Faulkner, L.R. *J. Am. Chem. Soc.*, 1994, 116, 5444-5452.
31. Forster, R.J., Kelly, J.P. *J. Phys. Chem.*, 1996, 100, 3695-3704.
32. Kavanagh, P., Leech, D. *Tetrahedron Letters*, 2004, 45, 121-123.
33. Mosurkal, R., Samuelson, L.A., Kumar, J. *Inorg. Chem.*, 2003, 42, 5450-5452.
34. Cornel, V.M., Liotta, D.C. *J. Org. Chem.*, 1998, 63, 210-216.
35. Arounaguiri, S., Maiya, B.G. *Inorg. Chem.*, 1999, 38, 842-843.
36. Sortino, S., Petralia, S., Conoci, S., Di Bella, S. *J. Am. Chem. Soc.*, 2003, 125, 1122-1123.
37. Handy, E.S., Pal, A.J., Rubner, M.F. *J. Am. Chem. Soc.*, 1999, 121, 3525.
38. Collinson, M.M., Taussig, J., Martin, S.A. *Chem. Mater.*, 1999, 11, 2594.
39. Rudmann, H., Rubner, M.F. *J. Appl. Phys.*, 2001, 90, 4338.
40. Sullivan, B.P., Salmon, D.J., Meyer, T.J. *Inorg. Chem.*, 1978, 17, 3334-3341.
41. Cameron, C.G. *Enhanced Rates of Electron Transport in Conjugated-Redox Polymer Hybrids*. PhD Thesis. Memorial University, Newfoundland. 2000
42. Forster, R.J., Keyes, T.E., Bond, A.M. *J. Phys. Chem.*, 2000, 104, 6389-6396.
43. Orgel, L.E. *J. Chem. Soc.*, 1961, 6, 3683.
44. Mayoh, B., Day, P. *Theor. Chim. Acta*, 1978, 49, 259.
45. Wacholtz, W.F., Auerbach, R.A., Schmehl, R.H. *Inorg. Chem.*, 1986, 25, 227-234.
46. Johnson, E.C., Sullivan, B.P., Salmon, D.J., Adeyemi, S.A., Meyer, T.J. *Inorg. Chem.*, 1978, 17, 2211-2215.
47. Mabrouk, P.A., Wrighton, M.S. *Inorg. Chem.*, 1986, 25, 526-531.
48. Kober, E.M., Caspar, J.V., Sullivan, B.P., Meyer, T.J. *Inorg. Chem.*, 1988, 27, 4587-4598.

49. Nakamoto, K. *J. Phys. Chem.*, 1960, 64, 1420.
50. Fergusson, J.E., Harris, G.M. *J. Chem. Soc. A*, 1966, 1293-1296.
51. Audebert, P., Sadki, S., Miomandre, F., Clavier, G., Vernières, M.C., Saoud, M., Hapiot, P. *New J. Chem.*, 2004, 28, 387-392.
52. Veening, H., Greenwood, J.M., Shanks, W.H., Willeford, B.R. *J. Chem. Soc. Chem. Comm.*, 1969, 1305.
53. O'Laughlin, J.W. *Anal. Chem.*, 1982, 54, 178-181.
54. Buchanan, B., Mc Govern, E., Harkin, P., Vos, J.G. *Inorg. Chim. Acta*, 1988, 154, 1-4.
55. Buchanan, B., Wang, R., Vos, J.G., Hage, R., Haasnoot, J. G., Reedijk, J. *Inorg. Chem.*, 1990, 29, 3263-3265.
56. Gama Sauaia, M., Tfouni, E., de Almeida Santos, R.H., de Prado, M.T., Gambardella del Lama, M.P.F.M., Guimarães, L.F., Santana da Silva, R. *Inorg. Chem. Comm.*, 2003, 6, 864-868.
57. Elytle, F., Petrosky, L.M., Carlson, L.R. *Analytica Chimica Acta*, 1971, 57, 239-247.
58. Walsh, J.L., Durham, B. *Inorg. Chem.*, 1982, 21, 329.
59. Forster, R.J., Keyes, T.E., Bond, A.M. *J. Phys. Chem. B*, 2000, 104, 6389-6396.
60. Warren, L.F., Bennet, M.S. *Inorg. Chem.*, 1976, 15, 3126.
61. Sarapu, A.C., Fenske, R.F. *Inorg. Chem.*, 1975, 14, 247-253.
62. Hogan, C.F. *Electrochemiluminescent Sensing based on Ruthenium Poly (Pyridyl) Systems*. Ph.D. Thesis. Dublin City University. 1999.
63. Forster, R.J., Keyes, T.E., Bond, A.M. *J. Phys. Chem. B*, 2000; 104, 6389-6396.
64. Loughman, J.P. *Ph.D. Thesis*. Dublin City University. 2001.
65. Abruña, H.D., Meyer, T.J., Murray, R.W. *Inorg. Chem.*, 1979, 18, 3233-3240.
66. Lever, A.B.P. *Inorg. Chem.*, 1990, 29, 1271-1285.
67. Matsumura-Inoue, T., Tomono, H., Kasai, M., Tominaga-Morimoto, T., Takeuchi, T., Tanabe, F. *Nara Kyoiku Daigaku*, 1979, 28, 51-60.
68. Armando J.L., Pombiero, A.J.L. *Inorg. Chim. Acta*, 1985, 103, 95-103

3. Electrochemistry of ruthenium and osmium complexes

3.1. Introduction

The solution phase properties of the ruthenium and osmium polypyridyl complexes were investigated using cyclic voltammetry. For an electroactive species dissolved in solution, mass transport to the electrode surface is controlled primarily by diffusion; defined as the movement of molecules or ions under the influence of a concentration gradient. The species will move from an area of high concentration to an area of low concentration until such time as the concentration is uniform. The rate of diffusion (diffusional flux) under the influence of a concentration gradient, is characterised by a constant known as the diffusion co-efficient. Cyclic voltammetry is widely used to determine diffusion co-efficients of redox species by performing heterogeneous electron transfer reactions using experimental conditions where the rate of electron transfer is controlled by the diffusional mass transfer of the redox species to the electrode surface. In this study all diffusion co-efficients were determined using a glassy carbon electrode as the working electrode and scan rates ranging between 0.05 V s^{-1} and 10 V s^{-1}. Between these scan rates the peak to peak separation remained constant and the peak current for the anodic and cathodic currents scaled linearly with the square root of the scan rate as expected for a species under diffusion control.

The electron transfer rate constant can be estimated by a number of electrochemical techniques including cyclic voltammetry [1], square wave voltammetry [2] and chronamperometry [3]. In this study the standard rate constants for the solution phase reactants were determined by cyclic voltammetry. From the voltammograms, equations derived by Laviron where the difference (ΔE_p) between the anodic and cathodic peak were used to calculate the standard rate constant (k^o) and the transfer co-efficient (α), the relative error in ΔE_p can be determined from slopes of the graph of ΔE_p vs. ln scan rate (V s^{-1}). With increasing scan rate the point is reached where the time scale of the experiment and the rate of electron transfer become comparable, with the result that the

separation between the anodic and cathodic peak becomes larger. At higher scan rates the effect of ohmic loss on ΔE_p must be determined to allow calculation of meaningful rate constants. Although these effects were minimised by using a sufficiently high concentration of supporting electrolyte and using a 12.5 μm radius platinum microelectrode, the contribution due to ohmic loss was compensated using the CH 606 iR compensation option.

In addition to solution phase studies, electrochemical properties of redox molecules can also be investigated when immobilised on electrode surfaces. Adsorption and desorption of these monolayers has been the focus of many studies over the last number of years. The formation of alkanethiols on gold has been the most popular choice for the study of self-assembled monolayers [4-10]. Osmium and ruthenium polypyridyl complexes that contain a pyridine ligand are capable of surface attachment to clean polycrystalline platinum surfaces through the pendant nitrogen of the pyridine. Monolayers that incorporate a redox active metal centre that is stable in more than one oxidation state have the potential to make a significant contribution in the field of molecular electronics, optical devices and sensors, since the oxidation state can be reversibly switched by simply changing the applied potential of the electrode [11].

To be useful in sensor applications in the real world, it is essential that monolayers of these redox molecules can be immobilised in a reproducible fashion. For this to be possible, the factors which affect their formation including the concentration and time in the deposition solution, pH, electrolyte concentration and possibly the potential of the electrode during deposition must be fully understood. The formation of monomolecular layers of ruthenium and osmium complexes has been the focus of such studies in recent times [12-18]. These complexes have the general formula $Ru(bpy)_2(L)Cl$ or $Ru(bpy)_2(L_2)$ where bpy is bipyridyl and L is a ligand with a pendant pyridine group that spontaneously adsorbs to platinum or gold substrates when immersed in solvents in which the complex is dissolved.

Abruña and co-workers performed detailed studies of the adsorption of osmium complexes from aqueous solutions of 0.1M $KClO_4$ using cyclic voltammetry. The effects of different concentrations of the complex and the applied potential during adsorption on the progress of monolayer formation were investigated *in-situ*. This was possible since the concentrations of the complex in the deposition solution were in the micromolar range and therefore the contribution from the species in solution, in relation to the overall current, was negligible [19, 20].

Adsorption of both osmium and ruthenium complexes onto a freshly cleaned and polished platinum microelectrode were investigated in this research. Adsorption occurred through the nitrogen of the pendant pyridine group of the ligand not attached to the metal. Since the monolayer being deposited contained an electroactive metal centre, progress could be monitored in real time and non-invasively. Where the electrochemical area of the electrode used is accurately known, the surface coverage (Γ) can be determined from the area of the voltammetric peak using the equation below as discussed previously in Chapter 1.

$$\Gamma = \frac{Q}{nFA} \qquad (1)$$

Previous studies have shown that the composition of the deposition solution and the immersion time can influence the surface coverage for self-assembled monolayers [21, 22]. The equilibrium surface coverage is dependant on the concentration of the complex in the deposition solution, however the kinetics of adsorption are only marginally affected, even if the concentration is decreased significantly. Thus changes in the rate constant over a range of concentrations have been shown to be insignificant, more ordered monolayers being achieved from solutions where the adsorbate is in the micromolar range [23, 24].

Abruña and Bretz [25] demonstrated that the amount of material deposited on the working electrode varied with the applied potential during deposition. At potentials negative of the potential of zero charge (EPZC) for the metal electrode, the amount deposited is

dependant on the applied potential, whilst at potentials positive of EPZC the amount deposited is much less and is independent of the applied potential. These potentials of zero charge were determined by varying the applied potential while depositing charged osmium complexes and noting the potential where a distinct change occurred in the amount of material deposited.

The choice of solvent can also have a significant effect on monolayer formation. To become adsorbed a species in solution must first displace from the electrode surface any pre-adsorbed solvent molecules or ions present in the solution. Therefore adsorption can be regarded as a competition for available binding sites between solvent, ions and adsorbate as expressed in equation 2, where A represents the adsorbate and S represents both solvent and ions present [26].

$$A_{(sol)} + S_{(ads)} \rightleftharpoons A_{(ads)} + S_{(sol)} \qquad (2)$$

In general terms adsorption of organic compounds in non-aqueous solvents is much weaker than in aqueous solvents [27]. Studies have shown that non-aqueous solvents such as acetonitrile and DMSO interact very strongly with platinum surfaces [28, 29]. Aqueous solvents in which complexes are not readily soluble, together with the fact that adsorption of the solvent to the electrode surface is weaker, results in a higher free energy yielding a higher surface coverage for a given concentration.

The adsorption of three complexes $[Os(bpy)_2\text{-}(4\text{-tet})\text{-}Cl](PF_6)$, $[Ru(bpy)_2\text{-}(4\text{-tet})\text{-}Cl](PF_6)$ and $[Ru(bpy)_2\text{-}(4\text{-tet})_2](PF_6)_2$ at concentrations ranging from 30-400 μM from acetone/water (50/50, v/v) was investigated in this research programme. Monolayer formation was monitored in real time and non-invasively by cyclic voltammetry.

As described in Chapter 1 the peak current for a monolayer is directly proportional to the scan rate as shown in equation 3:

$$Ip = \frac{n^2 F^2}{4RT} \Gamma v A \tag{3}$$

However for a species in solution it is proportional to the square root of the scan rate as shown in equation 4:

$$Ip = (2.69 \times 10^5) n^{\frac{3}{2}} A D^{\frac{1}{2}} v^{\frac{1}{2}} C \tag{4}$$

Therefore for relatively low concentrations in the micromolar range, as the scan rate is increased the contribution to the overall current from the species in solution becomes less and less (Figure 3.1).

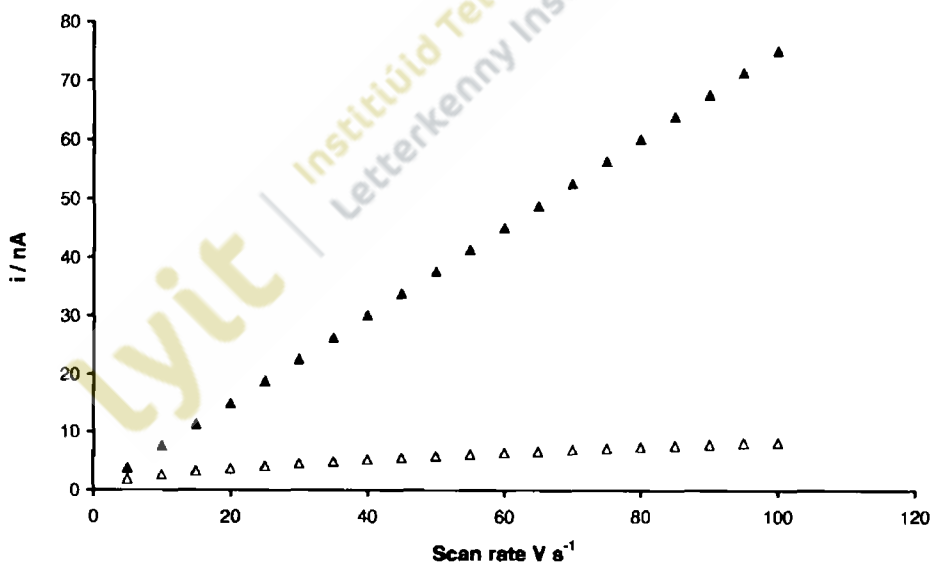

Figure 3.1. Theoretical peak current vs. scan rate for a 300 μM solution of $[Os(bpy)_2\text{-}(4\text{-}tet)\text{-}Cl](PF_6)$(Δ) and a monolayer of the same complex (▲). The data was calculated for a 12.5 μm radius electrode with a surface roughness factor of 1.8. The diffusion co-efficient of $[Os(bpy)_2\text{-}(4\text{-}tet)\text{-}Cl](PF_6)$ was calculated as 1.64 x 10^{-6} cm^2 s^{-1}.

All adsorption measurements in this study were performed at a scan rate of 100 V s^{-1}. This scan rate was selected because even at the highest concentration used the contribution to the peak current emanating from the solution phase was less than 10 % of the total current for all complexes studied. This was confirmed after each deposition experiment, where the electrode was removed from the deposition solution, rinsed thoroughly in acetone/water (50/50 v/v) and cyclic voltammograms recorded in blank electrolyte to ensure that the surface coverage determined in real time was representative of the actual surface coverage.

After adsorption, electron transfer kinetics of the complexes as self assembled monolayers on platinum microelectrodes were investigated. Self-assembled monolayers are useful systems for the study of interfacial electron transfer and provide an alternative method of examining the theories of electron transfer at electrodes since transport of the species to the electrode surface by diffusion is eliminated [8, 30, 31, 32]. The rate of electron transfer can be altered dramatically by modifying electrode surfaces with SAMs [33]. Where an electroactive molecule is immobilised on an electrode through a bridging ligand, the distance over which the electrons are transferred and hence the electron transfer rate can be controlled by careful selection of the bridging ligand itself [34, 35]. The electron transfer rates of osmium and ruthenium polypyridyl complexes have recently been studied in great detail [36, 37, 38].

For a redox species in solution, the standard heterogeneous electron transfer rate constant is designated as k_s (cm s^{-1}). When the redox species is immobilised as a monolayer on the electrode surface, the standard rate constant is described by $k_s \Gamma$ (s^{-1}). The rate of electron transfer is influenced by the nature of the working electrode, the type of redox molecule under study, as well as the electrolyte and the solvent used [39].

3.2. Methodology

Cyclic voltammetry was performed with a conventional three-electrode assembly and results recorded on a CHI Model 606A potentiostat. Working electrodes of platinum, glassy carbon, gold and indium tin oxide (ITO) were used during these investigations. A reference electrode of silver/silver chloride (Ag/AgCl) and a platinum wire counter electrode completed the three-electrode assembly. All solutions were thoroughly degassed using nitrogen before any measurements were recorded and a blanket of nitrogen maintained over the solution at all times. The direction of the scan in all cyclic voltammograms is signified by a black arrow.

3.2.1. Diffusion coefficients

Accurate weights of each complex were dissolved in acetonitrile containing 0.1 M tetrabutyl ammonium tetrafluoroborate to provide a 10 ml volume of the concentration shown in Table 3.1. Cyclic voltammograms were recorded using a 0.5 mm radius glassy carbon electrode over the range of potentials shown in Table 3.1 for each complex at scan rates from 0.05 to 10 V s^{-1}.

Metal complex	E/V range	Conc. (mM)
$[Os(bpy)_2\text{-}(4\text{-tet})\text{-}Cl](PF_6)$	-0.2 – 0.8	1.0
$[Ru(bpy)_2\text{-}(4\text{-tet})\text{-}Cl](PF_6)$	0.5 – 1.1	2.0
$[Os(bpy)_2\text{-}(py\text{-}4\text{-}COOH)\text{-}Cl](PF_6)$	-0.2 – 0.8	1.0
$[Ru(bpy)_2\text{-}(py\text{-}4\text{-}COOH)\text{-}Cl](PF_6)$	0.5 – 1.1	0.5
$Ru(bpy)_2\text{-}(4\text{-tet})_2(PF_6)_2$	0.7 – 1.7	0.5

Table 3.1. E/V range and concentration of each of the complexes under investigation.

3.2.2. Electron transfer rate constants in solution

Solutions of each of the complexes were prepared as in Section 3.2.1. Cyclic voltammograms were recorded using a 12.5 μm radius platinum microelectrode over the range of potentials shown in Table 3.1 for each complex at scan rates ranging from 1.0 to 10,000 V s^{-1}.

3.2.3. Adsorption and desorption

For all adsorption studies, the cell containing the deposition solution was covered and kept in an ice bath to prevent evaporation of the solvent and to ensure for all practical purposes that a known concentration was maintained.

For adsorption studies, concentrations of 300, 200, 100, 50 and 30 μM of each of the complexes in Table 3.2 were prepared in acetone/water (50/50 v/v). A freshly cleaned and polished platinum microelectrode of 12.5 μm radius was immersed in each solution. Cyclic voltammograms were recorded over the range of potentials shown in Table 3.2 at a scan rate of 100 V s^{-1} with 1-min intervals between each scan. After 10 min the electrode was removed from the deposition solution, rinsed in ultra pure water and cyclic voltammograms recorded at 100 V s^{-1} in blank electrolyte (0.1 M $LiClO_4$).

Metal complex	E/V range
$[Os(bpy)_2\text{-}(4\text{-tet})\text{-}Cl](PF_6)$	-0.2 – 0.8
$[Ru(bpy)_2\text{-}(4\text{-tet})\text{-}Cl](PF_6)$	0.3 – 1.2
$Ru(bpy)_2\text{-}(4\text{-tet})_2(PF_6)_2$	0.7 – 1.7

Table 3.2. E/V range for each of the complexes under investigation.

For follow-on desorption studies, platinum microelectrodes modified with a self-assembled monolayer of each complex were placed in blank electrolyte (0.1 M $LiClO_4$). Cyclic voltammograms were recorded over a six-hour period at 10 min intervals over the range of potentials shown in Table 3.2 for each complex and at a scan rate of 100 V s^{-1}. The rate of desorption was calculated from the surface coverage determined from the area under the voltammetric peak

Formation of self-assembled monolayers of $[Os(bpy)_2$-(pyridine-4-COOH)-Cl] or $[Ru(bpy)_2$-(pyridine-4-COOH)-Cl] by spontaneous adsorption on platinum microelectrodes or alternatively on gold electrodes proved unsuccessful. Monolayers of these complexes on gold electrodes were achieved using a two-step assembly as outlined below and reported in the literature [40, 41, 42, 43, 44]. Gold electrodes (1mm rad.) were prepared by successive polishing with 12, 5, 1, 0.3 and 0.05 μm alumina. Carryover of polishing material between each step was avoided by sonication for 3 min in ultra pure water. Electrodes were then electrochemically cleaned in 0.5 M H_2SO_4.

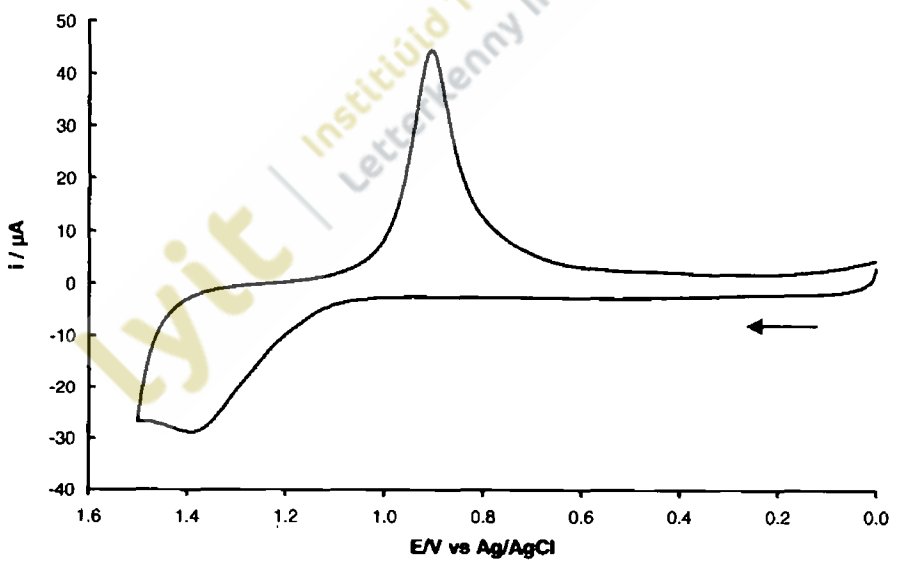

Figure 3.2. Cyclic voltammogram for a 1 mm rad. gold electrode immersed in 0.5 M H_2SO_4. Potential limits 0 to 1.5 V and scan rate 0.1 V s^{-1}. The area under the oxide reduction peak was used to calculate the electrochemical area of the electrode.

Using Figure 3.2 as an example of a typical cyclic voltammogram for a clean gold electrode, the area under the reduction peak was determined as 3.08 x 10^{-5} cm^2. Applying the correction factor of 390 $\mu C\ cm^{-2}$ for gold the electrochemical area of the electrode was calculated as 0.079 cm^2 [45].

For adsorption of either complex by the two-step assembly process, the cleaned gold electrode was immersed in 1 mM cysteamine for 12 hr, washed in ultra pure water and immersed overnight in a 1 mM solution of the complex in acetone/water (50/50 v/v) in the presence of 1-ethyl-3-(3-dimethyaminopropyl) carbodiimide hydrochloride (EDC). After removal of the electrode from the deposition solution, it was thoroughly rinsed in ultra pure water to remove any physically adsorbed molecules. The electrode was dried under a stream of nitrogen and immersed in blank electrolyte (0.1 M $LiClO_4$). Cyclic voltammograms were recorded at various scan rates to ensure that the peak current scaled linearly with scan rate as would be expected for a surface confined species.

Spontaneous monolayer formation of $Os(bpy)_2$-(pyridine-4-COOH)-Cl, although unsuccessful on platinum or gold, was achieved on an indium tin oxide (ITO) slide. Slides for adsorption were cleaned by sonication in acetone, in ethanol and in ultra pure water, with rinsing in ultra pure water between each step, and then dried in an open-ended, glass tube for 15 min using a stream of hot air (450 °C) from a heat gun. After cooling to room temperature, an area of 0.36 cm^2 was prepared as the electrode by insulating the remainder of the slide with PVC tape. The electrode was then immersed in a 1 mM solution of the complex in acetone/water (50/50 v/v) for 24 hr. After removal from the deposition solution, the electrode was rinsed thoroughly in ultra pure water to remove any physically adsorbed molecules and cyclic voltammograms recorded at various scan rates in blank electrolyte (0.1 M $LiClO_4$) to confirm monolayer formation.

In a desorption study from the ITO electrode, cyclic voltammograms in 0.1 M $LiClO_4$ were recorded at 10-min intervals using a scan rate of 1 V s^{-1} over a five-hour period. The rate of desorption was calculated from the decrease in surface coverage determined from the area under the voltammetric peak.

3.2.4. Electron transfer rate constants for monolayers

Using the platinum electrodes modified with self-assembled monolayers formed by spontaneous adsorption, cyclic voltammograms were recorded in blank electrolyte (0.1 M $LiClO_4$) over the range of potentials shown in Table 3.2 at scan rates ranging from 1-20,000 V s^{-1}. From each series of voltammograms, electron transfer rate constants were determined from the peak-to-peak separation.

3.3. Results and Discussion

3.3.1. Diffusion coefficients

Cyclic voltammograms for each complex at scan rates (v) ranging from 0.05 to 10 V s^{-1} were recorded using a 0.5 mm radius glassy carbon electrode. Examples of the voltammograms recorded for $Os(bpy)_2$-(pyridine-4-COOH)-Cl and $Ru(bpy)_2$-(pyridine-4-COOH)-Cl. are provided in Figure 3.3 and Figure 3.5 respectively. Cathodic and anodic peak currents and peak separations were determined from the cyclic voltammograms at the different scan rates for each complex. Over the range of scan rates used in this investigation separation of the anodic and cathodic peaks for each complex were less than 100 mV. Plots of i_{pa} vs. $v^{1/2}$ and i_{pc} vs. $v^{1/2}$ for all complexes were linear with excellent correlation coefficients suggesting that the process was under diffusion control. Examples of these plots and correlation coefficients are provided in Figure 3.4 for $Os(bpy)_2$-(pyridine-4-COOH)-Cl and in Figure 3.6 for $Ru(bpy)_2$-(pyridine-4-COOH)-Cl.

The slopes of the best-fit lines through the data points on graphs of i_{pa} vs. $v^{1/2}$ and i_{pc} vs. $v^{1/2}$ were used in the modified Randles-Sevcik equation to determine the diffusion coefficients for each complex.

The diffusion coefficients determined for all five complexes are provided in Table 3.3.

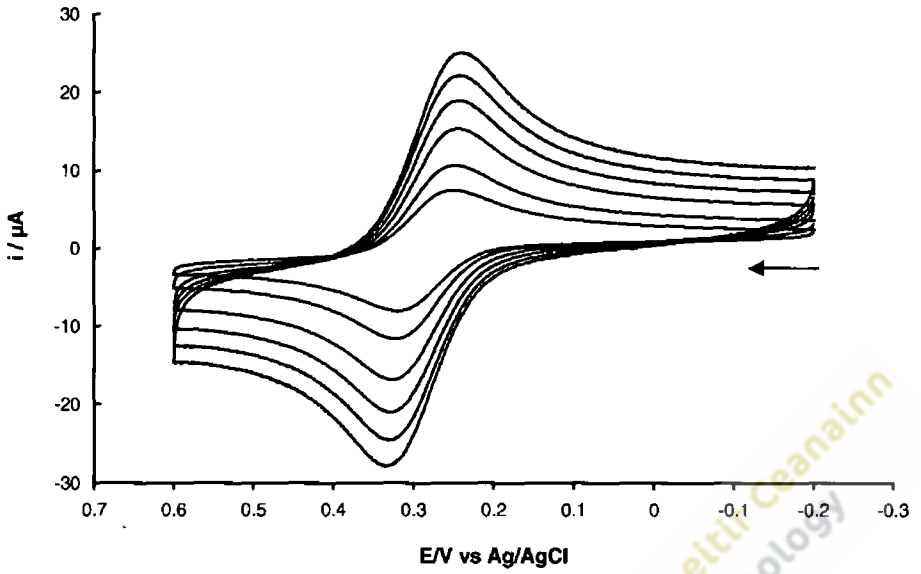

Figure 3.3. Cyclic voltammograms for a 1mM solution of $Os(bpy)_2$-(pyridine-4-COOH)-Cl in acetonitrile containing 0.1 M tetrabutyl ammonium tetrafluoroborate recorded using a 0.5 mm radius glassy carbon electrode. Scan rates 1 V s^{-1} to 10 V s^{-1}.

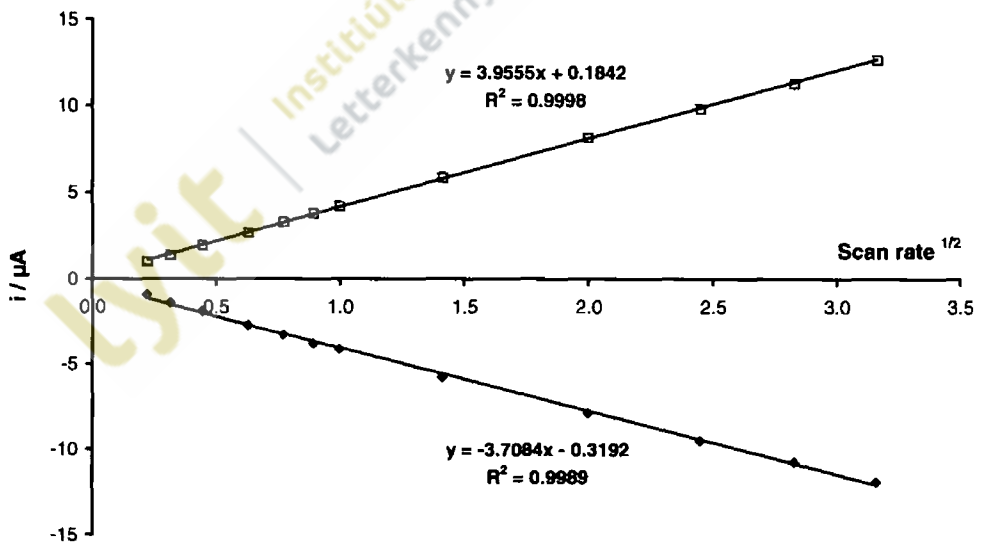

Figure 3.4. i_{pa} vs. $v^{1/2}$ and i_{pc} vs. $v^{1/2}$ plots based on data from Figure 3.3 for $Os(bpy)_2$-(pyridine-4-COOH)-Cl. Cathodic currents are shown above the *x*-axis and anodic currents below the *x*-axis.

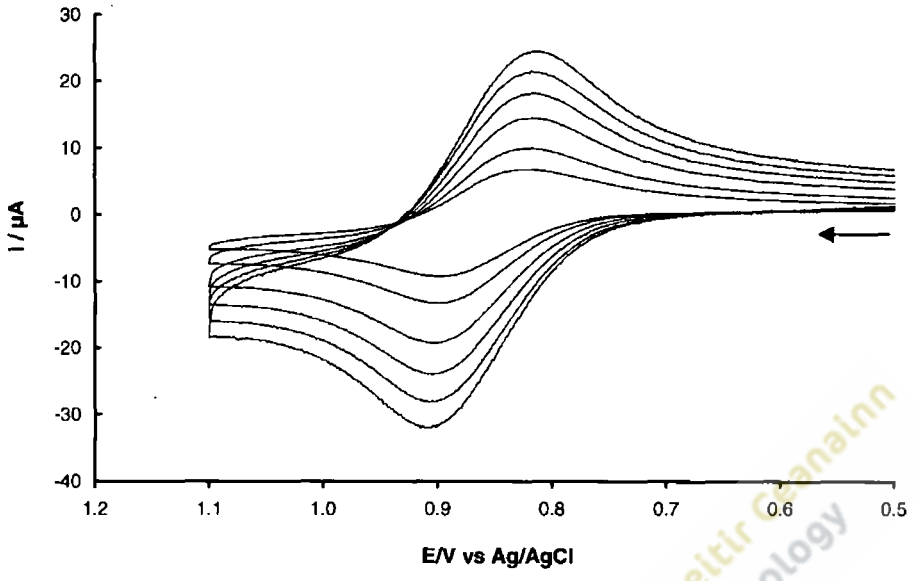

Figure 3.5. Cyclic voltammograms for a 2mM solution of $Ru(bpy)_2$-(pyridine-4-COOH)-Cl in acetonitrile containing 0.1 M tetrabutyl ammonium tetrafluoroborate recorded using a 0.5 mm radius glassy carbon electrode. Scan rates 1 V s^{-1} to 10 V s^{-1}.

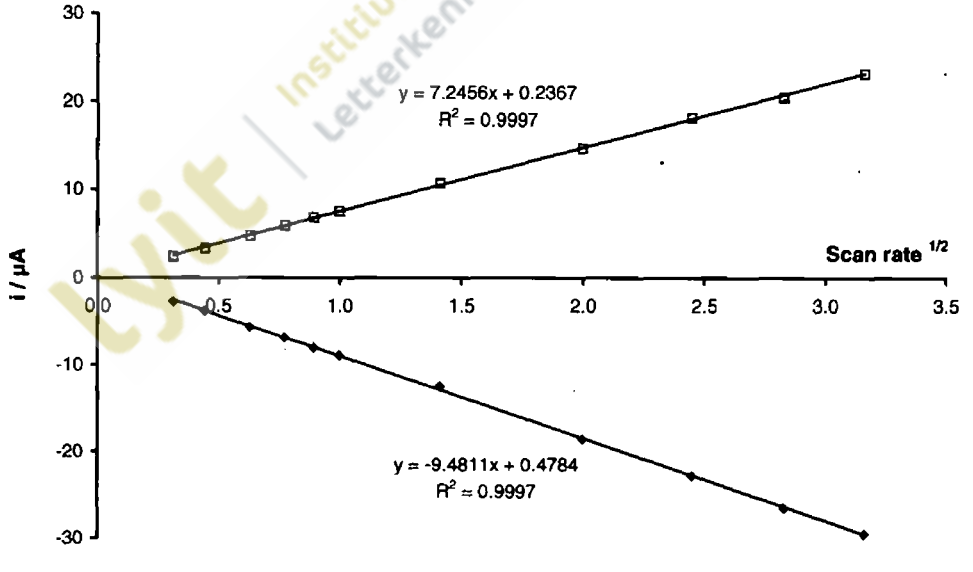

Figure 3.6. i_{pa} vs. $v^{1/2}$ and i_{pc} vs. $v^{1/2}$ plots based on data from Figure 3.5 for $Ru(bpy)_2$-(pyridine-4-COOH)-Cl. Cathodic currents are above the *x*-axis and anodic currents below the *x*-axis.

Metal complex	Diffusion coefficient ($cm^2\ s^{-1}$)
$[Os(bpy)_2$-(4-tetrazine)-Cl$](PF_6)$	1.51×10^{-6}
$[Ru(bpy)_2$-(4-tetrazine)-Cl$](PF_6)$	2.39×10^{-5}
$[Os(bpy)_2$-(pyridine-4-COOH)-Cl$](PF_6)$	3.28×10^{-6}
$[Ru(bpy)_2$-(pyridine-4-COOH)-Cl$](PF_6)$	4.76×10^{-5}
$[Ru(bpy)_2$-$(4\text{-tetrazine})_2](PF_6)_2$	3.96×10^{-5}

Table 3.3. Diffusion coefficients for the five complexes.

In electroanalytical chemistry, many techniques involve the transport of electroactive species from the bulk solution to the electrode surface; among these transport processes, diffusion is the one most often encountered. The transport properties of redox molecules are of great importance since there movement in solution must be fully understood to access their suitability for particular applications. The diffusion coefficient is a parameter expressing the transfer rate of a substance by random molecular motion. Mathematically, it is defined as the specific transfer rate, i.e. the transfer rate per unit cross-sectional area, under a unit driving concentration gradient in unit time and is expressed in $cm^2\ s^{-1}$. Many factors can affect the determination of diffusion coefficients such as the solvent used, the concentration of the diffusing electroactive species, the nature and concentration of other ionic and non ionic species present, as well as temperature, viscosity and density of the solution [46, 47]. Several electrochemical techniques can be used for measuring the diffusion coefficients of redox molecules. In this study diffusion coefficients were determined from variations in the peak current (i_p) with the scan rate (v) in a series of cyclic voltammograms at a stationary electrode. For this analysis the only other information required is the electrochemical area of the electrode used and the concentration of the material under investigation. Diffusion coefficients can also be determined by performing voltammetry at rotating disc electrodes by variation of the peak current with the rotation rate of the electrode. In addition to the information required in the previous method, knowledge of the viscosity/density of the material is also required with this technique. Although both of these techniques are

conventional electrochemical measurements, both are indirect measurements of transport, since in fact what is being measured is the current generated due to electron transfer. For this reason it essential to consider the possibility that some of the measured current may not be due to diffusional transport but may have arisen from charging of the electrode double layer. Further, there is also the possibility that adsorption of material onto the electrode surface during measurement may lead to enhanced or diminished currents depending on the type of substance adsorbed, the timescale of the experiment or the concentration of electroactive species present. The magnitude of the faradaic current due to diffusion alone is controlled by the rate at which the reactant in the electrochemical process moves towards the electrode/solution interface. As described in Section 3.1 in solution phase electrochemical measurements where diffusion is solely responsible for transport, the peak current should scale linearly with the square root of the scan rate according to equation 4.

In this investigation there was negligible deviation from this relationship ($R^2 > 0.99$) indicating that over the range of scan rates used the process was under diffusion control. Adsorption of material onto the electrode surface was deemed to be minimal since for adsorbed species peak current scales linearly with scan rate [11]. The use of platinum or gold electrodes where fast adsorption of pyridine-type molecules has been widely reported was avoided in this investigation and all diffusion coefficients were determined using glassy carbon electrodes where adsorption of these types of complexes was not anticipated to any significant degree.

The separation of the anodic and cathodic peaks for all complexes was less than 100 mV, somewhat greater than the theoretical value of approximately 60 mV, and remained constant over the range of scan rates used. The slopes of the cathodic and anodic currents vs. the square roots of the scan rate were in good agreement. These two characteristics demonstrated that electron transfer was fast and reversible over the range of scan rates used and that ohmic effects were not a factor in diffusion of the electroactive species to the electrode surface.

In all instances and under identical conditions, diffusion coefficients were greater for ruthenium complexes than for osmium complexes even when the same ligands were attached to the metal centre. Diffusion coefficients have been reported to decrease as the physical size of the molecule increases, however, both the osmium and ruthenium centres have a similar physical size and hence this is unlikely to be the cause of the differences recorded [48]. The osmium metal centre has a greater mass than ruthenium but there is no evidence in the literature to suggest that this would affect the transport of molecules by diffusion. Similar findings where ruthenium complexes have been shown to have higher diffusion coefficients than osmium complexes have been reported previously [49]. A range of diffusion coefficients for similar sizes and types of transition metal complexes are provided in Table 3.4.

Metal complex	Diffusion coefficient ($cm^2\ s^{-1}$)
$Os(bpy)_3$	3.90×10^{-6}
$Ru(bpy)_3$	2.39×10^{-5}
$Os(bpy)_2(p_3p)_2$	5.40×10^{-6}
$Ru(bpy)_2(Qbpy)$	6.80×10^{-6}
$Co(phen)_3$	3.76×10^{-5}
$Fe(bpy)_3$	2.80×10^{-6}
$Fe(phen)_3$	4.90×10^{-6}
Ferrocene	7.71×10^{-6}
Ferrocyanide	2.40×10^{-5}

Table 3.4. Diffusion coefficients for similar complexes [47, 48, 50-54].

The diffusion coefficients recorded in this study are within the range for similar complexes reported in the literature. One possible explanation for the slower diffusion of the osmium complexes might be that greater interaction occurs with either the solvent or the electrolyte ions causing solvent drag which results in slower transport to the electrode surface.

3.3.2. Electron transfer rate constants in solution

The electron transfer rate constant for each complex dissolved in solution was determined by the Laviron method. From a series of voltammograms at increasing scan rates, the peak-to-peak separation (ΔE) was plotted against ln v for each complex. An example of the voltammograms obtained with $Ru(bpy)_2$-(pyridine-4-COOH)-Cl is provided in Figure 3.7 together with a corresponding plot of ΔE against ln v in Figure 3.8.

The heterogeneous electron transfer rate constant (k^o) can be determined from the slope of the graph using equation 5 as explained in Chapter 1.

$$k^o = 2.18\left(\frac{DnF}{RT}\right)^{1/2}(\alpha v)^{1/2}\exp\left(\frac{-\alpha^2 nF\Delta E}{RT}\right) \qquad (5)$$

The electron transfer rate constant for redox processes is affected by changes in the electrode potential because the activation free energy for oxidation and reduction is altered by the applied voltage as shown in equation 6:

$$\Delta G'_{ox} = \Delta G' - (1-\alpha)FV \quad \text{and} \quad \Delta G'_{red} = \Delta G' + \alpha FV \qquad (6)$$

where $\Delta G'_{ox}$ = activation free energy for oxidation, $\Delta G'_{red}$ = activation free energy for reduction, $\Delta G'$ = activation free energy and V = voltage.

The parameter α is known as the transfer coefficient and would ideally have a value of 0.5 indicating that the transition state will occur midway between the reactants and the products response to the applied voltage. Experimentally this seldom occurs however, $\alpha_{anodic} + \alpha_{cathodic}$ will always equal 1 [55].

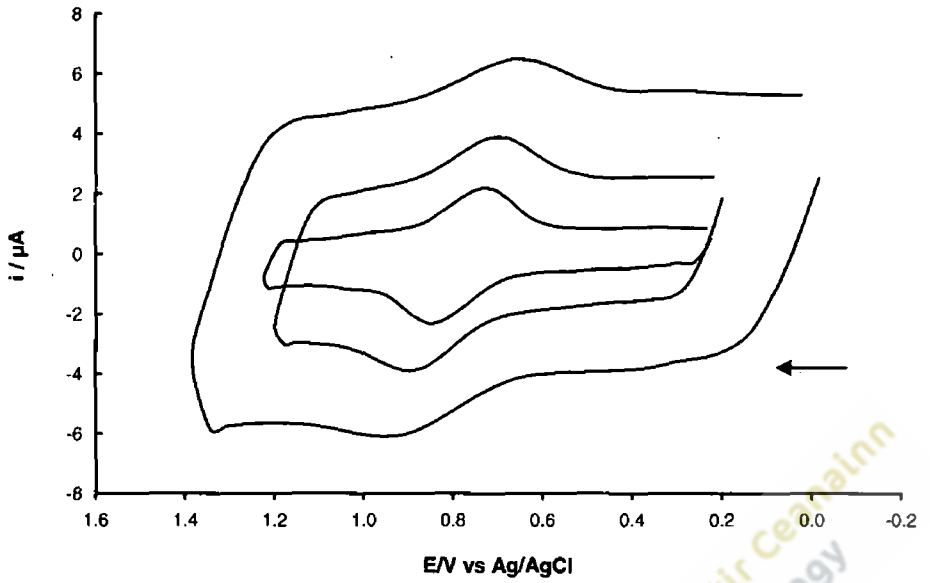

Figure 3.7. Cyclic voltammograms for a 0.5 mM solution of $Ru(bpy)_2$-(pyridine-4-COOH)-Cl in acetonitrile containing 0.1 M tetrabutyl ammonium tetrafluoroborate (TBATF) recorded using a 12.5 µm radius Pt microelectrode. Cathodic currents are up and anodic currents are down. Scan rates from top to bottom on the cathodic side are 20,000, 10,000 and 5000 V s^{-1}.

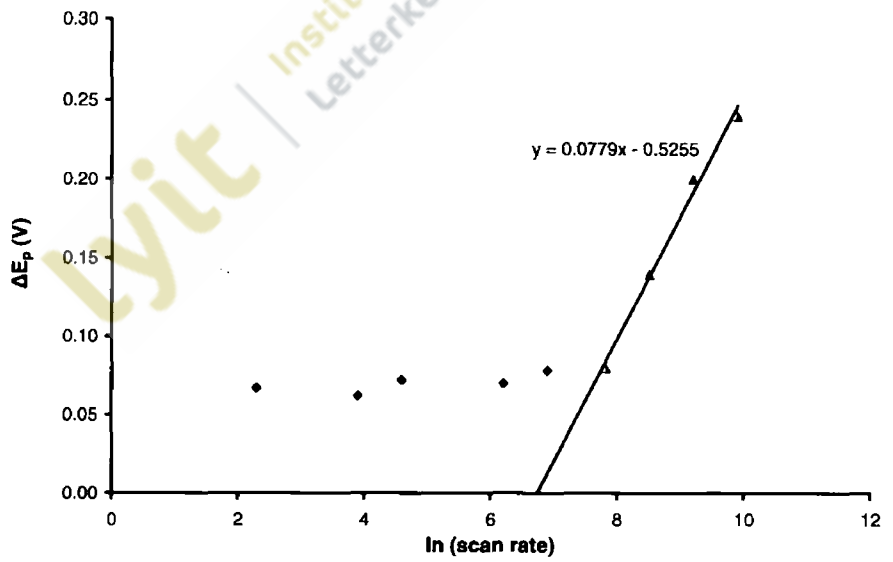

Figure 3.8. Laviron method for determination of the electron transfer rate constant for a 0.5 mM solution of $Ru(bpy)_2$-(pyridine-4-COOH)-Cl in acetonitrile containing 0.1 M TBATF recorded using a 12.5 µm radius Pt microelectrode.

The separation in the potential between the anodic peak and the cathodic peak remains relatively constant at slow scan rates. When the time scale of the experiment becomes sufficiently short this separation increases exponentially with increasing scan rate. The heterogeneous electron transfer rate can then be determined for solution phase reactants from the dependence of ΔE_p on v in conjunction with the Laviron equation [56] shown in equation 7:

$$k^o_{soln} = 2.18(D\alpha nFv)^{1/2} \exp(-\alpha nF(E_{pa}-E_{pc})/RT) \quad (7)$$

where D is the diffusion coefficient, α the transfer coefficient, n the number of electrons transferred, F the Faraday constant, E_{pa} and E_{pc} are the anodic and cathodic peak potentials, R the real time constant and T is the temperature.

When a current is flowing in an electrochemical cell there is a drop in potential between the reference electrode and the working electrode. For meaningful results, it is necessary to determine if this voltage drop is significant with respect to the overall result. Using Ohms law the voltage drop can be calculated and is equal to the product of the current (i) and the resistance (R_Ω) as shown in equation 8:

$$\Delta E_{ohmic} = i \times R_\Omega \quad (8)$$

where ΔE_{ohmic} is the ohmic or iR drop, i the current and R_Ω is the ohmic resistance.

In this study iR compensation was achieved by measuring the specific conductance of the electrolyte under identical conditions to that used for the experimental electrochemical measurements and from this the resistance of the cell (R) determined by equation 9:

$$R = \frac{1}{4\pi\kappa r_o} \quad (9)$$

where k is the specific conductance and r_o is the electrode radius.

The specific conductance of the solvent (0.1 M TBATF in acetonitrile) was determined as 10.21 mS cm^{-1} and approximated to 0.01 mho cm^{-1}. Using equation 9 and a 12.5 μm radius platinum microelectrode, the resistance for the cell was calculated as 6369 ohms. This resistance was entered into the iR compensation mechanism of the CHI workstation.

From Figure 3.8, it can be seen that a best-fit straight line was plotted through the data points from the point where ΔE_p increases. The slope and intercept of this straight line was then used with a rearrangement of the Laviron equation as shown in equation 10:

$$k^{\circ}_{soln} = 2.18\exp\left[\frac{Intercept}{2}\right]\left[\frac{D}{2\alpha Slope}\right]^{1/2} \qquad (10)$$

Equation (7) was used to determine the standard electron transfer rate constant (k°) and the transfer coefficient (α) for the different complexes. A summary of the heterogeneous electron transfer rate constants (k°) with and without iR compensation and the transfer coefficients (α) for the five ruthenium and osmium complexes studied are shown below in Table 3.5.

Metal complex	k° ($cm.s^{-1}$) (no iR comp)	k° ($cm.s^{-1}$) (iR comp)	α (iR comp)
$[Os(bpy)_2$-(4-tetrazine)-Cl$](PF_6)$	0.26	0.29	0.47
$[Ru(bpy)_2$-(4-tetrazine)-Cl$](PF_6)$	0.70	0.93	0.50
$[Os(bpy)_2$-(pyridine-4-COOH)-Cl$](PF_6)$	0.27	0.50	0.46
$[Ru(bpy)_2$-(pyridine-4-COOH)-Cl$](PF_6)$	1.27	1.61	0.49
$Ru(bpy)_2$-$(4\text{-tetrazine})_2(PF_6)_2$	0.43	0.69	0.60

Table 3.5. Values for the heterogeneous electron transfer rate constant (k°) and the transfer coefficient (α) for the five ruthenium and osmium complexes.

The driving force for homogeneous electron transfer is dictated by the electronic nature of the reactants, whereas heterogeneous electron transfer can be controlled externally by variation of the applied potential. A problem encountered in determination of electron transfer rates is that the faradaic processes can be distorted by the effects of ohmic drop through uncompensated resistance. These distortions rapidly increase as the timescale of experiments are decreased. This has the result that ohmic effects need to be considered when sufficiently high scan rates are used, even with microelectrodes of radius 12.5 μm such as those used in the present study.

Up to scan rates of 500 V s^{-1}, iR compensation has no influence on separation of the cathodic and anodic peak (ΔE). At higher scan rates separation of the cathodic and anodic peak is reduced after iR compensation. This is illustrated below in Figure 3.9 for $Ru(bpy)_2$-$(4\text{-tet})_2$ using a scan rate of 10,000 V s^{-1}.

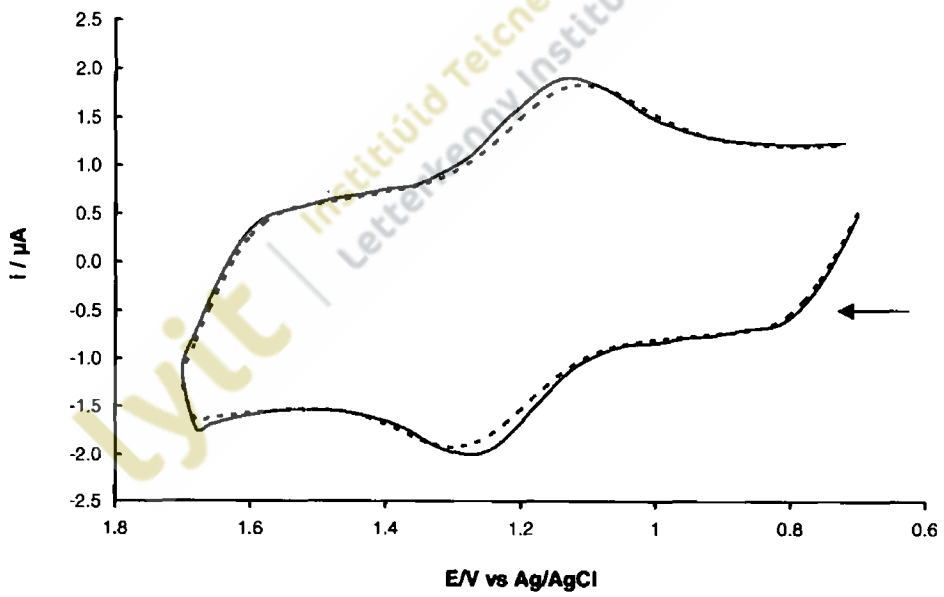

Figure 3.9. Cyclic voltammograms for a 1 mM solution of $Ru(bpy)_2$-$(4\text{-tet})_2$ in acetonitrile containing 0.1 M tetrabutyl ammonium tetrafluoroborate recorded using a 12.5 μm radius Pt microelectrode. Scan rate shown is 10,000 V s^{-1} before (---) and after (—) iR compensation.

From Table 3.5 it is apparent that for all of the complexes investigated higher values for the electron transfer rate constant were determined after iR compensation highlighting the importance of accounting for solution resistance.

Comparison of the osmium complexes with each other and the two mono-substituted ruthenium complexes with each other, demonstrated that slightly higher values were determined for the electron transfer rate constants across the carboxylic acid ligand compared to the tetrazine ligand. This may be attributed to greater separation between the redox centre and the platinum electrode occurring with the tetrazine ligand. Slightly lower values for the electron transfer rate constant of the di-substituted ruthenium compound by comparison with the analogous mono-substituted complex were recorded. For all complexes considered, higher electron transfer rate constants were reported for ruthenium complexes compared to equivalent complexes with an osmium centre.

For comparative purposes, literature values for k^o of 0.24 cm s^{-1} have been reported for $Ru(bpy)_3^{2+/3+}$ in DMF with platinum electrodes and 0.072 cm s^{-1} for ferrocene in 1 M KNO_3 with iridium electrodes [57, 58]. Wipf *et al.* in a study of ferrocene in acetonitrile reported k^o values of 3.1, 0.95 and 1.1 cm s^{-1} with gold, platinum and mercury respectively, demonstrating that the nature of the electrode can have an influence on the rate of electron transfer [51]. Comparison between reported k^o values is now accepted to be valid only if measurements are recorded under identical conditions. Factors to be considered include the solvent used, the electrode and the pH of the electrolyte solution for complexes containing ligands capable of protonation /deprotonation [52, 57-59].

Electron transfer rate constants determined for the complexes under investigation in this study exhibited only limited variation ranging from 0.29-1.61 cm s^{-1}. These constants have been reported in the literature spanning over ten orders of magnitude. Molecules that are capable of being reduced with very little change in bond angles or length have been reported to exhibit very large k^o values whilst molecules that are distorted to a large degree have been reported to have values as small as 10^{-9} cm s^{-1} [60].

Transfer coefficients (α) for the five complexes ranged from 0.46 – 0.60 with most values close to the ideal value of 0.5 indicating that the transition state occurs midway on the reaction co ordinate between the reactant and the product. Recent papers have shown that the transfer coefficient can be influenced by the ionic strength of the contacting electrolyte [61].

3.3.3. Adsorption and desorption

Adsorption results for the different osmium and ruthenium complexes under investigation in this study have been presented separately for the purposes of clarity.

Cyclic voltammograms for the adsorption of one concentration of each complex on a platinum microelectrode at a scan rate of 100 V s^{-1} with 1-min intervals between each scan have been provided. After 10 min the electrode was removed from the deposition solution, rinsed in ultra pure water and cyclic voltammograms recorded at 100 V s^{-1} in blank electrolyte (0.1 M $LiClO_4$).

Cyclic voltammograms recorded at 1-min intervals for the first five minutes during the adsorption of $[Os(bpy)_2\text{-}4\text{-}tet\text{-}Cl](PF_6)$ as an example are provided in Figure 3.10.

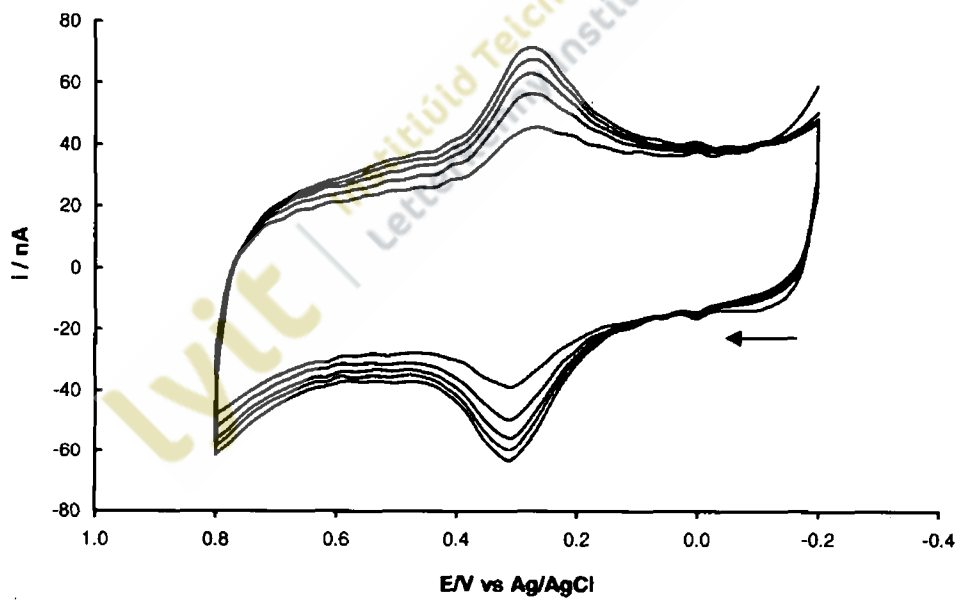

Figure 3.10. Cyclic voltammograms for the adsorption of $[Os(bpy)_2\text{-}4\text{-}tet\text{-}Cl](PF_6)]$ onto a 12.5 μm radius Pt microelectrode at different deposition times recorded in 0.1 M $LiClO_4$ electrolyte. The deposition solution contained 300 μM of the complex in acetone/water (50/50, v/v). Scan rate 100 V s^{-1}.

The series of cyclic voltammograms presented in Figure 3.10 demonstrate that as adsorption of $[Os(bpy)_2\text{-}4\text{-}tet\text{-}Cl](PF_6)]$ proceeded, so the faradaic current increased. Although surface coverage increased with time, a decrease in the double layer capacitance due to monolayer formation was not evident. Adsorption studies with similar osmium complexes have reported a significant reduction in the capacitative current as surface coverage progressed and attributed this to the displacement of solvent molecules and ions due to adsorption of the complex [11]. The absence of a decrease in capacitative current may have been due to the formation of a more porous monolayer or possibly to the fact that a tightly packed monolayer was not formed.

Other studies in the literature have reported that the $Os^{2+/3+}$ redox couple shifts to more positive potentials with increasing surface coverage. This shift was attributed to the effect of surface coverage on interactions among oxidised and reduced forms of the redox couple. According to the theory of Brown and Anson [62] the anodic and cathodic peak potential are related to the surface coverage by equation 11:

$$E_{peak} = E^0 + \left(\frac{RT}{nF}\right)(r_R - r_o)\Gamma_T \qquad (11)$$

where r_R and r_o are the interaction parameters for the reduced and oxidised forms respectively.

In this theory shifts in formal potential due to monolayer formation result in a positive shift when negative interactions are greater among the oxidised form, however these only become evident at higher surface coverages. Information about the interactions between adsorbed species, whether repulsive or attractive, can be established by examining the full width at half maximum (ΔE_{fwhm}) as discussed in Chapter 1. In circumstances where repulsive forces exist $\Delta E_{fwhm} > 90.6$ mV, whereas attractive interactions lead to $\Delta E_{fwhm} < 90.6$ mV. With the $[Os(bpy)_2\text{-}4\text{-}tet\text{-}Cl](PF_6)]$ complex, ΔE_{fwhm} was determined as 135 ± 5 mV, a value consistent with the presence of repulsive interactions between the adsorbed molecules, however the formal potential remained almost constant during monolayer

formation. The absence of a shift to a more positive formal potential with increasing surface coverage despite ΔE_{fwhm} values larger than ideal, suggests that repulsive forces amongst oxidised molecules are relatively insignificant.

Lane and Hubbard were the first to study in detail electrode reactions at a metal surface deliberately coated with an organic substance. One such study described the strong adsorption of open chain hydrocarbon (olefinic) compounds on platinum electrodes where one adsorbed carbon of the olefin interacted with one platinum [63]. Two types of adsorption are possible, physisorption and chemisorption. Physisorbed molecules are held at the surface only by weak van der Waal forces whereas in chemisorption, redox molecules are covalently bonded to the electrode surface and tethered within the double layer region allowing the mechanism of electron transfer to be probed in detail without the need for diffusion to the electrode surface [64]. The bonding of aromatic molecules on metal surfaces has also been widely studied. The $\pi - \pi^*$ orbitals of benzene have been shown to interact with metal orbitals to form a chemisorption bond [65]. Pyridine-type molecules used in the present study have been shown to be very useful molecules in the study of adsorption of transition metals due to the fact that they have distinctive molecular sites; an aromatic ring and a lone pair containing nitrogen which can co-ordinate to metal surfaces. The pyridyl moiety has been shown to bond to platinum surfaces through both the nitrogen atom and the π and π^* orbitals of the pyridine ring which can interact with the metal orbitals to form the chemisorption bond. These π and π^* orbitals have been reported to react only at low surface coverages and have been shown to adopt a flat configuration. At higher surface coverages, generally greater than 50% of a monolayer, there is conversion from the π bonded to σ-donor-type, where the adsorbing molecules adopt a vertical orientation and chemisorption occurs predominantly through the nitrogen atom [66]. The orientation of adsorbed molecules has been reported to have significant practical implications since different orientations can affect the surface coverage, oxidation/reduction processes, surface chemical reactions or heterogeneous catalysis [67].

After formation of the [Os(bpy)$_2$-4-tet-Cl](PF$_6$)] monolayer from a 300 μM deposition solution, the electrode was thoroughly rinsed in ultra pure water to remove any physically adsorbed molecules and cyclic voltammograms recorded at a range of scan rates in blank electrolyte (0.1 M $LiClO_4$). Typical cyclic voltammograms over a range of scan rates between 0.2-1 V s^{-1} for the [Os(bpy)$_2$-4-tet-Cl](PF$_6$)] monolayer are presented in Figure 3.11.

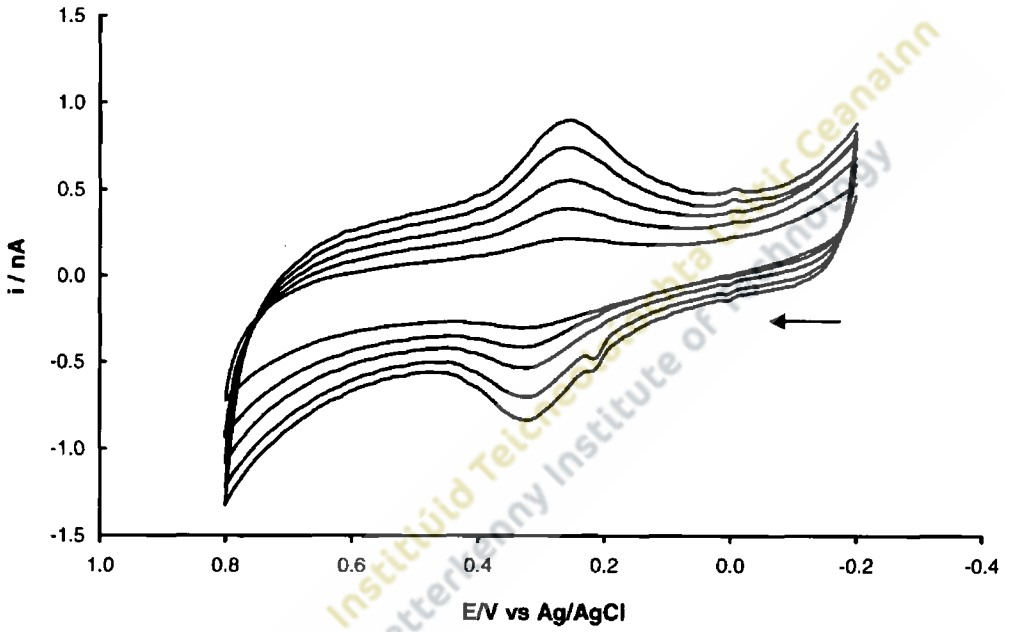

Figure 3.11. Cyclic voltammograms for the $Os^{2+/3+}$ redox reaction for a spontaneously adsorbed monolayer of [Os(bpy)$_2$-4-tet-Cl](PF$_6$) on a 12.5 μm radius Pt electrode. Scan rates from top to bottom are 1, 0.8, 0.6, 0.4, 0.2 V s^{-1}. Surface coverage was determined as 8.0 x 10^{-11} mol cm^{-2}. The supporting electrolyte was 0.1 M $LiClO_4$. The initial potential was –0.2 V and anodic currents are shown down and cathodic currents up.

The linear relationship between the peak current and the scan rate for this monolayer presented in Figure 3.12 confirmed that the osmium complex was confined to the electrode surface. The ratio of cathodic to anodic charge determined at a low scan rate of close to one confirmed that the complex could be oxidised and reduced completely.

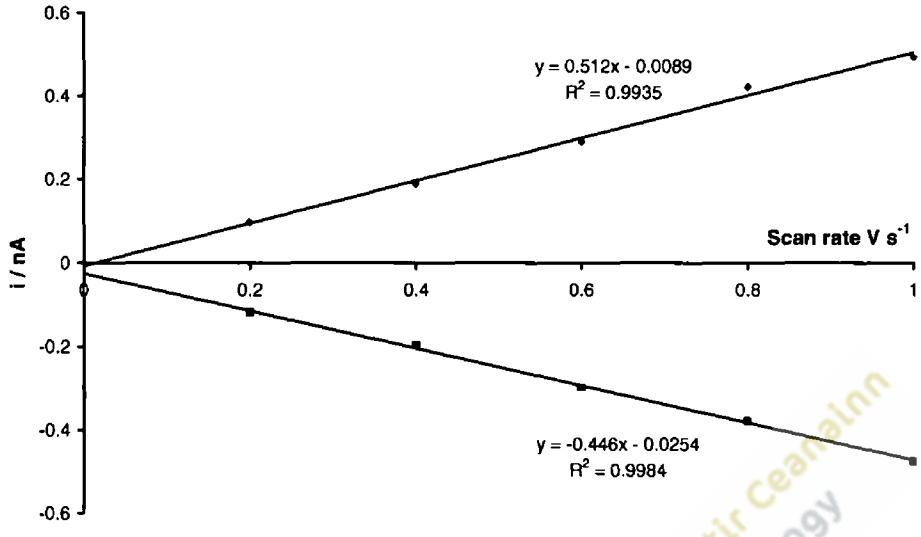

Figure 3.12. The relationship between the peak current and the scan rate determined from the voltammograms in Figure 3.11. Cathodic currents are shown above the *x*-axis and anodic currents below the *x*-axis.

Comparison of the cyclic voltammograms for $[Os(bpy)_2\text{-}4\text{-}tet\text{-}Cl](PF_6)$ after completion of 10 min in the deposition solution (acetone/water, 50/50, v/v) and in blank electrolyte (0.1 M $LiClO_4$) after rinsing in ultra pure water demonstrated the possible contribution to the charge from the complex in solution or alternatively the removal of physically-adsorbed molecules from the electrode surface (Figure 3.13). The faradaic charge was estimated from the area under the cathodic peak and together with the real surface area of the electrode used to calculate the surface coverage, or the number of moles of the complex per cm^2. Surface coverages determined in the deposition solution and in the blank electrolyte after rinsing were calculated as 1.04×10^{-10} mol cm^{-2} and 0.98×10^{-10} mol cm^{-2} respectively. The small difference between the surface coverage values confirmed that the solution phase contribution to the overall current was minimal as anticipated. Using the Avogadro constant and the surface coverage, the number of molecules per cm^2 was determined and hence the area occupied by one molecule of the complex.

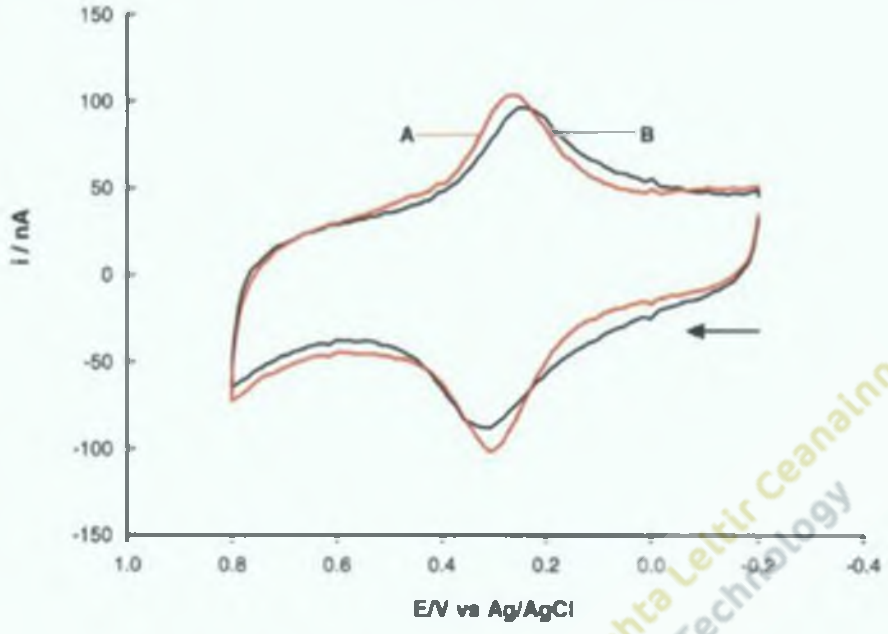

Figure 3.13. Cyclic voltammograms for $[Os(bpy)_2\text{-}4\text{-}tet\text{-}Cl](PF_6)$ after 10 min in the deposition solution (acetone/water, 50/50, v/v) (A) and in blank electrolyte (0.1 M $LiClO_4$) after removal from the deposition solution and rinsing in ultra pure water (B). The scan rate in each case was 100 V s^{-1} and the electrode used was a 12.5 μm radius Pt electrode with a surface roughness of 2.2.

From the real-time data in the deposition solution, the area occupied by one molecule was calculated as 160 $Å^2$ whereas from the slightly reduced surface coverage determined in blank electrolyte containing none of the metal complex, the area occupied by one molecule was calculated as 169 $Å^2$. This area of occupation is smaller than that found for adsorbed $[Os(bpy)_2Cl(p3p)]^+$ molecules of 240 $Å^2$ [36], closely resembles the 175 $Å^2$ determined for adsorbed $[Os(bpy)_2py(p3p)]^{2+}$ and $[Os(bpy)_2(p3p)_2]^{2+}$ molecules [13, 15] and is somewhat larger than the 140 $Å^2$ determined for $[Os(bpy)_2bptCl]^{2+}$ molecules [18]. When the additional contributions to the molecular volume are considered, e.g. a solvent shell or a counterion, this area of occupation is consistent with that expected for a close packed monolayer in which the radius of the metal complex (approximately 6.7 Å) rather than the length of the bridging ligand dictate the surface coverage [18].

The change in surface coverage (Γ) with time for deposition solutions containing 30 μM, 50 μM, 100 μM, 200 μM and 300 μM concentrations of $[Os(bpy)_2\text{-}4\text{-}tet\text{-}Cl](PF_6)$ is shown in Figure 3.14. For each concentration, surface coverage initially increased relatively rapidly and then began to slowdown.

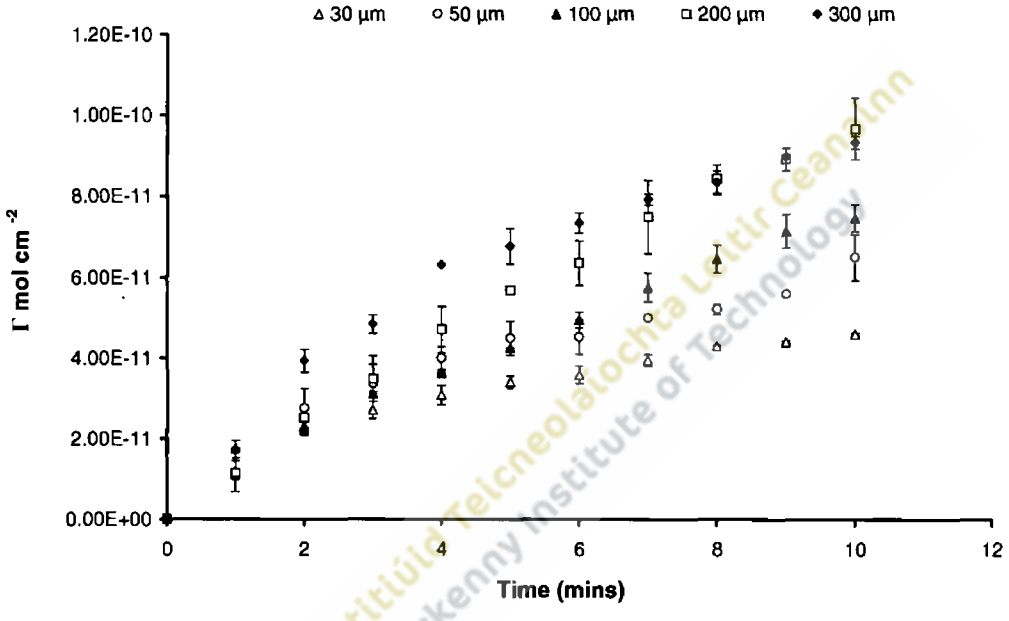

Figure 3.14. Temporal changes in the surface coverage of $[Os(bpy)_2\text{-}4\text{-}tet\text{-}Cl](PF_6)$ adsorbed on a Pt microelectrode from deposition concentrations between 30-300 μM. Error bars represent data taken from at least three independent monolayers.

An equilibrium relationship exists between the concentration of a species in solution (C*) and the concentration of the species on the electrode surface (Γ). This relationship can be described by an adsorption isotherm [68] as reported in Chapter 1. Different isotherms exist; the simplest being the Langmuir isotherm which assumes that a monolayer of adsorbate forms on the surface and describes the adsorption process when the only adsorbate-adsorbate interaction is due to size.

The Langmuir isotherm is represented by equation 12:

$$\beta C^* = \frac{\theta}{1-\theta} \tag{12}$$

where β is the adsorption coefficient and describes the relationship between the concentration in the bulk solution and the surface coverage and θ is the fractional coverage defined as Γ/Γ_s where Γ_s is the saturation surface coverage. To allow experimental data to be compared to this isotherm, values for β and Γ_s must be calculated. By mathematical rearrangement, the Langmuir isotherm can be written as shown in equation 13:

$$\frac{C^*}{\Gamma} = \frac{1}{\Gamma s \beta} + \frac{C^*}{\Gamma s} \tag{13}$$

Figure 3.15 shows a plot of C^*/Γ vs. C^* based on the experimental data with a slope of $1/\Gamma_S$ and an intercept of $1/\Gamma_S/\beta$ allowing values to be calculated for both the adsorption coefficient (β) and the saturation surface coverage (Γ_s) [20].

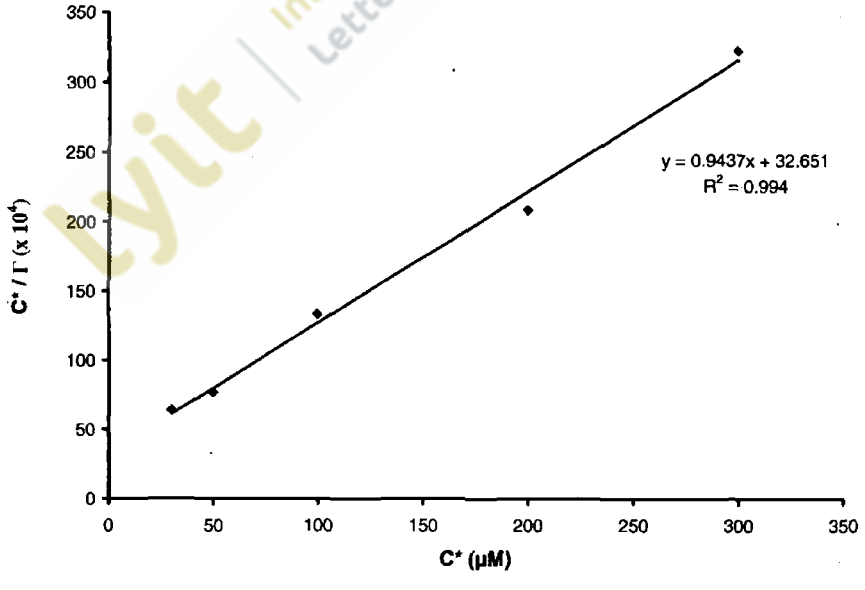

Figure 3.15. Plot of concentration of $[Os(bpy)_2\text{-}4\text{-}tet\text{-}Cl](PF_6)$ in the bulk solution vs. the concentration in the bulk solution divided by the surface coverage in mol cm^{-2}.

From the slope and intercept of Figure 3.15 values of Γ_s of 1.1 x 10^{-10} mol cm^{-2} and β of 2.67 x 10^4 M^{-1} were determined.

The saturation surface coverage (Γ_s) gives an area/molecule of approximately 160 $Å^2$ suggesting that the estimated saturation coverage is the equivalent of a full monolayer on the electrode surface. The Langmuir curve was calculated from the saturation coverage (Γ_s) and the adsorption coefficient (β) using a further rearrangement of the Langmuir isotherm shown at equation 14:

$$\Gamma = \frac{C^* \Gamma_S}{C^* + (1/\beta)} \tag{14}$$

If repulsive or attractive forces exist between the adsorbed molecules the extent of these forces can be quantified using an extension of the Langmuir isotherm proposed by Frumkin shown in equation 15:

$$\beta C = \frac{\theta}{1-\theta} \exp(g\theta) \tag{15}$$

In this equation, g is the interaction parameter. Attractive interactions are indicated by $g < 0$ and repulsive interactions by $g > 0$, while for $g = 0$ the Langmuir isotherm is obtained. Using a least squares best fit, values of g that best describe the experimental data can be determined providing an insight into the type of intermolecular interactions that exist within the system under investigation.

In Figure 3.16 the experimental data for the deposition of $[Os(bpy)_2\text{-}4\text{-}tet\text{-}Cl](PF_6)$ is shown fitted to the Langmuir isotherm and the Frumkin isotherm using an interaction parameter (g) of 0.05. Whilst the Langmuir curve exhibited a reasonable fit to the experimental data, the best fit was exhibited by the Frumkin isotherm with $g = 0.05$ suggesting that repulsive forces do exist, but to a somewhat lesser extent than those reported in the literature with similar complexes [13].

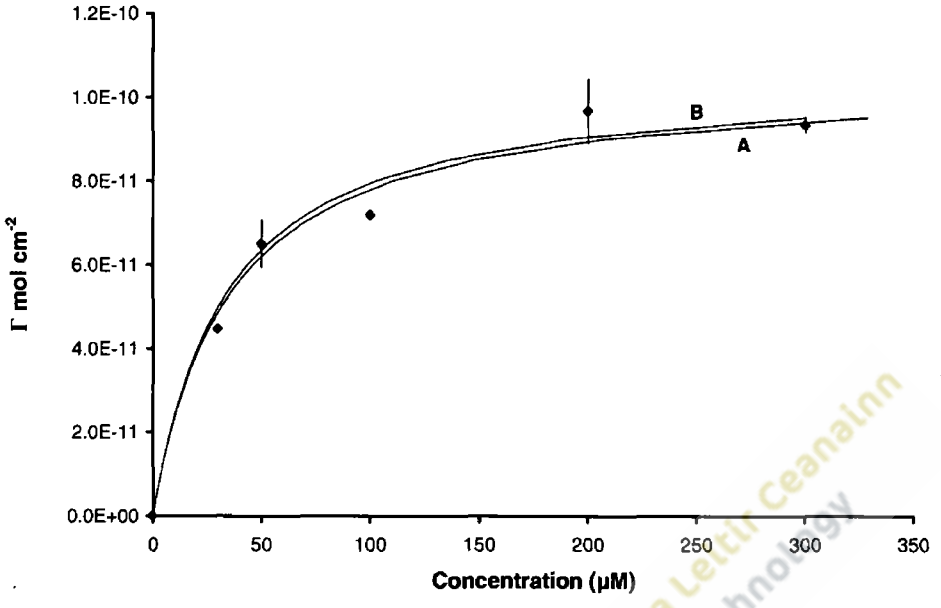

Figure 3.16. Experimental data fitted to the Langmuir isotherm, (curve A) and Frumkin isotherm with $g = 0.05$ (curve B) for the deposition of $[Os(bpy)_2\text{-}4\text{-}tet\text{-}Cl](PF_6)$.

Walsh *et al.* in an adsorption study with the same complex found that the Frumkin curve with an interaction parameter of $g = 0.1$ best described the experimental data [59]. However, monolayers in this latter study were formed by immersion in lower concentrations of the metal complex for up to 12 hr on gold electrodes and these differences may have contributed to the greater interaction parameter reported. Another difference between the two studies, in addition to the above is that voltammograms were recorded in 1 M $LiClO_4$ as compared to the 0.1 M $LiClO_4$ used in this study.

Acevedo *et al.* [19] studied the adsorption of closely related complexes and reported values for the interaction parameter (g) of 0.2 for $Os(bpy)_2$-L-Cl where L was either 1,2 bis(4-pyridyl)ethane or 1,2 bis(4-pyridyl)ethylene. Although the complex was dissolved in acetone it was diluted 10,000 fold in 0.1 M $KClO_4$ with the result that adsorption occurred from what was essentially an aqueous electrolyte solution.

Adsorption under kinetic control can be described by equation 16:

$$\theta_t = (1\text{-}\exp(-kC^*t) \qquad (16)$$

where k is the rate constant and C^* the concentration in the bulk solution.

The kinetic Langmuir equation of surface coverage with time is shown in equation 17:

$$\Gamma_t = \Gamma_e (1\text{-}\exp(k\,C^*t) \qquad (17)$$

Figure 3.17 shows the fit of the experimental data for 30 μM and 300 μM concentrations of $[Os(bpy)_2\text{-}4\text{-}tet\text{-}Cl](PF_6)$ to equation 17. There is reasonably good agreement between the experimental data and the Langmuir curve suggesting that the system is under kinetic control.

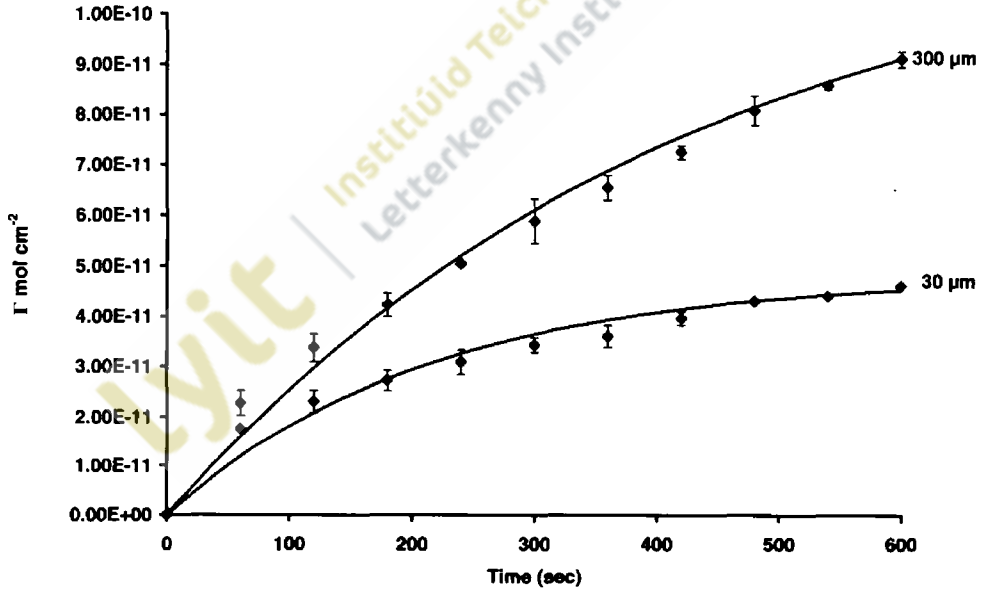

Figure 3.17. Surface coverage vs. time of $[Os(bpy)_2\text{-}4\text{-}tet\text{-}Cl](PF_6)$ adsorbed onto a Pt microelectrode. The bulk concentrations of the complex dissolved in acetone/water (50/50, v/v) are 300 μM (top) and 30 μM (bottom). The solid line represents the best fit to the Langmuir kinetic equation. Error bars represent data from three independent monolayers.

A second process, diffusion-controlled adsorption, can be described by equation 18:

$$\frac{\Gamma_t}{\Gamma_s} = k(\frac{C^*}{\Gamma_s})(Dt)^{1/2} \qquad (18)$$

Figure 3.18 shows the fit of the experimental data for 30 μM, 50 μM, 100 μM and 200 μM concentrations of $[Os(bpy)_2\text{-}4\text{-}tet\text{-}Cl](PF_6)$ to equation 18.

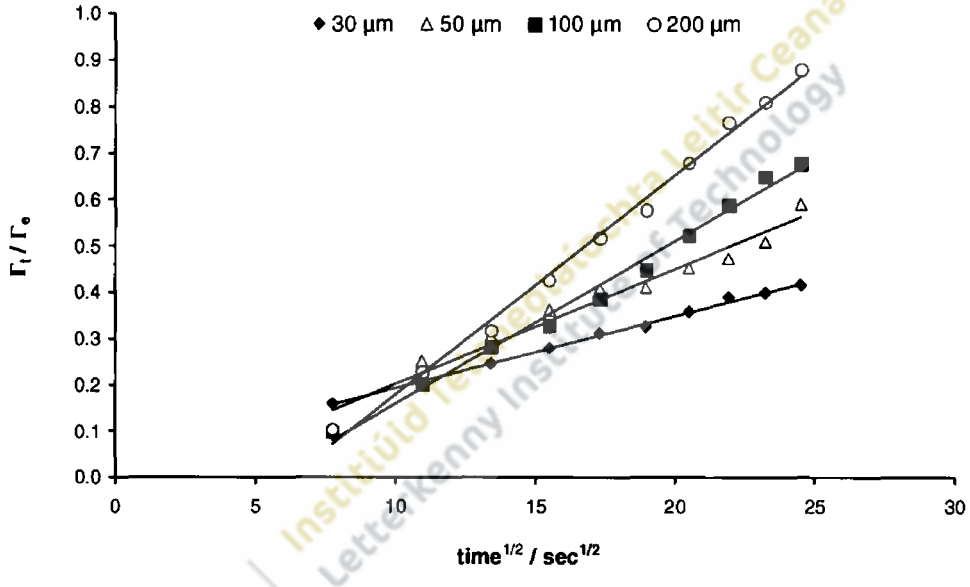

Figure 3.18. Variation of the normalised surface coverage vs. $t^{1/2}$ for $[Os(bpy)_2\text{-}4\text{-}tet\text{-}Cl](PF_6)$ at various concentrations.

At all of the concentrations investigated, linear relationships typical of adsorption under diffusion control were recorded. Since the experimental results were in agreement with both the kinetic model (Figure 3.17) and a process under diffusion control (Figure 3.18), it was necessary to establish which model best described the experimental data. This was achieved by plotting the slopes of Γ_t / Γ_s vs. $t^{1/2}$ against the concentration as shown in Figure 3.19. The best fit to the plots using the diffusion-controlled model were calculated using the slope at the lowest concentration as a reference point and calculating the slopes at all other concentrations from the ratio of C^*/ Γ_s [23].

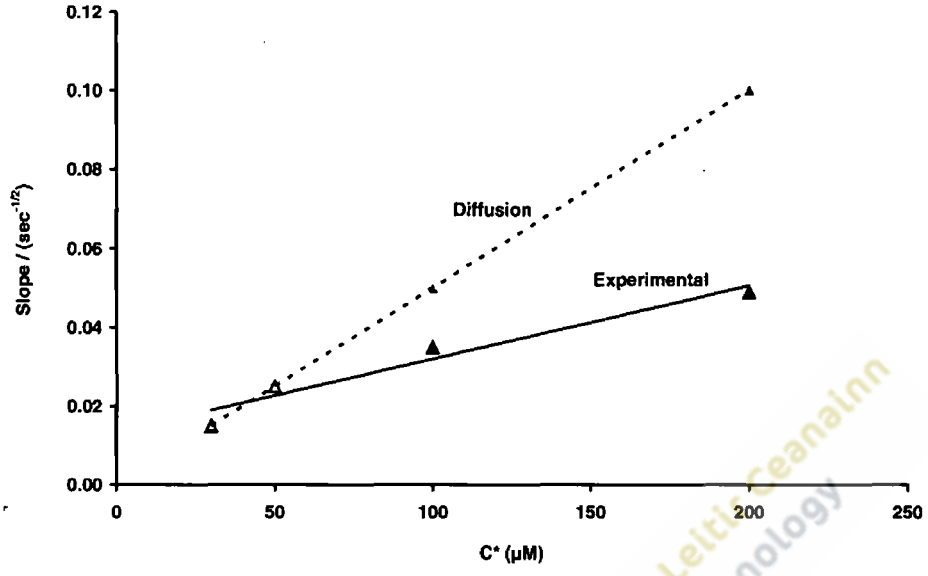

Figure 3.19. Slope vs. concentration for experimental data calculated from the slopes of Figure 3.18 at different concentrations (solid line) and best fits to the diffusion model (dashed line).

The experimental data did not support a model under diffusion control. Another factor which argues against the diffusion model is that under linear diffusion conditions, a monolayer of surface coverage 1.1×10^{-10} mol cm^{-2} where the diffusion layer thickness is typically around 0.01 cm for a stagnant solution [11], the time t for a diffusive process is given by equation 19:

$$t = \frac{\delta^2}{\pi D} \tag{19}$$

where δ is the film thickness and D is the diffusion coefficient. The diffusion coefficient calculated by cyclic voltammetry of solutions of the complex under study was determined as 1.64×10^{-6} cm^2 s^{-1}. Hence a dense monolayer should form in less than 20 seconds for the complex under study whereas Figure 3.14 shows that at least 10 min or more are required suggesting that diffusional mass transport does not describe the system under study.

Similar investigations to those outlined with the complex $[Os(bpy)_2\text{-}4\text{-}tet\text{-}Cl](PF_6)$ were performed with $[Ru(bpy)_2\text{-}4\text{-}tet\text{-}Cl](PF_6)$.

Cyclic voltammograms recorded at 1-min intervals for the first five minutes during the adsorption of $[Ru(bpy)_2\text{-}4\text{-}tet\text{-}Cl](PF_6)$ are provided in Figure 3.20.

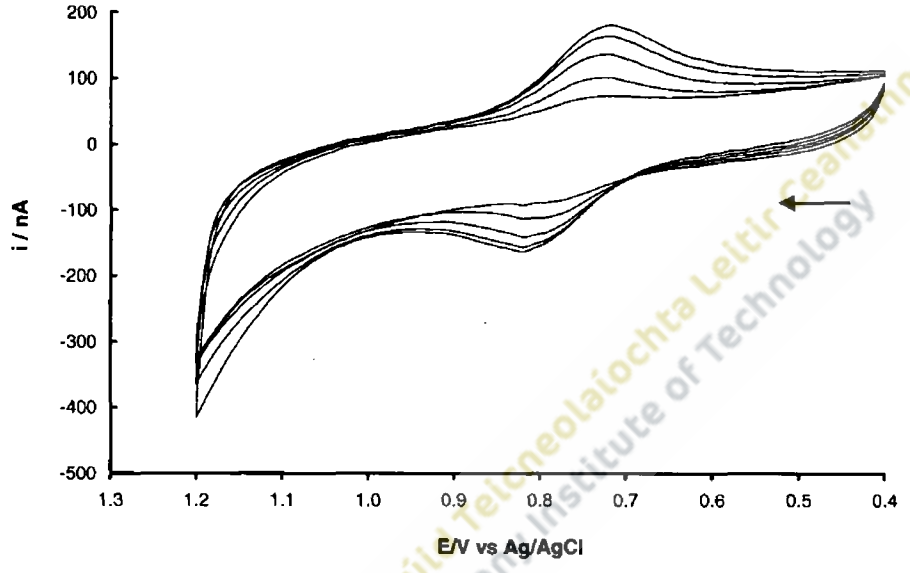

Figure 3.20. Cyclic voltammograms for the adsorption of $[Ru(bpy)_2\text{-}4\text{-}tet\text{-}Cl](PF_6)]$ onto a 12.5 μm radius Pt microelectrode at different deposition times. The deposition solution contained 300 μM of the complex in acetone/water 50/50 v/v. Scan rate 100 V s^{-1}.

Similar results were recorded with the ruthenium complex to those reported previously with the analogous osmium complex. An increase in faradaic current attributed to monolayer formation and no reduction in capacitative current were recorded. The formal potential of the $Ru^{2+/3+}$ remained constant during monolayer assembly. Values for the ΔE_{fwhm} of 130 ± 5 mV were similar to those recorded for the osmium complex and significantly larger than the ideal value of 90.6 mV, suggesting that repulsive forces exist between the assembled molecules. Following monolayer formation, cyclic voltammograms were recorded in blank electrolyte over a range of scan rates and confirmed that the peak current was linear with scan rate as anticipated for a surface-confined species.

Surface coverages on the platinum electrode determined in real time, in the deposition solution and in the blank electrolyte, were 1.32 x 10^{-10} mol cm^{-2} and 1.23 x 10^{-10} mol cm^{-2} respectively. The slight reduction recorded in the blank electrolyte suggested that a stable monolayer of the complex was chemisorbed to the electrode surface.

The change in surface coverage (Γ) with time for a 300 μM deposition solution of [Ru(bpy)$_2$-4-tet-Cl](PF$_6$) on a platinum microelectrode is shown in Figure 3.21.

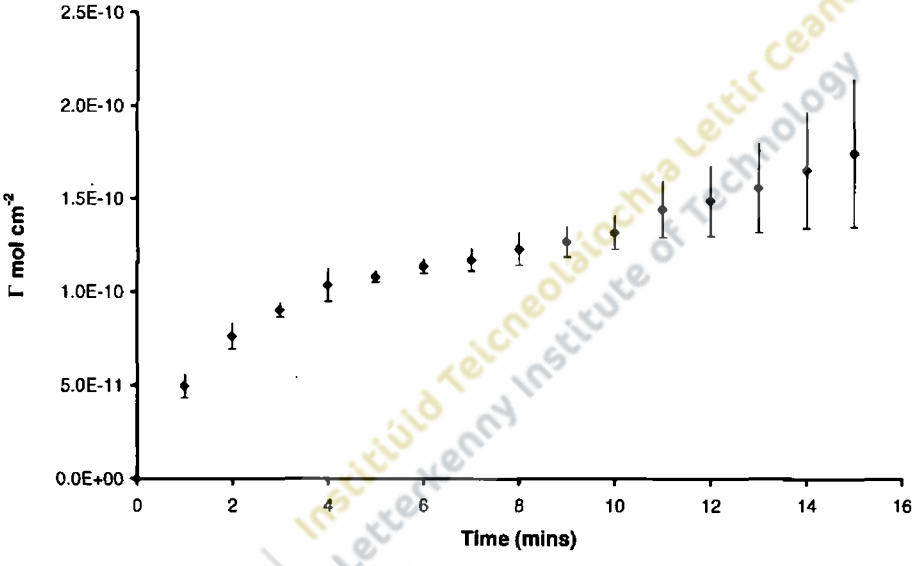

Figure 3.21. Temporal changes in the surface coverage of [Ru(bpy)$_2$-4-tet-Cl](PF$_6$) adsorbed on a Pt microelectrode from a 300 μM deposition solution of the complex. Error bars represent data taken from at least three independent monolayers.

Adsorption up to a surface coverage of approx 1.3 x 10^{-10} mol cm^{-2} was initially rapid and reproducible. After a relatively stationary period during which the surface coverage increased only slowly, adsorption became increasingly irreproducible as multilayer formation commenced. Further replicates of this experiment always demonstrated irreproducibility at higher surface coverages. Similar complex kinetic behaviour and multilayer formation has been reported for the deposition of osmium bipyridyl complexes at concentrations above 50 μM on platinum microelectrodes from a 2:1 H_20:DMF

solution. After a plateau in surface coverage at approximately 1.5 x 10^{-10} mol cm^{-2}, there was a significant increase in surface coverage as multilayers were formed [11].

The change in surface coverage (Γ) with time for deposition solutions containing 30 μM, 50 μM, 100 μM, 200 μM and 300 μM concentrations of [Ru(bpy)$_2$-4-tet-Cl](PF$_6$) is shown in Figure 3.22. For each concentration, surface coverage initially increased relatively rapidly and then began to slowdown.

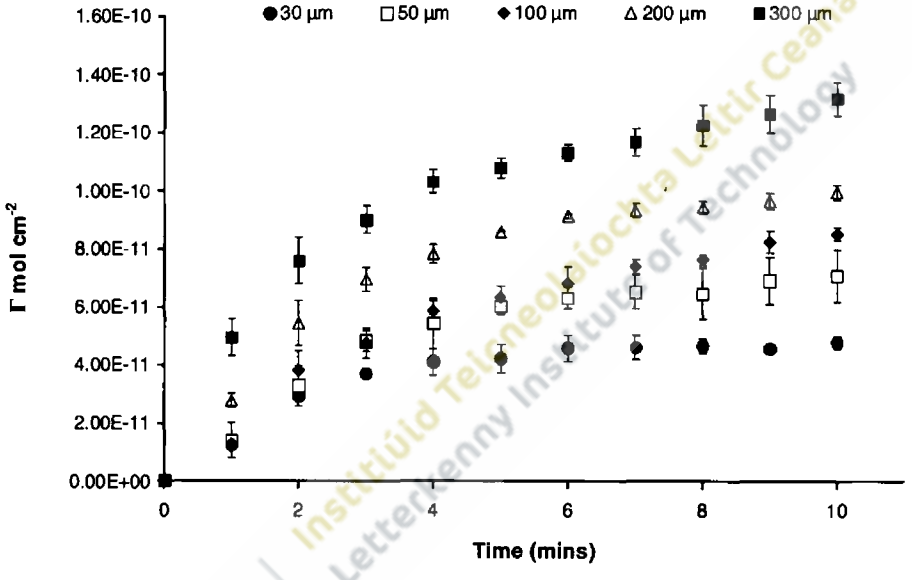

Figure 3.22. Temporal changes in the surface coverage of [Ru(bpy)$_2$-4-tet-Cl](PF$_6$) adsorbed on a Pt microelectrode from deposition concentrations between 30-300 μM. Error bars represent data taken from at least three independent monolayers.

As with the osmium complexes, values of the saturation surface coverage (Γ_s) and the adsorption coefficient (β) of [Ru(bpy)$_2$-4-tet-Cl](PF$_6$) were calculated from plots of C^*/Γ vs. C^* to establish which isotherm best described the experimental data. For this complex values of Γ_s of 1.42 x 10^{-10} mol cm^{-2} and β of 1.7 x 10^4 M^{-1} were determined.

Under the conditions employed in this investigation, the adsorption of [Ru(bpy)$_2$-4-tet-Cl](PF$_6$) exhibited a better fit to the Langmuir isotherm (Figure 3.23) than to the Frumkin isotherm using either negative or positive values for the interaction parameter (g). This suggests that minimal repulsive or attractive forces existed between the molecules adsorbed as a monolayer on the electrode surface.

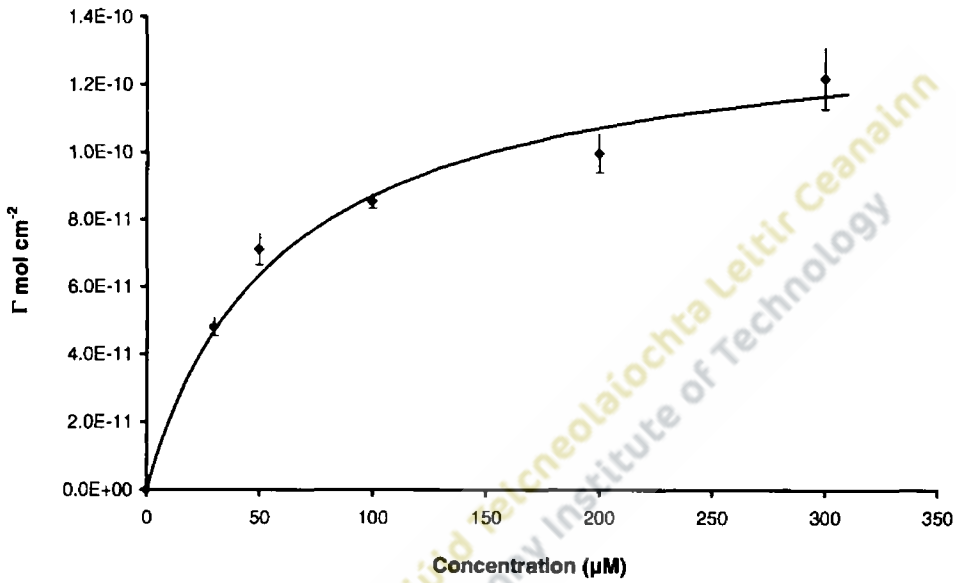

Figure 3.23. Experimental data fitted to the Langmuir isotherm for the deposition of [Ru(bpy)$_2$-4-tet-Cl](PF$_6$). Error bars represent data from three independent monolayers.

Figure 3.24 shows the fit of the experimental data for 30 μM and 300 μM concentrations of [Ru(bpy)$_2$-4-tet-Cl](PF$_6$) to the kinetic Langmuir equation (17). As with the previous osmium complex, this Langmuir model adequately described the experimental data suggesting that adsorption of [Ru(bpy)$_2$-4-tet-Cl](PF$_6$) was under kinetic control, particularly at the lower concentration.

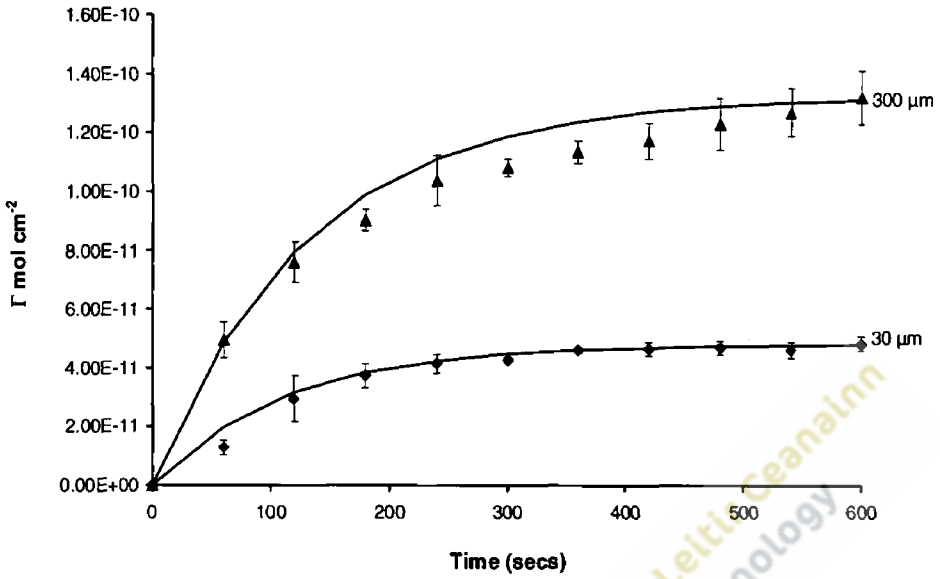

Figure 3.24. Surface coverage vs. time of $[Ru(bpy)_2\text{-}4\text{-}tet\text{-}Cl](PF_6)$ adsorbed onto a Pt microelectrode. Bulk concentrations of 300 µM and 30 µM of complex dissolved in acetone/water (50/50, v/v) are shown. The solid line represents the best fit to the Langmuir kinetic equation. Error bars represent data from three independent monolayers.

Consideration was also given to the model for diffusion-controlled adsorption as represented in equation 18. Figure 3.25 shows the fit of the experimental data for a 100 µM concentration of $[Ru(bpy)_2\text{-}4\text{-}tet\text{-}Cl](PF_6)$. A linear curve typical for adsorption which is under diffusion control was recorded. Since the experimental results were in agreement with both the kinetic model (Figure 3.24) and a process under diffusion control (Figure 3.25), the model that best described the experimental data was established by plotting the slopes of Γ_t / Γ_s vs. $t^{1/2}$ against the concentration as shown in Figure 3.26. The best fit to the plots using the diffusion-controlled model were calculated using the slope at the lowest concentration as a reference point and calculating the slopes at all other concentrations from the ratio of C^*/ Γ_s [23]. Figure 3.26 demonstrated that the experimental data did not support a model under diffusion control.

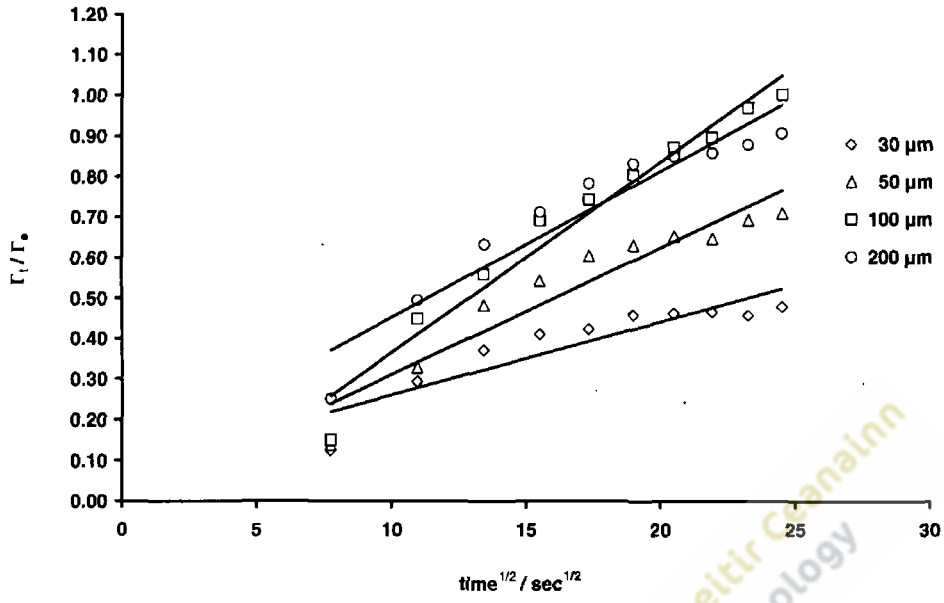

Figure 3.25. Variation of the normalised surface coverage vs. $t^{1/2}$ for [Ru(bpy)$_2$-4-tet-Cl](PF$_6$) at various concentrations.

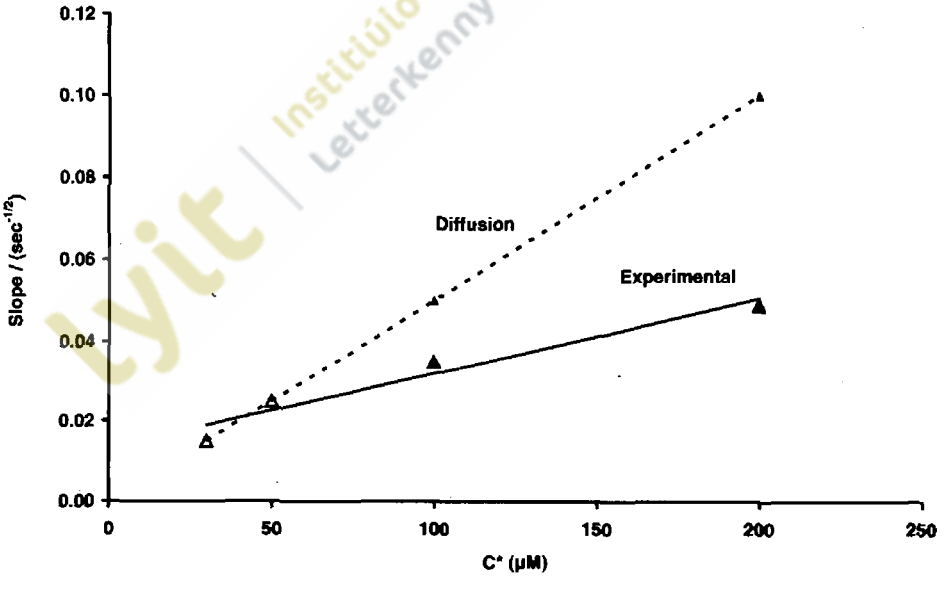

Figure 3.26. Slope vs. concentration for experimental data (solid line) calculated from the slopes at different concentrations and best fits to the diffusion model (dashed line).

Similar investigations to those outlined with the two monosubstituted tetrazine complexes $[Os(bpy)_2\text{-}4\text{-}tet\text{-}Cl](PF_6)$ and $[Ru(bpy)_2\text{-}4\text{-}tet\text{-}Cl](PF_6)$ were performed with the disubstituted $[Ru(bpy)_2\text{-}(4\text{-}tet)_2](PF_6)_2$. In this complex both of the chlorides of $Ru(bpy)_2Cl_2$ have been replaced by tetrazine ligands and as such the free pendant nitrogen of each ligand should be capable of attachment to the platinum electrode surface.

Cyclic voltammograms recorded at 20-second intervals during the adsorption of $[Ru(bpy)_2\text{-}(4\text{-}tet)_2](PF_6)_2$ are provided in Figure 3.27.

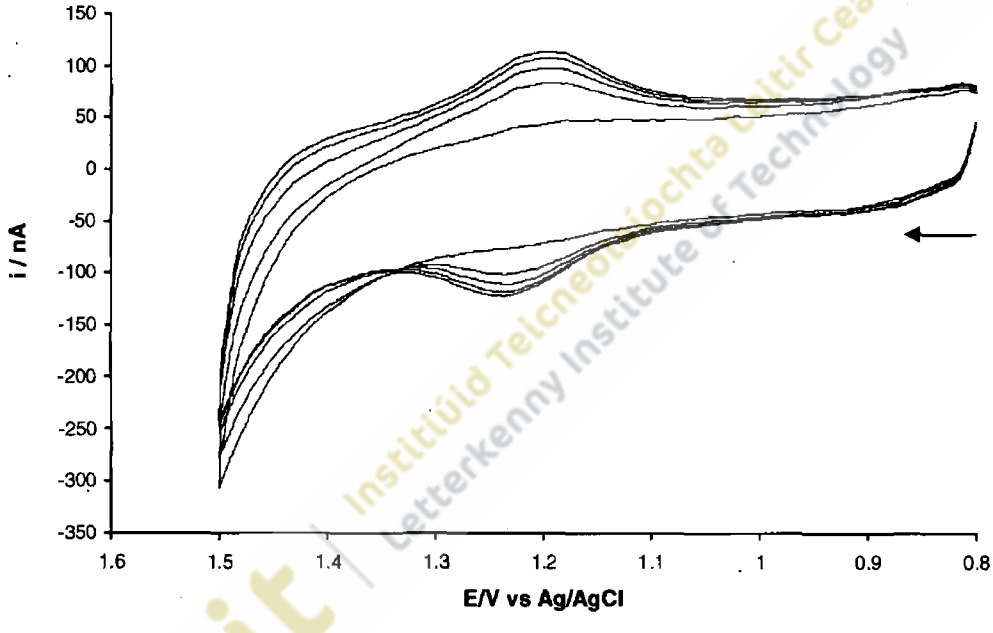

Figure 3.27. Cyclic voltammograms for the adsorption of $[Ru(bpy)_2\text{-}(4\text{-}tet)_2](PF_6)_2$ on a 12.5 μm radius platinum microelectrode at different deposition times. The deposition solution contained 300 μM of the complex in acetone/water (50/50, v/v). The cyclic voltammograms shown are for the first five scans in the deposition solution with scans recorded at 20-second intervals.

The faradaic current increased with time at a much faster rate with the disubstituted complex and because of this, cyclic voltammograms were recorded at 20-second intervals rather than the 1-minute intervals used for the complexes containing a single tetrazine

ligand. There was no decrease in double layer capacitance and no significant shift in the formal potential due to monolayer formation. The ΔE_{fwhm} value was 135 ± 5 mV, which indicated that repulsive forces existed between the molecules in the adsorbed monolayer. After removal of the electrode from the deposition solution, it was thoroughly rinsed in ultra pure water to remove any physically adsorbed molecules. The electrode was then allowed to dry and placed in blank electrolyte (0.1 M $LiClO_4$) that contained none of the dissolved complex. Cyclic voltammograms were recorded in blank electrolyte over a range of scan rates and confirmed that the peak current scaled linearly with scan rate as anticipated for a surface-confined species.

Surface coverages on the platinum electrode determined in real time in the deposition solution and in the blank electrolyte were 1.39 x 10^{-10} mol cm^{-2} and 1.35 x 10^{-10} mol cm^{-2} respectively. The slight reduction recorded in the blank electrolyte suggested that a stable monolayer of the complex was chemisorbed to the electrode surface. Formal potentials were slightly less positive in blank electrolyte compared to deposition solution suggesting that the Ru^{2+} centre is more easily oxidised in the former.

The change in surface coverage (Γ) with time for deposition solutions containing 50 μM, 100 μM, 200 μM, 300 μM and 400 μM concentrations of $[Ru(bpy)_2\text{-}(4\text{-tet})_2](PF_6)_2$ is shown in Figure 3.28. For each concentration, surface coverage initially increased relatively rapidly and then began to slowdown. This was followed by the commencement of multilayer formation similar to that observed with the monosubstituted ruthenium complex.

As with the two monosubstituted complexes, values of the saturation surface coverage (Γ_s) and the adsorption coefficient (β) of $[Ru(bpy)_2\text{-}(4\text{-tet})_2](PF_6)_2$ were calculated from plots of C^*/Γ vs. C^* (Figure 3.29) to establish which isotherm best described the experimental data. For the disubstituted complex values of Γ_s of 1.61 x 10^{-10} mol cm^{-2} and β of 1.25 x 10^4 M^{-1} were determined.

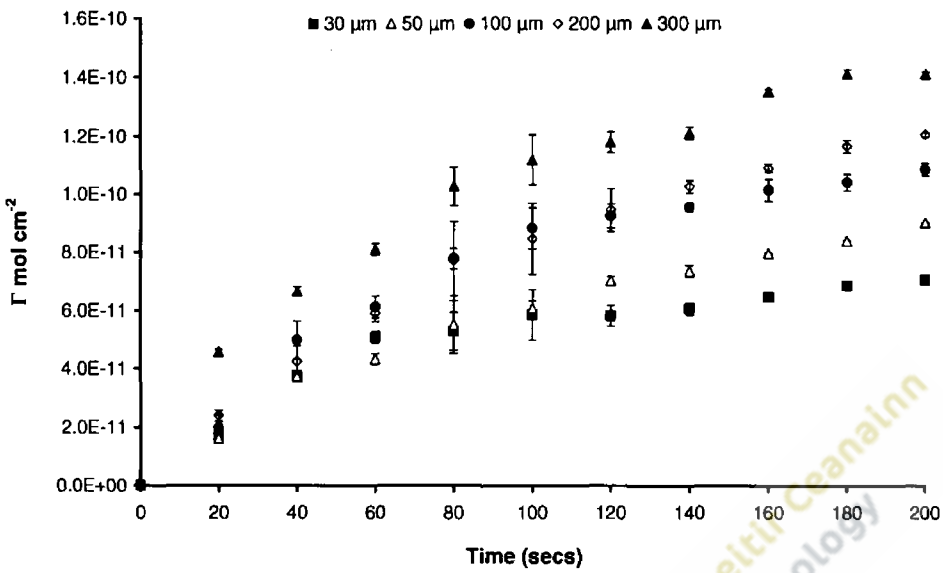

Figure 3.28. Temporal changes in the surface coverage of $[Ru(bpy)_2\text{-}(4\text{-tet})_2](PF_6)_2$ adsorbed on a Pt microelectrode from deposition concentrations between 50-400 µM. Error bars represent data taken from at least three independent monolayers.

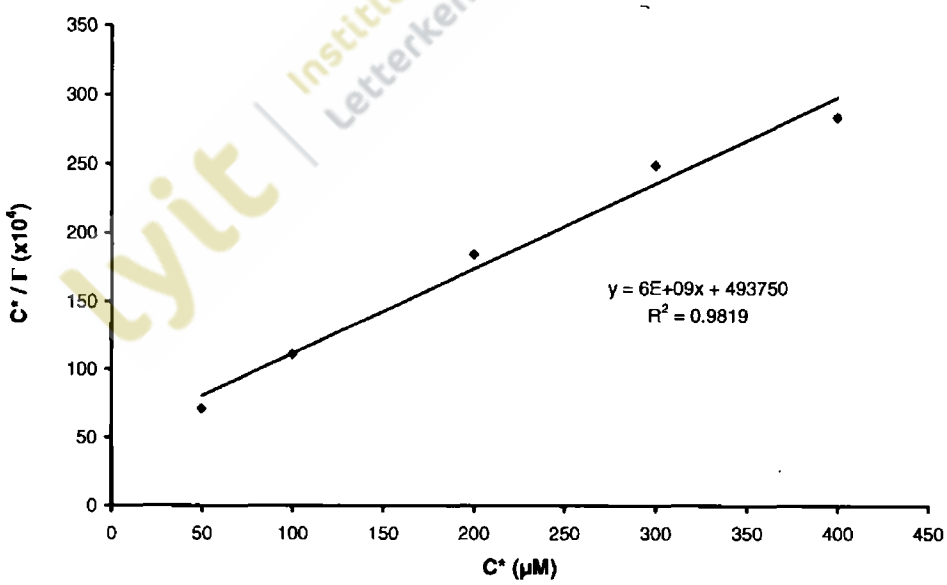

Figure 3.29. Plot of concentration of $[Ru(bpy)_2\text{-}(4\text{-tet})_2](PF_6)_2$ in the bulk solution vs. the concentration in the bulk solution divided by the surface coverage in mol cm^{-2}.

Under the conditions employed in this investigation, adsorption of $[Ru(bpy)_2\text{-}(4\text{-}tet)_2](PF_6)_2$ exhibited a better fit to the Langmuir isotherm shown in Figure 3.30 than to the Frumkin isotherm using either negative or positive values for the interaction parameter (g). This suggests that minimal repulsive or attractive forces existed between the molecules adsorbed as a monolayer on the electrode surface.

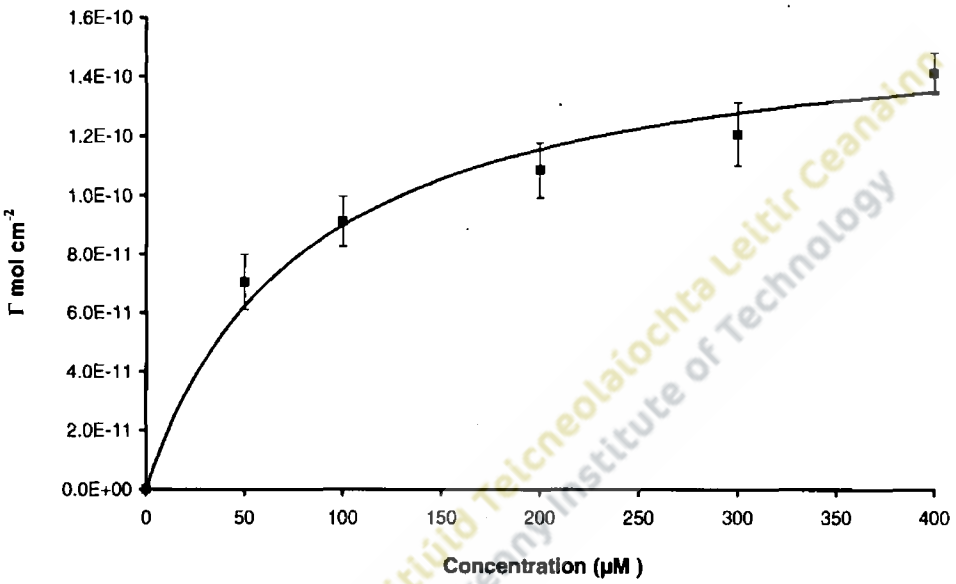

Figure 3.30. Experimental data fitted to the Langmuir isotherm for the deposition of $[Ru(bpy)_2\text{-}(4\text{-}tet)_2](PF_6)_2$. Error bars represent data from three independent monolayers.

The kinetic Langmuir equation of surface coverage with time was used to establish if the experimental data described a system under kinetic control. Figure 3.31 shows the fit of the experimental data for two concentrations of $[Ru(bpy)_2\text{-}(4\text{-}tet)_2](PF_6)_2$ to equation 17. As with the two monosubstituted tetrazine complexes, this model adequately described the experimental data suggesting that adsorption of $[Ru(bpy)_2\text{-}(4\text{-}tet)_2](PF_6)_2$) was under kinetic control.

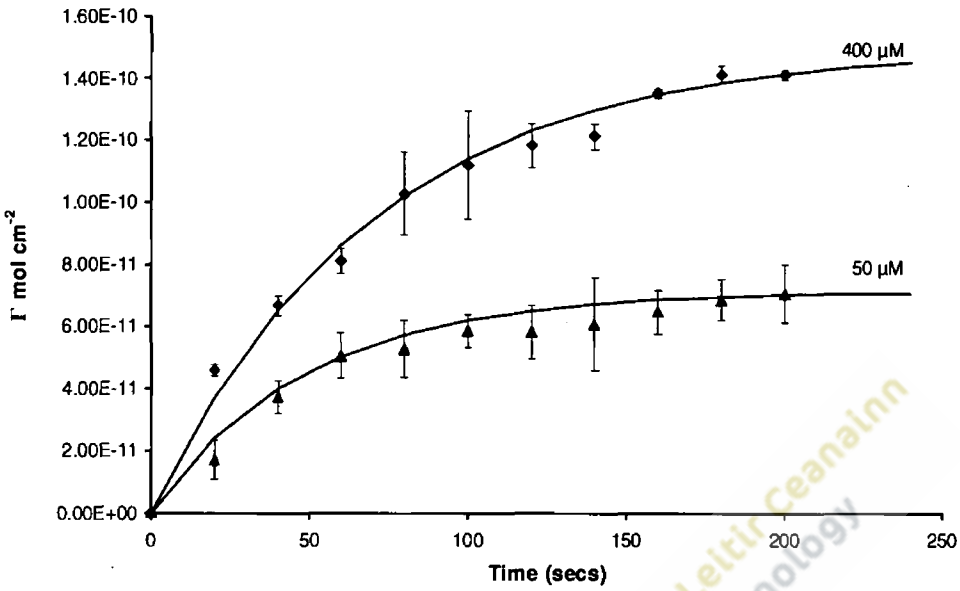

Figure 3.31. Surface coverage vs. time of $[Ru(bpy)_2\text{-}(4\text{-}tet)_2](PF_6)_2$ adsorbed onto a Pt microelectrode. Bulk concentrations of 400 µM and 50 µM of complex dissolved in acetone/water (50/50, v/v) are shown. The solid line represents the best fit to the Langmuir kinetic equation. Error bars represent data from three independent monolayers.

As with the two previous complexes, consideration was given to the model for diffusion-controlled adsorption as represented in equation 18. Figure 3.32 shows the fit of the experimental data for four concentrations of $[Ru(bpy)_2\text{-}(4\text{-}tet)_2](PF_6)_2$. Linear curves, typical of adsorption under diffusion control, were recorded. Since the experimental results were in agreement with both the kinetic model (Figure 3.31) and a process under diffusion control (Figure 3.32), the model that best described the experimental data was established by plotting the slopes of Γ_t / Γ_s vs. $t^{1/2}$ against the concentration as shown in Figure 3.33. The best fit to the plots using the diffusion-controlled model were calculated using the slope at the lowest concentration as a reference point and calculating the slopes at all other concentrations from the ratio of C^*/ Γ_s [23]. The experimental data did not support a model under diffusion control, similar to the two monosubstituted complexes.

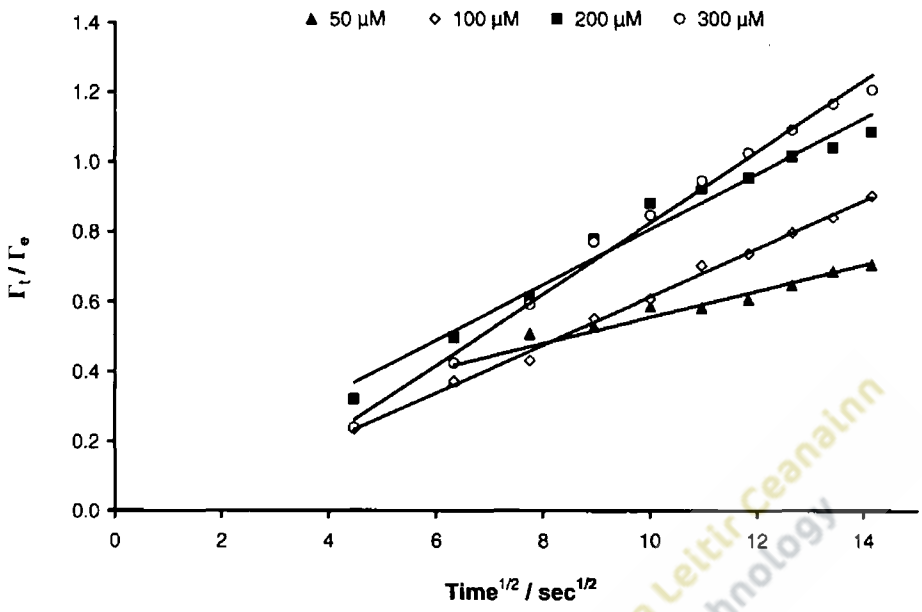

Figure 3.32. Variation of the normalised surface coverage vs. $t^{1/2}$ for $[Ru(bpy)_2\text{-}(4\text{-}tet)_2](PF_6)_2$ at concentrations of 300 µM, 200 µM, 100 µM and 50 µM (top to bottom).

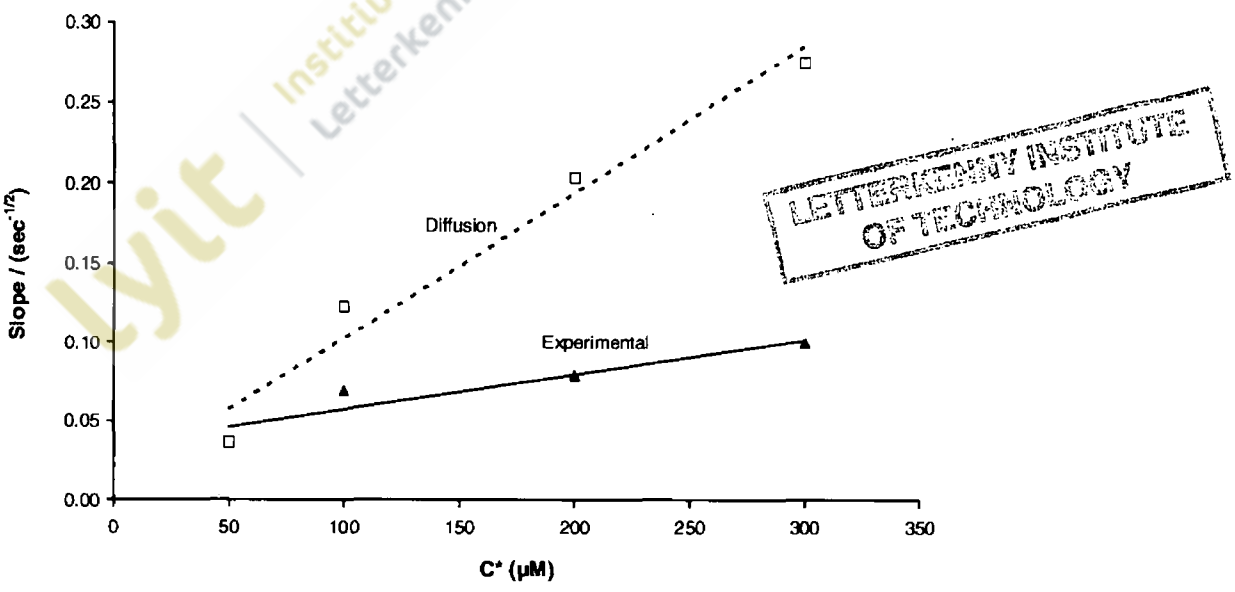

Figure 3.33. Slope vs. concentration for experimental data (solid line) calculated from the slopes at different concentrations and best fits to the diffusion model (dashed line).

The adsorption rate constant (k) for the two monosubstituted tetrazine complexes, $[Os(bpy)_2\text{-}4\text{-}tet\text{-}Cl](PF_6)$ and $[Ru(bpy)_2\text{-}4\text{-}tet\text{-}Cl](PF_6)$ and the disubstituted tetrazine complex, $[Ru(bpy)_2\text{-}(4\text{-}tet)_2](PF_6)_2$ at each concentration were calculated from the kinetic Langmuir equation represented by equation 20:

$$\theta(t) = 1 - e^{-kC^*t} \qquad (20)$$

where $\theta = \Gamma / \Gamma_s$, $e^{-kC^*t} = 1-\theta(t)$ and $-kC^*t = \ln(1-\theta)$

Using $[Os(bpy)_2\text{-}4\text{-}tet\text{-}Cl](PF_6)$ as an example, the adsorption rate constant (k) can be calculated from the slope of the plot of time vs. $\ln(1-\theta)$ as shown in Figure 3.34 where $\Gamma s = 1.11 \times 10^{-10}$ mol cm^{-2}.

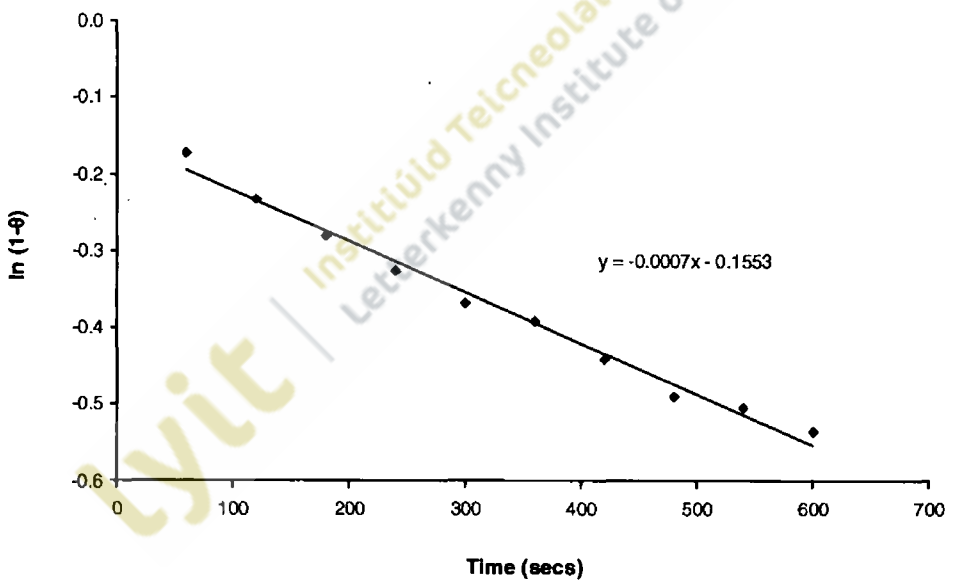

Figure 3.34. Time vs. $\ln(1-\theta)$ for a 30 μM concentration of $[Os(bpy)_2\text{-}4\text{-}tet\text{-}Cl](PF_6)$.

Since the slope of the plot equals $-k$ Conc., the adsorption rate constant can be determined from $-k$ = Slope / Conc.

Adsorption rate constants for all three complexes at the different concentrations investigated are provided in Table 3.6. These values assume that binding takes place on a single site and ideally should be equal at all concentrations.

Metal complex	k ($M^{-1}s^{-1}$) 30μM	k ($M^{-1}s^{-1}$) 50μM	k ($M^{-1}s^{-1}$) 100μM	k ($M^{-1}s^{-1}$) 200μM	k ($M^{-1}s^{-1}$) 300μM	k ($M^{-1}s^{-1}$) 400μM	Mean k ± SD ($M^{-1}s^{-1}$)
$[Os(bpy)_2\text{-}4\text{-}tet\text{-}Cl](PF_6)$	23.33	24.00	19.00	18.50	19.60	-----	20.88 ± 2.58
$[Ru(bpy)_2\text{-}4\text{-}tet\text{-}Cl](PF_6)$	16.66	20.00	14.00	8.50	12.33	-----	14.30 ± 4.35
$[Ru(bpy)_2\text{-}(4\text{-}tet)_2](PF_6)_2$	-----	44.00	37.00	25.50	22.66	25.50	30.93 ± 9.15

Table 3.6. Values of the adsorption rate constant (k) for each of the three complexes at different concentrations assuming adsorption occurs on a single site.

In contrast, values for the adsorption rate constant were also calculated assuming that adsorption requires two sites and the adsorption layer is mobile. In such circumstances the two-site model is described by equation 21:

$$\theta(t) = 1\text{-}1/\,ktC^* \qquad (21)$$
$$1/\,ktC^* = 1\text{-}\theta(t)$$
$$1/1\text{-}\theta(t) = ktC^*$$

Again using $[Os(bpy)_2\text{-}4\text{-}tet\text{-}Cl](PF_6)$ as an example, the adsorption rate constant (k) can be calculated from the slope of a plot of $1/1\text{-}\theta(t)$ vs. time as shown in Figure 3.35 where the slope equals kC^*. Hence if the slope = k Conc*, then k = Slope/Conc*.

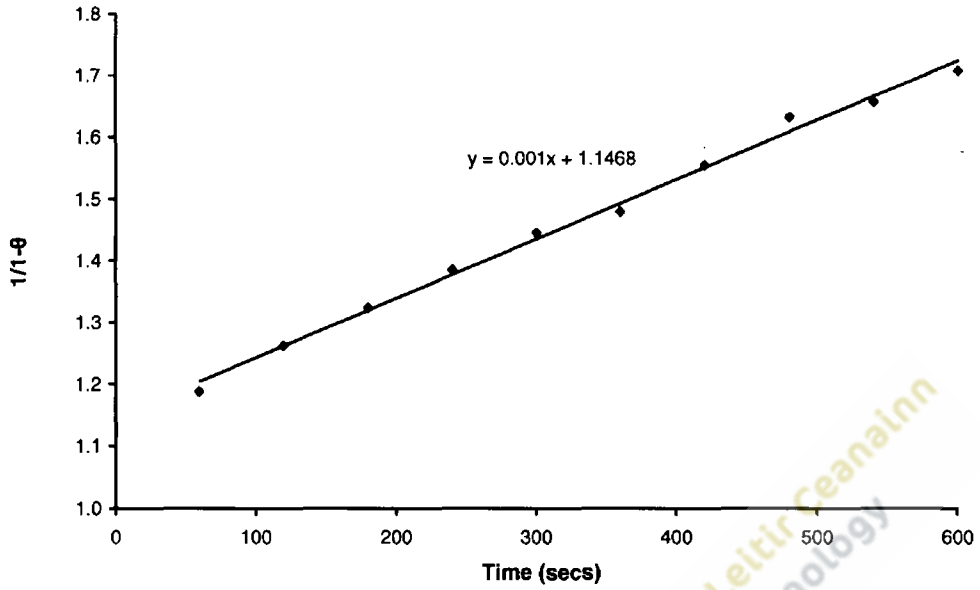

Figure 3.35. $1/(1-\theta)$ vs. time for a 30 μM concentration of $[Os(bpy)_2\text{-}4\text{-}tet\text{-}Cl](PF_6)$.

Values for the adsorption rate constant for all three complexes at the different concentrations investigated, assuming that adsorption requires two sites, are provided in Table 3.7.

Metal complex	k ($M^{-1}s^{-1}$) 30μM	k ($M^{-1}s^{-1}$) 50μM	k ($M^{-1}s^{-1}$) 100μM	k ($M^{-1}s^{-1}$) 200μM	k ($M^{-1}s^{-1}$) 300μM	k ($M^{-1}s^{-1}$) 400μM	Mean k ± SD ($M^{-1}s^{-1}$)
$[Os(bpy)_2\text{-}4\text{-}tet\text{-}Cl](PF_6)$	33.33	40.00	36.00	48.33	29.00	-----	37.33 ± 7.34
$[Ru(bpy)_2\text{-}4\text{-}tet\text{-}Cl](PF_6)$	20.00	30.00	25.00	19.00	36.00	-----	26.00 ± 7.11
$[Ru(bpy)_2\text{-}(4\text{-}tet)_2](PF_6)_2$	-----	64.00	61.00	51.50	52.00	59.00	57.50 ± 5.54

Table 3.7. Values of the adsorption rate constant (k) for each of the three complexes at different concentrations assuming adsorption requires two sites.

Surfaces modified by spontaneous adsorption of redox active components find applications in molecular electronics, sensors and many other display devices. Advances in our understanding of such surface modifications depend not only on investigation of the structure of such molecular assemblies at equilibrium but also of the dynamic processes occurring during their formation. Valuable insights into the strength of the substrate-adsorbate bond and adsorbate-adsorbate interactions have been provided using cyclic voltammetry in this study. With the monosubstituted complexes, $[Os(bpy)_2\text{-}4\text{-}tet\text{-}Cl](PF_6)$ and $[Ru(bpy)_2\text{-}4\text{-}tet\text{-}Cl](PF_6)$ and the disubstituted tetrazine complex, $[Ru(bpy)_2\text{-}(4\text{-}tet)_2](PF_6)_2$, the absence of a significant shift in redox potential or peak broadening was indicative of the existence of weak adsorbate-substrate and adsorbate-adsorbate interaction [69, 70]. Adsorption studies also provide important information about the packing density of the monolayer and from this the area occupied by each individual molecule. This gives an insight into the orientation of the molecule on the electrode surface, for example whether it adopts a flat- or edge-on orientation and provides information about the rate at which such monolayers are formed. In this study the radius of the head group appears to have dictated the surface coverage which can be attained for all of the complexes investigated. Thus it was deduced that these molecules were predominantly immobilised through the nitrogen present on the pyridine of the tetrazine ligand(s) and are orientated perpendicular with respect to the electrode surface [71]. At higher concentrations, in some instances, multilayers were formed, particularly with longer deposition times.

Two general experimental strategies have been used to study the formation of redox active monolayers [72]. In this study, monolayer formation was determined *in situ*, in real-time under actual deposition conditions. By contrast, many other studies have investigated monolayer formation by removing the substrate and partial monolayer from the deposition solution at selected time intervals and performed electrochemical investigations in blank electrolyte. There are clear advantages to using the *in situ* method since it avoids the issue of whether the quenching process alters the film structure under formation, there being clear evidence in the literature that quenching can alter both the surface coverage and change the monolayer morphology [72]. Whilst *in situ* investigations

are suitable where electrochemical methods are being used, they have clearly no role in conjunction with techniques such as X-ray photoelectron spectroscopy and atomic force microscopy. Disadvantages associated with *in situ* measurements for the determination of the kinetics of adsorption arise due to the fact that the complex dissolved in solution may affect the determination of the surface coverage, this being of particular significance at very low packing densities. In the investigations in this study, great care has been taken to minimise this interference by using high scan rates and concentrations in the micromolar range.

Clean transition metal surfaces have been shown to react with almost any reagent to form an adsorbed layer [73]. For covalent immobilisation, functional groups present on redox active molecules must be capable of displacing other molecules from the electrode surface and show a stability that is resistant to electrochemical decomposition in order to be suitable for surface modification. Adsorption is influenced by the solvent comprising the deposition solution and tends to be greater in aqueous solutions [23]. Deposition solutions used with osmium and ruthenium bipyridyl complexes which are reported in the literature include water, acetone, dimethylformamide (DMF), acetonitrile, 1:1 acetone/water, 2:1 water/DMF and 0.1 M $KClO_4$ [11, 23, 74]. With mixed deposition solutions, reductions in adsorption have been reported with even small quantities of organic solvent, e.g. the addition of only 10 mM acetone to an aqueous deposition solution resulted in a significant reduction in the surface coverage of 2,2', 5,5'-tetrahydroxyphenyl on platinum [29]. The extent of this reduction is dependant on the solubility of the adsorbing complex in the deposition solvent and also on the tendency for the solvent to adsorb to the substrate resulting in increased competition for the available sites on the electrode surface [75]. This is particularly salient with organic solvent molecules for which slow displacement from the electrode surface has been reported and in contrast to both water and perchlorate solution, both of which are easily displaced from the electrode surface by organic molecules and show only weak reversible adsorption once displaced [19, 23, 76]. In this study all three osmium and ruthenium complexes containing the tetrazine ligand(s) were highly soluble in acetone:water (50:50, v/v) which was used as the deposition solution. A consequence of using a deposition solution

comprising only 50% water was reduction in the rate of adsorption and surface coverage achieved at a given concentration compared to that which might have been expected from more aqueous solutions [77].

Adsorption investigations with each of the three complexes under investigation were undertaken at concentrations ranging from 30-400 μM. Concentrations of osmium and ruthenium bipyridyl complexes used in adsorption studies in the literature range from 0.012-1000 μM. Abruña and co-workers reported that data collected at very low concentrations (<0.070 μM) exhibited a high degree of uncertainty and were deemed unreliable, whereas above 1 μM the rate of adsorption was quite fast and saturation coverage was reached in a relatively short time [23]. Adsorption of many other osmium and ruthenium bipyridyl complexes at concentrations up to 200 μM have been reported [11, 52, 78]. Bertoncello *et al.* used concentrations of 1000 μM with thiolated ruthenium bipyridyl complexes [74]. The concentration and the deposition time have been reported to affect the structure of the monolayer. At low bulk concentrations, monolayer formation may require times between 10-20 hr to reach equilibrium surface coverage suggesting that either a very large number of adsorbate molecules must be rearranged before an energy-minimised structure is obtained or that the probability of binding is very low [52]. At concentrations above 20 μM with some related complexes, multilayer formation in a number of different deposition solutions has been reported [11].

With each of the three complexes under investigation, adsorption proceeded rapidly at first and then progressed towards an equilibrium surface coverage dependent on the bulk concentration of the complex. Similar trends have been reported with related osmium and ruthenium bipyridyl complexes [11]. Over the range of concentrations studied, results suggested the formation of partial monolayers, full monolayers and the initiation of multilayers. Surface coverages attained for the two monosubstituted osmium and ruthenium complexes at similar concentrations were broadly similar as might be expected for two complexes with the same bridging ligand and the same overall charge. The effect of changing the overall charge in analogous osmium and ruthenium complexes on the limiting surface coverage has previously been highlighted [14]. At low surface coverages,

molecules of osmium and ruthenium bipyridyl compounds similar to those used in this study have been shown to exhibit a flat orientation on the platinum electrode surface and chemisorption between the substrate and the aromatic ring. By contrast, at higher surface coverages, a well-orientated, adsorbed layer develops where platinum-nitrogen bonding is the predominant mode of surface attachment [71]. Several other workers in this field have suggested that higher repulsive interactions between molecules may contribute to lower surface coverage [17, 79].

The processes of adsorption and self-organisation has been shown to occur in several steps comprising the transport of molecules to the solid-liquid interface followed by a much slower process of two-dimensional re-organisation on the electrode surface leading to a specifically aligned monolayer. The overall adsorption process may be diffusion-controlled, kinetically-controlled or an intermediate mixed regime [72]. Experimental results for the complexes under study in this work suggested that the adsorption process was not controlled by diffusional mass transfer. In contrast Langmuir kinetics, with the inclusion in some instances of relatively small interaction parameters, provided an adequate description of the rate of monolayer formation. Studies by Forster on closely related complexes demonstrated that Langmuirian kinetics did not adequately describe the adsorptive process, however better agreement was reported for studies when *in situ* measurements were used to generate data [11, 19, 23].

This study probed the question of whether this kinetically-controlled adsorption was better described as adsorption requiring a single site as represented by equation 20 or if adsorption required two sites and the adsorbed monolayer was mobile (i.e. a film where adsorbed molecules can move from one site to a neighbouring site so that at any instant the adsorbed atoms can redistribute themselves on the electrode surface) as represented by equation 21. Adsorption rate constants (k) determined for the three complexes using the first order (Table 3.6) and second order (Table 3.7) models, established that values determined using the second order model were approximately twice those using the first order model. The values of the adsorption rate constants for the ruthenium disubstituted tetrazine complex were approximately double those for the monosubstituted complex in

either the first or second order models. This higher value in the disubstituted complex may be attributed to the additional tetrazine ligand providing two free pyridine groups, both of which could potentially bind to the electrode surface [11]. Adsorption rate constants (k) of related osmium and ruthenium complexes quoted in the literature have been determined using either first order or second order kinetic models. Concentration-independence, i.e. where the adsorption rate constant exhibits limited variation at different concentrations, is taken as an indicator of the model that best describes the kinetics of the adsorptive process. The mean adsorption rate constants, standard deviations and relative standard deviations for the complexes under study determined using both first order and second order kinetic models are provided in Table 3.8. Values exhibited limited variation over the 30-400 μM concentration range under both the first and second order models and clarification as to which of the models best described the experimental data was inconclusive. Adsorption rate constants determined experimentally were somewhat smaller than k values reported for similar related complexes in the literature [11, 23, 68].

	First order model		Second order model	
Metal complex	Mean k ± SD ($M^{-1}s^{-1}$)	R.S.D. (%)	Mean k ± SD ($M^{-1}s^{-1}$)	R.S.D. (%)
$[Os(bpy)_2\text{-}(4\text{-tet})\text{-}Cl](PF_6)$	20.88 ± 2.58	12.4	37.33 ± 7.34	19.7
$[Ru(bpy)_2\text{-}(4\text{-tet})\text{-}Cl](PF_6)$	14.30 ± 4.35	30.4	26.00 ± 7.11	27.3
$[Ru(bpy)_2\text{-}(4\text{-tet})_2](PF_6)_2$	30.93 ± 9.15	29.6	57.50 ± 5.54	9.6

Table 3.8. Mean adsorption rate constants for the three complexes under study determined using first order and second order kinetic models.

The temporal evolution in surface coverage for the three complexes at the lowest concentrations investigated is provided in Figure 3.36 together with the best fits obtained with first order and second order models. With all three complexes under investigation

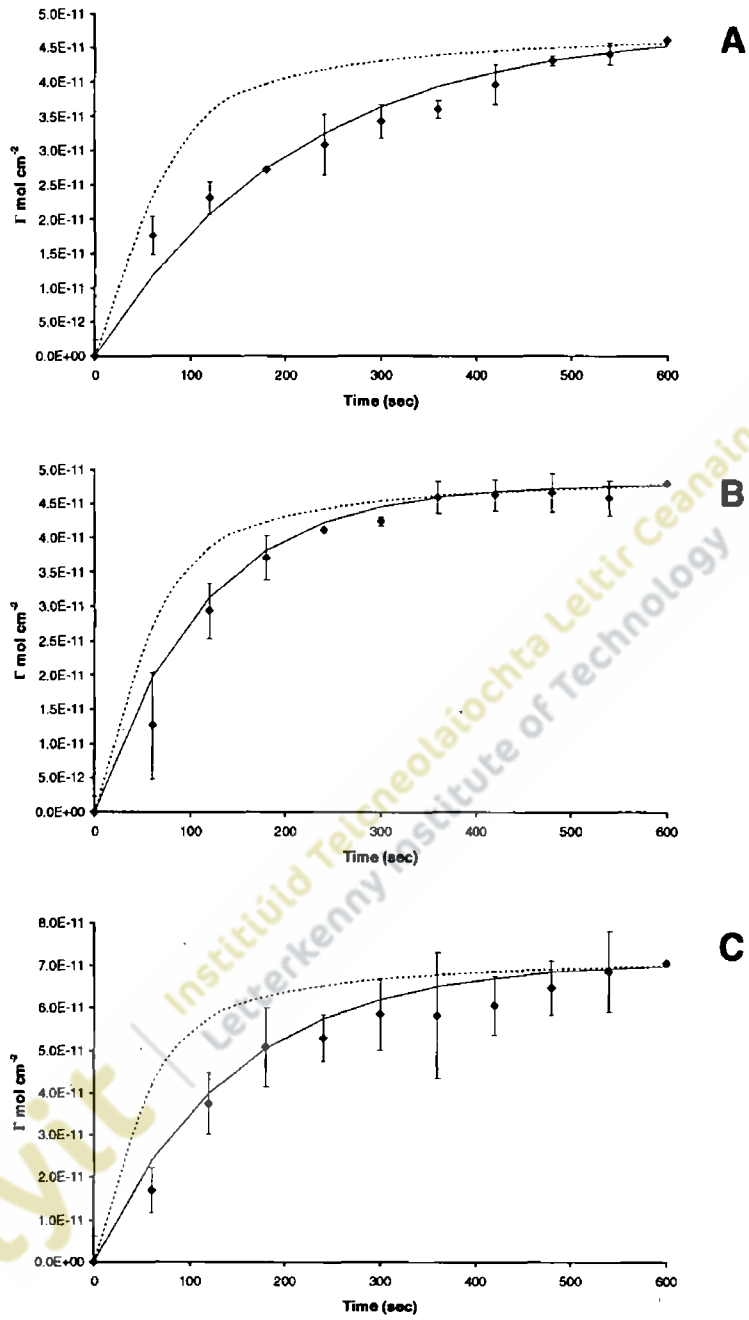

Figure 3.36. Temporal evolution in surface coverage of A. $[Os(bpy)_2\text{-}4\text{-}tet\text{-}Cl](PF_6)$, B. $[Ru(bpy)_2\text{-}4\text{-}tet\text{-}Cl](PF_6)$ and C. $[Ru(bpy)_2\text{-}(4\text{-}tet)_2](PF_6)_2$ absorbed onto a platinum microelectrode at concentrations of 30 μM for the monosubstituted complexes and 50 μM for the disubstituted complex. The thick solid and dashed lines represent best fits of the first and second order models respectively. Error bars represent data taken from three independent monolayers.

the first order model exhibited the best fit to the experimental data. Similar conclusions were determined using higher concentrations of all three complexes (data not shown).

Tirado and co-workers with two related osmium complexes of the type $[Os(bpy)_2LCl]^+$ where L = trans-1,2-bis(4-pyridyl)ethylene (py=py) or 1,3-bis(4-pyridyl)propane (dipy) in 0.1 M $KClO_4$ reported that adsorption on platinum followed first order Langmuirian kinetics and was concentration-independent between 0.070-1 μM. Apparent rate constants were determined as 1560 $M^{-1}s^{-1}$ and 1416 $M^{-1}s^{-1}$ respectively [23]. Conversely work reported on the adsorption of $[Os(bpy)_2(p3p)_2]^{2+}$ where p3p is 4,4'-trimethylenedipyridine on platinum in 2:1 H_2O/DMF demonstrated that adsorption followed second order Langmuirian kinetics and was concentration-independent between 10-50 μM. The adsorption rate constant was determined to be 220 $M^{-1}s^{-1}$. Adsorption of this same complex on gold electrodes under identical conditions similarly followed second order kinetics and was concentration-independent between 10-100 μM. The adsorption rate constant was determined to be 460 $M^{-1}s^{-1}$ [11]. Recently the mechanism for the formation of monolayers of $[Ru(bpy)_2Qbpy]^{2+}$ where Qbpy is 2,2':4,4":4'4"-quarterpyridyl on platinum microelectrodes in 2:1 H_2O:DMF was investigated by monitoring the time evolution of surface coverage using in-situ voltammetry. Adsorption followed first order Langmuirian kinetics and was concentration-independent between 1-200 μM. The adsorption rate constant was determined to be 5.1 x 10^{-6} s^{-1} [68]. An adsorption rate constant of 0.54 $M^{-1}s^{-1}$, much less than those reported experimentally for the complexes under investigation in this study, was reported for a $[Ru(bpy)_2(bpySH)]^{2+}$ monolayer formed in 1:1 acetone:water. Adsorption followed first order kinetics and was concentration-independent between 10-1000 μM. The lower adsorption rate constant in this instance may in part be attributed to adsorption through a thiol group to the platinum surface rather than adsorption through the nitrogen of the free pyridine group(s) in all of the other complexes considered previously [74].

An understanding of the stability of monolayers of the three complexes over time is essential to support their use as modifiers of electrode surfaces. To provide such information, the adsorbed molecules were cycled at selected time intervals over a number of hours to determine their desorption rate into aqueous solution.

Cyclic voltammograms for desorption from platinum microelectrodes into blank electrolyte (0.1 M $LiClO_4$) of the monosubstituted $[Ru(bpy)_2\text{-}4\text{-}tet\text{-}Cl](PF_6)$ and the disubstituted $[Ru(bpy)_2\text{-}(4\text{-}tet)_2](PF_6)_2$ are shown as examples in Figure 3.37 and Figure 3.38 respectively. The faradaic current decreased with time as each of the complexes desorbed into solution. Desorption caused no increase in capacitative current as would have been anticipated if a compact monolayer impermeable to electrolyte ions existed. Significantly, there was no discernible shift in the formal potential as the monolayer of each complex desorbed in contrast to data for related complexes which reported a negative shift in potential indicating that it became increasingly easier to oxidise the osmium and ruthenium centres as surface coverage decreased [11].

The kinetics of desorption were followed by measuring the surface coverage as a function of time. Monolayers of the three complexes under investigation were very stable and even after 6 hr duration of repetitive cycling more than 50% of the monolayer still remained on the platinum electrode surface. The steady decrease in surface coverage over time as the monosubstituted complex $[Ru(bpy)_2\text{-}4\text{-}tet\text{-}Cl](PF_6)$ desorbed into solution is shown as an example in Figure 3.39.

All desorption data were recorded in circumstances where there was no complex dissolved in solution, i.e. they represent a non-equilibrium situation. Therefore, desorption and adsorption may follow different rate laws. When desorption occurs into blank electrolyte, no significant level of re-adsorption is assumed. Desorption of each complex followed an exponential decay [80] according to equation 22:

$$\Gamma_t = \Gamma_o[\exp(-k_{app}t)] \qquad (22)$$

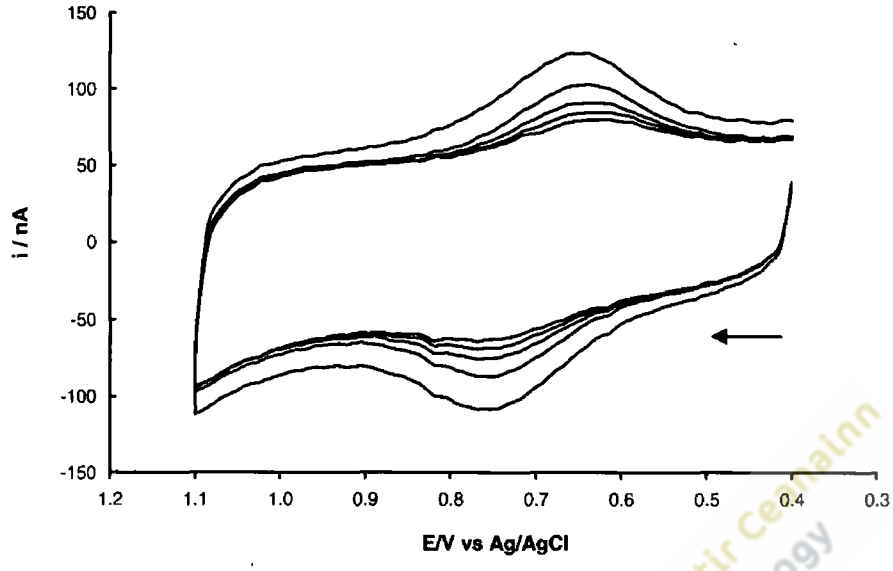

Figure 3.37. Cyclic voltammograms showing the desorption of $[Ru(bpy)_2\text{-}4\text{-}tet\text{-}Cl](PF_6)$ from a 12.5 μm radius platinum electrode into blank electrolyte (0.1 M $LiClO_4$). Cathodic currents are up and anodic currents are down. From top to bottom on the cathodic side, desorption times are 1, 50, 100, 150 and 250 min. Scan rate 100 V s^{-1}.

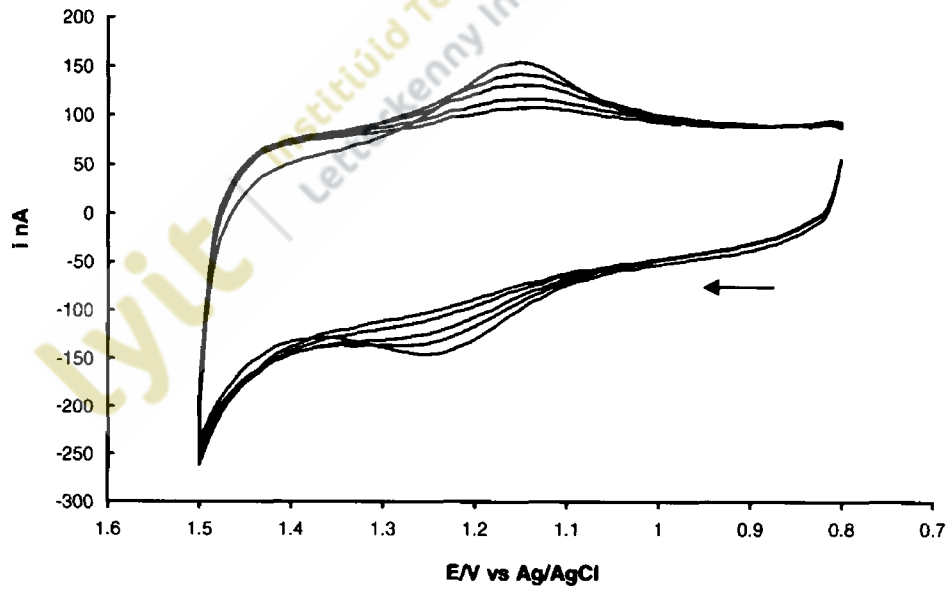

Figure 3.38. Cyclic voltammograms showing the desorption of $[Ru(bpy)_2\text{-}(4\text{-}tet)_2](PF_6)_2$ from a 12.5 μm radius platinum electrode into blank electrolyte (0.1 M $LiClO_4$). Cathodic currents are up and anodic currents are down. From top to bottom on the cathodic side, desorption times are 1, 50, 100, 150 and 250 min. Scan rate 100 V s^{-1}.

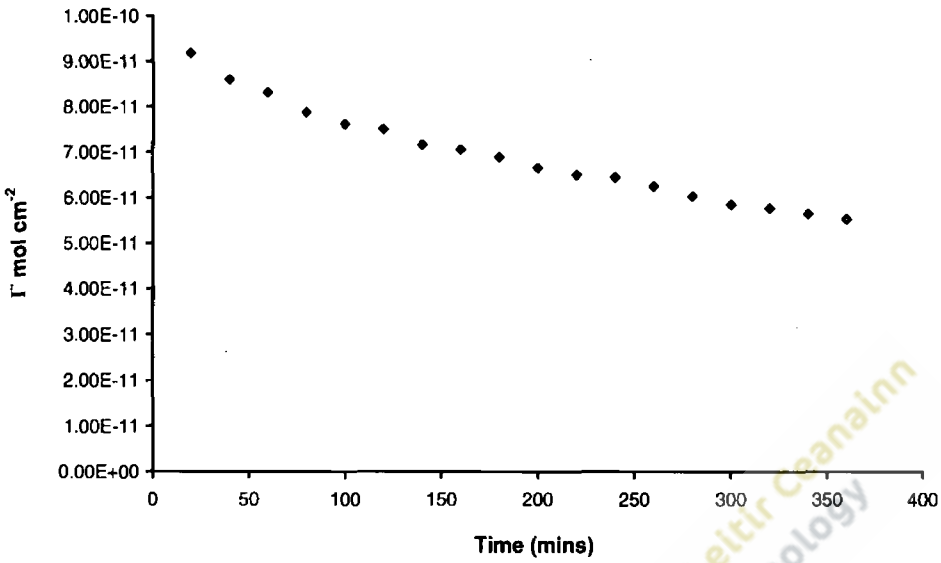

Figure 3.39. Surface coverage of $[Ru(bpy)_2\text{-}4\text{-}tet\text{-}Cl](PF_6)$ desorbing from a 12.5 μm radius platinum electrode into blank electrolyte (0.1 M $LiClO_4$). Surface coverage was determined from the voltammograms in Figure 3.37.

Semi-log plots of the surface coverage vs. time data for all three complexes were prepared. An example for $[Ru(bpy)_2\text{-}(4\text{-}tet)\text{-}Cl](PF_6)$ prepared using data from Figure 3.39 is provided in Figure 3.40. All semi-log plots were linear demonstrating that the process is in agreement with first order kinetics over durations extending at least until the surface coverage had decreased to less than 60% of its initial value. Forster working with similar osmium polypyridyl complexes reported that since first order kinetics were observed, all adsorption sites could be considered equivalent and that relatively few of the adsorbates existed in unusual low energy configurations [11]. This might suggest that the films on the electrode surface were not highly ordered or that the adsorbates did not interact strongly in a lateral direction.

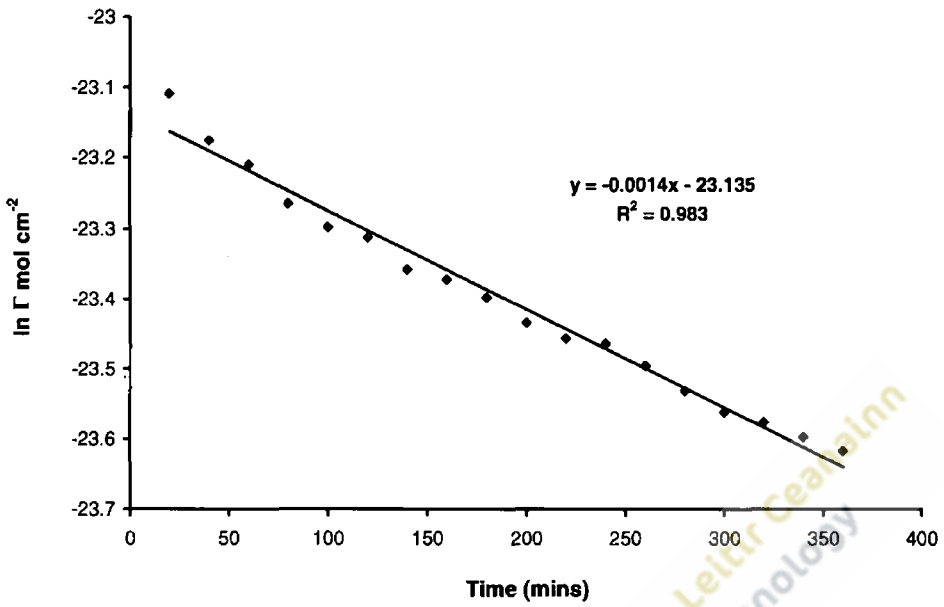

Figure 3.40. Semi-log plot of the desorption data for $[Ru(bpy)_2\text{-}4\text{-}tet\text{-}Cl](PF_6)$ from Figure 3.39.

The first order desorption rate constants for the three complexes from a platinum microelectrode into blank electrolyte (0.1 M $LiClO_4$) are provided in Table 3.9.

Metal complex	Desorption rate constant (s^{-1})
$[Os(bpy)_2\text{-}4\text{-}tet\text{-}Cl](PF_6)$	2.51×10^{-5}
$[Ru(bpy)_2\text{-}4\text{-}tet\text{-}Cl](PF_6)$	2.33×10^{-5}
$[Ru(bpy)_2\text{-}(4\text{-}tet)_2](PF_6)_2$	5.66×10^{-5}

Table 3.9. Desorption rate constants from monolayers of the three complexes determined from the semi-log plots.

Desorption rate constants (k) in this study are slower than those reported for similar mono-substituted osmium and ruthenium complexes. Tirado and Abruña reported desorption rate constants of 2.5 x 10^{-3} s^{-1} and 1.5 x 10^{-3} s^{-1} respectively for monosubstituted osmium and ruthenium complexes of the type $[Os(bpy)_2LCl]^+$ and $[Ru(bpy)_2LCl]^+$ where L = 1,3-bis(4-pyridyl)propane desorbed from platinum electrodes into 0.1 M $KClO_4$ aqueous solution [20]. Values of 1.4 x 10^{-4} s^{-1} for desorption of the monosubstituted osmium complex $[Os(bpy)_2$ 1,2-bis(4-pyridyl)ethane $Cl]^+$ from gold electrodes into 0.1 M $KClO_4$ aqueous solution have been reported [80]. Desorption rate constants for thiolated osmium bipyridyl complexes from platinum electrodes greater than the rate constants in this study have been determined [30, 68].

Desorption rate constants of 4.1 x 10^{-5} s^{-1} and 1.8 x 10^{-5} s^{-1}, a similar magnitude to that for the disubstituted complex in this study, were determined for $[Os(bpy)_2(4,4'$-trimethylenedipyridine$)_2]^{2+}$ desorbing from gold and platinum respectively into 2:1 H_2O/DMF [11]. This osmium complex is highly soluble in DMF and it would have been expected that this high solubility might have resulted in faster desorption.

The ruthenium disubstituted tetrazine complex exhibited desorption rate constants more than double those for the monosubstituted complex. This higher value for the disubstituted complex is somewhat surprising and contrasts with the results reported for the $[Os(bpy)_2(p3p)_2]^{2+}$ complex where the possibility of surface attachment through two binding sites was given as a reason for slow desorption [11].

The formation of self-assembled monolayers of [Os(bpy)$_2$-(pyridine-4-COOH)-Cl] or [Ru(bpy)$_2$-(pyridine-4-COOH)-Cl] by spontaneous adsorption on platinum or gold electrodes proved unsuccessful. To form monolayers of these complexes on gold electrodes a two-step assembly procedure was followed as shown below.

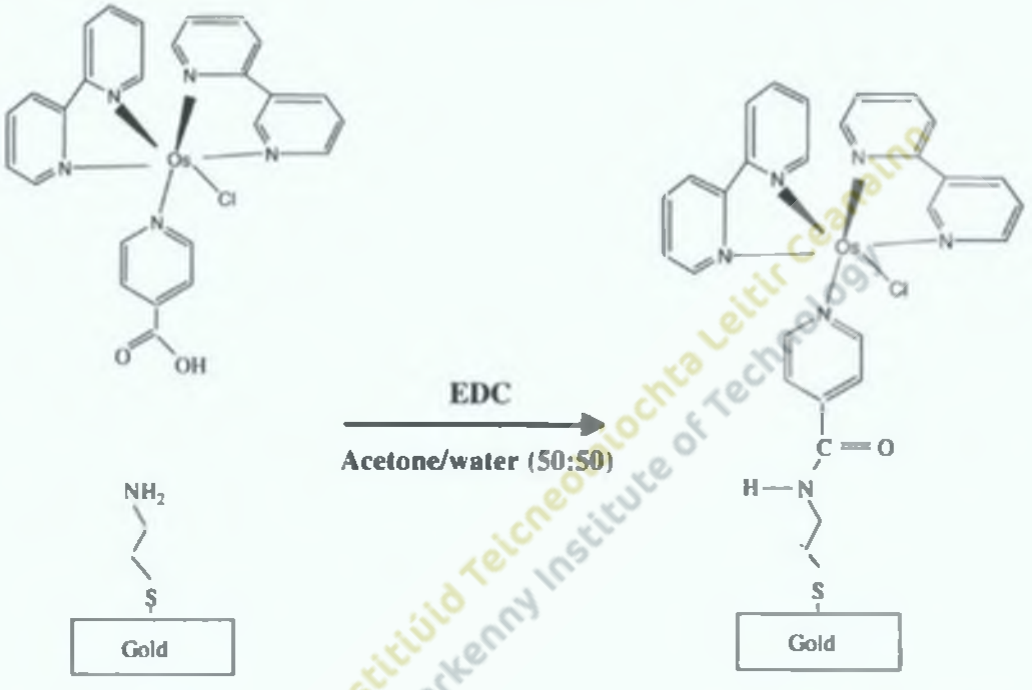

Figure 3.41. Diagrammatic representation of the two-step assembly procedure with the complex [Os(bpy)$_2$-(pyridine-4-COOH)-Cl].

Cyclic voltammograms for Os(bpy)$_2$-(pyridine-4-CO-NH-(CH$_2$)$_2$-SH)Cl recorded at various scan rates are provided in Figure 3.42 and showed a reversible oxidation-reduction wave at potentials expected for an osmium complex with a pyridyl ligand.

The linear relationship between the peak current and the scan rate for this monolayer presented in Figure 3.43 confirmed that the osmium complex was confined to the electrode surface. The ratio of cathodic to anodic charge determined at a low scan rate of close to one confirmed that the complex could be oxidised and reduced completely.

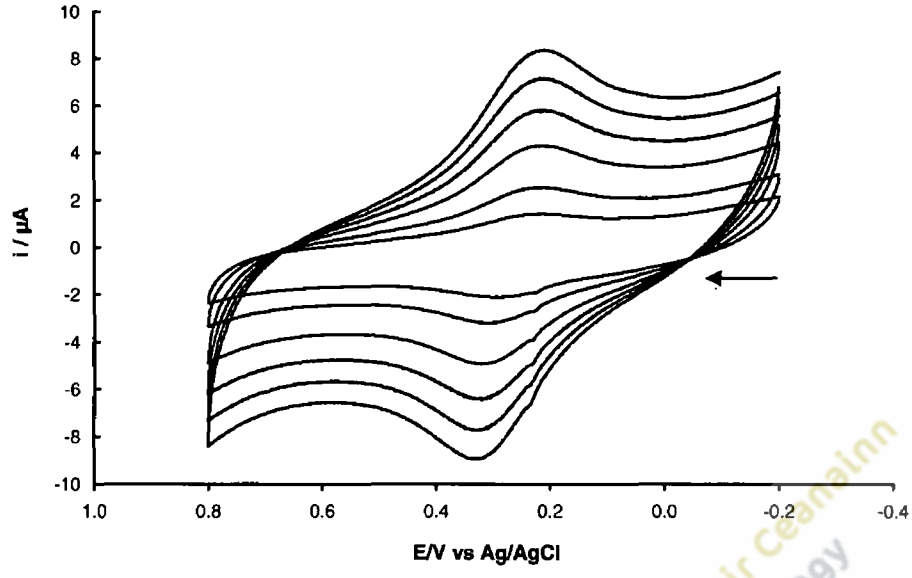

Figure 3.42. Cyclic voltammograms for a spontaneously adsorbed monolayer of $Os(bpy)_2$-(pyridine-4-CO-NH-$(CH_2)_2$-SH)Cl on a 1 mm radius gold electrode. Scan rates from top to bottom are 1, 0.8, 0.6, 0.4, 0.2 and 0.1 V s^{-1}. The supporting electrolyte was 0.1 M $LiClO_4$. The initial potential was –0.2 V and anodic currents are shown down and cathodic currents up.

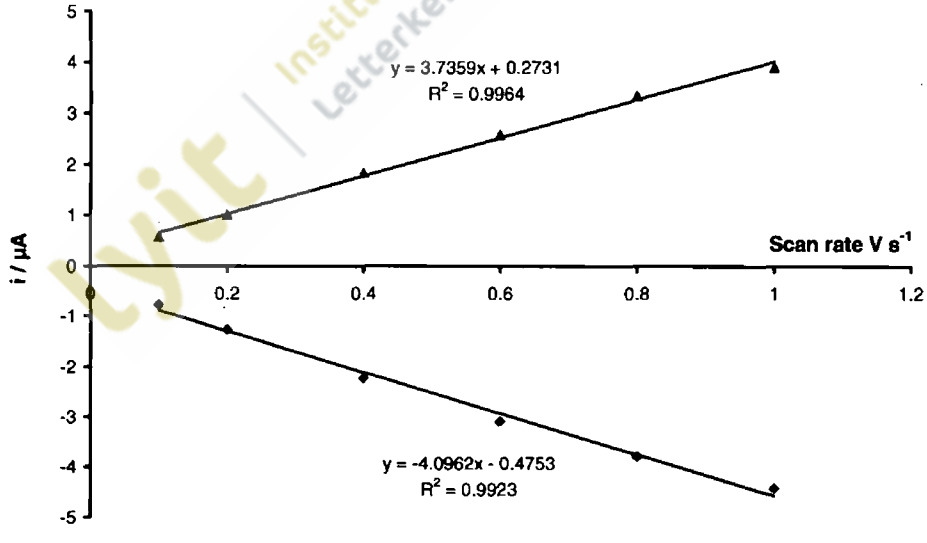

Figure 3.43. The relationship between the peak current and scan rate determined from the voltammograms in Figure 3.42. Cathodic currents are shown above the *x*-axis and anodic currents below the *x*-axis.

The faradaic charge was estimated from the area under the cathodic peak and together with the real surface area of the electrode used to calculate the surface coverage, or the number of moles of the complex per cm^2. The surface coverage (Γ) was calculated as 1.09×10^{-10} mol cm^{-2} and was in good agreement with values reported elsewhere for closely related complexes [15, 18, 36, 38, 59]. Using the Avogadro constant, the number of molecules per cm^2 was determined and the area occupied by one molecule of the complex calculated as 152 $Å^2$. When additional contributions to the molecular volume are considered this area of occupation is consistent with that expected for a closely packed monolayer in which the radius of the metal complex (approximately 6.7 Å) rather than the length of the bridging ligand dictates the surface coverage [18].

The heterogeneous electron transfer rate constant was determined from the cyclic voltammograms in Figure 3.44 using the Laviron approach shown in Figure 3.45.

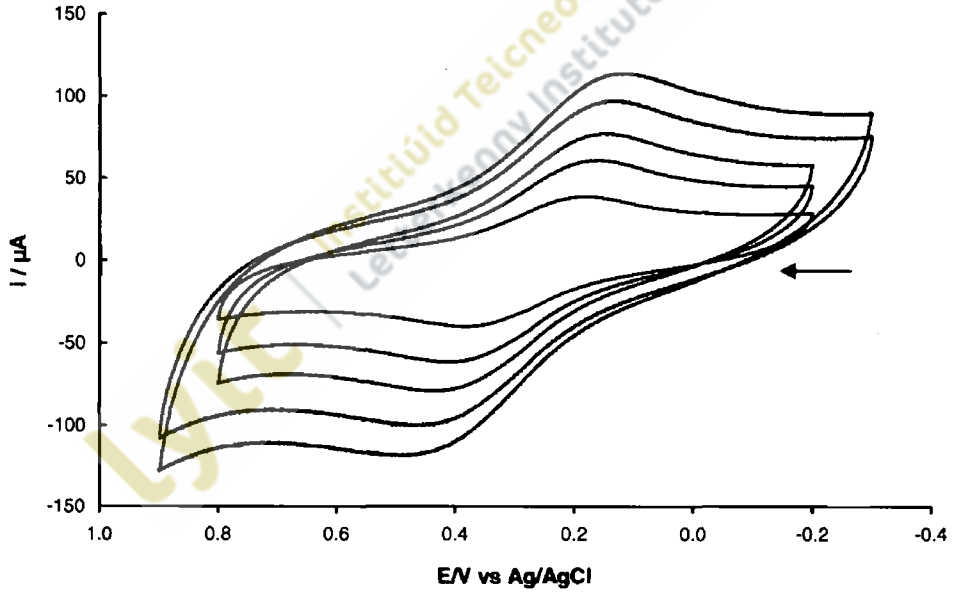

Figure 3.44. Cyclic voltammograms for a spontaneously adsorbed monolayer of $Os(bpy)_2$-(pyridine-4-CO-NH-$(CH_2)_2$-SH)Cl on a 1mm radius gold electrode. The supporting electrolyte used was 0.1 M $LiClO_4$. Cathodic currents are up and anodic currents are down. Scan rates shown from top to bottom on the cathodic side are 50, 40, 30, 20 and 10 V s^{-1}.

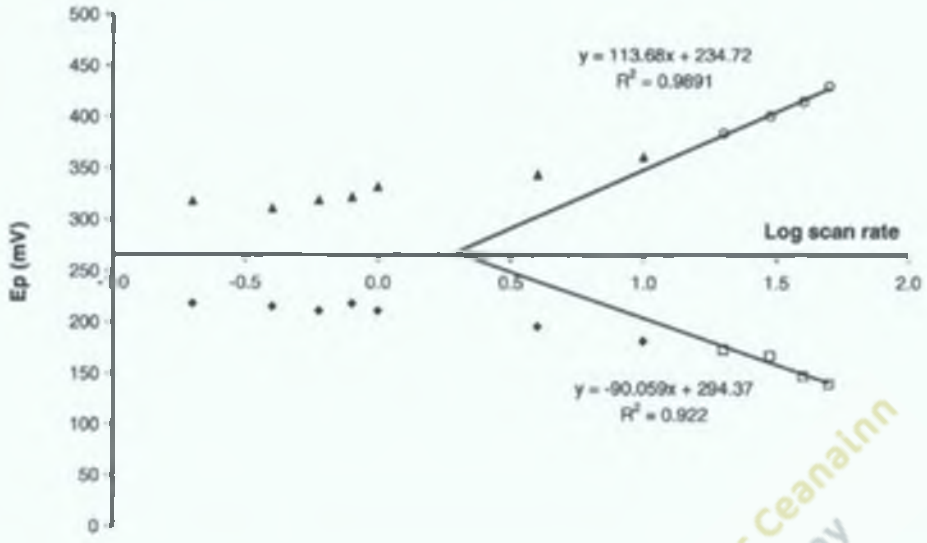

Figure 3.45. Laviron approach for determination of standard rate constant. Plots of the peak potential vs. log (scan rate) for a monolayer of $Os(bpy)_2$-(pyridine-4-CO-NH-$(CH_2)_2$-SH)Cl on a 1 mm radius gold electrode. The potentials for the cathodic currents are shown above the *x*-axis and the anodic currents below the *x*-axis.

The electron transfer rate constant was determined to be 33.86 s^{-1} and the transfer coefficient (α) 0.44. The resistance of the cell using the iR compensation test on the CH606A workstation was measured as 56 ohms and the peak current at the highest scan rate used (50 V s^{-1}) was 3.5 x 10^{-4} amps. These values suggested a voltage drop of approximately 19 mV due to iR loss, small compared to the overall peak-to-peak separation of 290 mV, and should therefore have limited influence on the result. Since a macroelectrode rather than a microelectrode was used in this study some doubt is cast on the precise values reported. However, it is clearly evident that the rate of electron transfer was much reduced in comparison to literature values for closely related complexes where the ligand is directly coupled to the electrode surface [15, 17, 59].

A similar two-step assembly was used to immobilise the ruthenium complex containing the free carboxylic acid ligand. Cyclic voltammograms for $Ru(bpy)_2$-(pyridine-4-CO-NH-$(CH_2)_2$-SH)Cl recorded at various scan rates are provided in Figure 3.46 and the linear relationship between the peak current and the scan rate presented in Figure 3.47.

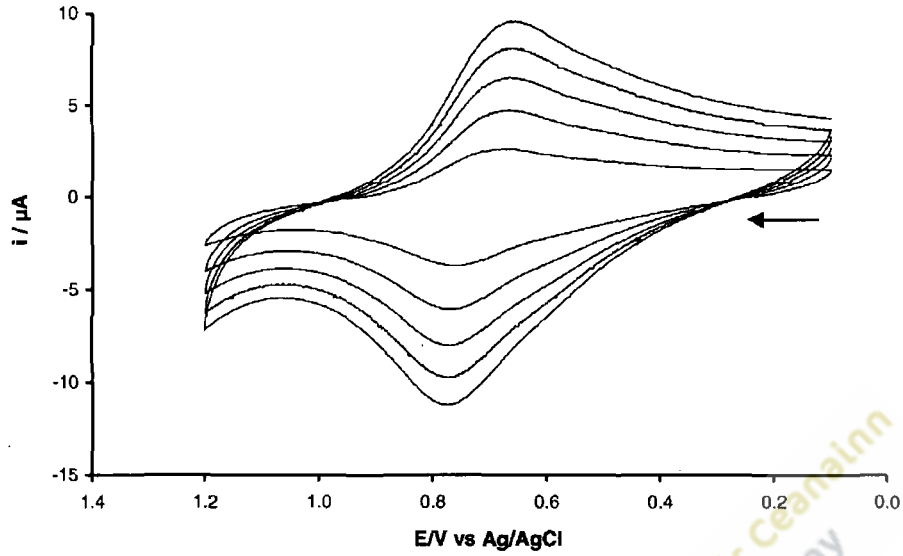

Figure 3.46. Cyclic voltammograms for a spontaneously adsorbed monolayer of $Ru(bpy)_2$-(pyridine-4-CO-NH-$(CH_2)_2$-SH)Cl on a 1 mm radius gold electrode. Scan rates from top to bottom are 1, 0.8, 0.6, 0.4 and 0.2 V s^{-1}. The supporting electrolyte used was 0.1 M $LiClO_4$. Cathodic currents are shown up and anodic currents are shown down.

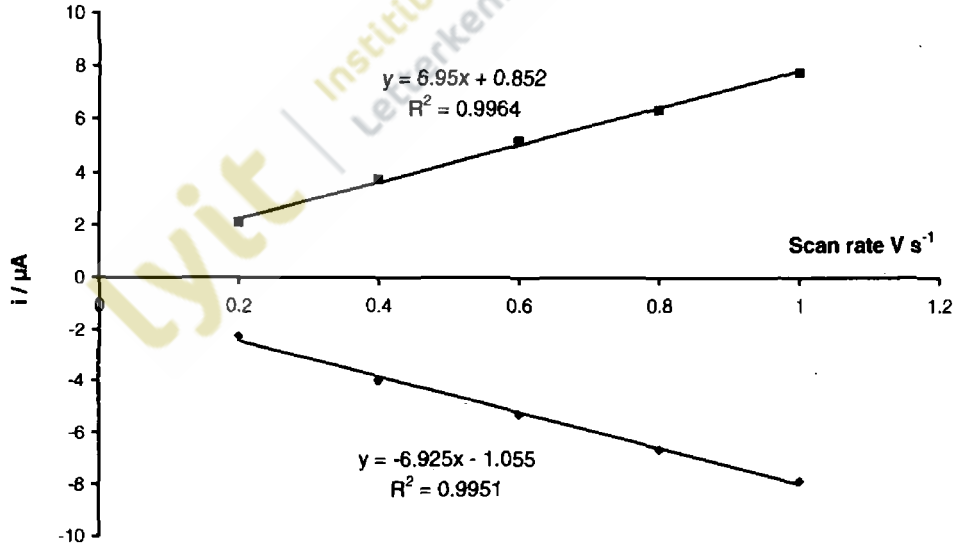

Figure 3.47. The relationship between the peak current and scan rate determined from the voltammograms in Figure 3.46. Cathodic currents are shown above the *x*-axis and anodic currents below the *x*-axis.

The surface coverage (Γ) was determined to be 1.71 x 10^{-10} mol cm^{-2}. The number of molecules per cm^2 was calculated and the area occupied by one molecule of the complex determined as 97 $Å^2$. For a closely packed monolayer in which the radius of the metal complex is approximately 6.7 Å, the area occupied per molecule would be 140$Å^2$. In this instance it would appear that multilayer formation had commenced, similar to that recorded with adsorption of the ruthenium complex containing the tetrazine ligand.

From the cyclic voltammograms for $Os(bpy)_2$-(pyridine-4-CO-NH-$(CH_2)_2$-SH)Cl (Figure 3.42) and $Ru(bpy)_2$-(pyridine-4-CO-NH-$(CH_2)_2$-SH)Cl (Figure 3.46) formal potentials of 0.26 V and 0.71 V were reported for the complexes respectively. Peak-to-peak separation for both complexes was 100 mV. There was some indication to suggest that photochemical decomposition may have commenced in the latter complex in aqueous electrolyte [81]. Whilst in principle both the chloride and/or the monodentate ligand could be photochemically displaced, replacement of the chloride ligand by water in aqueous solution has been reported previously [82]. Photochemical displacement has also been reported with other similar ruthenium complexes, even in the presence of low intensity light, but to our knowledge not for any osmium complexes [14].

In addition to the two-step assembly procedure used to form monolayers of the complexes which did not spontaneously adsorb to gold or platinum, a monolayer of the complex [$Os(bpy)_2$-(pyridine-4-COOH)-Cl] was formed on indium-coated tin oxide (ITO) glass slides through the free carboxyl group of the pyridine ligand [83]. Comparative studies have reported that when redox molecules containing a thiol ligand or a carboxylic acid ligand were spotted on gold and ITO electrodes, thiolated molecules preferentially adsorbed to a gold surface by a factor of 100:1, while those with a carboxyl group showed a preference for ITO by a factor of 45:1 [84]. This type of selective attachment, known as orthogonal self-assembly, whereby two unique molecular reagents can be simultaneously assembled onto two different surfaces has potential in the development of molecular wires where contact could be made across two closely spaced electrodes of different materials. Assembly on indium tin oxide is also of interest because this substrate has excellent electrical conductivity coupled with high optical

transparency, properties making it attractive as a surface for chemical modification with monomolecular layers for applications such as solar panel displays or biosensing [85, 86]. In addition use of this substrate provides a means of overcoming the drawback of quenched photocurrents produced during electron transfer on gold [87].

Cyclic voltammograms of the [Os(bpy)$_2$-(pyridine-4-COOH)-Cl] monolayer recorded at various scan rates are provided in Figure 3.48. The linear relationship between the peak current and the scan rate for this monolayer is presented in Figure 3.49. A desorption study of these monolayers was performed in blank electrolyte to determine the stability of the surface attachment.

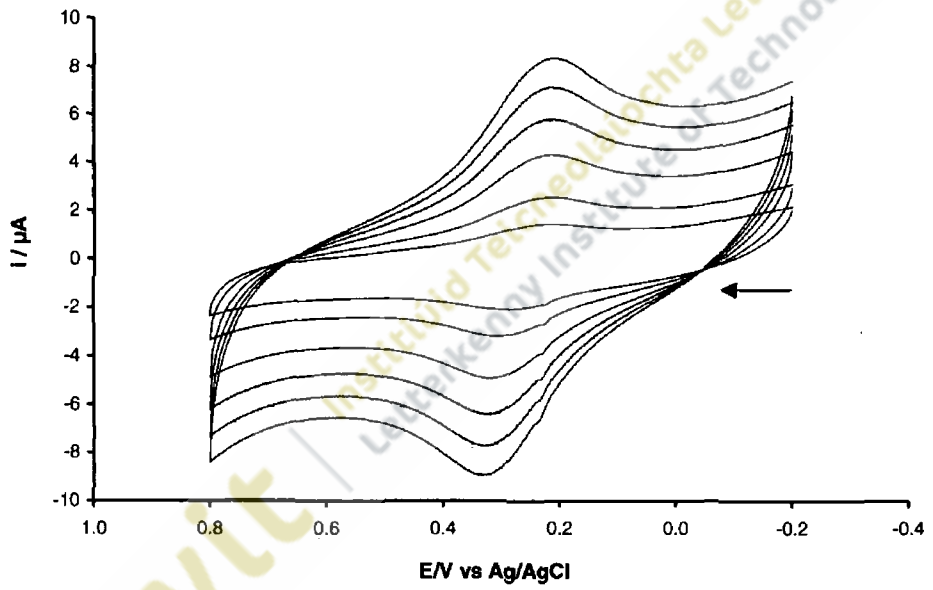

Figure 3.48. Cyclic voltammograms for a spontaneously adsorbed monolayer of [Os(bpy)$_2$-(pyridine-4-COOH)-Cl] on an ITO glass slide. Scan rates from top to bottom are 1.0, 0.8, 0.6, 0.4, and 0.2 V s^{-1}. The supporting electrolyte was 0.1 M $LiClO_4$. Cathodic currents are shown up and anodic currents are shown down.

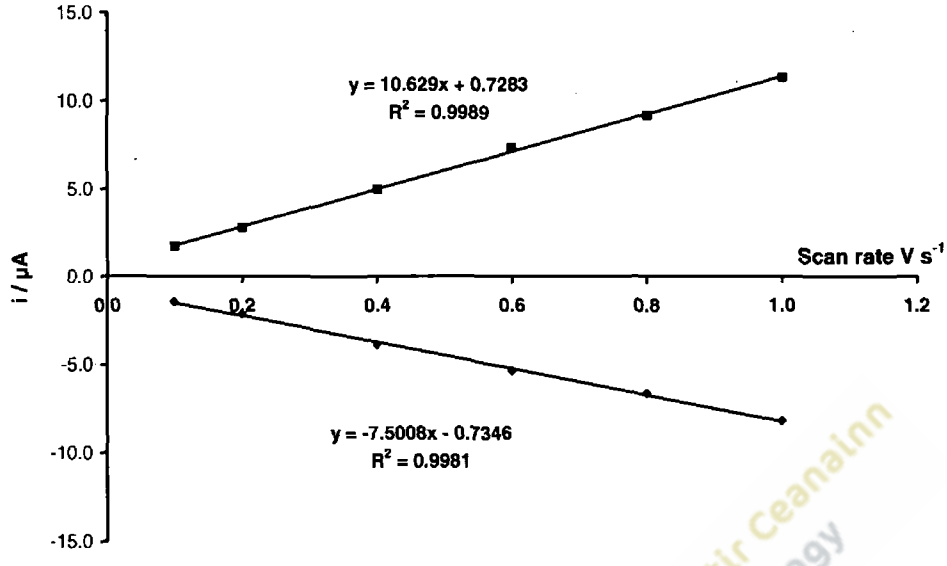

Figure 3.49. The relationship between the peak current and scan rate determined from the voltammograms in Figure 3.48. Cathodic currents are shown above the *x*-axis and anodic currents below the *x*-axis.

The linear relationship between the peak current and scan rate for this monolayer confirmed that the osmium complex was confined to the electrode surface. This was attributed to covalent coupling between the carboxylic acid group of the ligand and ITO. Surface coverage (Γ) was determined to be 9.4×10^{-11} mol cm^{-2}. The number of molecules per cm^2 was calculated and the area occupied by one molecule of the complex determined as 177 Å^2 suggesting that a closely packed monolayer had been formed on the electrode surface. In this example no allowance has been made for the surface roughness of the ITO surface and the geometric area was used to determine the surface coverage. Since the electrochemical area available to the adsorbing molecules may well be significantly greater than the geometric area the area occupied per molecule may in fact be somewhat greater than that reported above.

Cyclic voltammograms for desorption of [Os(bpy)$_2$-(pyridine-4-COOH)-Cl] from ITO into blank electrolyte (0.1 M $LiClO_4$) are shown in Figure 3.50. The faradaic current decreased with time as the complex desorbed into solution. As desorption progressed, somewhat surprisingly there was an increase in the peak-peak separation (ΔE) indicative of slower rates of electron transfer.

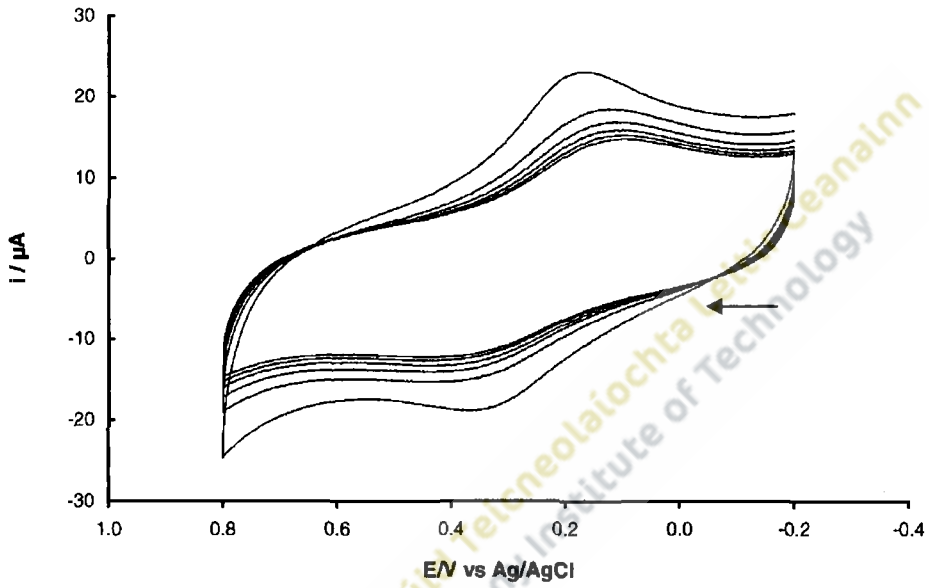

Figure 3.50. Cyclic voltammograms showing the desorption of [Os(bpy)$_2$-(pyridine-4-COOH)-Cl] from an ITO electrode into blank electrolyte (0.1 M $LiClO_4$). Cathodic currents are up and anodic currents are down. From top to bottom on the cathodic side, desorption times are 1, 60, 120, 180, 240 and 300 min. Scan rate 1 V s^{-1}.

The kinetics of desorption were followed by measuring the surface coverage as a function of time. The monolayer was very stable and even after 5 hr duration of repetitive cycling more than 50% of the monolayer still remained on the ITO surface. The steady decrease in surface coverage over time as the [Os(bpy)$_2$-(pyridine-4-COOH)-Cl] desorbed into blank electrolyte is shown in Figure 3.51.

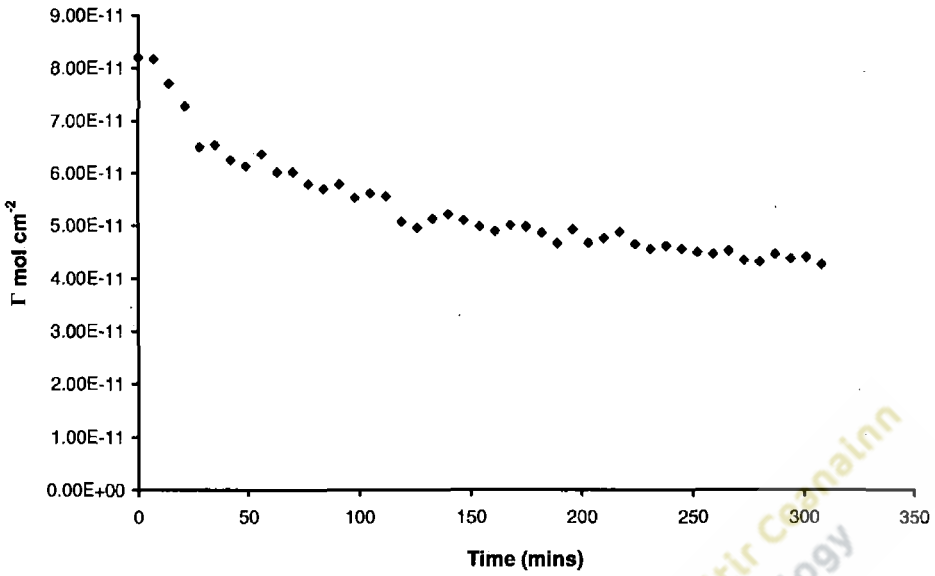

Figure 3.51. Surface coverage of [Os(bpy)$_2$-(pyridine-4-COOH)-Cl] desorbing from an ITO electrode into blank electrolyte (0.1 M $LiClO_4$). Surface coverage was determined from the cyclic voltammograms.

According to equation 22, an exponential decrease is expected in the surface coverage with time. A semi-log plot of surface coverage vs. time for [Os(bpy)$_2$-(pyridine-4-COOH)-Cl] prepared using data from Figure 3.51 is provided in Figure 3.52. With the exception of the first few points there was a linear relationship demonstrating that the process is in agreement with first order kinetics over durations extending at least until the surface coverage had decreased to less than 50% of its initial value.

The stability of the monolayer reflects a combination of the bonding strength of the free functional group on the adsorbing molecule and the substrate and also the attraction or repulsion between the adsorbate molecules [88]. There are several reports in the literature covering the kinetics of monolayer formation on ITO surfaces using different functional groups however limited information is available on the kinetics of desorption [89-91].

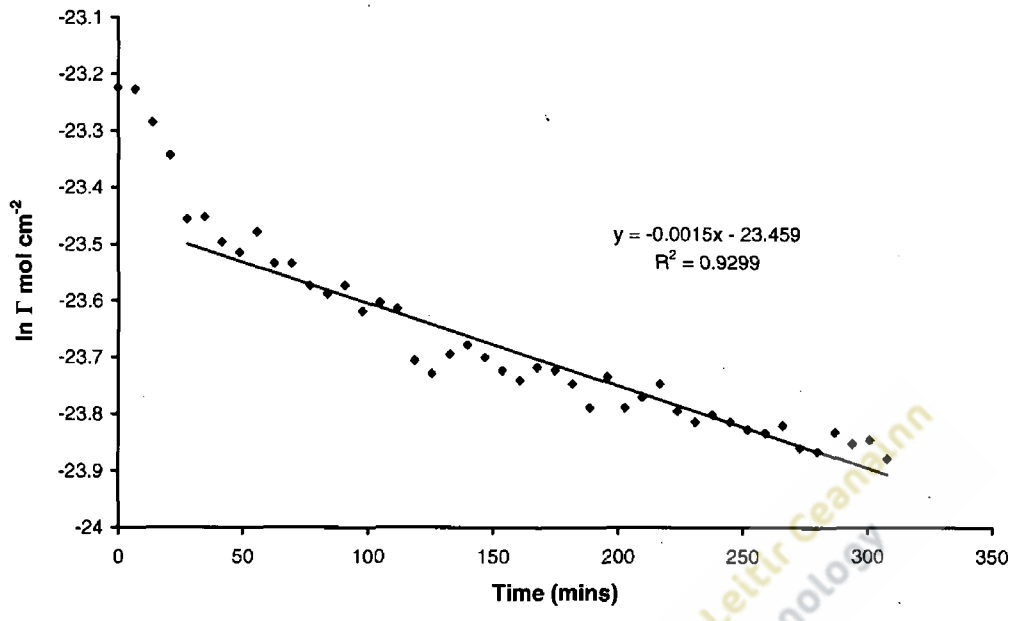

Figure 3.52. Semilog plot of the desorption data for [Os(bpy)$_2$-(pyridine-4-COOH)-Cl] from Figure 3.51.

From the slope of the best-fit line in Figure 3.52, the desorption rate constant was determined as 2.50 x 10^{-5} s^{-1}, similar to the values ranging from 2.33 x 10^{-5} s^{-1} to 5.66 x 10^{-5} s^{-1} reported for the other complexes investigated in this study where the pendant nitrogen of the pyridine is adsorbed to a platinum surface. The stability of the monolayer formed on ITO was similar to or better than that reported in the literature for osmium and ruthenium complexes containing pyridine ligands desorbing from gold and platinum and osmium thiol complexes desorbing from gold [36, 85, 87, 92].

3.3.4. Electron transfer rate constants for monolayers

Using the platinum electrodes with spontaneously-adsorbed monolayers of the three complexes under investigation, cyclic voltammograms were recorded in blank electrolyte (0.1 M $LiClO_4$) at scan rates ranging from 1-20,000 V s^{-1}. An example of the cyclic voltammograms for a monolayer of $[Os(bpy)_2\text{-}4\text{-}tet\text{-}Cl](PF_6)$ are shown in Figure 3.53.

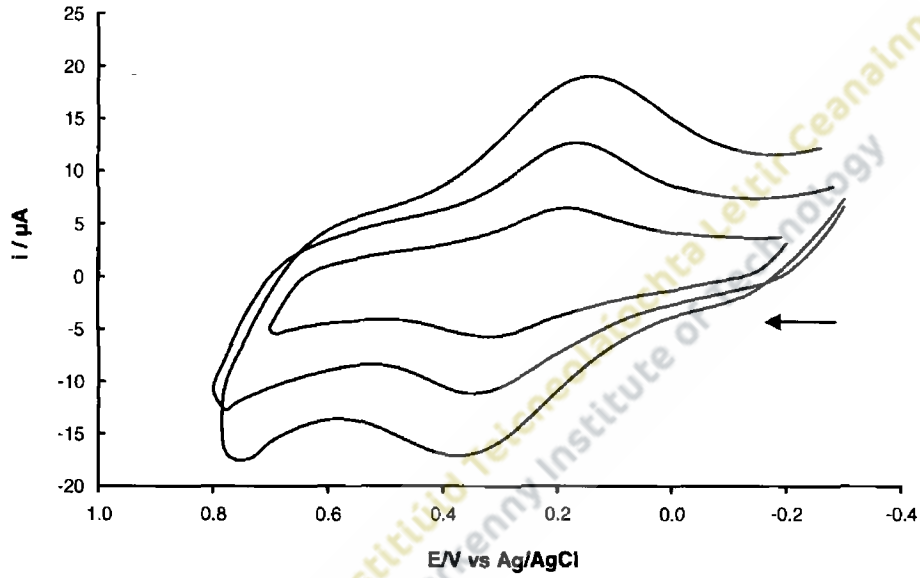

Figure 3.53. Cyclic voltammograms for a spontaneously adsorbed $[Os(bpy)_2\text{-}4\text{-}tet\text{-}Cl](PF_6)$ monolayer on a 12.5 µm radius Pt microelectrode. The supporting electrolyte used was 0.1 M $LiClO_4$. Cathodic currents are up and anodic currents are down. Scan rates shown from top to bottom on the cathodic side are 20,000, 10,000 and 5,000 V s^{-1}.

Using the Laviron approach shown in Figure 3.54 the heterogeneous electron transfer rate constant (k^o) was determined from the peak-to-peak separation from each series of voltammograms [11].

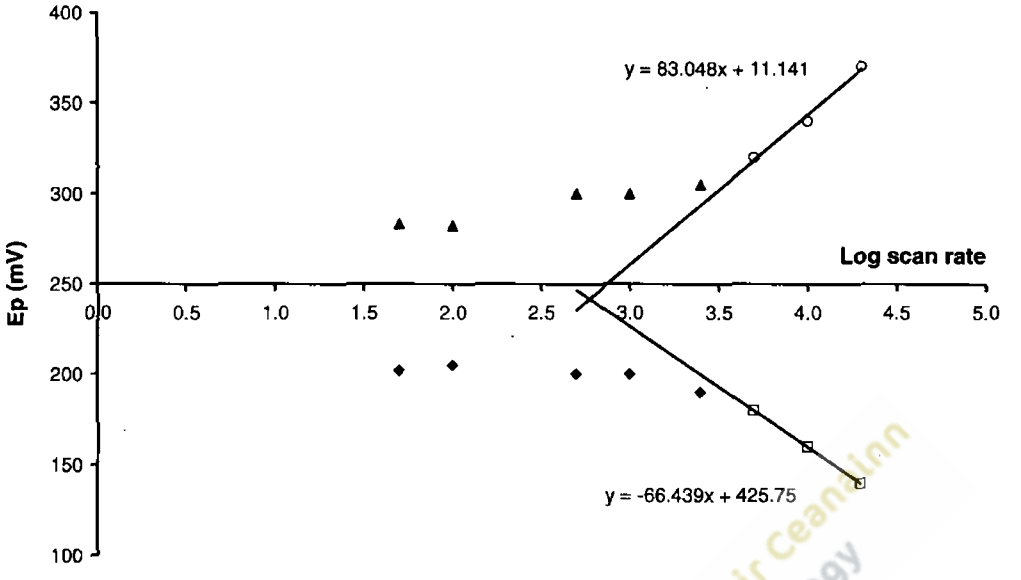

Figure 3.54. Laviron approach for determination of the standard rate constant. Plots of the peak potential vs. log (scan rate) for a monolayer of $[Os(bpy)_2\text{-}4\text{-}tet\text{-}Cl](PF_6)$ on a 12.5 μm radius platinum microelectrode. The potentials for the cathodic currents are shown above the *x*-axis and the anodic currents below the *x*-axis.

For this complex the electron transfer rate constant was determined to be $1.03 \times 10^4\ s^{-1}$ and the transfer coefficient (α) 0.44. The specific conductance of the electrolyte used was 0.014 $ohms^{-1}\ cm^{-1}$ and compensation was made for ohmic loss as in the solution phase analysis.

Different to determination of the heterogeneous electron transfer rate constants in solution undertaken previously, each complex in this instance was immobilised and hence diffusion to the electrode surface was eliminated from the equation. At slow scan rates, the anodic and cathodic peak potentials remained relatively constant with ΔE_p values of 94 ± 8 mV. At higher scan rates, the peak potential separation increased significantly. The best-fit straight line through the data points where increases in ΔE_p occurred linearly was used to determine the electron transfer rate constant from the intercept on the *x*-axis and the slope of the line in conjunction with the Laviron equation shown in equation 23:

$$k^o = \frac{\alpha n F v_a}{RT} = \frac{(1-\alpha) n F v_c}{RT} \qquad (23)$$

where α is the transfer coefficient, v is the scan rate and F, R and T have their usual meaning.

At high scan rates, slow electron transfer causes the potential of the anodic and cathodic peak separation to increase. Under ideal circumstances this increase would be evenly distributed about the formal potential and the transfer coefficient (α) would have a value of 0.5. In the example shown in Figure 3.54 the slopes of the best-fit lines are similar though not identical as would occur in an ideal situation. When extrapolated back to the horizontal axis, these two lines did not intersect at the formal potential as would have been expected. With the complex $[Os(bpy)_2\text{-}4\text{-}tet\text{-}Cl](PF_6)$ the transfer coefficient (α) was determined as 0.44, close to the ideal value of 0.5.

For the three complexes under investigation, the heterogeneous electron transfer rate constants before and after iR compensation and the transfer coefficients are provided in Table 3.10.

Metal complex	k^o (s^{-1}) No iR comp	k^o (s^{-1}) iR comp	α iR comp
$[Os(bpy)_2\text{-}4\text{-}tet\text{-}Cl](PF_6)$.	9.0×10^3	1.0×10^4	0.44
$[Ru(bpy)_2\text{-}4\text{-}tet\text{-}Cl](PF_6)$.	5.7×10^3	9.8×10^3	0.44
$[Ru(bpy)_2(4\text{-}tet)_2](PF6)_2$	1.4×10^4	1.7×10^4	0.48

Table 3.10. Electron transfer rate constants (k^o) before and after iR compensation and transfer coefficients for the three complexes.

Self-assembled monolayers on electrode surfaces are useful in the study of electron transfer because they are stable and structurally well-defined. In addition, because they have a controllable thickness, investigations of electron transfer through monolayers can be undertaken without any complications associated with diffusion of the redox species from the bulk solution to the electrode surface [93]. Such characteristics make monolayers very useful for investigations of electron transfer kinetics between a redox species and an electrode [94, 95].

Peak-to-peak separations (ΔE_p) for the three tetrazine complexes under investigation were relatively constant up to a scan rate of approximately 1000 V s^{-1} but increased significantly at faster scan rates (Figures 3.54). These increases may be attributed to two processes; slow heterogeneous electron transfer and/or distortions due to ohmic loss. Distortions become particularly significant with higher scan rates and larger electrodes [96]. In these investigations, ohmic loss was minimised by using a high concentration of supporting electrolyte and a microelectrode of 12.5 μm radius. However, using the Laviron approach and the complexes under study, scan rates of up to 20,000 V s^{-1} were necessary to achieve sufficient separation of the peak-to-peak potentials (ΔE_p). With such high scan rates, compensation for distortions due to ohmic loss was essential [27, 30]. Table 3.10 showing k^o values before and after iR compensation highlighted the erroneous values that would have been reported if effects due to ohmic loss had been ignored. Heterogeneous electron transfer rate constants after iR compensation were always higher than those before iR compensation.

The values reported in this study are similar to those reported in the literature for related complexes. In a study investigating the influence of pH on the heterogeneous electron transfer rate constant of $[Os(bpy)_2\text{-}4\text{-}tet\text{-}Cl]^+$ on a gold microelectrode, values of k^o reported were 1.1 x 10^4 s^{-1} at pH 6.0 and 1.2 x 10^3 s^{-1} at pH 0.9 [59]. The k^o value reported for the same complex with an unprotonated bridging ligand in this study is in excellent agreement with the k^o value at pH 6. The effect of protonation of the bridging ligand on the heterogeneous electron transfer rate constant has also been demonstrated with other related complexes including the monosubstituted $[Os(bpy)_2\text{-}4\text{-}bpt\text{-}Cl]^+$ where 4-bpt is

3,5-bis(pyridin-4-yl)-1,2,4-triazole and the disubstituted complex $[Os(bpy)_2(p3p)_2]^{2+}$ where p3p is 4,4'-trimethylenedipyridine [15, 38]. With monolayers of conjugated and non-conjugated, monosubstituted osmium complexes on platinum microelectrodes, a heterogeneous electron transfer rate constant of 9.4×10^3 s^{-1} for the conjugated $[Os(bpy)_2(bpe)Cl]^+$ complex where the ligand bpe is *trans*-1,2 bis(4-pyridyl)ethylene and 3.0×10^5 s^{-1} for the non-conjugated $[Os(bpy)_2(p2p)Cl]^+$ complex where the ligand p2p is 1,2-bis(4-pyridyl)ethane have been reported. Significantly the k^o value was approximately 30-times larger in the p2p-complex with a non-conjugated bridging ligand [96]. Clearly for comparative assessments of values of k^o it is essential that not only the pH and the structure of the bridging ligand be considered but also the nature of the electrode material. Using chronoamperometry, the heterogeneous electron-transfer rate constants for $[Os(OMe\text{-}bpy)_2(p3p)Cl]^+$, where OMe-bpy is 4,4'-dimethoxy-2,2'-bipyridyl were determined on platinum, mercury, gold, silver, carbon, and copper microelectrodes. Values of k^o from 4.0×10^4 s^{-1} on platinum to 3.0×10^3 s^{-1} on carbon demonstrated the profound effect of the electrode material on electron transfer kinetics [97].

Heterogeneous electron transfer rate constants for the ruthenium monosubstituted and disubstituted complexes reported in this study are of a similar order of magnitude to those for related complexes in the literature. The heterogeneous electron transfer rate constant of $[Ru(bpy)_2PIC]^{2+}$ where PIC is 2-(4-carboxyphenyl)imidazo[4,5-f][1,10]phenanthroline on a fluorine doped tin oxide microelectrode ranged from 9.5×10^3 s^{-1} for oxidation to 2.2×10^4 s^{-1} for reduction of the ruthenium centre within the monolayer [98]. For the thiolated ruthenium complex $[Ru(bpy)_2(bpySH)]^{2+}$, a k^o value of 0.9×10^4 s^{-1} was reported, a similar magnitude to the ruthenium tetrazine complexes in this study [74]. Somewhat elevated k^o values ranging between 2.1×10^5 s^{-1} to 1.4×10^6 s^{-1} were reported for the $[Ru(bpy)_2$ 2,2′:4,4″:4′4″-quarterpyridyl$]^{2+}$ complex. The range of k^o values for this ruthenium bipyridyl complex substituted with a bidentate ligand varied by almost an order of magnitude depending on the equilibration time of the assembled monolayers over a 10-20 hour period. The higher values for k^o suggested that adsorption involved binding of both available pyridines to the platinum surface [52].

Although the k^o value determined under similar conditions for the disubstituted ruthenium complex was larger than that for either of the two monosubstituted complexes, the magnitude of the variation was not considered to be of undue significance given the scale of the variations reported in the literature.

3.4. References

1. Laviron, E.J. *Electroanal. Chem.*, 1979, 101, 19-28.
2. Reeves, J.H., Song, S., Bowden, D.F. *Anal. Chem.*, 1979, 97, 135-149.
3. Chidsey, C.E.D. *Interface Science*, 1991, 251, 919-922.
4. Finklea, H.O., Hanshew, D. *J. Am. Chem. Soc.*, 1992, 114, 3175-3181.
5. Collard, D.M., Fox, M.A. *Langmuir*, 1991, 7, 1192-1197.
6. Finklea, H.O., Ravenscroft, M.S., Snider, D.A. *Langmuir*, 1993, 9, 223-227.
7. Widrig, C.A., Chung, C., Porter, M.D. *J. Electroanal. Chem.*, 1991, 310, 335-359.
8. Haddox, R.M., Finklea, H.O. *J. Phys. Chem. B*, 2004, 108, 1694-1700.
9. Koichi, A., Kakuichi, T. *J. Electroanal. Chem.*, 1998, 452, 188-192.
10. Finklea, H.O., Yoon, K., Allen, C.J. *J. Phys. Chem. B*, 2001, 105, 3088-3092.
11. Forster, R.J., O'Kelly, J.P. *J. Electrochem. Soc.*, 2001, 148, 31-37.
12. Hudson, J.E., Abruña, H.D. *J. Phys. Chem.*, 1996, 100, 1036-1042.
13. Forster, R.J. *Inorg. Chem.*, 1996, 35, 3394-3403.
14. Forster, R.J., Figgemeier, A., Lees. A.C., Hjelm, J. *Langmuir*, 2000, 16, 7867-7870.
15. Forster, R.J., O'Kelly, J.P. *J. Phys. Chem.*, 1996, 100, 3695-3704.
16. Forster, R.J., Keyes, T.E. *J. Phys. Chem. B*, 1998, 102, 10004-10012.
17. Figgemeier, E., Merz, L. *J. Phys. Chem. B*, 2003, 107, 1157-1162.
18. Forster, R.J., Vos, J., Keyes, T.E. *Analyst*, 1998, 123, 1905-1911.
19. Acevedo, D., Bretz, R.L., Tirado, J.D., Abruña, H.D. *Langmuir*, 1994, 10, 1300-05.
20. Tirado, J.D., Abruña, H.D. *J. Phys. Chem.*, 1996, 100, 4556-4563.
21. Folkers, J.P., Labinis, P.E., Whiteside, G.M. *J. Phys. Chem.*, 1994, 98, 563-571.
22. Rowe, C.K., Creager, S.E. *Langmuir*, 1994, 10, 1186-1192.
23. Tirado, J.D., Acevedo, D., Bretz, R.L., Abruña, H.D. *Langmuir*, 1994, 10, 1971-79.
24. Tamada, K., Hara, M., Sasabe, H., Knoll, W. *Langmuir*, 1997, 1558.
25. Bretz, R., Abruña, H.D. *J. Electroanal. Chem.*, 1995, 388, 123-132.
26. Trassati, S. *J. Electroanal. Chem. & Interfacial Chem.*, 1974, 53, 335-363.
27. Laviron, E. *J. Electroanal. Chem.*, 1995, 382, 111-127.
28. Song, D., Soriaga, M.P., Hubbard, A.T. *J. Electroanal. Chem. Interfacial Electrochem.*, 1986, 201, 153.

29. Song, D., Soriaga, M.P., Hubbard, A.T. *J. Electrochem. Soc.*, 1987, 134, 874.
30. Gyeong, S.B. *Bull. Korean Chem. Soc.*, 2001, 22, 281.
31. Brevnov, D.A., Finklea, H.O. *J. Electroanal. Chem.*, 2001, 500, 100-107.
32. Buess-Herman, C. *Prog. Surface Science*, 1994, 46, 335-375.
33. Murray, R.W., Bard, A.J. *J. Electroanal. Chem.*, 1984, 13, 191.
34. Chidsey, C.E.D., Bertozzi, T. *J. Am. Chem. Soc.*, 1990, 112, 4301.
35. Finklea, H.O., Hanshew, D.D. *J. Am. Chem. Soc.*, 1992, 114, 3173.
36. Forster, R.J., Faulkner, L.R. *J. Am. Chem. Soc.*, 1994, 116, 5453- 5461.
37. Finklea, H.O., Yoon, K., Chamberlain, E., Allen, J., Haddox, R. *J. Phys. Chem. B*, 2001, 105, 3088-3092.
38. Walsh, D. A., Keyes, T. E., Forster, R. J. *J. Phys. Chem. B*, 2004, 108, 2631-2636.
39. Bard, A.J., Abruña, H.D. *J. Phys. Chem.*, 1993, 97, 7147-7173.
40. Takehara, K., Takemura, H., Ide, Y. *Electrochem. Acta*, 1994, 39, 817.
41. Mukae, F., Takehara, K., Takemura, H. *Bull. Chem. Soc. Japan*, 1996, 69, 2461.
42. Glenn, J.D.H., Bowden, E.F. *Chem. Lett.*, 1996, 399.
43. Kanayama, N., Kitano, H. *Langmuir*, 2000, 16, 577.
44. Zhang, S., Wang, N., Yu, H., Niu, Y., Sun, C. *Bioelectrochem.*, 2005, 67, 15-22.
45. Woods, R. Chemisorption at electrodes. In: *Electroanalytical Chemistry*, A.J. Bard (Ed.), Marcel Dekker, New York, 1976, 9, 1.
46. Tsierkezos, N.K. *J. Solution Chem.*, 2007, 36, 289-302.
47. Bishop, E., Galus, Z. *Pure & Applied Chem.*, 1979, 51, 1575-1582.
48. Goldsmith, J.I., Takada, K., Abruña, H.D. *J. Phys. Chem. B*, 2002, 106, 8504-13.
49. Loughman, P.J. *Ph.D. Thesis*, Dublin City University, 2001.
50. Carter, M.T., Rodriguez, M., Bard, A.J. *J. Am. Chem. Soc.*, 1989, 111, 8901-8911.
51. Wipf, D.O., Kristensen, E.W., Deakin, M.R., Wightman, M. *Anal. Chem.*, 1988, 60, 306-310.
52. Forster, R.J., Pellegrin, Y., Leane, D., Brennan, J.L. Keyes, T.E. *J. Phys. Chem. C*, 2007, 111, 2063-2068.
53. Kadish, K.M., Ding, J.Q., Mallinski, T. *Anal. Chem.*, 1984, 56, 1741-1744.
54. Feeney, R., Samuel P., Kounaves, S.P. *Electrochemistry Comm.*, 1999, 1, 453-458.
55. Brett, C.M.A., Brett, A.M.O. *Electroanalysis*, Oxford University Press, 1998.

56. Forster, R.J., O'Kelly, J.P. *J. Electroanal. Chem.*, 2001, 498, 127-135.
57. Saji, T.J., Aigagui, S.J. *J. Electroanal. Chem.*, 1975, 63, 401.
58. Feeny, R., Kounaves, S.P. *Electrochem. Comm.*, 1999, 1, 453-458.
59. Walsh, D.A., Keyes, T.E., Hogan, C.F., Forster, R.J. *J. Phys. Chem. B*, 2001, 105, 2792-2799.
60. Forster, R.J. *The Electrochemical Society Interface*, 2000, 24, 28.
61. Sakata, T., Nakamura, H. *Bull. Chem. Soc. Japan*, 2001, 74, 2285-2293.
62. Brown, A.P., Anson, F.C. *Anal. Chem.*, 1977, 49, 1589.
63. Lane, R.F., Hubbard, A.T. *J. Phys. Chem.*, 1973, 77, 1411-1421.
64. Lane, R.F., Hubbard, A.T. *J. Phys. Chem.*, 1973, 77, 1401-1410.
65. Soriaga, M.P., Hubbard, A.T. *J. Phys. Chem.*, 1984, 88, 1089-1094.
66. Grassian, V.H., Muetterties, E.L. *J. Phys. Chem.*, 1986, 90, 5900-5907.
67. Song, D., Soriaga, M.P., Vjeira, K.L., Zapien, D.C., Hubbard, A.T. *J. Phys. Chem.*, 1985, 89, 3999-4002.
68. Bretz, R., Abruña, H.D. *J. Electroanal. Chem.*, 1996, 408, 199-211.
69. Rosei, F., Schunack, M., Naitoh, Y., Jiang, P., Gourdon, A., Laegsgaard, E., Stensgaard, I., Joachim, C., Besenbacher, F. *Prog. Surface Sci.*, 2003, 71, 95-146.
70. Soriaga, M. P., Hubbard, A. T. *J. Am. Chem. Soc.*, 1982, 104, 2735-2742.
71. Stern, D.A., Laguren-Davidson, L., Frank, D.G., Gui, J.Y., Lin, C.H., Lu, F., Salaita, G.N., Walton, N., Zapien, D.C., Hubbard, A.T. *J. Am. Chem. Soc.*, 1989, 111, 877-891.
72. Schwartz, D.K. *Annual Rev. Chem.*, 2001, 52, 107-137.
73. Stickney, J.L., Soriaga, M.P., Hubbard, A.T. *J. Electroanal. Chem. Inter. Electrochem.*, 1985, 125, 73-88.
74. Bertoncello P., Dennany, L., Forster, R.J., Unwin, P.R. *Anal. Chem.*, 2007, 79, 7549-7553.
75. Bartell, L.S., Betts, J.F. *J. Phys. Chem.*, 1960, 64, 1075-76.
76. Bain, C.D., Troughton, E.B., Tao, Y.T., Evall, J., Whitesides, G.M., Nuzzo, R.G. *J. Am. Chem. Soc.*, 1989, 111, 321-335.
77. Levine, O., Zisman, W.A. *J. Phys. Chem.*, 1957, 61, 1188-1196.
78. Acevedo, D., Abruña, H.D. *J. Phys. Chem.*, 1991, 95, 9590-9594.

79. Inose, Y., Moniwa, S., Aramata, A., Yamagishi, A., Naing, K. *Chem. Comm.*, 1997, 1, 111-112.

80. Campbell, J.L.E., Anson, F.C. *Langmuir*, 1996, 12, 4008-4014.

81. Buchanan, B.E., McGovern, E., Harkin, P., Vos, J.G. *Inorg. Chim. Acta*, 1988, 154, 1.

82. Haas, O., Kriens, M., Vos, J.G. *J. Am. Chem. Soc.*, 1981, 103, 1318.

83. Hong, S., Zhu, J., Mirkin, C.A. *Science*, 1999, 286, 523.

84. Gardner, T.J., Frisbie, D.C., Wrighton, M.S. *J. Am. Chem. Soc.*, 1995, 117, 6927-6933.

85. Kelepouris, L., Krysinski, P., Blanchard, G.C. *J. Phys. Chem. B*, 2003, 107, 4100-4106.

86. Tang, C., Feller, L., Rossbach, P., Keller, B., Vörös, J., Textor, M., Tosatti, S. *Surface Science*, 2006, 600, 1510-1517.

87. Imahori, L., Nishimura, Y., Norieda, H., Karita, H., Yamasaki, I., Sakata, Y. *Chem. Comm.*, 2000, 661, 2.

88. Brewer, S.H., Brown, D.A., Franzen, S. *Langmuir*, 2002, 18, 6857-6865.

89. Zotti, G., Schiavon, G., Zecchin, S., Berlin, A., Pagani, G. *Langmuir*, 1998, 14, 1728-1733.

90. Hedges, D.H.P., Richardson, D.J., Russell, D.A. *Langmuir*, 2004, 20, 1901-1908.

91. Elliott, C.M., Caramori, S., Bignozzi, C.A. *Langmuir*, 2005, 21, 3022-3027.

92. Safford, L.K., Weaver, M.J. *J. Electroanal. Chem.*, 1992, 96, 6962.

93. Bard, A.J., Abruña, H.D., Chidsey, C.E., Faulkner, L.R., Feldberg, S.W., Itaya, K., Majda, M., Melroy, O., Murray, R.W., Porter, M.D., Soriaga, M., White, H.S. *J. Phys. Chem.*, 1993, 97, 7147-7173.

94. Hong, H.G., Park, W., Yu, E. *Bull. Korean Chem. Soc.*, 2000, 21-25.

95. Smith, C.P., White, H.S. *Anal. Chem.*, 1992, 64, 2398-2405.

96. Forster, R.J., Figgemeier, E., Loughman, P., Lees, A., Hjelm, J., Vos, J.G. *Langmuir*, 2000, 16, 7871-7875.

97. Forster, R.J., Loughman, P., Keyes, T.E. *J. Am. Chem. Soc.*, 2000, 122, 11948.

98. Forster, R.J., Pellegrin, Y., Keyes, T.E. *Electrochem. Comm.*, 2007, 9, 1899-1906.

4. Application of redox probe-labelled DNA to the development of electrochemical-DNA biosensors

4. 1. Introduction

Electrochemical DNA (E-DNA) biosensors have attracted considerable attention due to their potential for commercial application in diverse fields including clinical medicine, food analysis, environmental monitoring, biosecurity and defence. Advantages reported for such sensors include their high sensitivity and specificity allowing the analysis of complex mixtures without the need for initial purification, their low cost of production, the simple instrumentation requirements for their operation, the speed of response, their accuracy, and their potential for miniaturisation allowing portable devices to be developed for point-of-care diagnostics and field use [1-8].

The development of DNA biosensors has employed a range of different strategies for the detection of hybridisation. The attachment of labels to the target DNA, for example by biotin-modification of the target and subsequent complexing with avidin-modified fluorescent labels or the use of redox-active labels to modify the target and the inference of hybridisation by detection of electrochemical change have both been utilised for hybridisation detection [9-12]. However, biosensors based on these operational models are disadvantaged by the need for pre-labelling of the target DNA before detection can proceed, complicating use of the assay for the end-user. Electrochemical detection of the hybridisation event has also been achieved with redox-active intercalating substances with a higher affinity for dsDNA than ssDNA allowing hybridisation detection through the production of an increased electrochemical signal [13-19]. Such systems however, depend on the difference between the pre- and post-hybridisation electrochemical signal and are disadvantaged by the presence of a significant background signal limiting the sensitivity of such devices. More recently, electrochemical DNA biosensors based on an immobilised molecular beacon or hairpin DNA model, with a redox-active label rather than a fluorophore have been reported. Such E-DNA biosensors have generated considerable interest in the field of sensor technology because of the reported higher sensitivity and specificity of

molecular beacons compared to linear probes in solution-based hybridisation detection; the fact that such systems are reagentless, i.e. no reagents other than the DNA sample need to be added; and the potential for regeneration of such systems after use, allowing possibly many measurements with the same sensor [20-26].

A widely used approach for the construction of E-DNA biosensors on gold electrodes is the two-step procedure comprising self-assembly of thiolated DNA probes (SH-ssDNA) on the conducting electrode surface followed by coverage of the remaining surface by mercaptoethanol or mercaptohexanol [27-30]. The thiol molecules covalently attached to the end of the ssDNA allow spontaneously adsorbed monolayers to assemble on the surface from dilute solutions of the probe DNA. The role of this immobilised probe is to provide a capture site at which hybridisation may occur with a specific complementary sequence of DNA. In solution, hybridisation has been shown to involve first a nucleation step and then a "zippering-up" of the two DNA strands. The hybridisation process at solid surfaces has been assumed to closely resemble that which occurs in solution, however the kinetics are inevitably reduced. Surface hybridisation rates have been reported to be 20-40 times slower than solution phase rates for identical sequences and conditions [31, 32]. This reduction has been attributed principally to the loss of configurational freedom following immobilisation of ssDNA probe. As a consequence, it is now accepted that the success of DNA diagnostic sensors depends to a large extent on optimisation of the surface chemistry at the recognition interface [33]. Many factors influence this interface including:

- Nature, cleanliness and reproducibility of the substrate for immobilisation [27, 34-41]
- Surface chemistry used for probe attachment [42, 43]
- Functional group used for covalent attachment of ssDNA to the surface [44]
- Choice and ionic strength of the buffers [27]
- Concentration and pre-treatment of the probe prior to immobilisation [36,45-47]
- Duration of the immobilisation step in the deposition solution [48]
- Probe density on the electrode surface [37, 39]
- Nature of diluent spacer molecules used to fill vacant sites on the electrode surface after probe attachment [12, 47, 49-52].

However, understanding and optimising the conditions for hybridisation represents only one aspect to the development of a successful E-DNA sensor; of equal if not greater significance is the ability to detect whether specific hybridisation has occurred.

Considerable research since the 1990's has been undertaken on the use of transition metal complexes as reporting systems in electrochemical molecular devices such as biosensors. In many of these applications, the redox properties of iron, ruthenium and osmium have been exploited. Ferrocene has been shown to be a relatively stable detection label with simple one electron electrochemistry within a suitable potential range for DNA sensor applications and as a consequence several research groups have attached ferrocene to the end of DNA strands [53-64]. In most instances, the attachment has been performed in solution rather than by a two-step assembly on the surface, where firstly a monolayer of thiolated DNA is immobilised and then suitably functionalised redox labels are attached. More recently, the properties of osmium bipyridyl complexes, in particular their low redox potentials, have been exploited. Osmium complexes are particularly advantageous since extensive knowledge exists on their synthesis with a range of bridging ligands. Such knowledge allows the redox potentials to be tuned for a particular application by a careful choice of electron donating or electron withdrawing bridging ligands [65-67]. For the future, the immobilisation of mixtures of DNA probes labelled with different redox molecules whose potentials are suitably separated, would support the multiplex identification of more than one organism or species in a single measurement, of particular significance for the development of electrochemical DNA microchips and point-of-care diagnostics.

This chapter reports on attempts to assemble an E-DNA biosensor using a thiolated DNA probe labelled with a ferrocene molecule as the redox-active label on both a disposable sensor and a gold disc electrode. For these investigations the thiolated hairpin probe with attached ferrocene label was provided by commercial oligo suppliers. Following assembly and characterisation of the biosensors, hybridisation studies using complementary target DNA were undertaken using the E-DNA biosensor assembled on the gold disc electrode. The knowledge and practical experience from these investigations was then applied to the assembly and characterisation of an E-DNA biosensor using the osmium complex $[Os(bpy)_2$-

(pyridine-4-COOH)-Cl] synthesized in Chapter 2 as the redox label. Unlike the ferrocene label which is available as an optional modification from several commercial suppliers of oligos, agreement to attempt labelling with an osmium complex by specialist oligo suppliers proved to be prohibitively expensive. As a consequence, attachment of the osmium complex was attempted in-house. A successful procedure for the attachment of the osmium complex [$Os(bpy)_2$-(pyridine-4-COOH)-Cl] to the DNA hairpin probe was developed. This two-step procedure comprised formation of a monolayer of a commercially available 3' thiolated ssDNA hairpin probe having a free amine functional group at the 5' end, followed by covalent bonding of the osmium redox label to the free amine group using carbodiimide coupling. Osmium bipyridyl molecules possess simple one electron electrochemistry, are stable in more than one oxidation state and have a suitable redox potential for DNA biosensor applications. However there are no reports in the literature describing the covalent attachment of this type of molecule to ssDNA probes for the detection of hybridisation.

4.2. Apparatus and Reagents

Four types of sensor/electrode configurations were used in this investigation. Disposable, screen printed sensors (product code AC1.W.R.) comprising a gold working electrode of 0.5 mm radius, a Ag/AgCl reference electrode and a gold auxillary electrode configured on a ceramic base were manufactured by BVT Technologies A.S., Czech Republic and supplied by Palm Instruments BV, Holland. Disposable BVT gold working electrodes of 0.5 mm radius, screen printed on a ceramic base (product code AC3.W.) were supplied by the same company. Gold working electrodes comprising an electrodeposited rectangular electrode of 3 mm x 2 mm were fabricated and supplied by the Tyndall Institute, University College Cork. Commercial gold disc electrodes of 1 mm radius were supplied by IJ Cambria, Wales. Polishing of gold disc electrodes was performed with alumina (Buehler, Chicago, Illinois) on nap polishing pads (Struers).

A customised 21-base pair oligonucleotide specific to the blue mussel *Mytilus edulis*: 5' Ferrocene-$(CH_2)_6$-CCG AAC GCA CGG CTC TGA CCT CGC GGA GTT CGG-$(CH_2)_6$-S-S-$(CH_2)_6$-OH 3' was supplied by Friz Biochem, Germany. At each end of the probe sequence was a 6-bp complementary stem sequence (underlined) to allow formation of a hairpin loop. The electroactive label, ferrocene carboxylic acid was attached to the 5' end spaced from the oligo by six methylene units. At the 3' end spaced from the oligo by a six methylene linker was a disulphide bond for attachment to the gold surface. A complementary 21-bp target sequence: 5' TCC GCG AGG TCA GAG CCG TGC 3' was also supplied by Friz Biochem.

A customised 17-base oligonucleotide specific to the bacterial genus *Salmonella* spp.: 5' SH-$(CH_2)_6$- GCA GTA ACA AGA ATA AAA CGC CAC TGC- $(CH_2)_6$- NH_2 3' was supplied by Sigma- Aldrich. At each end of the probe sequence was a 5-bp complementary stem sequence (underlined) to allow formation of a hairpin loop. The 5' end was modified with a thiol group for attachment to the gold surface spaced from the oligo by six methylene units. At the 3' end was an amine group similarly spaced from the oligo by six methylene units. A complementary 17-bp target sequence was supplied by Sigma-Aldrich.

All DNA probes were reconstituted at a stock concentration of 100 μM using 10 mM Tris-EDTA (TE) buffer (Sigma Aldrich) at pH 7.4. Stock solution was divided into 10μl aliquots and stored at -20°C. Prior to utilisation, probe ssDNA stock solution was diluted to the required concentration using 10 mM Tris/HCl buffer (Sigma Aldrich) in 1M $NaClO_4$. Target ssDNA stock solution was diluted to the required concentration in hybridisation buffer comprising 10 mM Tris/HCl, 0.1M KCl and 1M $NaClO_4$. All buffers and reagents were prepared with ultrapure water from a Millipore Milli-Q system and sterilised prior to use. Reconstitution and dilution of all oligos was performed in a laminar flow cabinet using aseptic techniques.

Unless stated all electrochemical measurements were performed at room temperature using a CHI 660A electrochemical workstation (CH Instruments, Austin, Texas). Connections to the potentiostat were adapted for use with the BVT dispoable sensor and disposable gold working electrodes. The normal three electrode configuration comprising a gold working electrode, Ag/AgCl reference electrode and platinum counter electrode was used for all electrochemical measurements. All solutions were thoroughly degassed and a blanket of nitrogen maintained over the solution during electrochemical measurements.

Reagent grade chemicals including mercaptoethanol, N-ethyl-N[diethylaminopropyl] carbodiimide (EDC), N-hydroxysuccinimide (NHS) were supplied by Sigma Aldrich. The osmium carboxylic acid complex was synthesised as reported in Chapter 2.

4.3. Methodology

4.3.1. Determination of electrochemical area of electrodes

For DNA immobilisation, smooth surfaces on the gold disc electrodes were prepared by successive polishing with 12.5 μm, 5 μm, 1 μm, 0.3 μm and 0.05 μm alumina. Polishing of the gold electrode of the BVT sensor, BVT electrode or Tyndall electrode was not feasible. All electrodes were immersed in 0.5M H_2SO_4, the solution thoroughly degassed and cyclic voltammograms recorded between potential limits of 0.0V and 1.5V at a scan rate of

100mV s^{-1}. Replicate measurements for gold electrodes from the three different sources were recorded to estimate the degree of reproducibility between electrodes.

4.3.2. Assembly of the DNA biosensor

Immediately prior to modification, electrodes were immersed in 0.5M H_2SO_4. Cyclic voltammograms were recorded between potential limits of 0.0V and 1.5V at a scan rate of 100mV s^{-1} until the voltammogram for a clean gold electrode was recorded. Electrodes were then sonicated in ethanol for 3 min, left immersed for a further 30 min to remove any adsorbed oxygen and then sonicated in ultra pure water and dried under a stream of N_2 gas.

For modification of the disposable electrodes with 5' ferrocene labelled DNA, a 10 µl droplet of probe DNA at the required concentration was spotted onto the gold working area of the electrode. To serve as a control, a second electrode was spotted with blank buffer/electrolyte. Electrodes after spotting were maintained in a covered Petri dish to reduce the rate of evaporation of the solution. After 6 hr electrodes were washed in 1M $NaClO_4$, rinsed in ultra pure water and dried under a stream of nitrogen. A 10 µl droplet of 1 mM mercaptoethanol was then spotted onto each electrode. After 1hr electrodes were rinsed as before and immersed in 1M $NaClO_4$ overnight. Gold disc electrodes were modified in a similar manner with the exception that after spotting, the electrode was held upside down and a plastic cap fitted to protect the deposition solution from evaporation. Modified electrodes were cycled periodically until stable voltammograms were recorded.

The same protocol was used for monolayer formation with oligos having a thiol group at the 5'end and an amine group at the 3' end as that described above. After immobilisation of the oligos with the amine group at the 3' end, electrodes were immersed for 96 hr at 4°C in ethanol/water (50/50 v/v) activation solution containing 30 mM EDC, 5 mM NHS and 5 mM osmium carboxylic acid complex. Electrodes were rinsed in 50% ethanol and dried under nitrogen. A 10 µl droplet of 1 mM mercaptoethanol was then spotted onto each electrode. After 1hr electrodes were rinsed as before and immersed in 1M $NaClO_4$ overnight. Modified electrodes were cycled periodically until stable voltammograms were recorded.

4.3.3. The effect of probe DNA concentration

Ferrocene labelled, thiolated hairpin DNA concentrations of 1 μM, 5 μM and 10 μM were used to modify the surface of gold disc electrodes. The protocol for DNA immobilisation outlined previously was modified to allow an overnight period (>16hr) after spotting with probe ssDNA. To determine the reproducibility of the modification, triplicate investigations at each DNA concentration were performed.

4.3.4. The effect of temperature on immobilised hairpin DNA

A monolayer of the ferrocene labelled hairpin probe ssDNA was formed on a 1mm diameter BVT gold electrode using the protocol described at 4.3.2. The modified electrode was subjected to cyclic voltammetry in 1M $NaClO_4$ at 10min intervals until a stable peak current was observed. The electrochemical cell was then placed in a thermostatically controlled heating block. The temperature of the electrolyte was heated slowly and cyclic voltammograms recorded at 10°C intervals up to a maximum of 85°C. The electrochemical cell was removed from the heating block, allowed to cool to room temperature and a final cyclic voltammogram recorded.

4.3.5. Hybridisation studies with complementary DNA

Three independent attempts to conduct hybridisation studies with DNA biosensors were undertaken, firstly using modified Tyndall gold electrodes and subsequently with gold disc electrodes.

Monolayers of the ferrocene labelled, thiolated hairpin probe DNA were formed as described in 4.3.2 on Tyndall gold electrode surfaces. The modified electrodes were subjected to cyclic voltammetry in 1M $NaClO_4$ at 10 min intervals for 90 min by which time stable electrochemical signals were recorded. Cyclic voltammograms at different scan rates were recorded to confirm that the peak current scaled linearly with the scan rate as would be expected for a surface confined species. Each electrode was removed from the

electrochemical cell, rinsed in ultra pure water and dried under nitrogen. Electrodes were then immersed in blank hybridisation buffer for 2 hr and cyclic voltammograms recorded in 1M $NaClO_4$ as the pre-hybridisation signal. Each electrode was then spotted with 10µl of 5 µM complementary target DNA dissolved in hybridisation buffer for 2 hr and cyclic voltammograms recorded in 1M $NaClO_4$ as the post-hybridisation signal. Three replicate measurements were performed to establish the reproducibility of the hybridisation step.

Limited availability of Tyndall gold electrodes resulted in the use of 1 mm gold disc electrodes in subsequent attempts to establish a working DNA biosensor. Monolayers of the ferrocene labelled, thiolated hairpin probe DNA were established as described in 4.3.2 and stabilised as before. Cyclic voltammograms were recorded at different scan rates to confirm that the peak current scaled linearly with scan rate. Hybridisation studies were undertaken as described with Tyndall electrodes except that modified electrodes were immersed in 1 µM complementary ssDNA for 90 min and maintained in a shaking hybridisation chamber at 50°C, approximately 10°C below the temperature at which the stem would theoretically open, before recording of the post-hybridisation signal. The electrode was then washed with hot 1M $NaClO_4$ (90°C), rinsed in ultra pure water and dried under a stream of nitrogen to regenerate the surface. Electrodes were immersed in blank hybridisation buffer for 2 hr and cyclic voltammograms recorded as the post-regeneration signal. Three replicate measurements were performed to establish the reproducibility of the hybridisation and regeneration steps.

The success of the protocol for assembly of a DNA biosensor on the gold disc electrodes resulted in application of the same procedure with monolayers of the osmium labelled, thiolated hairpin probe DNA. Studies to confirm the stability of the monolayer, its surface confined nature, hybridisation in 1 µM complementary ssDNA at 50°C in a shaking hybridisation chamber and the regeneration step were performed using the protocol above. Cyclic voltammograms of the pre-hybridisation, post-hybridisation and post-regeneration signals were recorded. Three replicate measurements were performed to establish the reproducibility of the hybridisation and regeneration steps.

4.4. Results and Discussion

4.4.1. Determination of the electrochemical area

For meaningful data to be extracted from electrochemical measurements, the electrochemical area rather than the geometrical area of the electrode must be determined. Surface roughness of an electrode is important since the electrochemical area is used to calculate the surface coverage (Γ) of a monolayer immobilised on the electrode surface using the equation:

$$\Gamma = \frac{Q}{nFA} \qquad (1)$$

where Q is the area under the peak in a cyclic voltammogram due to the oxidation or reduction of the electroactive species immobilised as a monolayer on the electrode surface, n the number of electrons transferred in the redox process, F the Faraday constant and A is the electrochemical area of the electrode.

In this study the electrochemical area rather than the geometric area was always used for determination of the surface coverage.

Cyclic voltammograms recorded in 0.5M H_2SO_4 for the three types of electrodes under investigation are provided in Figure 4.1. Mean peak area data from the oxide reduction peaks of the cyclic voltammograms are provided in Table 4.1.

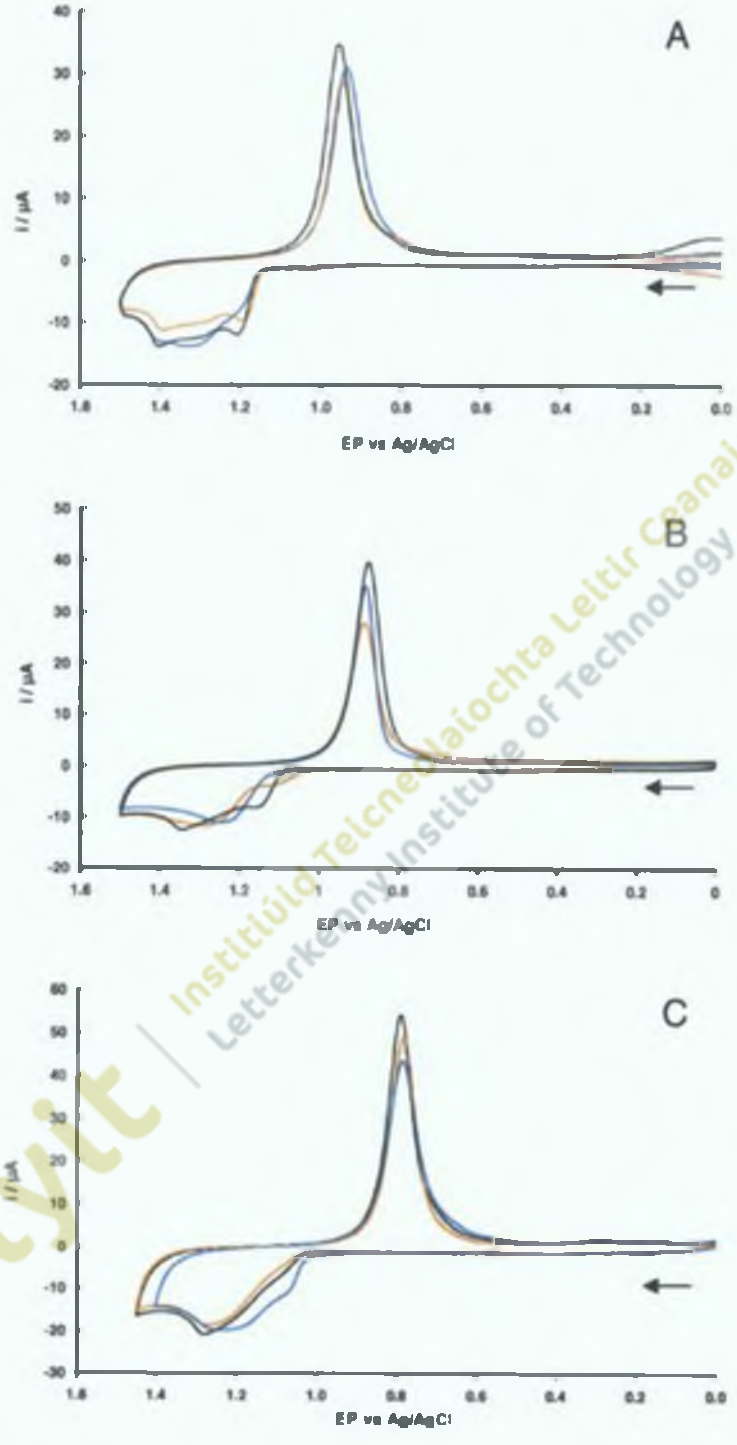

Figure 4.1. Triplicate cyclic voltammograms for the Tyndall (A), BVT sensor (B) and IJ Cambria gold disc (C) electrodes immersed in 0.5M H_2SO_4. Potential limits were from 0 to 1.5V and the scan rate was 0.1V s^{-1}. The area under the oxide reduction peak was used to calculate the electrochemical area of the electrodes

Electrode type	Electrode No	Peak area x 10^{-5} (C)	Mean peak area ± S.D. x 10^{-5} (C)
Tyndall	A1	2.70	2.87 ± 0.17
	A2	2.87	
	A3	3.05	
BVT	B1	2.48	2.74 ± 0.25
	B2	2.76	
	B3	2.98	
IJ Cambria	C1	3.42	3.07 ± 0.34
	C2	3.07	
	C3	2.73	

Table 4.1. *Mean area under the reduction peaks in the cyclic voltammograms in Figure 5.1 for the three electrodes of each type.*

Using the mean peak area under the reduction peak for each electrode and a correction factor for gold of 390 μC cm^{-2}, the mean electrochemical area of each type of electrode was determined. By comparison of the electrochemical area with the geometric area, the surface roughness factor of each type of electrode was calculated. Average surface roughness factors for the three types of electrode are presented in Table 4.2.

Electrode type	Electrochemical area (cm^2)	Geometric area (cm^2)	Surface roughness
Tyndall	0.074	0.0600	1.23 ± 0.14
BVT	0.070	0.0078	8.97 ± 0.82
IJ Cambria	0.079	0.0314	2.51 ± 0.14

Table 4.2. Surface roughness factors and standard deviation for the three different electrodes

Mean surface roughness of the gold disc electrodes was 2.51 ± 0.14. Reproducibility between these electrodes was very good and achieved only after successive polishing steps which in many cases were repeated several times to create surfaces of comparable smoothness. For the development of rapid and reproducible sensors, this step which was both tedious and time consuming would be impractical. The highest surface roughness factor was reported for the commercially available BVT disposable sensors (8.97 ± 0.82) while the lowest surface roughness was recorded for the Tyndall electrode (1.23 ± 0.14). These surface roughness factors possibly stem from the different fabrication processes used during manufacture; the BVT sensors being produced using screen printing technology as compared to the Tyndall electrodes produced using electrodeposition. The importance of smooth and atomically clean electrode surfaces for biosensor applications is widely reported in the literature [68-70]. The electrochemical results suggested that the Tyndall electrodes would be the more suitable type for development of a disposable DNA biosensor.

Microscopic images of the bare surface of the two disposable electrodes are provided in Figure 4.2 and show the rougher surface of the gold working area of the BVT sensor compared to the Tyndall gold electrode.

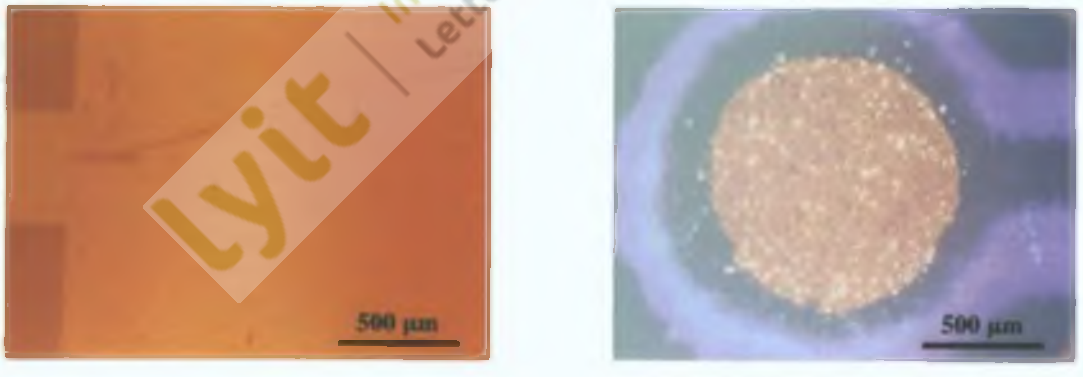

Figure 4.2. Images of the working area of the Tyndall gold electrode (left) and gold electrode of the BVT sensor (right) at 100x magnification. Scale bar = 500 µm

The objectives of this study were to determine the electrochemical surface area available for immobilisation and the reproducibility of the electrochemical area between different electrodes. The electrochemical surface area is of significance since this measure affects the amount of probe that can be attached as a monolayer on the electrode surface. The reproducibility between different electrodes of the same type is of importance particularly if comparisons of different treatments are to be undertaken. The higher surface roughness of the BVT sensors would suggest that it should be possible to attach more probe molecules to the BVT sensors than to the Tyndall electrodes. However, deep crevices or heights on an electrode surface may affect the molecular orientation on the electrode surface and render probe molecules buried in deep crevices inaccessible to target molecules.

4.4.2. Assembly of the DNA biosensor

Before attempting the immobilisation of thiolated probe DNA, it is widely acknowledged as critically important that the surface of the gold electrode be thoroughly clean and free of impurities [14]. As a consequence, a wide range of cleaning protocols have been reported in the literature, most comprising a combination of a period of immersion in acidic solution, often H_2SO_4 or piranha solution (H_2SO_4 / H_2O_2), a sonication step in ultrapure water or ethanol and finally oxidative and reductive electrochemical cleaning [10, 33, 71-75]. In this study the protocol used for electrode cleaning prior to assembly of the DNA biosensor was based on a compilation of trial and error experiences and literature reports from other researchers in the field. By comparison with the much more extensive cleaning procedure advocated by some workers, the protocol employed here was relatively straightforward [47].

Suppliers of thiolated DNA oligonucleotides provide instructions with their probes as to how they should be handled. Some suppliers advocate direct spotting of probe solution on the electrode whilst others suggest a reduction step using DTT (dithiothreitol), or more recently TCEP (Tris-(2-carboxyethyl) phosphine hydrochloride), to ensure that any disulphide bridges between thiolated probe molecules have been broken prior to the spotting. Since neither of the probe suppliers for this study, Friz Biochem or Sigma Aldrich, advocated disulphide reduction with their probes, accordingly no reduction protocol was employed.

The concentration of probe DNA for spotting electrodes, the duration of the immobilisation step, the buffer and salts present in the spotting solution vary widely in the literature. Utilisation of a 1 μM concentration of probe DNA has been most commonly reported and at the commencement of the study was considered an appropriate concentration to employ. Following spotting with DNA, the electrode surface is passivated with an alkane thiol compound which has the effect of reducing non-specific DNA binding, re-orientating the DNA probe molecules into a perpendicular position and filling any gaps in the DNA monolayer. The nature of the alkane thiol, its concentration and the duration of this passivation step vary widely. In this study, mercaptoethanol was used because of its successful application in the literature [10], although many alkane thiols including 1-mercaptopropane [76], mercaptopropanol [72], 6-mercaptohexanol [71, 75, 76, 77], 3-mercaptopropionic acid [76], pentanethiol [74] and undecanethiol [73] have all been utilised. Most researchers utilise a 2-step approach comprising spotting firstly with the DNA probe and then secondly with alkane thiol; others report a 1-step approach to monolayer formation using a mixture of probe DNA and alkane thiol in a range of different proportions. In this study the more common 2-step approach was employed for monolayer formation. Prolonged application of the alkane thiol is widely acknowledged to result in loss of immobilised DNA from the electrode and 1 hr duration was selected as appropriate in this study on the basis that such a period was intermediate by comparison with that used by many other workers.

Using the protocol outlined in section 4.3.2, different concentrations of thiolated ssDNA probe were used for monolayer formation with BVT sensors. Cyclic voltammograms recorded in 1M $NaClO_4$ between potential limits from -0.3 to 0.4V at a scan rate of 0.1V s^{-1} are provided in Figure 5.3. Oxidation reduction peaks were recorded with 10μM and 5μM concentrations of ferrocene labelled thiolated ssDNA and were similar to those reported by Jenkins *et al.* [78] which were attributed to the proximity of the redox probe molecule to the electrode surface (Figure 4.3A and 4.3B). However, similar oxidation-reduction peaks were also recorded in voltammograms using BVT sensors which had been spotted with blank buffer containing no ferrocene labelled thiolated ssDNA (Figure 4.3C).

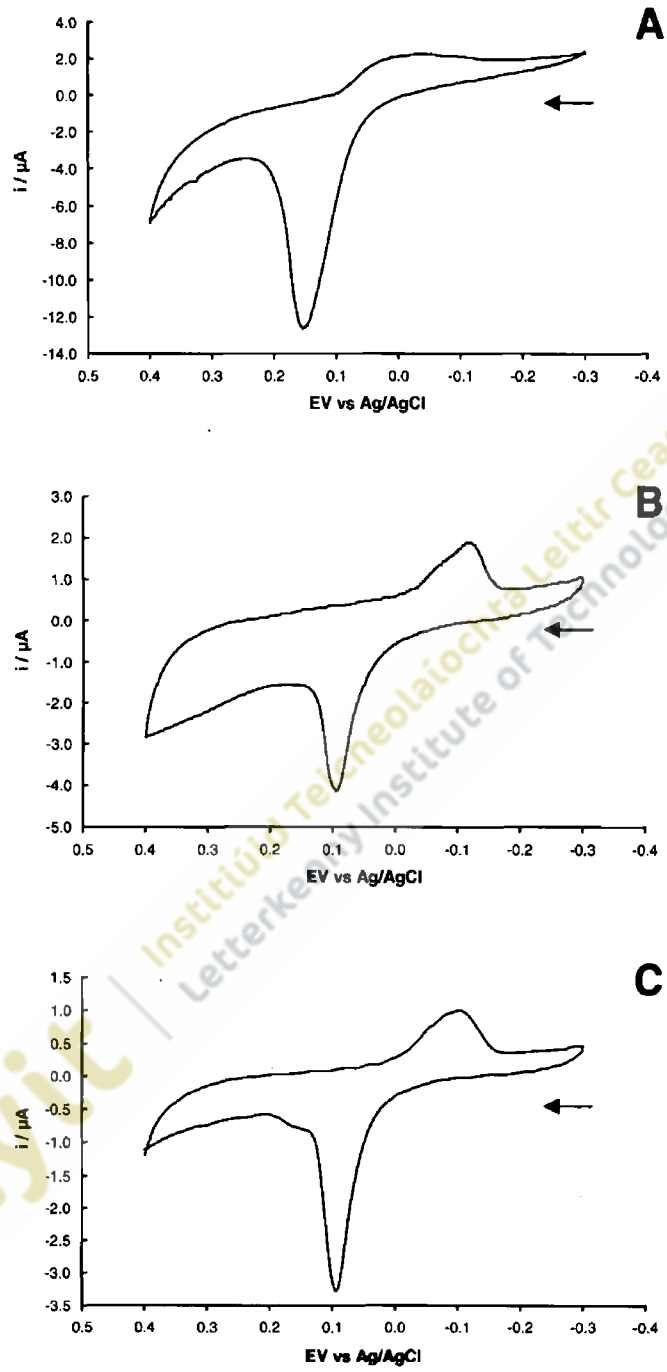

Figure 4.3. Cyclic voltammograms for BVT sensors modified with 10 µM Fc-DNA-SH (A), 5 µM Fc-DNA-SH (B) and with blank buffer (C). The electrolyte was 1 M $NaClO_4$. Potential limits were from -0.3 to 0.4V. Scan rate was 100mV s^{-1}.

Although the cause of these redox peaks is presently uncertain, the potentials at which they occur suggest that they may have resulted from the leaching of silver from the reference electrode of the sensor and its deposition on the surface of the gold working electrode [79]. Despite many replicated attempts, the BVT sensor spotted with blank buffer always exhibited similar peaks after incubation in 1M $NaClO_4$. Because of these difficulties, efforts to use the BVT sensors for immobilisation of thiolated ssDNA and the detection of hybridisation were discontinued. The voltammograms recorded clearly demonstrated the importance of using controls to ensure that the signals produced on electrodes resulted from the immobilised ferrocene labelled thiolated DNA. In all further work, control experiments using blank buffer and mercaptoethanol were always included.

Using a similar protocol for DNA immobilisation, a 1 μM concentration of ferrocene labelled thiolated ssDNA probe was used for spotting Tyndall disposable gold electrodes. Following mercaptoethanol treatment and overnight immersion in 1M $NaClO_4$, cyclic voltammograms were recorded in 1M $NaClO_4$ between potentials from -0.2 to 0.6V at a scan rate of 0.1V s^{-1}. A significant redox response for the Tyndall sensor modified with the probe was recorded and a typical cyclic voltammogram is provided in Figure 4.4.

In contrast to the BVT electrode, no redox peaks were recorded for the Tyndall electrode spotted with the blank buffer solution and treated with mercaptoethanol, hence the electrochemical signal was attributed to the ferrocene present in the spontaneously adsorbed monolayer. The formal potential of the electroactive label ($E_{½}$) was estimated as188mV as determined from the equation $(E_{½}) = (E_{pa} + E_{pc})/2$. This formal potential is somewhat lower than the 280mV vs. Ag/AgCl (492mV vs. NHE) quoted by Fan *et al.* 2003 [10]. With the exception of the BVT sensors all other electrodes used in this study yielded similar results for control experiments.

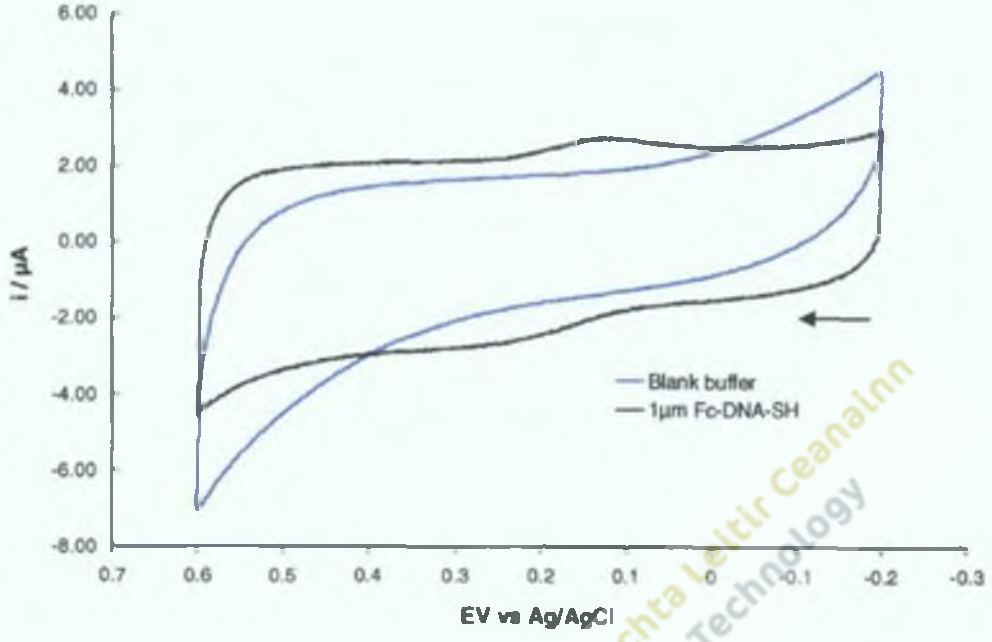

Figure 4.4. Cyclic voltammograms for the $Fe^{2+/3+}$ redox reaction for a spontaneously adsorbed monolayer of Fc-DNA-SH formed on a Tyndall gold electrode (black) and with blank buffer and 1mM mercaptoethanol (blue). The supporting electrolyte was 1M $NaClO_4$. Potential limits were from -0.2 to 0.6V. Scan rate was 500 mV s^{-1}. Anodic currents are down and cathodic currents are up.

To investigate the kinetics of stem-loop folding, freshly-modified Tyndall electrodes were subjected to cyclic voltammetry in 1M $NaClO_4$ immediately after DNA immobilisation and mercaptoethanol treatment and repetitively at 30 min intervals. Cyclic voltammograms recorded in situ between potential limits of -0.2V to 0.5V at a scan rate of 500 mV s^{-1} are provided in Figure 4.5.

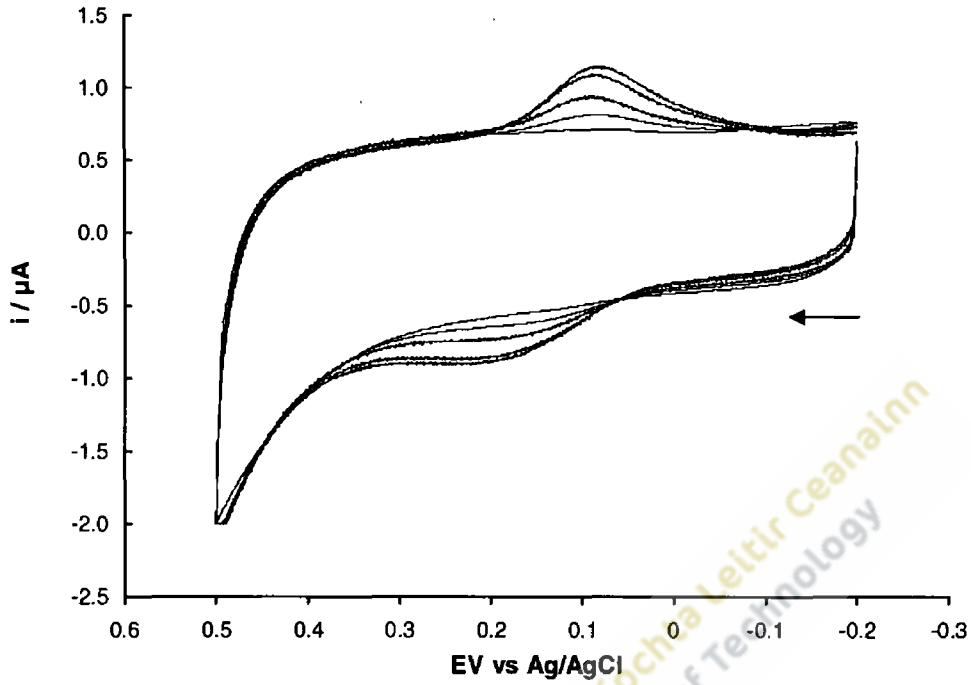

Figure 4.5. Overlay of five cyclic voltammograms for the $Fe^{2+/3+}$ redox reaction for a spontaneously adsorbed monolayer of Fc-DNA-SH on a Tyndall gold electrode recorded immediately after mercaptoethanol treatment and at 30 min intervals showing increasing peak currents. The supporting electrolyte was 1M $NaClO_4$. Potential limits were –0.2V to 0.5V. Scan rate was 500 mV s^{-1}. Anodic currents are down and cathodic currents are up.

Results in the literature have reported that electrodes modified with redox labelled hairpin ssDNA show no significant electrochemical response until incubated in high ionic strength electrolyte solutions, a 1M perchlorate being reported as necessary [10, 80]. In this study an electrochemical response of relatively small magnitude was recorded in freshly modified electrodes, and this gradually increased attaining a maximum after approximately 3hr. High ionic strength solutions are reported to be necessary for the formation of the stem loop structure of the hairpin DNA molecule. Without formation of the stem loop structure, the ferrocene molecule has been reported to be distanced from the electrode surface and a much reduced current flows between the redox molecule and the electrode [10, 80]. Based on these results, it would seem that even in high ionic strength solutions, the stem loop structure forms only slowly. This experiment has been repeated on several occasions and cyclic

voltammograms always showed an electrochemical response immediately after DNA immobilisation and increases in peak currents over the first few hours. These results support the observation that the redox peaks are due to the immobilised Fc- DNA-SH.

The change in apparent surface coverage with time is provided in Figure 4.6. The data recorded in 1M $NaClO_4$ supporting electrolyte suggests that surface coverage increases gradually over 2 hr before reaching a stable level after 3 hr. However in reality the surface coverage remains constant but due to the slow formation of the hairpin structure, attached redox labels only produce signals after the immobilised probes are in the fully formed hairpin structure. The results clearly demonstrate that determination of the surface coverage of thiolated DNA can only be undertaken after stable signals have been observed, in practise after a minimum 3 hr period. To ensure that sufficient time has elapsed for the development of a stable signal, modified electrodes post-mercaptoethanol treatment were always incubated overnight in 1M $NaClO_4$ before cyclic voltammetry was performed.

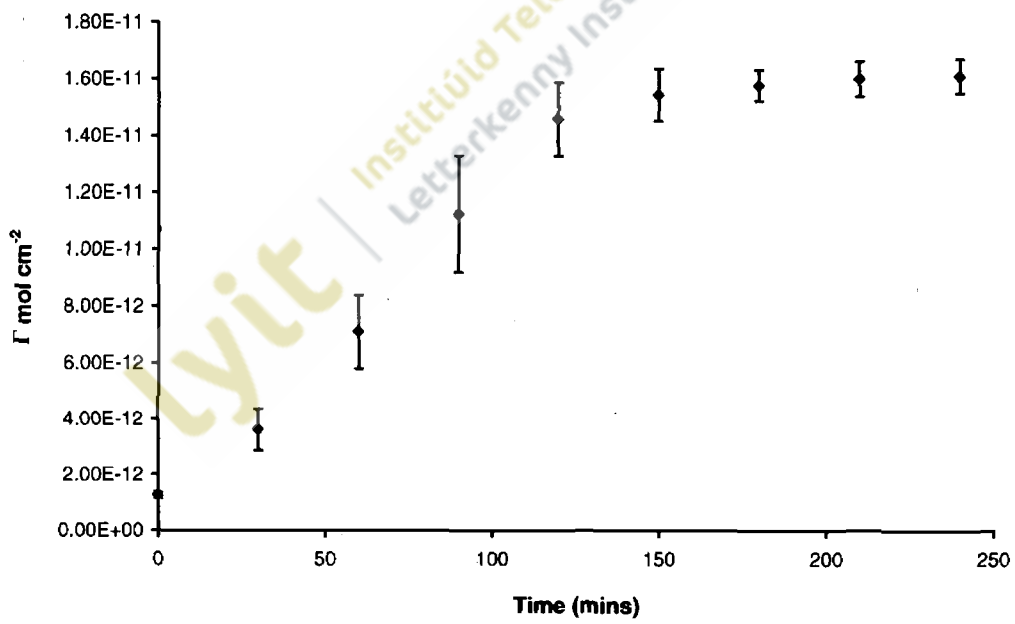

Figure 4.6. Relationship between mean surface coverage (Γ) and time for a spontaneously adsorbed monolayer of Fc-DNA-SH on a Tyndall gold electrode recorded immediately after mercaptoethanol treatment and at 30 min intervals (n = 3). The supporting electrolyte was 1M $NaClO_4$. Potential limits were from –0.2V to 0.5V. Scan rate was 500 mV s^{-1}.

The surface coverage of 1.6 x 10^{-11} mol cm^{-2} recorded after 3 hr was comparable with values reported in the literature for immobilised redox labelled hairpin DNA probes on gold electrodes as shown in Table 4.3.

	Probe Density (mol cm^{-2})	Reference
Hairpin DNA probe	6.5 x 10^{-14}	Ricci, Lai, Heeger, Plaxco, Sumner 2007 [26]
Hairpin DNA probe	2.0 x 10^{-12}	Nakamura, Ueda, Watanabe, Kumamato, Yamana 2007 [81]
Hairpin DNA probe	3.5 x 10^{-12}	Steichen, Buess-Herman 2005 [82]
Hairpin DNA probe	3.5 x 10^{-12}	Ricci, Lai, Heeger, Plaxco, Sumner 2007 [26]
Hairpin DNA probe	5.6 x 10^{-12}	Wei, Wang, Liao, Zimmermann, Wong, Ho 2008 [83]
Hairpin DNA probe	9.0 x 10^{-12}	Nakamura, Ueda, Watanabe, Kumamato, Yamana 2007 [81]
Hairpin DNA probe	1.6 x 10^{-11}	THIS STUDY
Hairpin DNA probe	1.0 x 10^{-10}	Mao, Luo, Ouyang 2003 [11]
Hairpin DNA probe	1.7 x 10^{-10}	Zauner, Wang, Lavesa-Curto, MacDonald, Mayes, Bowater, Butt 2005 [84]
Hairpin DNA probe	5.0 x 10^{-10}	Mao, Luo, Ouyang 2003 [11]

Table 4.3. Comparison of the hairpin DNA probe density determined in this study with literature values.

Since electrochemical detection of DNA hybridisation relies on differences in the pre-hybridisation and post-hybridisation peak currents, it is essential that a stable peak current has been established before the sensor is used. Figure 4.7 shows the reductive peak current vs. time for a redox labelled DNA hairpin monolayer cycled at 10min intervals after overnight immersion to determine the stability of the ssDNA monolayer on the electrode surface over 90min duration. Mean reductive peak current over this period was 1.17 ± 0.05 x 10^{-8} A.

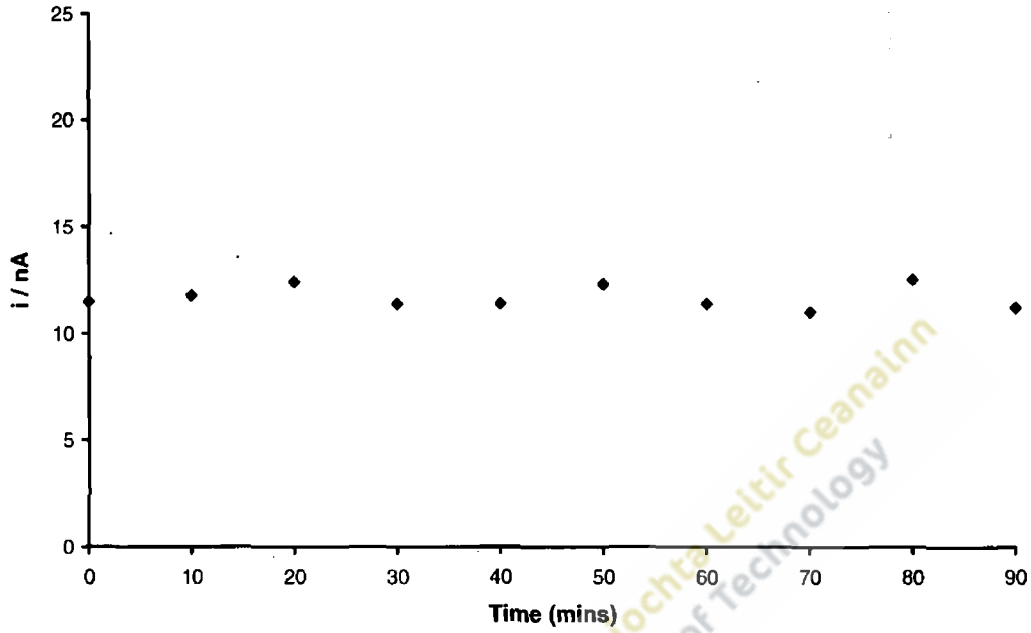

Figure 4.7. Stability of the peak current for a spontaneously adsorbed Fc-DNA-SH monolayer on a Tyndall gold electrode after cycling in 1M $NaClO_4$ at 10 min intervals over a 90 min duration following overnight immersion in 1M $NaClO_4$.

Further support for the presence of a monolayer of thiolated hairpin loop DNA with ferrocene modification immobilised on a Tyndall gold electrode was provided from cyclic voltammograms recorded at different scan rates. Peak currents and scan rate scaled linearly as would be expected for a surface-confined species (Figure 4.8) in contrast to peak current being proportional to the square-root of the scan rate, a characteristic of diffusion-controlled electrochemical reactions [10]. Redox peaks in the cyclic voltammograms, though of limited magnitude, were attributed to the reduction/oxidation of the ferrocene molecule attached to the hairpin loop DNA and its close proximity to the electrode surface.

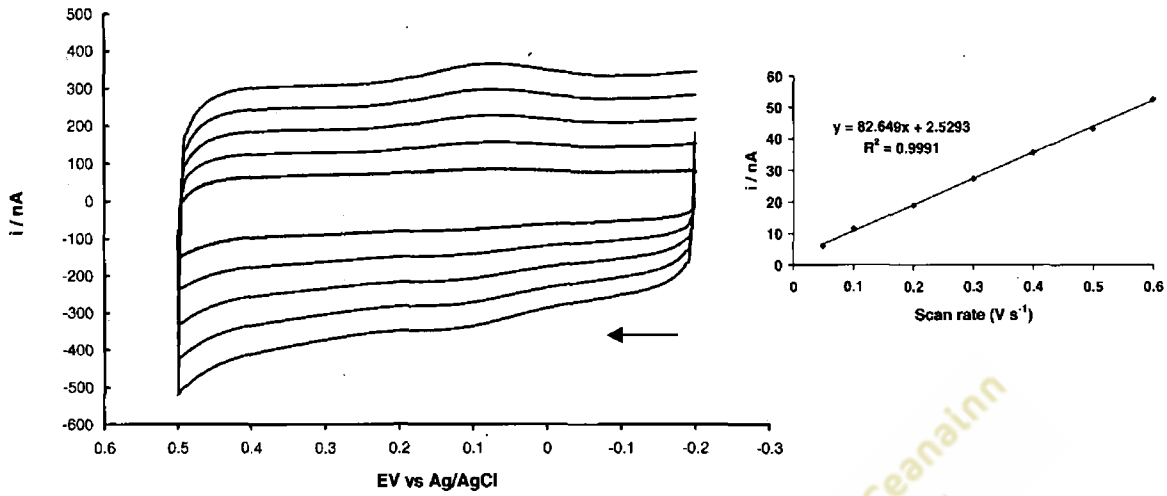

Figure 4.8. Cyclic voltammograms at different scan rates for the $Fe^{2+/3+}$ redox reaction for a spontaneously adsorbed monolayer of Fc-DNA-SH on a Tyndall gold electrode. From top to bottom the scan rates are 0.5, 0.4, 0.3, 0.2 and 0.1 V s^{-1}. The supporting electrolyte was 1M $NaClO_4$. The inset shows the linear relationship between the cathodic peak current and scan rate.

4.4.3. Concentration of probe DNA for spotting

The rapid formation of monolayers on gold surfaces by thiolated hairpin DNA has been widely reported in the literature. Overall performance of electrochemical DNA sensors has been shown to be significantly affected by the density of DNA hairpins immobilised on the electrode surface [26]. Higher densities of redox-labelled probe should support an increased electrochemical response at hybridisation; lower probe densities provide abundant space for hybridisation leading to optimal hybridisation efficiency [28, 85-87]. Hence optimal sensor performance will occur when the balance between these two opposing influences has been identified. Many of the studies of hairpin DNA immobilisation in the literature report the use of a 1 μM concentration of probe DNA for the production of monolayers of medium density and for this reason a comprehensive investigation of the effect of the concentration of probe DNA for electrode spotting was not undertaken [72, 75, 82]. Nevertheless to ensure

that sufficient probe DNA was immobilised, surface coverages resulting from two concentrations higher than 1 μM were investigated together with an examination of the reproducibility at different concentrations.

Gold disc electrodes modified with Fc-DNA-SH at 1 μM, 5 μM and 10 μM concentrations were subjected to cyclic voltammetry. Using the area under the cathodic peak of the cyclic voltammogram and the real surface area of the electrode, the surface coverage (Γ) achieved at each probe concentration was determined using equation 1. To estimate the reproducibility of the surface coverage at the different concentrations of probe DNA the investigation was performed in triplicate. The relationship between surface coverage and probe concentration is provided in Figure 4.9.

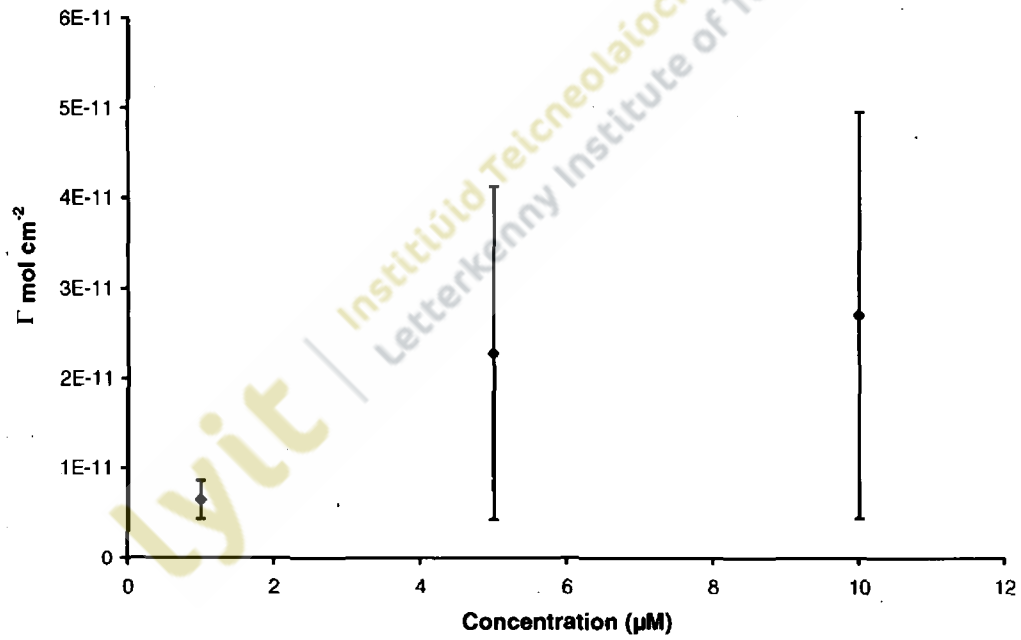

Figure 4.9. The relationship between surface coverage of Fc-DNA-SH on gold disc electrodes at probe DNA spotting concentrations of 1 μM, 5 μM, and 10 μM. Error bars represent standard deviation in surface coverage following triplicate investigations.

Surface coverage increased with the concentration of probe DNA used for spotting, although values reported for the 5 μM and 10 μM concentrations were very similar and exhibited poor reproducibility. Although the mean surface coverage for the 1 μM probe concentration was less than that for the other two concentrations and reproducibility much improved, statistical analysis using ANOVA indicated that the mean surface coverage at the three probe concentrations was not significantly different at the 95% confidence level with a *p*-value of 0.35. Similar results indicating that increasing the concentration of probe DNA for spotting has little effect on surface coverage have been reported in the literature [36]. Between 0.02 μM and 0.5 μM, variation in probe DNA spotting concentration has proved an effective tool for controlling probe surface density (8.47×10^{-14} mol cm^{-2} to 2.66×10^{-12} mol cm^{-2}) [75]. Statistical F-tests on the standard deviation at each probe concentration demonstrated that although these was no significant difference between the 5μM and 10μM probe concentrations, there was a significant difference between the 1μM probe concentration and the 5 μM and 10 μM concentrations respectively ($p = 0.013$ and $p = 0.008$).

Mean surface coverage values reported for hairpin DNA probes in this concentration study ranged from 6.5×10^{-12} mol cm^{-2} to 2.7×10^{-11} mol cm^{-2} and are similar to those reported in Table 4.3. These values are comparable with those reported in the literature for dsDNA and approximately 40% less than those for linear DNA probes under the same deposition conditions [88]. The lower surface coverage of hairpin DNA in the unhybridised state compared to linear DNA probes has been attributed to the larger molecular surface occupied on the gold electrode resulting from a combination of conformational, electrostatic and steric influences [30, 89].

With extended time periods for immobilisation, monolayers have been reported to become more ordered allowing them to adopt an orientation perpendicular or tilted with respect to the electrode surface. For this reason, the time allowed for monolayer formation in this investigation of the effect of probe concentration was extended from the 6 hr in the immobilisation protocol to an overnight period (>16 hr). Although the 1 μM concentration resulted in lower surface coverage than the higher probe concentrations, the better reproducibility together with the enhanced stability, reduced non-specific adsorption and

better accessibility for hybridisation reported in the literature at lower probe DNA concentrations were considered to be of significance [90, 91]. The surface coverages reported at the 1 μM probe concentration suggest that much of the electrode surface is covered by mercaptoethanol spacer molecules. Another influence on the degree of surface coverage that can be attained is the ionic strength of the deposition solution [10, 80]. At high ionic strength, repulsion between the negatively charged ssDNA probe molecules is screened to a large extent and should result in improved surface coverage. Because only moderate surface coverages were required, no salt was added to the deposition buffer with the intention of ensuring sufficient space between the attached probes to allow efficient hybridisation with the target DNA. On the basis of the results obtained in this study, the 1 μM concentration of probe DNA was deemed the most appropriate of the probe concentrations examined for immobilisation of hairpin DNA on gold electrodes.

4.4.4. Temperature study

Contrasting opinions regarding the necessity for heating during the hybridisation step with complementary target DNA are reported in the literature. In some instances hybridisation of the immobilised hairpin probe DNA with complementary target DNA has been reported to occur spontaneously at room temperature [10, 23, 78, 83], whereas others report that the temperature should be increased to effect opening of the hairpin DNA and facilitate hybridisation with the complementary target DNA as cooling occurs [82, 88, 92-94]. Several researchers have undertaken comparative studies at increasing temperatures, some reporting that no significant change of voltammetric signals occurred [95] and others that more significant changes were recorded when elevated temperatures were used [96, 97]. With immobilised fluorescent labelled hairpins, both enhanced signals and faster hybridisation have been reported at 37 °C, although the need to ensure that no signal was produced as a result of the increased temperature alone was emphasized [98]. From an analogous point of view, it is important in this electrochemical investigation that if temperature is to be used to either encourage hybridisation or as a prerequisite for hybridisation to occur, that the effect on the voltammetric signal as a result of heating alone is understood.

As stated previously since electrochemical detection of DNA hybridisation relies on differences in the peak current before and after hybridisation, it is important to establish that the peak current is stable before a sensor is used. Figure 4.10 shows the relationship between the peak current vs. time for a probe DNA monolayer on a BVT gold electrode prior to its use in this study of the effect of temperature. Unlike the relationship shown in Figure 4.7 with the Tyndall gold electrode where after overnight immersion in 1M $NaClO_4$ a stable peak current was recorded from the commencement of cyclic voltammetry, with the BVT gold electrode despite overnight immersion in 1M $NaClO_4$, peak current stability was only approached after 40 min of cyclic voltammetry. This current was approximately 66% of that recorded at the initiation of cyclic voltammetry and emphasized the importance of the stabilisation step before application of the DNA biosensor in target detection.

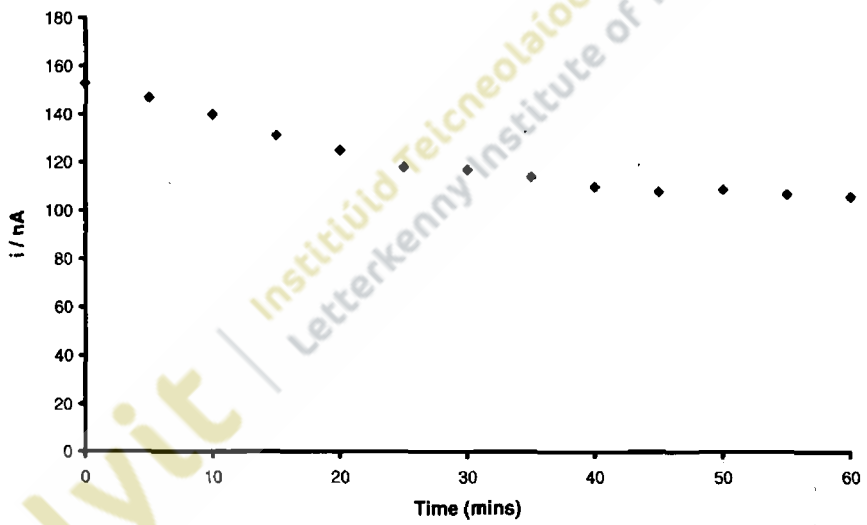

Figure 4.10. Stability of the peak current for a spontaneously adsorbed Fc-DNA-SH monolayer on a BVT gold electrode after cycling in 1M $NaClO_4$ at 5 min intervals over a 60 min duration.

After attainment of a stable current the modified BVT electrode was heated in 1M $NaClO_4$ within an electrochemical cell and cyclic voltammograms recorded at 10°C intervals up to a maximum of 85°C. Cyclic voltammograms recorded at 55°C, 65°C, 75°C, and 85°C are shown in Figure 4.11.

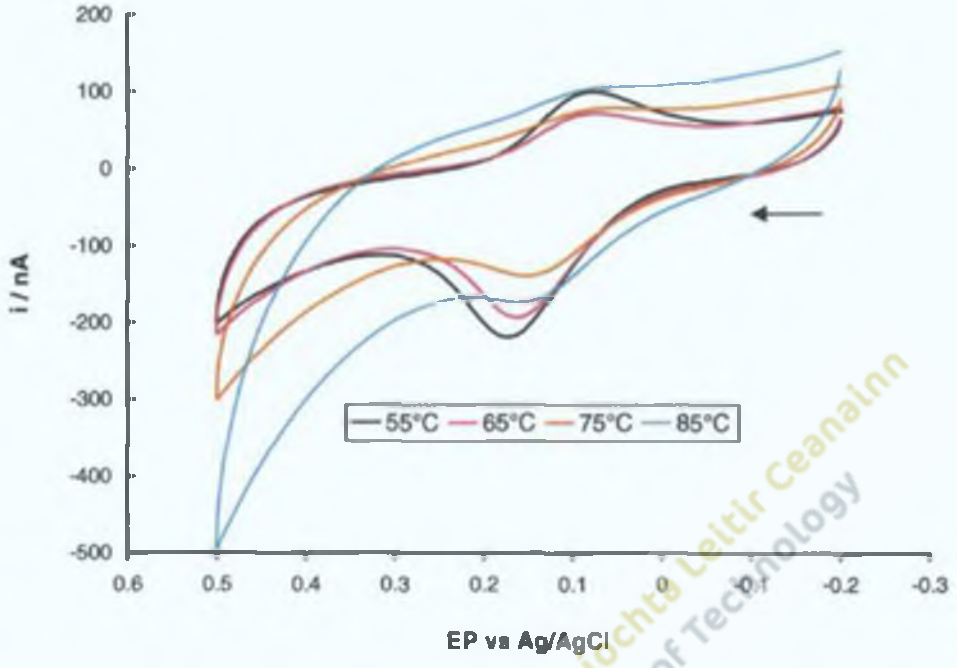

Figure 4.11. Cyclic voltammograms for the $Fe^{2+/3+}$ redox reaction for a spontaneously adsorbed monolayer of Fc-DNA-SH on a BVT gold electrode at different temperatures. The supporting electrolyte was 1M $NaClO_4$. Potential limits were from –0.2 to 0.5V.

Cyclic voltammograms recorded at 35°C and 45°C (data not shown) exhibited only minor differences compared to those recorded at 55°C. At temperatures above 65°C there was a marked decrease in the peak current as shown by the typical results in Figure 4.11. The melt temperature of the stem of a hairpin probe, i.e. the temperature at which the hairpin opens, varies with the number of nucleotides in the stem and the GC content. In general, GC-rich stems of 5-bp melt between 55-60°C, those of 6-bp melt between 60-65°C, and those of 7-bp melt between 65-70°C[99]. The melt temperature of the stem of the DNA hairpin used in this investigation with a fluorophore rather than the redox label at the 5' end and a quencher molecule rather than the thiol group at the 3' end was determined by rtPCR as approximately 62°C i.e. within the range 60-65°C for a 6-bp stem (data not shown). Thus the observed reduction in peak current above 65°C might have resulted from opening of the hairpin and distancing of the redox label from the electrode surface with an ensuing reduction in the peak current.

At 75°C and at 85°C, not only were the peak currents significantly less than those at 65°C, there was also a significant increase in the capacitive current, particularly at the higher temperature. This increase could be due to the fact that when the hairpin is in the open formation more of the electrode surface is available to electrolyte ions or possibly due to the loss of some of the probe DNA from the electrode surface at higher temperatures. It was not possible to use the area under the peaks at 75°C and 85°C to determine the probe density and hence elucidate whether probe had been lost from the electrode surface because as shown in Figure 4.6, a low value for the surface coverage does not necessarily infer that the probe had been lost since it may still be attached but not in the folded configuration with the redox label close to the electrode surface.

Following heating to 85°C, the electrochemical cell was removed from the heating block, allowed to cool to room temperature for several hours and a final cyclic voltammogram recorded. For comparative purposes the cyclic voltammograms recorded at 85°C and after cooling to room temperature are shown in Figure 4.12.

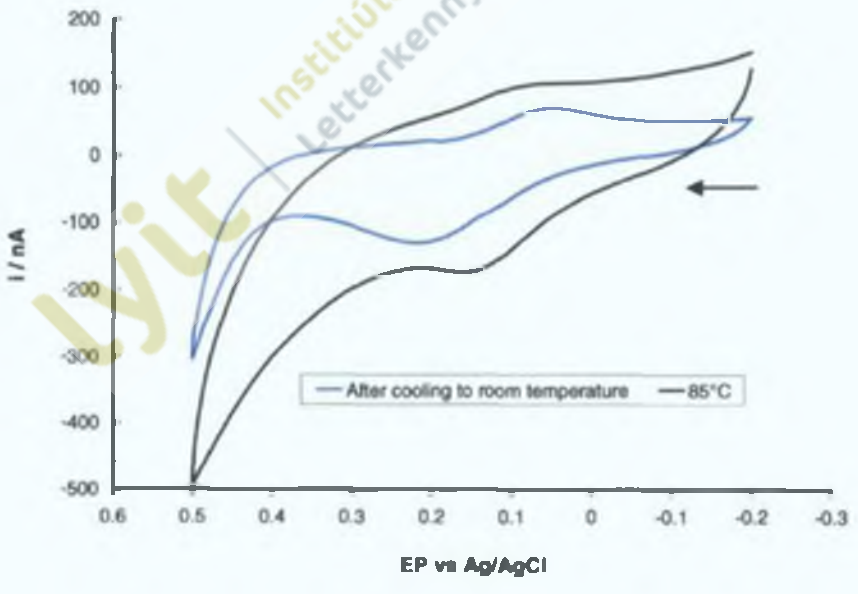

Figure 4.12. Cyclic voltammograms for the $Fe^{2+/3+}$ redox reaction for a spontaneously adsorbed monolayer of Fc-DNA-SH on a BVT gold electrode at 85°C (black) and after cooling to room temperature (blue).

The cyclic voltammograms in Figure 4.12 provided further support for the presence of a monolayer of redox-labelled hairpin DNA on the electrode surface. The enhanced peak current recorded after cooling to room temperature could be attributed to re-folding of the DNA hairpin into the stem-loop configuration and return of the redox label into close proximity to the electrode surface. A similar trend in peak current for hairpin loop DNA immobilised on a gold electrode as temperatures were cooled from 60°C to 5°C has been reported in the literature [26]. In this study the peak current following regeneration of the stem-loop configuration was considerably less than that observed prior to heating and peak to peak separation had increased. The reduced electrochemical signal may have resulted from instability of ferrocene in aqueous solutions at high temperatures, a slower than anticipated rate of re-formation of the stem-loop configuration than that in Figure 4.6 and/or release of thiolated DNA from the gold surface resulting in loss of probe molecules [10, 100]. The reason for the increased peak to peak separation is presently unknown however the orientation of the redox molecules with respect to the electrode surface may have been altered after the stem of the hairpin probe was denatured and then reformed.

For comparative purposes, peak currents from the cyclic voltammograms at room temperature prior to the study, at each of the different temperatures in the study and at room temperature following regeneration are shown in Figure 4.13. Although the melt temperature of the hairpin probe was determined as 62°C, the peak current recorded at 65°C was of a similar magnitude to those recorded at lower temperatures. Peak currents recorded at temperatures up to and including 65°C were significantly different to those recorded at 75°C and above ($p = 0.012$). The data suggested that either opening of the hairpin and transfer of the redox label away from the electrode surface had not occurred by 65°C but had been largely completed by 75°C or desorption of thiolated probe occurred above 65°C. Peak current after cooling was approximately 50% of that at room temperature prior to the temperature study.

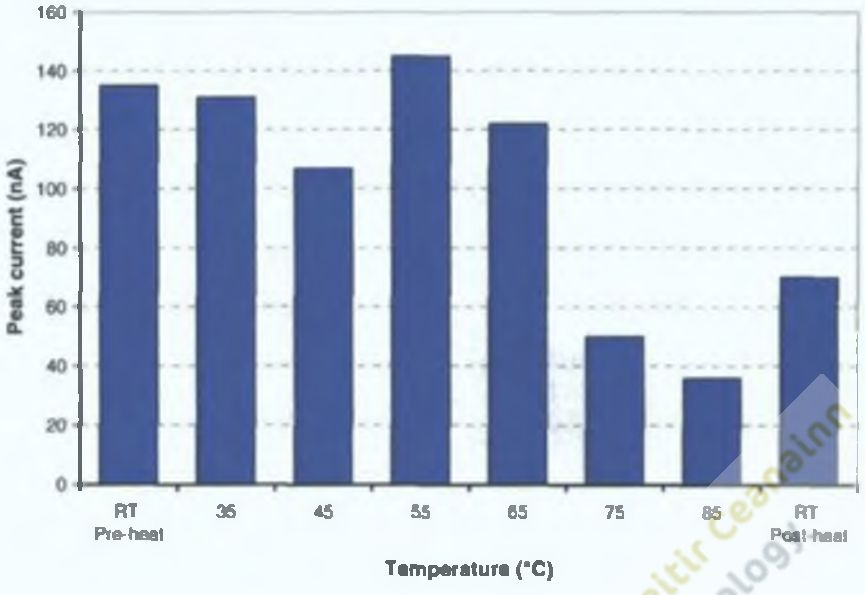

Figure 4.13. Peak currents from the cyclic voltammograms for the $Fe^{2+/3+}$ redox reaction for a spontaneously adsorbed monolayer of Fc-DNA-SH on a BVT gold electrode at different temperatures.

4.4.5. Hybridisation studies with complementary DNA

Hybridisation studies were undertaken using Tyndall electrodes modified with Fc-DNA-SH, gold disc electrodes modified with Fc-DNA-SH and gold disc electrodes modified with Os-DNA-SH. In all instances, hybridisation of the complementary target with the immobilised probe DNA should result in distancing of the electroactive redox molecule away from the electrode surface and either partial or complete loss in the peak current.

Results from the hybridisation study with Tyndall electrodes are provided in Figure 4.14. Transfer of the electrode from 1M $NaClO_4$ in the electrochemical cell, immersion in blank hybridisation buffer for 2 hr and return of the electrode to 1M $NaClO_4$ in the electrochemical cell back had negligible effect on the peak current. The purpose of this step was to confirm that no change in signal occurred upon transfer from the 1M $NaClO_4$ solution to the hybridisation buffer over the 2 hr period so that had a change been recorded with the complementary DNA in hybridisation buffer over the same duration, the change could have more easily been attributed to hybridisation.

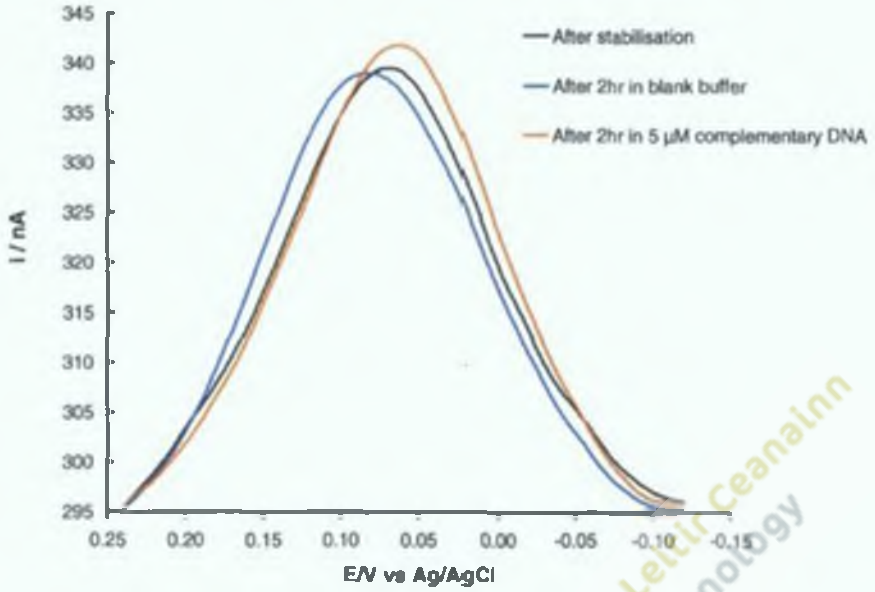

Figure 4.14. Overlay of the baseline-corrected faradaic current from cyclic voltammograms recorded in 1M $NaClO_4$ after deposition of thiolated DNA hairpin on Tyndall electrodes (black), after 2 hr in blank hybridisation buffer (blue) and after 2 hr in 5 µM complementary ssDNA in hybridisation buffer (red). The scan rate used was 0.5 V s^{-1}.

After immersion in complementary ssDNA target in hybridisation buffer for 2hr, there was no reduction or loss of signal as had been expected suggesting that despite the presence of a Fc-DNA-SH monolayer on the electrode and a stable peak current at a similar potential to that encountered in the developmental work for the $Fe^{2+/3+}$ redox reaction, hybridisation did not occur. To assist in understanding why hybridisation failed to occur, a comparison of the hybridisation conditions and other related factors reported in the literature that might influence this step was undertaken (Table 4.4).

Many of the successful trials shown in Table 4.4 were performed on commercially available, gold disc electrodes rather than on fabricated electrodes or sensors. Given the limited supply of Tyndall electrodes, further attempts at biosensor assembly in this work programme were performed by necessity, on similar gold disc electrodes of 2 mm diameter.

	THIS STUDY	Fan *et al.* 2003	Park *et al.* 2004	Steichen *et al.* 2005	Lai *et al.*2005	Jenkins *et al* 2006	Ricci *et al.* 2007	Berganza *et al* 2007
ELECTRODE								
Electrode type	Tyndall 2 mm x 3 mm	Gold disc 1.6 mm dia.	Gold disc 2 mm dia.	Gold disc 1.6 mm dia.	Gold sensor 0.88 mm^2	BVT sensor 1 mm dia.	Gold disc 2 mm dia.	Gold sensor 0.5 mm dia.
SENSOR ASSEMBLY								
Hairpin loop length	21-bp	16-bp	N/A	16-bp	17-bp	24-bp	22-bp	N/A
Hairpin stem length	6-bp	6-bp	N/A	6-bp	5-bp	6-bp	6-bp	N/A
Hairpin stem GC content	67%	83%	N/A	60%	60%	80%	67%	N/A
Spacer between thiol and hairpin	$(CH_2)_6$	$(CH_2)_6$	$(CH_2)_6$	$(CH_2)_6$	$(CH_2)_6$	$(CH_2)_3$	$(CH_2)_6$	$(CH_2)_6$
Redox label	Ferrocene	Ferrocene	None	None	Methylene blue	Ferrocene	Methylene blue	None
Spacer between label and hairpin	$(CH_2)_6$	$(CH_2)_6$	N/A	N/A	$(CH_2)_3$	None	$(CH_2)_3$	N/A
DNA spotting concentration	1µM	1µM	0.06mM	25µM	0.5µM	2.5µM	1µM	1µM
DNA spotting time	6-hr	2-hr	24-hr	Overnight	15-min	1.5-hr	1-hr	2-hr
Diluent molecule	Mercaptoethanol	Mercaptoethanol	None	Mercaptobutanol	Mercaptohexanol	Mercaptoethanol	Mercaptohexanol	Mercaptohexanol
Diluent concentration	1mM	1mM	N/A	25µM	2mM	10mM	1mM	1mM
Diluent application time	1-hr	No. info	N/A	Overnight	2.5-hr	5 min	2-hr	2-hr
HYBRIDISATION CONDITIONS								
Complementary DNA concentration	5µM	5µM	10pM	1µM	2µM	10nM	200nM	1µM
Hybridisation time	120-min	30-min	5-hr	60-min	45-min	60-min	60-min	120-min
Hybridisation temperature	Room temp.	Room temp.	37°C	37°C	Room temp.	Room temp.	Room temp.	Room temp.
Mechanical assistance	None	None	None	Gentle stirring	None	None	None	None
Hybridisation buffer comp.	10mM Tris/HCl 0.1M KCl 1M $NaClO_4$	1M $NaClO_4$	0.25M Na_2PO_4 0.2M $MgCl_2$	10mM Tris/HCl 1M NaCl	10mM Tris/HCl 51.2mM KCl 0.2mM $MgCl_2$	1 M $NaClO_4$ 0.1 M KCl	1M NaCl 10mM K_2PO_4	5x SSC 1mM EDTA 0.1% Tween
VOLTAMMETRY								
Electrolyte for voltammetry	1M $NaClO_4$	1M $NaClO_4$	5mM Na_2PO_4 10mM NaCl 5mM $K_3Fe(CN)_6$	10mM K_2PO_4 1mM EDTA 5mM $K_3Fe(CN)_6$	10mM Tris/HCl 51.2mM KCl 50mM $MgCl_2$	1M $NaClO_4$	1M NaCl 10mM K_2PO_4	5mM $K_3Fe(CN)_6$

Table 4.4. Comparison of hybridisation conditions and related factors that might influence the hybridisation step.

The structure and composition of the DNA hairpin probe and the protocol for sensor assembly were not dissimilar from those reported in the literature. Bockisch *et al.* reported that stem stability was the most important factor governing detection functionality, while other features such as the length of linker molecules attaching the label to the stem-loop structure and the nature of the solid support were less critical [96]. However, hairpin loop length, stem length and GC content, the redox label, the number of methylene groups in the linker between the thiol group and DNA and between the DNA and the redox label were relatively standard and comparable with labelled probes used in successful biosensor assembly.

Other researchers highlighted the immobilisation of DNA probes onto gold substrates at an optimum surface density relative to the spacer molecule as the critical factor for successful DNA biosensor development. Keighley *et al.* using simultaneous co-immobilisation of thiolated DNA probes and mercaptohexanol reported that above a threshold DNA probe surface density of 4.1 x 10^{-12} mol cm^{-2}, electrostatic repulsion from negatively charged DNA modulated the charge transfer resistance and allowed hybridisation to be detected. Below this threshold density no change in charge transfer resistance was reported and hybridisation could not be detected [101]. However, assuming that the probe surface density of 1.6 x 10^{-11} mol cm^{-2} reported with the Tyndall electrode in Figure 4.6 was typical; a value almost 4-fold greater than the threshold value, the failure to detect hybridisation could not be explained on the basis of low surface density of the DNA probe. Similarly, if such a threshold value was valid, the hairpin DNA sensors assembled successfully by other groups using lower surface probe densities should have failed to detect hybridisation [75, 82, 102]. As shown in Table 4.4 concentrations of both DNA probe and alkane thiol used for sensor assembly were not dissimilar to those in the literature. However, the duration of the two immobilisation steps were somewhat different to those reported, particularly with regard to the spotting of DNA. Mercaptoethanol was used as the spacer molecule in this study based on reports that it can result in a more or less pinhole-free monolayer [10]. This has the effect that when target ssDNA molecules are present in the electrochemical cell, direct contact with the electrode surface is impossible and the signal from the electrode is only altered when redox active molecules interact with immobilised ssDNA probe. In addition, the double layer capacitance

is reduced increasing the proportion of faradaic current to charging current. This spacer, like mercaptohexanol and mercaptobutanol, can displace non-specifically adsorbed DNA molecules on the electrode surface and align the molecules perpendicular to the electrode surface such that they are accessible to target ssDNA [18].

With regard to the hybridisation step, the 5 μM concentrations of complementary DNA target applied to the Tyndall gold sensor were high by comparison with those reported in the literature, with only Plaxco's group using a similar concentration in their early trials with immobilised DNA hairpins [10]. Although the presence of abundant complementary DNA target should have encouraged hybridisation rather than acted as a deterrent, the concentration used in future hybridisation studies was reduced to 1 μM, the concentration cited most commonly in the literature. Most studies reported that hybridisation occurred spontaneously at room temperature without any heating or shaking. However, heating of gold electrodes coated with DNA probe has resulted in dramatically improved signals at hybridisation; a 140-fold increase in the ACV signal for a 20-bp ferrocene-labelled target has been reported when the electrode was heated from 3°C to 48°C during hybridisation [95, 96]. Given the peak current stability of the thiolated DNA probe in these investigations at temperatures up to 65°C, with maximum currents recorded at 55°C, trials were undertaken in which the temperature during the hybridisation step was set at 50°C. Since the incubator available for this work incorporated a shaking capability, future hybridisation trials were performed at 50°C with gentle agitation [82]. The composition of the hybridisation buffer and the electrolyte used for voltammetry was based on 1M $NaClO_4$. This electrolyte possesses a dual function, both inhibiting the decomposition of the oxidised-state of the ferrocene label and providing the high ionic strength solution required to ensure formation of the stem loop configuration of the hairpin DNA on the electrode surface [10, 80].

Following the study on Tyndall electrodes, further investigations were undertaken with cleaned and polished 2 mm gold disc electrodes. Following assembly using the identical Fc-DNA-SH probe, cyclic voltammograms were recorded periodically at regular intervals to establish the stability of the peak current. Reversible oxidative and reductive peak currents were recorded as shown in Figure 4.15A.

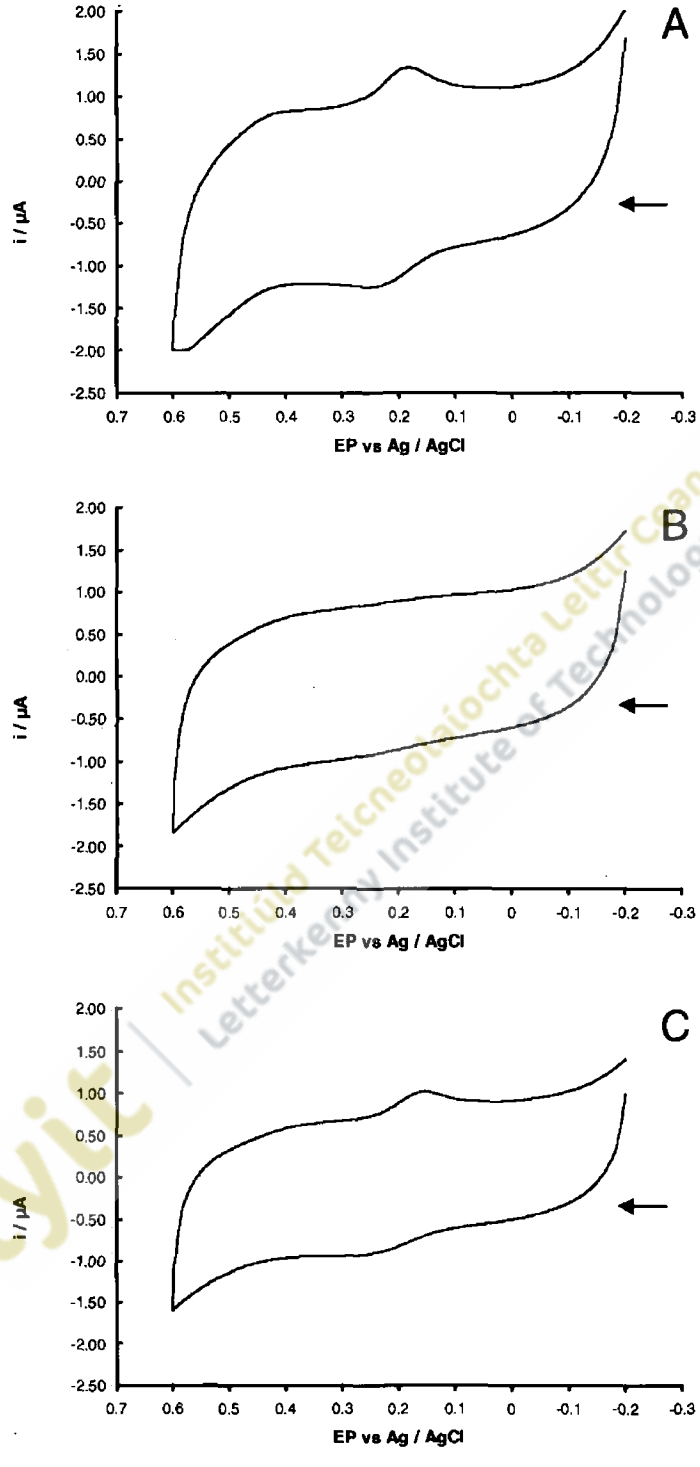

Figure 4.15. Cyclic voltammograms for the $Fe^{2+/3+}$ redox reaction for a spontaneously adsorbed monolayer of Fc-DNA-SH on a 2 mm gold disc electrode: pre-hybridisation (A), post-hybridisation (B) and post-regeneration (C). Supporting electrolyte 1M $NaClO_4$. Potential limits –0.2V to 0.6V. Anodic currents are down and cathodic currents are up.

The electrode was immersed in 1 μM complementary target ssDNA and incubated in a shaking hybridisation chamber at 50°C for 2 hr. Cyclic voltammograms recorded after hybridisation exhibited a much diminished electrochemical response as shown in Figure 4.16B.

In an attempt to regenerate the sensor, hot sodium perchlorate solution was used to denature the dsDNA. Following treatment, the electrochemical response returned as shown by the cyclic voltammogram in Figure 4.16C and was attributed to regeneration of the hairpin configuration on the electrode surface. The assembly-hybridisation-regeneration procedure was repeated on three independent monolayers to determine the reproducibility of the process. A significant decrease in peak current following hybridisation with complementary DNA was recorded with all three monolayers. Although the electrochemical signal was re-established with the three monolayers, peak currents never returned to pre-hybridisation levels and the relative regeneration exhibited poor reproducibility.

To attain a clearer understanding of the extent of signal loss and signal regeneration for the three monolayers, baseline-corrected and background-subtracted faradaic currents for the $Fe^{2+/3+}$ redox reaction rather than cyclic voltammograms are shown in Figure 4.16. Considering pre-hybridisation, post-hybridisation and post-regeneration signals for the three monolayers, the cathodic peak potential ranged between 0.13V to 0.18V and as anticipated exhibited better within-sensor reproducibility than between-sensor reproducibility. Overall cathodic peak potential (E_{pc}) was determined as 0.16 ± 0.02V. Cathodic peak currents at the pre-hybridisation step between the three monolayers were of similar magnitude and ranged between 0.35 μA to 0.57 μA, comparable with equivalent currents quoted for similar work of this nature [10, 47, 93]. To provide a clearer appreciation of the changes in peak current after hybridisation and after regeneration, values relative to the pre-hybridisation current for each sensor were determined and are shown in Figure 4.17.

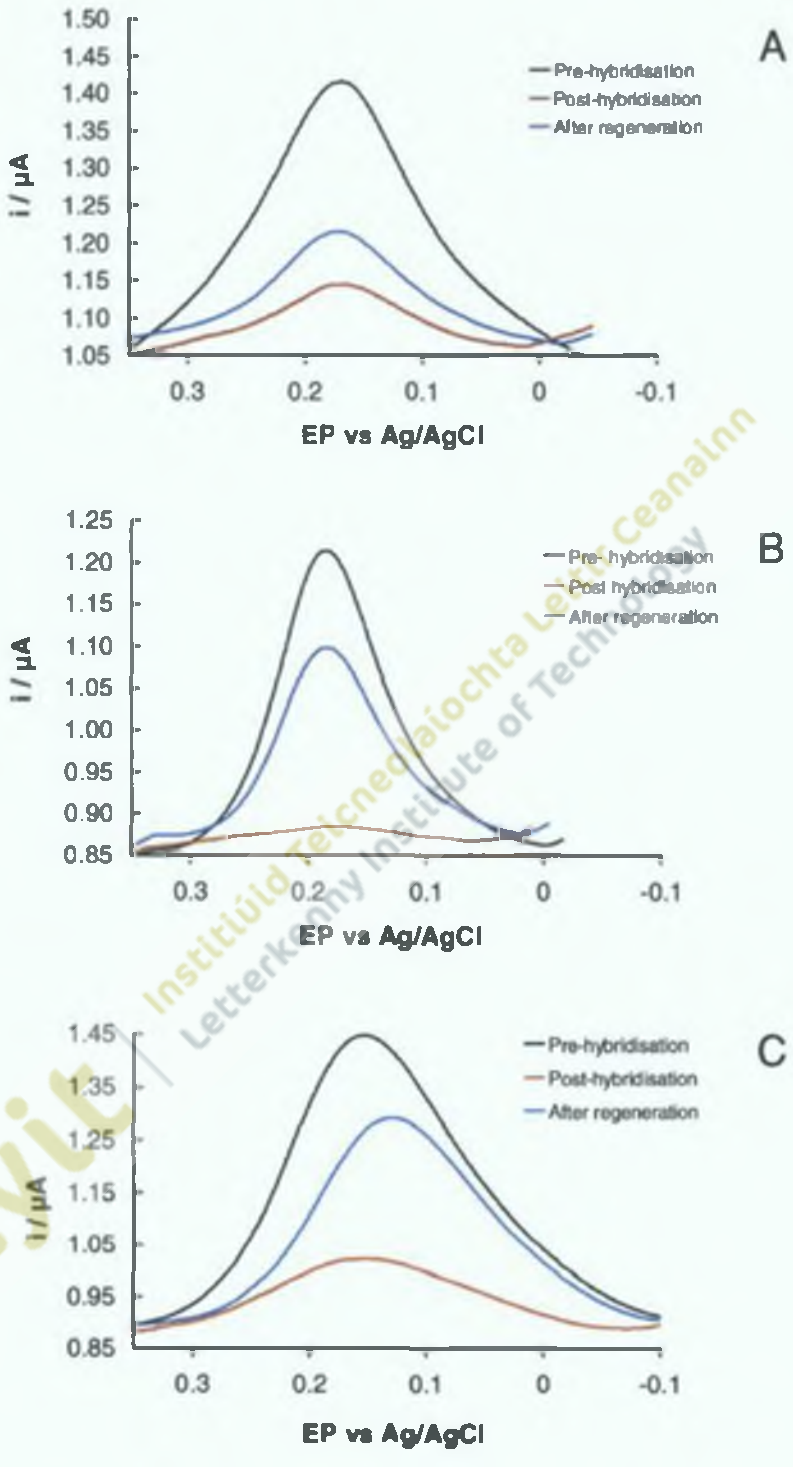

Figure 4.16. Overlay of baseline-corrected and background-subtracted faradaic currents for the $Fe^{2+/3+}$ redox reaction of three spontaneously adsorbed monolayers denoted A, B and C of Fc-DNA-SH on 2 mm gold disc electrodes: pre-hybridisation, post-hybridisation and post-regeneration.

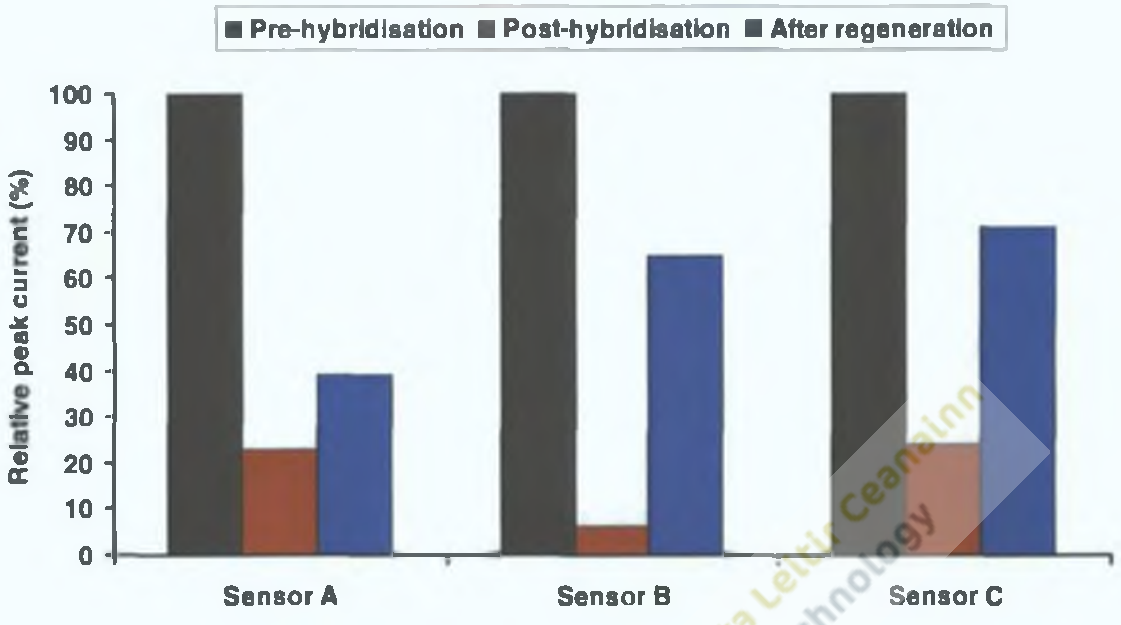

Figure 4.17. Baseline-corrected and background-subtracted faradaic currents post-hybridisation and after regeneration relative to the pre-hybridisation current for three spontaneously adsorbed monolayers denoted A, B and C of Fc-DNA-SH on 2 mm gold disc electrodes.

Combining the data from the three sensors, the relative peak current post-hybridisation was determined as 18 ± 10% within a range from 6-24%, indicative of levels of signal suppression of approximately 80%. This figure compares favourably with literature values for signal suppression of as high as 70% reported after optimisation of the probe DNA surface density and challenging with 200 nM complementary target [26, 102]. Values of signal suppression as low as 30%, i.e. the peak current after hybridisation represents 70% of the pre-hybridisation value have been advocated as a level suitable for hybridisation detection. On this basis, the results in this study suggest that the detection limit for this sensor is considerably below the 1 μM concentration of complementary target probe.

Attempts to regenerate the sensor with hot sodium perchlorate were less successful. The relative peak current after regeneration was determined as 58 ± 17% within a range from 39-71%. Comparable figures of approximately 80% recovery based on the use of hot

sodium perchlorate have been cited in the literature; signal loss being attributed to the relative instability of ferrocene in aqueous solution at high temperature [10]. An alternative explanation for the lower regeneration encountered in this study is the release of the immobilised probe DNA due to the effect of hot perchlorate solution on the sulphur bond with the gold electrode surface [103]. More recently, attempts at regeneration have utilised the denaturing effect of low ionic strength solutions on dsDNA. Using a short washing step with deionised or distilled water (30sec) at room temperature, regeneration efficiencies between 97-100% have been reported [47, 24, 102].

In summary, by contrast with the results reported for the Tyndall electrode, a functioning E-DNA biosensor was assembled on a 2 mm gold disc electrode. Levels of signal suppression exceeded those cited in the literature suggesting that the detection limit of the sensor was considerably below the 1 μM concentration of target probe used in the investigation; however attempts at sensor regeneration were less successful. The practical experience and expertise accumulated during the steps of electrode preparation, sensor assembly and hybridisation/regeneration provided an excellent foundation from which to address the construction and operation of an electrochemical DNA hybridisation sensor using one of the osmium complexes synthesised in Chapter 2 as the redox label.

Unlike the thiol- and ferrocene- modifications to DNA probes, both of which are available on a routine basis from several commercial suppliers of oligonucleotides, labelling with an osmium complex is not available as a standard service. The costs associated with developing a new protocol for attachment and for the provision of a small quantity of Os-labelled probe by the specialist probe supplier, Ellabiotech, Germany were prohibitively expensive. On this basis, attempts were undertaken to firstly immobilise onto gold disc electrodes a hairpin oligo having a 5' hexamethylene thiol group for attachment to the gold and a 3' hexamethylene amine group; and then secondly to conjugate to the oligo through coupling the succinimide ester of the osmium complex with the 5' amine group. This two step assembly procedure is illustrated diagrammatically in Figure 4.18.

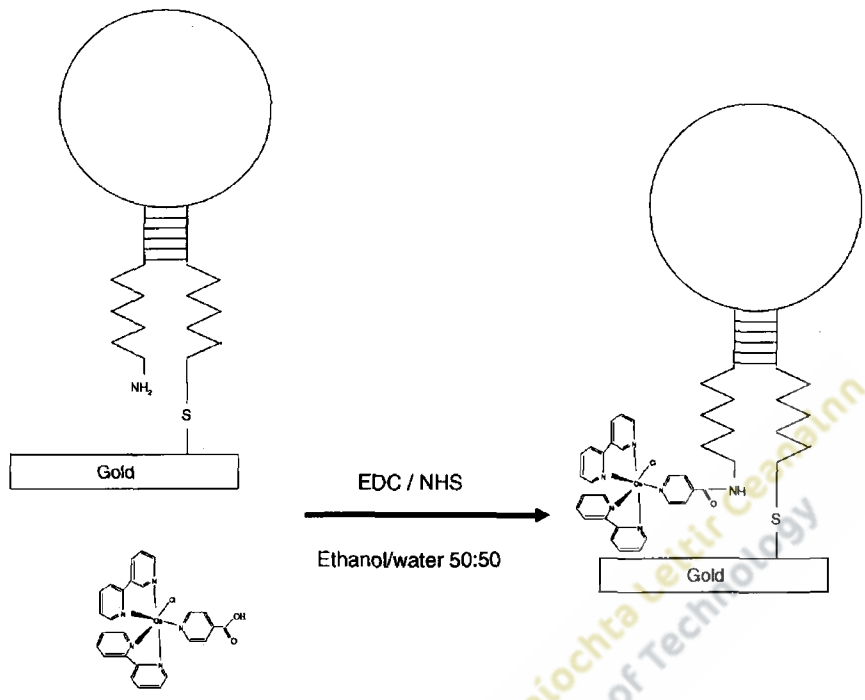

Figure 4.18. Diagrammatic representation of the two-step assembly procedure used to build a monolayer of Os-labelled hairpin using the complex [$Os(bpy)_2$-(pyridine-4-COOH)-Cl].

After completion of the immobilisation procedure and a stringent washing with Tris/HCl buffer, the response of the modified electrode in blank buffer was recorded by cyclic voltammetry to determine if an electrochemical signal was present. Reversible oxidative and reductive peak currents were recorded as shown in Figure 4.19. The formal electrode potential was determined as 239 mV, slightly more positive than the 211 mV recorded for the ferrocene modified electrode (Figure 4.15A & C) but somewhat more negative than the 320 mV recorded for the osmium complex in solution reported previously. Since control electrodes in blank buffer showed no electrochemical response, the oxidation and reduction peaks were attributed to the $Os^{2+/3+}$ redox reaction occurring in close proximity to the gold surface.

Prior to using the sensor in the hybridisation study the stability of the peak current was established by periodic cycling at 3 min intervals over a 60 min duration. Figure 4.20 shows the stable peak current vs. time for an Os-DNA-SH monolayer on a gold disc electrode.

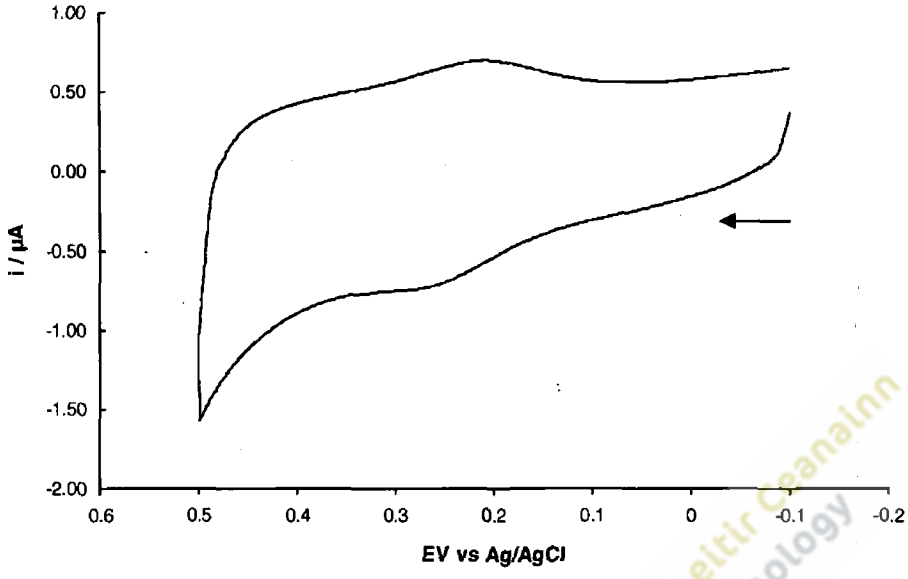

Figure 4.19. Cyclic voltammogram for the Os^{2+3+} redox reaction for a monolayer of Os-DNA-SH formed on a gold disc electrode. The supporting electrolyte was 1M $NaClO_4$. Potential limits were from –0.1V to 0.5V. Scan rate was 500 mV s^{-1}. Anodic currents are down and cathodic currents are up.

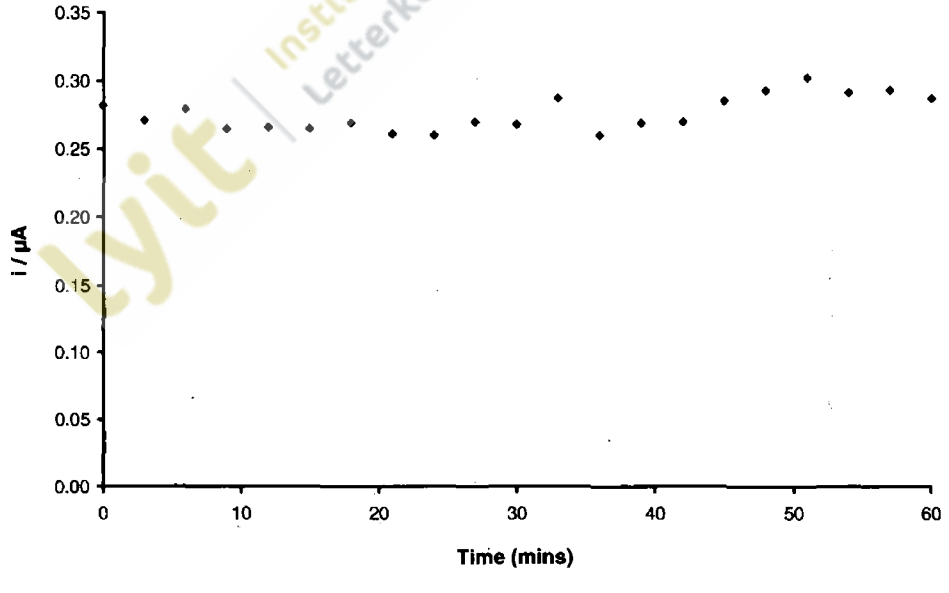

Figure 4.20. Stability of the peak current for a monolayer of Os-DNA-SH on a gold disc electrode after cycling in 1M $NaClO_4$ at 3 min intervals over 60 min duration.

AC voltammograms of gold electrodes exhibiting a stable peak current were recorded to provide a pre-hybridisation signal. This technique, which was not available for the study with the ferrocene-labelled hairpins, was used in the work with the osmium-labelled hairpins because it has been shown to be an extremely useful technique for the study of redox processes in circumstances where the amount of electrochemically active groups are small [104]. In addition analysis can be performed on extremely small peaks which are difficult and sometimes impossible to analyse using cyclic voltammetry [105]. For these reasons AC voltammetry is increasingly being reported for signal detection with electrochemical DNA biosensors. Electrodes were then immersed in 2 μM complementary target ssDNA and incubated in a shaking hybridisation chamber at 50°C for 2 hr and post-hybridisation AC voltammograms were recorded. Following regeneration, using a hot sodium perchlorate solution, AC voltammograms were again recorded. The assembly-hybridisation-regeneration steps were repeated on three independent monolayers to determine the reproducibility of the procedure. Baseline-corrected and background-subtracted faradaic currents for the $Os^{2+/3+}$ redox reaction are shown in Figure 4.21. Two of the three monolayers exhibited a significant decrease in peak current following hybridisation with complementary DNA, whereas the monolayer on sensor C showed only limited response either at hybridisation or regeneration. Peak currents using the gold disc electrode and the two-step assembly procedure of an Os-DNA-SH monolayer ranged from 150-390 nA compared to 350-600 nA with the Fc-DNA-SH monolayer on a similar electrode. With the two Os-labelled sensors that exhibited a reduced current at hybridisation, the electrochemical signal was re-established at the regeneration step using hot perchlorate at 85°C , although as before, peak currents never returned to the pre-hybridisation levels.

Considering pre-hybridisation, post-hybridisation and post-regeneration signals for the three monolayers, the peak potential ranged between 0.23V to 0.25V with a mean peak potential of 0.24 ± 0.01V. For the two working sensors, peak currents were somewhat higher than those reported by Plaxco's group in the first reports of immobilised redox-labelled DNA hairpin probes [10, 47, 93].

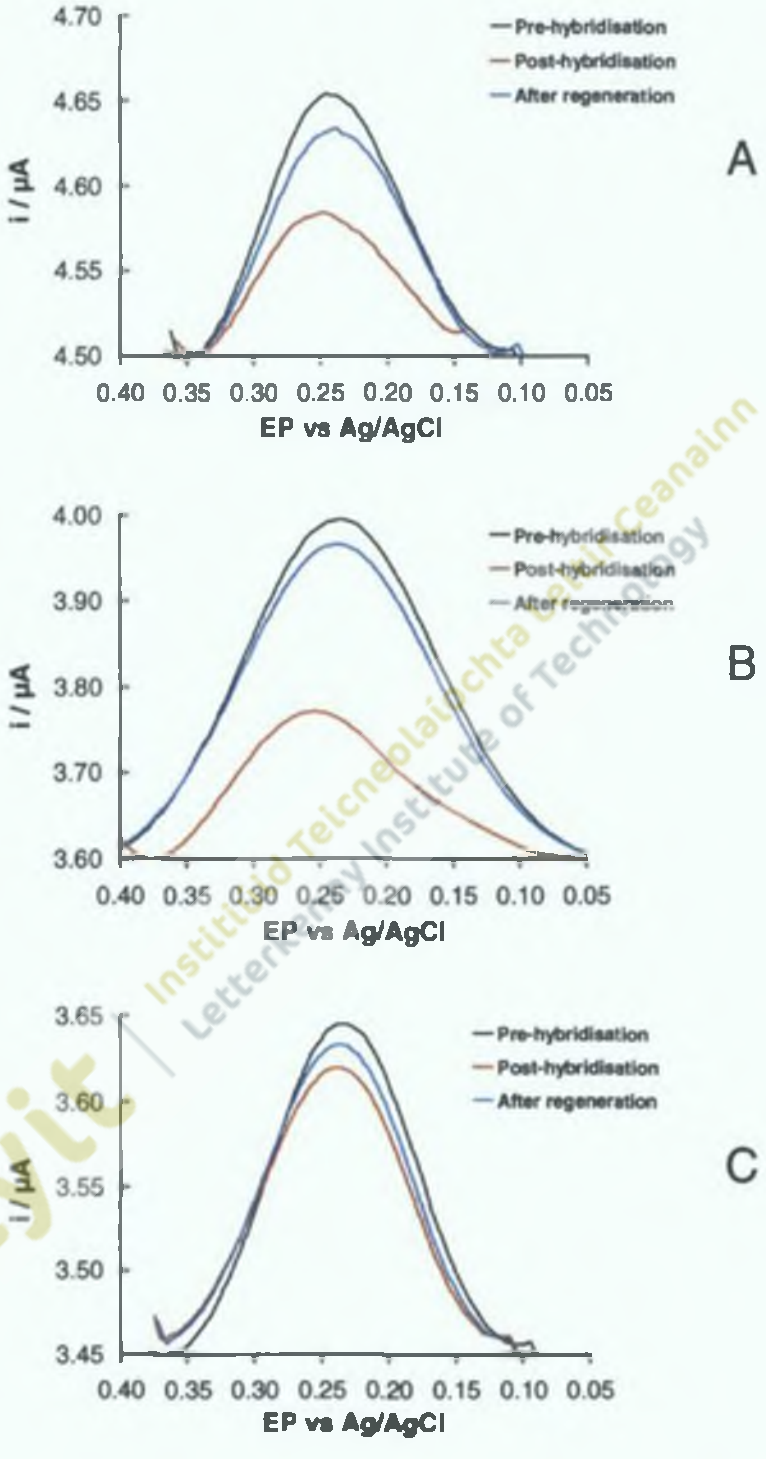

Figure 4.21. Overlay of baseline-corrected AC currents for the $Os^{2+/3+}$ redox reaction of three monolayers denoted A, B and C of Os-DNA-SH on 2mm gold disc electrodes: pre-hybridisation, post-hybridisation and post-regeneration.

To provide a clearer appreciation of the changes in peak current after hybridisation and after regeneration, values relative to the pre-hybridisation current for each sensor were determined as previously and are shown in Figure 4.22.

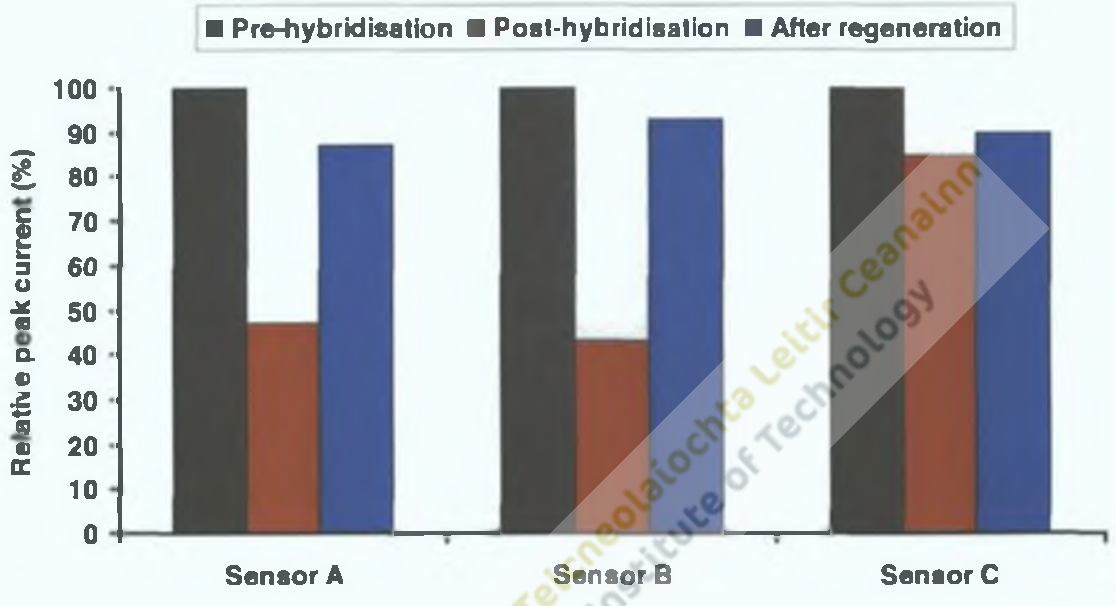

Figure 4.22. Peak currents post-hybridisation and after regeneration relative to the pre-hybridisation current for three spontaneously adsorbed monolayers denoted A, B and C of Os-DNA-SH on 2mm gold disc electrodes.

Using the data from the two working sensors only, the relative peak current post-hybridisation was determined as 45 ± 3% within a range from 43-47%, indicative of a reduced level of suppression compared to the ferrocene-labelled monolayer but with improved reproducibility, though only two working sensors were considered in this appraisal. Peak current suppression of approximately 55% compares favourably with literature values given that signal suppression as low as 30% have been considered adequate for hybridisation detection [93, 102]. As with the ferrocene-labelled monolayer, the results for the Os-DNA-SH monolayer suggest that the detection limit for this sensor is considerably below the 1 μM concentration of complementary target probe.

Regeneration of the signal by rinsing in hot perchlorate solution was more successful than that achieved for the ferrocene-labelled monolayer. Using data from the two working sensors, the relative peak current after regeneration was determined as 90 ± 4% within a range from 87-93% suggesting a reduced effect on the probe or redox label compared with the ferrocene-labelled sensor of high temperature aqueous solutions. As stated previously, recent reports with deionised or distilled water (30 sec) at room temperature have produced regeneration efficiencies between 97-100% allowing re-use of assembled DNA hairpin sensors [47, 24, 102].

Similar to the ferrocene-labelled DNA sensor, a functioning E-DNA biosensor was assembled on a gold disc electrode using the [$Os(bpy)_2$-(pyridine-4-COOH)-Cl] complex synthesised in this project. Although the osmium-based sensor exhibited reduced levels of signal suppression compared to the ferrocene-based sensor, regeneration efficiency was much improved. In both cases, the levels of signal suppression recorded suggested that detection limits were well below the levels of 1 μM concentration of target probe used in the investigations. The different redox potentials of the complexes used suggested that it may be possible, by careful design of the attached bridging ligands, to tune redox complexes such that multiplex detection of hybridisation might be possible allowing more than one target organism to be identified in a single measurement.

4.5 References

1. Wang. J., Rivas, G., Cai, X., Paleček, E., Nielsen, P., Shiraishi, H., Dontha, N., Luo, D., Parrado, C., Chicharro, M., Farias, P.A.M., Valera, F.S., Grant, D.H., Ozsoz, M., Flair, M.N. *Anal. Chim. Acta*, 1997, 347, 1-8.
2. Wang, J. *Chemistry-A European Journal*, 1999, 5, 1681-1685.
3. E. Paleček, M. Fojta, *Anal. Chem.*, 2001, 73, 74A.
4. Gooding, J.J. *Electroanalysis*, 2002, 14, 1149-1156.
5. Ozkan, D. *Electrochemistry Communications*, 2002, 4, 796–802.
6. Kelley, S.O., Barton, J.K. *Bioconjugate Chem.*, 1997, 8, 31 -37.
7. Junhui, Z., Hong, C., Ruifu, Y. *Biotechnology Advances*, 1997, 15, 43-58.
8. Mikkelsen, S.R. *Electroanalysis*, 1996, 8, 15.
9. Tyagi, S., Kramer, F.R. *Nature Biotechnology*, 1996, 14, 303-308.
10. Fan, C., Plaxco, K.W., Heeger, A.J. *P.N.A.S.*, 2003, 100, 9134-9137.
11. Mao, Y., Luo, C., Ouyang, Q. *Nucleic Acid Research*, 2003, 31(18), e108.
12. Immoos, C.E., lee, S.J., Grinstaff, M.W. *Chembiochem.*, 2004, 6, 1100-1103.
13. Lucarelli, F., Marrazza, G., Mascini, M. *Biosensors and Bioelectronics*, 2005, 20, 2001-2009.
14. Metfies, K., Huljic, S., Lange, M., Medlin, L.K. *Biosensors and Bioelectronics*, 2005, 20, 1349-1357.
15. Fojta, M., Havran, L., Billova, S., Kostecka, P., Masarik, M., Kizek, R. *Electroanalysis*, 2003, 15, 431-440.
16. Paleček, E., Fojta, M., Jelen, F. *J. Am. Chem. Soc.*, 2002, 56, 85-90.
17. Drummond, T.G., Hill, M.G., Barton, J.K. *Nature Biotechnology*, 2003, 21, 1192-1199.
18. Steel, A.B., Herne, T.M., Tarlov, M.J. *Analytical Chemistry*, 1998, 70, 4670-4677.
19. Del Pozo, M.V., Alonso, C., Pariente, F., Lorenzo, C. *Biosensors and Bioelectronics*, 2004, 20, 1549-1558.
20. Wong, E.L.S., Gooding, J.J. *Anal. Chem.*, 2006, 78: 2138 –2144.
21. Du, H., Strohsahl, C.M., Camera, J., Miller, B.L., Krauss, T.D. *J. Am. Chem. Soc.*, 2005, 127, 7932-7940.

22. Xiao, Y., Lubin, A.A., Heeger, A.J., Plaxco, K.W. *Angew. Chem. Int. Ed.*, 2005, 44, 5456-5459.
23. Lai, R.Y., Lagally, E.T., Lee, S.H., Soh, H.T., Plaxco, K.W., Heeger, A.J. *P.N.A.S.*, 2006, 103, 4017-4021.
24. Lubin, A.A., Lai, R.Y., Baker, B.R., Heeger, A.J., Plaxco, K.W. *Anal. Chem.*, 2006, 78, 5671-5677.
25. Lai, R.Y., Seferos, D.S., Heeger, A.J., Bazan, G.C., Plaxco, K.W. *Langmuir*, 2006, 22, 10796-10800.
26. Ricci, F., Lai, R.Y., Heeger, A.J., Plaxco, K.W., Sumner, J.J. *Langmuir*, 2007, 23, 6827-6834.
27. Herne, T.M., Tarlov, M.J. *J. Am. Chem. Soc.*, 1997, 119, 8916-8920.
28. Levicky, R., Herne, T.M., Tarlov, M.J., Satija, S.K. *J. Am. Chem. Soc.*, 1998, 120, 9787-9792.
29. Lee, C.Y., Gong, P., Harbers, G.M., Grainger, D.W., Castner, D.G., Gamble, L.J. *Anal. Chem.*, 2006, 78, 3316-3325.
30. Peterson, A. W., Heaton, R. J., Georgiadis, R. M. *Nucleic Acids Res.*, 2001, 29, 5163-5168.
31. Bunemann, T. *Nucleic Acid Res.*, 1982, 10, 7181-7196.
32. Gao, Y., Wolf, L.K., Georgiadis, R.M. *Nucleic. Acids. Res.*, 2006, 34, 3370-3377.
33. Wong, E.L.S., Chow, E., Gooding, J.J. *Langmuir*, 2005, 21, 6957-6965.
34. Steel, A.B., Herne, T.M., Tarlov, M. *J. Anal. Chem.*, 1998, 70, 4670.
35. Levicky, R., Herne, T.M , Tarlov M.J,. Satija, S.K. *J. Am. Chem. Soc.*, 1998, 120, 9787.
36. Steel, A.B., Levicky, R ., Herne, T.M., Tarlov M.J. *Biophys. J.*, 2000, 79, 975.
37. Peterson, A.W., Heaton, R.J., Georgiadis, R.M. *Nucleic Acids Res.*, 2001, 29, 5163.
38. Peterson, A.W., Heaton, R.J., Georgiadis, R.M. *J. Am. Chem. Soc.*, 2000, 122, 7837.
39. Peterson, A.W., Wolf, L.K., Georgiadis, R.M. *J. Am. Chem. Soc.*, 2002, 124, 14601.
40. Georgiadis, R.M., Peterlinz, K.P., Peterson, A.W. *J. Am. Chem. Soc.*, 2000, 122, 3166.
41. Luccarelli, F. *Biosensors and Bioelectronics*, 2004, 19, 515-530.
42. Li, Z., Jin, R.C., Mirkin, C.A., Letsinger, R.L. *Nucleic Acids Res.*, 2002, 30, 1558-1562.

43. Arihara, K., Ariga, T., Takashima, N., Arihara, K., Okajima, T., Kitamura, F., Tokuda, K., Ohsaka, T. *Phys. Chem. Chem. Phys.*, 2003, 5, 3758 – 3761.

44. Sakata, T.; Maruyama, S.T., Ueda, S., Otsuka, A., Miyahara, H. *Langmuir*, 2007, 23, 2269-2272.

45. Integrated DNA Technologies. 2003 FAQ: How do you reduce thiol modified oligos?

46. Lee, C.Y., Canavan, H.E., Gamble, L.J., Castner, D.G. *Langmuir*, 2005, 21, 5134-5141.

47. Xiao, Y., Lai, R.Y., Plaxco, K.W. *Nature Protocols*, 2007, 2, 2875-2880.

48. Huang, E., Satjapipat, M., Han, S., Zhou, F. *Langmuir*, 2001, 1215-1224.

49. Dharuman, V., Hahn, J. H. *Sensors and Actuators*, 2007, 127, 536-544.

50. Odenthal, K.J., Gooding, J.J. *Analyst*, 2007, 132, 603–610.

51. Wong, E.L.S., Chow, E., Gooding, J.J. *Langmuir*, 2005, 21, 6957-6965.

52. Arinagaa, K., Rantb, U., Kneževićb, J., Pringsheimb, E., Tornowb, M., Fujitaa, S., Abstreiterb, G., Yokoyamaa, N. *Biosensors and Bioelectronics*, 2007, 23, 326-331.

53. Wang, J., Li, J. H., Baca, A. J., Hu, J. B., Zhou, F. M., Yan, W., Pang, D. W. *Anal. Chem.*, 2003, 75, 3941.

54. Baca, A. J., Zhou, F. M., Wang, J., Hu, J. B., Li, J. H., Wang, J. X., Chikneyan, Z. S. *Electroanalysis*, 2004, 16, 73.

55. Le Floch, F., Ho, H. A., Harding-Lepage, P., Bedard, M.; Neagu-Plesu, R., Leclerc, M. *Adv. Mater.*, 2005, 17, 1251.

56. Wu, Z.-S., Jiang, J.-H., Shen, G.-L., Yu, R.-Q. *Hum. Mutat.*, 2007, 28, 630.

57. Cai, H., Xu, C., He, P. G., Fang, Y. Z. J. *Electroanal. Chem.*, 2001,510, 78.

58. Xu, C., Cai, H., He, P. G., Fang, Y. Z. *Analyst*, 2001, 126, 62.

59. Takenaka, S., Yamashita, K., Takagi, M., Uto, Y., Kondo, H. *Anal. Chem.*, 2000, 72, 1334.

60. Beilstein, A.E.,Grinstaff, M.W. *Chem.Comm.*, 2000, 509-510.

61. Kealy, T. J., Pausen, P. L. *Nature*, 1951, 168, 1039-1040.

62. Takenaka, S., Uto, , Y., Kondo, H., Ihara, T., Takagi, M. *Anal. Biochem.*, 1994, 218, 436-443.

63. Uto, Y., Kondo, H., Abe, M., Suzuki, T., Takenaka, S. *Anal.Biochem.*, 1997, 250, 122-124.

64. Ihara, T., Maruo, Y., Takenaka, S., Takagi, M. *Nucleic Acid Res.*, 1996, 24, 4273-4280.

65. Kober, E. M., Caspar, J.V., Sullivan, B.P., Meyer, T.J. *Inorg. Chem.*, 1988, 27, 4587-4598.

66. Lever, A.B.P. *Inorg. Chem.* 1990, 29(6), 1271-1285.

67. Danilowicz, C., Cortón, E., Battaglini, F. *J. Electroanal. Chem.*, 1998, 445, 89-94.

68. Dinsmore, M.J., Lee. J.S. *J. Electroanal. Chem.*, 2008, 23(10), 1555-1561.

69. Mao, X., Jiang, J., Xu, X., Chu, X., Luo, Y., Shen, G., Yu, R. *Biosensors and Bioelectronics*, 2007, 22, 2237-2243.

70. Steichen, M., Decrem, Y., Godfroid, E., Buess-Herman, C., Hashimoto, K., Ito, K., Ishimori, Y. *Anal. Chem.*, 1994, 66, 3830-3833.

71. Lao, R., Song, S., Wu, H., Wang, L., Zhang, Z., He, L., Fan, C. *Anal. Chem.*, 2005, 77, 6475-6480.

72. Du, H., Disney, M.D., Miller, B.L., Krauss, T.D. *J. Am. Chem. Soc.*, 2003, 125, 4012-4013.

73. Liepold, P., Wieder, H., Hillebrandt, H., Friebel, A., Hartwich, G. *Bioelectrochem.*, 2005, 67(2), 143-150.

74. Flechsig G., , Peter, J., Voss, K., Gründler, P. *Electrochem. Comm.*, 2005, 7(10), 1059-1065.

75. Ricci, F., Lai, R.Y., Plaxco, K.W. *Chem. Comm.*, 2007, 3768-3770.

76. Dharuman, V., Hahn, J.H. *Biosensors and Bioelectronics.*, 2008 (in press)

77. Song, Y., Liu, Y, Yang, M., Zhang, B., Li, Z. *Appl. Surface. Sci.*, 2006, 252, 5693-5699.

78. Jenkins, D.M., B. Chami, M. Kreuzer, G. Presting, A. Alvarez, Liaw, B.Y. *Anal. Chem.*, 2006, 78(7):2314-2318

79. Liu, Y.-C. *Langmuir*, 2003, 19, 6888-6893.

80. Han, S.W., Seo, H., Chung, Y.K., Kim, K. *Langmuir*, 2000, 16, 9493-9500.

81. Nakamura, M., Ueda, M., Watanabe, S., Kumamoto, S., Yamana, K. *Nucleic Acids Sympos. Ser.*, 2007, 51(1), 317-318.

82. Steichen, M., Buess-Herman, C. *Electrochem. Comm.*, 2005, 7, 416-420.

83. Wei, F., Wang, J., Liao, W., Zimmermann, B.G., Wong, D.T., Ho, C.M. *Nucleic Acids Res.*, 2008 (in press).
84. Zauner, G., Wang, Y., Lavesa-Curto, M., MacDonald, A., Mayes, A.G., Bowater, R.P., Butt, J.N. *Analyst*, 2005, 130, 345-349.
85. Southern, E.; Mir, K.; Shchepinov, M. *Nat. Genet.*, 1999, 21, 5-9.
86. Huang, E.; Satjapipat, M.; Han, S. B.; Zhou, F. M. *Langmuir*, 2001, 17, 6188-6190.
87. O'Connor, S. D.; Olsen, G. T.; Creager, S. E. *J. Electroanal. Chem.*, 1999, 466, 197-202.
88. Riccelli, P.V., Merante, F., Leung, K.T., Bortolin, S., Zastawny, R.L., Janeczko, R., Benight, A.S. *Nucleic Acids Res.*, 2001, 29, 996-1004.
89. Fan, C, Fahlman, R.P, Dipankar, S. *J. Am. Chem. Soc.*, 2002, 124, 4610-4616.
90. Schwartz, D. K. *Ann. Rev. Phys. Chem.*, 2001, 52, 107-137.
91. Taft, B.J., O'Keefe, M., Fourkas, J.T., Kelley, S.O. *Analytica Chimica Acta*, 2003, 496, 81–91.
92. Maruyama, K., Motonaka, J., Mishima, Y., Nakabayashi, Y. *Nucleic Acids Sympos. Ser.*, 1999, 42, 181—182.
93. Xiao, Y., Lubin, Baker, Plaxco, K.W., Heeger, A.J. *P.N.A.S.*, 2006 103(45), 16677–16680.
94. Park, N., Hahn, J.H. *Anal. Chem.*, 2004, 76, 900-906.
95. Bockisch, B., Grunwald, T., Spillner, E., Bredehorst, R. *Nucleic Acids Res.*, 2005, Vol. 33(11), e101, doi: 10.1093/nar/gni101.
96. Flechsig, G., Peter, J., Hartwich, G., Wang, J., Gründler, P. *Langmuir*, 2005, 21 (17), 7848 -7853.
97. Peter, J., Reske, T., Flechsig, G. *Electroanalysis*, 2007, 19(13), 1356 – 1361.
98. Strohsahl, C.M., Miller, B.L., Krauss, T.D. *Nature Protocols*, 2007, 2(9), 2105-2110.
99. Bustin, S.A. 2004. A-Z of Quantitative PCR. IUL Biotechnology Series. Publ. Int. Univ. Line, La Jolla, California.
100. Brewer, S.H., Anthireya, S.J., Lappi, S.E., Drapcho, D.L., Franzen, S. *Langmuir*, 2002, 18, 4460-4464.
101. Keighley, S.D., Li, P., Estrela, P., Migliorato, P. *Biosensors and Bioelectronics*, 2008, 23(8), 1291-1297.

102. Ricci, F., Plaxco, K.W. *Microchim. Acta*, 2008. DOI 10.1007/s00604-008-0015-4 (in press).

103. Herdt, A.R., Drawz, S.M., Kang, Y., Taton, T.A. *Colloids and Surfaces B: Biointerfaces*, 2006, 51, 130-139.

104. Wu, Z.S., Jiang, J.H., Shen, G.L. *Human Mutation*, 2007, 28, 630-637.

105. Creager, S.E.; Wooster, T.T. *Anal. Chem.*, 1998, 70(20), 4257-4263.

5. Conclusions and Future Work

Microelectrodes of small physical size which produce currents in the nanoamp range offer many advantages over macroelectrodes in the study of electrochemical processes for analytical purposes. Of these the most important are their much faster transport rates and their ability to detect tiny amounts of analyte even in highly resistive environments, allowing steady state currents to be generated in very small volumes in extremely fast times. In this study both platinum and gold microelectrodes of 12.5 μm radius were successfully fabricated and characterised. Although these microelectrodes produced currents in the nanoamp range, when high scan rates were used iR compensation had to be taken into account to avoid inaccuracies. These microelectrodes demonstrated many advantages for the study of electron transfer kinetics compared to conventional electrodes. Gold microelectrodes, though successfully fabricated, proved more problematic to assemble than platinum microelectrodes due to difficulties encountered with soldering of the aluminum hook-up wire to the gold microwire and to imperfections in the glass seal around the gold after heating. This latter difficulty was attributed to the different thermal expansion co-efficients between the glass and the gold microwire used for construction.

The desire to produce miniature devices for measurements in extremely small sample volumes has focussed attention on the development of microarrays comprising a series of microelectrodes in parallel. These allows currents similar to that of a macroelectrode to be generated while maintaining the advantages such as higher proportions of faradaic current to interfering or capacitative currents and their use in highly resistive environments. As an alternative, individual electrodes within the array may be read independently making possible the detection of multiple analytes on a single chip. Advances in microelectronics over the last number of years, has allowed the miniaturisation of such devices and this coupled with developments in instrumentation allows the tiny currents produced by these devices to be reproducibly quantified.

In this study a range of osmium and ruthenium bipyridyl complexes were successfully synthesised and characterised using chromatographic, spectroscopic and electrochemical techniques. With the exception of the di-substituted ruthenium complex, HPLC of all other complexes showed a single chromatographic peak indicative of the presence of a single product. Osmium complexes were easier to oxidise than similar ruthenium complexes, electrode potentials being some 300 – 500 mV more negative. Redox potentials for analogous ruthenium and osmium complexes were linearly related due to the fact that attached ligands on either metal centre, whether electron donating or electron withdrawing, shift the electrode potential negatively or positively by the same extent allowing the contribution from different attached ligands to be quantified.

The solution phase properties of the complexes as well as the electrochemical properties when immobilised as a monomolecular layer on platinum, indium tin oxide and gold electrode surfaces were investigated using cyclic voltammetry. Diffusion co-efficients and the solution phase electron transfer rate constants were determined for each of the complexes. Ruthenium complexes exhibited higher rates of diffusion than analogous osmium complexes. Although no clear explanation was established, values reported here were comparable with those in the literature for similar complexes where generally ruthenium complexes were reported to have higher rates of diffusion.

Self assembled monolayers of $[Os(bpy)_2\text{-}4\text{-}tet\text{-}Cl](PF_6)$, $[Ru(bpy)_2\text{-}4\text{-}tet\text{-}Cl](PF_6)$ and $[Ru(bpy)_2\text{-}(4\text{-}tet)_2](PF_6)_2$, all containing the tetrazine ligand, formed spontaneously on platinum surfaces from acetone:water solutions. No adsorption on platinum surfaces occurred from solutions of $[Os(bpy)_2$-(pyridine-4-COOH)-Cl] or $[Ru(bpy)_2$-(pyridine-4-COOH)-Cl], complexes containing the pyridine-4-carboxylic acid ligand.

The kinetics of monolayer formation on platinum for the complexes containing the tetrazine ligand were monitored in real time, and non-invasively, using relatively low concentrations and relatively fast scan rates so as to minimise the contribution to the overall current from the complex in solution. Monolayer formation was initially rapid and then progressed at a

much slower rate. The equilibrium surface coverage depended on the concentration of the complex. Generally experimental data agreed well with Langmurian adsorption, although in some instances it was better described by the Frumkin isotherm with small positive interaction parameters. The area occupied per molecule suggested that the radius of the head group determines the surface coverage which can be achieved and suggested that surface attachment is occurring through the pendant nitrogen of the pyridine. Cyclic voltammograms recorded with these modified electrodes in blank electrolyte produced peak currents which scaled linearly with the scan rate, typical of a surface-immobilised species.

The issue of whether adsorption is best described as a process under kinetic control, or is controlled by diffusion of the adsorbate to the electrode surface was investigated. The experimental data was in good agreement with both the kinetic Langmuir equation and also a linear relationship with the diffusion controlled model. However, comparison of the rates of increase in surface coverage at different concentrations of the complexes confirmed that the experimental data was in much better agreement with the kinetic control model.

Adsorption rate constants were calculated where adsorption takes place on a single site and also where adsorption requires two sites and the adsorbed layer is mobile. Rate constants determined using both methods were lower, in some cases by an order of magnitude, than values reported in the literature for similar complexes in aqueous solutions. This was not unexpected since these complexes have a much higher solubility in acetone solutions from which adsorption occurred in this study. Plots of surface coverage vs. time showed that experimental data was in much better agreement with the first order model suggesting that binding takes place on a single site.

Desorption into blank electrolyte was monitored by following surface coverage as a function of time. First order desorption kinetics were followed by all complexes. Monolayers were stable and even after several hours of repetitive cycling, more than 50% of the monolayer still remained on the electrode surface. Desorption rate constants were comparable with values reported in the literature.

Monolayers of [$Os(bpy)_2$-(pyridine-4-COOH)-Cl] and [$Ru(bpy)_2$-(pyridine-4-COOH)-Cl] were immobilised onto a gold surface in a two-step assembly process. Attachment was achieved using amide coupling between an amine group present on a cysteamine monlayer and a carboxylic acid group present on the complex. This type of attachment has been reported in the literature for the immobilisation of enzymes or single stranded DNA probes onto gold surfaces. By comparison, monolayers of these two osmium and ruthenium complexes containing the pyridine-4-carboxylic acid ligand spontaneously adsorbed onto ITO slides demonstrating that molecules containing different free functional groups may be preferentially adsorbed onto different electrode surfaces.

Over the last twenty years significant progress in the development of molecular biosensors has been achieved with in some instances commercial applications entering the marketplace. Considerable efforts have been directed towards the use of transition metal complexes in the development of electrochemical sensors for DNA hybridisation. Different models of electrochemically-based DNA biosensors have been investigated, many involving immobilisation of linear ssDNA onto an electrode surface with hybridisation detection being effected by an intercalating compound which binds preferentially to dsDNA if present. More recently, electrochemical versions of molecular beacons have been developed in which the fluorophore has been replaced by a redox compound and the quencher has been replaced by a thiol compound for immobilisation onto an electrode surface. These hairpin probes offer advantages over linear probes since the conformational change which occurs at hybridisation results in greater discrimination between the hybridised and unhybridised state. In this research study, hairpin ssDNA probes containing a sulphur group at the 5' end and a redox active molecule at the 3' end were successfully chemisorbed on gold electrodes. After immobilisation of the DNA probe, any remaining bare gold sites were filled with mercaptoethanol. These modified electrodes were used to detect hybridisation when challenged with a complementary ssDNA sequence. Two different electroactive detection labels were evaluated, one being a ferrocene modification which was commercially available and provided an opportunity for familiarisation with the workings of an E-DNA sensor and the other being an osmium bipyridyl complex synthesised as part of this work programme.

Applications using ferrocene have been reported in the literature however its use is disadvantaged by its poor stability at higher temperatures and the poor stability of ferrocenium (the oxidised form of ferrocene) in electrolytes such as chlorides, bromides, nitrates and sulphates. Some reports in the literature cite figures for decomposition of the monolayer of up to 95% after only 2- 3 scans, even when cycled between modest potential limits of 0.2 to 0.85V, though losses were less significant in perchlorate salts if the pH was maintained below 2 [1].

Of the complexes synthesised in this research programme, the osmium complex containing the carboxylic acid ligand was considered the best option for investigation as a redox molecule in an electrochemical hairpin DNA sensor. This complex was selected since the free carboxylic acid group should allow covalent attachment to an aminated ssDNA probe, a commercially available modification, through carbodiimide coupling and secondly on the basis that the redox potential of the complex is sufficiently low compared to the higher potential of the analogous ruthenium complex to avoid any damage to guanine bases [2]. In addition and by contrast with ferrocene, these complexes have been shown to be stable in a range of electrolytes and have good stability over a wide pH range. A working electrochemical DNA sensor using the selected osmium complex was assembled and results demonstrated improved sensor regeneration compared to sensors in which ferrocene was used as the redox label. Hence use of this complex as the redox label may result in a more robust sensor exhibiting less decomposition following repetitive oxidation reduction cycles and stringent washing steps. This is advantageous in terms of the stability, regeneration and re-use of the sensor.

The ferrocene and osmium DNA sensors assembled in this study exhibited a significant loss of signal following hybridisation with complementary ssDNA. However, if this technology is to be applied commercially, the issue of reproducibility highlighted in this work, must be addressed. Reproducibility in terms of the reduction in current in signal-off sensors of this type and enhancement of the current in signal-on sensors, which have not been considered here, has received only limited attention in the literature. To some extent, the reduction or

enhancement in the current at hybridisation has been hidden when results are expressed in terms of the percentage signal suppression or signal enhancement, parameters often used in the literature. Several factors may contribute to poor reproducibility and require optimisation if DNA sensors are to be used for commercial applications. Based on the experience gained in this work, two of the most salient features which may contribute to poor reproducibility and as a consequence poor reliability and which need to be addressed are the stability of the gold-sulphur bond and secondly the density of probe immobilised on the electrode surface.

With regard to the stability of the anchor used for immobilisation, although the thiol/gold bond provides a relatively strong bond between the DNA and the gold surface, doubts still remain as to whether the decrease in signal recorded at hybridisation is caused by conformational change of the hairpin and transfer of the redox label away from the surface of the electrode or whether some of the hairpin DNA immobilised through the thiol group has been displaced from the gold surface. This issue of displacement of monofunctional thiolated oligonucleotides has been widely reported at high salt concentrations and elevated temperatures and particularly in the presence of mercaptoethanol [3]. Improvement in the stability of DNA probes on gold nanoparticles has been reported in the literature when the monothiol anchor groups have been replaced by tri-thiol groups [4]. Recently the specialist oligonucleotide supply company, Friz Biochem has developed a new compound for probe immobilisation which is claimed to have performance far superior to other commercially available products. This product, DTPA is a disulphide-containing phosphoramidite which allows modification of synthetic DNA probes with multiple thiol groups. The number of monomer groups can be adapted depending on the stability requirements of the proposed application and has been likened to a 'super-glue' for probe immobilisation. Each monomer in this new DTPA (dithiol phosphoramidite) linker is capable of forming two gold-sulphur bonds as shown in Figure 5.1.

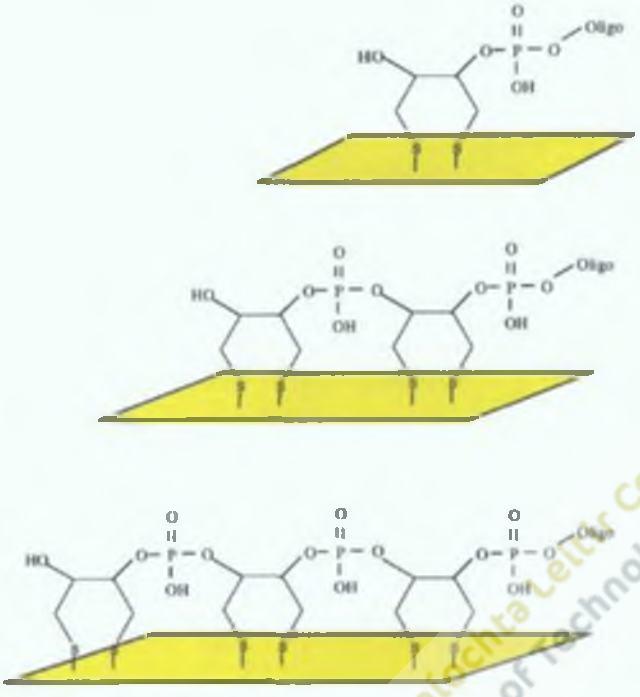

Figure 5.1. Molecular structure of the DTPA linker showing one, two and three monomers providing 2-, 4- and 6- sulphur-gold bonds respectively for attachment to the gold sensor.

Reports from the company comparing these new linkers comprising one, two and three monomers (2-, 4- and 6- gold-sulphur bonds) with a single thiol-modified oligonucleotide have demonstrated that although initially more of the single-thiolated oligo was attached, losses following treatment with mercaptoethanol were very much reduced. If reliable sensors and microarrays are to be assembled in the future based on such systems of immobilisation, it is essential that the question of stability of the DNA anchor (i.e. the anchor between the thiol and the gold surface) during the washing steps, the diluent filling steps, the hybridisation step and regeneration step can be addressed. Since the electrochemical DNA sensors assembled in this study were both signal-off sensors rather than signal-on sensors, there is a greater likelihood of misinterpretation of results due to false positives. For this reason, with signal-off sensors, it is vitally important that the stability of the bond between the probe and the electrode can be assured to eliminate this possibility.

The second issue of probe density on the electrode surface is of critical importance to the performance of the biosensor. Assuming that all the redox labelled probe is in the hairpin configuration with the redox labels held close to the electrode, at high probe densities although the current generated might be high, it is possible that the close proximity of the probes to one another may not allow sufficient space for hybridisation to occur efficiently. By contrast, if the probe density is low, hybridisation efficiency may be improved, but the low probe density might result in poor signal generation and hence poor sensitivity. Clearly an optimum balance is required where there is sufficient probe attached to generate a significant electrical signal, but not too much probe to hinder hybridisation.

In this study although a redox labelled hairpin was attached to the gold electrode and surface coverage was estimated from the areas of the voltammetric reductive or oxidative peaks, the results of surface coverage are only valid if all the probes attached were in the hairpin conformation with the redox labels in close proximity to the electrode surface. To obtain better estimates of the surface coverage, since it is possible that not all of the immobilised probe DNA is in the hairpin form, we are presently investigating the possibility of using reductive desorption at negative potentials in basic solutions to provide a more reliable method for determination of surface coverage. This method relies on the fact that one electron is consumed for each reductively desorbed sulphur molecule. Hence it may be possible to determine more accurately the probe density immobilised through these sulphur groups both with the thiol modification and with the DTPA modifications and thus to optimise the surface coverage in terms of signal generation and hybridisation efficiency

Preliminary results showing reductive desorption of a disulphide-protected ssDNA hairpin with a mercaptoethanol protecting group from a Tyndall gold electrode in 0.1M KOH after 60 min immersion in a 0.1 μM probe concentration are presented in Figure 5.2.

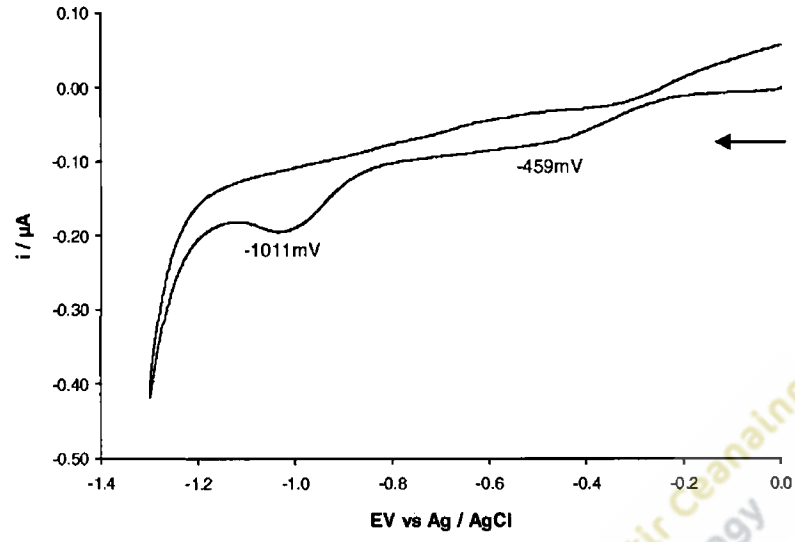

Figure 5.2. Cyclic voltammogram of the reductive desorption of a disulphide-protected ssDNA hairpin in 0.1M KOH from a Tyndall gold electrode after 60min immersion in a 0.1 µM probe concentration. Potential limits 0.0 to -1.3V. Scan rate 30 mV s^{-1}. Scan direction shown by black arrow.

Two cathodic peaks in potential in the desorption voltammogram are shown; a broad peak in potential at -459 mV attributed to desorption of the probe DNA and a second peak at -1011 mV attributed to desorption of mercaptohexanol. Surface coverages of the probe DNA and mercaptoethanol determined from the areas beneath the two peaks were 2.05×10^{-10} mol cm^{-2} and 1.95×10^{-10} mol cm^{-2} respectively. The molar ratio derived from the surface coverages of the two components of 1.05 lends support to the hypothesis that this technique may have potential as a means of better estimating the surface coverage on the electrode surface. Unfortunately the fact that the technique is destructive in terms of the monolayer and that reproducibility is also an issue suggests that further work is required before a complete understanding of the issues surrounding DNA sensor reproducibility can be attained.

5.1 References

1. Popenoe, D.D., Deinhammer, R.S., Porter, M.D. *Langmuir*, 1992, 8, 2521-2530.
2. Napier, M.E., Thorp, H.H. *Langmuir*, 1997, 13, 6342-6344.
3. Steel, A.B., Levicky, R.L., Herne, T.M., Tarlov, M.J. *Biophys. J.*, 2000, 79, 975-981.
4. Li, Z., Jin, R.C., Mirkin, C.A., Letsinger, R.L. *Nucleic Acids Res.*, 2002, 30, 1558-1562.